TECHNISCHE UNIVERSITÄT MÜNCHEN

Lehrstuhl für Aerodynamik und Strömungsmechanik

Numerical Simulation and Analysis of Shock Phenomena in Cavitating Flow and its Application to Ship Propellers

Bernd Budich

Vollständiger Abdruck der von der Fakultät für Maschinenwesen der Technischen Universität München zur Erlangung des akademischen Grades eines

Doktor-Ingenieurs (Dr.-Ing.)

genehmigten Dissertation.

Vorsitzender:		Prof. Dr.-Ing. Steffen Marburg
Prüfer der Dissertation:	1.	Prof. Dr.-Ing. Nikolaus A. Adams
	2.	Prof. Dr. Ir. Tom J. C. van Terwisga

Die Dissertation wurde am 27.06.2017 bei der Technischen Universität München eingereicht und durch die Fakultät für Maschinenwesen am 09.03.2018 angenommen.

Bernd Budich: *Numerical Simulation and Analysis of Shock Phenomena in Cavitating Flow and its Application to Ship Propellers*,
Dissertation, Technische Universität München, Germany

Released 03.07.2018

Address:
Reutberger Straße 18, 81371 München, Germany

E-Mail:
bernd.budich@tum.de

Numerical Simulation and Analysis of Shock Phenomena in Cavitating Flow and its Application to Ship Propellers

Bernd Budich

to my family and friends.

Danksagung

An dieser Stelle möchte ich einer Reihe von Personen danken, die ganz wesentlich zum Gelingen dieser Arbeit beigetragen haben.

Zu allererst gebührt mein Dank Prof. Nikolaus Adams. Mit Ihren Vorlesungen zur Fluidmechanik haben Sie bereits im Grundstudium mein Interesse an der Strömungsmechanik geweckt, und damit den Weg für alles Weitere geebnet. Ich entschloss mich, sowohl die Diplom-, also auch die Doktorarbeit am Lehrstuhl für Aerodynamik und Strömungsmechanik anzufertigen. Für die Betreuung und fortwährende Unterstützung in dieser Zeit möchte ich mich ganz herzlich bei Ihnen bedanken. In vielen Diskussionen haben Sie mir immer wieder neue Impulse gegeben, mir aber gleichzeitig auch sehr viel Freiheit bei der Ausgestaltung meiner wissenschaftlichen Arbeit gelassen.

Weiterhin möchte ich meinem Zweitgutachter, Prof. Tom van Terwisga ganz herzlich danken. Seit ich Sie in Austin auf meiner ersten Konferenz persönlich kennenlernen durfte, haben sich unsere Wege auf vielen Stationen immer wieder gekreuzt. Bedanken möchte ich mich für die vielen interessanten und anregenden Gespräche, die wir bei diesen Gelegenheiten führen konnten - dies blieb bis einschließlich der Verteidigung bestehen.

A special thanks goes to Prof. Steve Ceccio and Harish Ganesh for the fruitful exchange of ideas on cavitation and the wedge experiment. A discussion on the pecularities of condensation shocks while watching whales in Monterrey Bay is certainly one of the nicer things when pursuing a PhD.

An alle Kollegen am Lehrstuhl geht ein Dank für die offene, motivierende und nicht zuletzt freundschaftliche Atmosphäre. Bedanken möchte ich mich besonders bei Steffen. Auch wenn das “Aufnahmeritual” beim Italiener erst recht spät stattfand - du hast mich immer großartig unterstützt. Mit dir gemeinsam durch den Yosemite zu stiefeln war mir ein echtes Vergnügen. Außerdem möchte ich auch meinen (Nachbar-)Büro-Kollegen danken: Marcus, Michael, Felix, Jan, Vito, Bruno, Theresa, Polina, Daria. Mit vielen on- und noch mehr off-topic-Unterhaltungen und “Aktivitäten”, innerhalb wie außerhalb des Lehrstuhls habt ihr das manchmal doch etwas zähe Doktorandendasein nicht nur sehr viel angenehmer gemacht. Mehr noch, aus Kollegen sind Freunde geworden.

Zu guter Letzt, das Wichtigste. Ganz besonders möchte ich mich bei Thomas, Katja und meinen Eltern bedanken. Bei euch habe ich immer Rückhalt, sowie den notwendigen moralischen als auch organisatorischen Support finden können. Außerdem habt ihr immer geduldig zugehört, egal ob ich besonders entnervt, oder besonders euphorisch war ;-)

Abstract

Numerical Simulation and Analysis of Shock Phenomena in Cavitating Flow and its Application to Ship Propellers

In this thesis, numerical studies of the cavitating flow in two complementary, engineering-relevant applications are carried out. The first investigation considers the canonical flow configuration of a partial cavity, which exhibits sheet-to-cloud transition and shedding. The second application targets the numerical simulation of wetted and cavitating flow around a model ship propeller. The numerical method employed for both subjects relies on the assumption of a homogeneous mixture, equilibrium thermodynamics, and a closed-form barotropic equation of state. Utilizing a density-based approach, full two-phase compressibility is retained in the model. All relevant time-scales of cavitating flow are resolved by explicit integration in time. The devised method captures cavitation-induced shock-wave dynamics, its interaction with phase transition, and the feed-back with convective flow dynamics. The investigations provide novel insight into the flow physics of condensation shocks. Representing an intrinsic mechanism of instability for sheet cavitation, this phenomenon did not gain attention in the literature until recently. The configuration is dominated by inertial effects, phase transfer, and wave dynamics. It is demonstrated that an inviscid model is sufficient for capturing the flow dynamics for this type of flow. In the second part, the Potsdam Propeller Test Case (PPTC) is reproduced. In addition to the inviscid approach, also implicit large-eddy-simulations (ILES) are carried out. Juxtaposing results obtained with both numerical methods, a total of 10 different operating points is analyzed, in which the integral open-water performance, the propeller wake field, blade pressure distributions, the topology of cavitating flow, as well as a qualitative and quantitative evaluation of flow aggressiveness is studied. While important differences are found for wetted flow, it is shown that equivalent conclusions can be drawn with both schemes for cavitating flow conditions. Particularly, this also includes the quantitative assessment of flow aggressiveness. To the author's knowledge, the conducted studies represent the first fully-compressible investigations of cavitating propeller flow.

Zusammenfassung

Numerische Simulation und Analyse von Stoß-Phänomenen in kavitierenden Strömungen und ihre Anwendung auf Schiffsschrauben

In Rahmen dieser Arbeit werden numerische Analysen der kavitierenden Strömung für zwei technisch relevante Systeme durchgeführt. Der erste Teil der Arbeit betrachtet die kanonische Strömung einer partiellen Schichtkavitation, welche durch die wiederkehrende Ablösung großskaliger Wolkenkavitation gekennzeichnet ist. Anschließend wird im zweiten Teil die Umströmung eines Modell-Propellers mit und ohne Phasenübergang numerisch untersucht. Das für beide Studien benutzte numerische Model stützt sich auf die Annahme einer homogenen Mischung, Gleichgewichtsthermodynamik, und eine analytische, barotrope Zustandsgleichung. Alle relevanten Zeitskalen kavitierender Strömungen werden mittels expliziter Zeitintegration aufgelöst. Die verwendete Methode erfasst Kollaps-induzierte Stoßwellendynamiken, ihre Interaktion mit dem Phasenübergang, sowie die Rückkopplung mit konvektiven Skalen der Strömung. Die Untersuchungen liefern neue Einblicke in die Physik von Kondensationsstößen. Dieses Phänomen stellt einen zusätzlichen Instabilitätsmechanismus für Schichtkavitation dar, welches bis auf wenige Studien nicht Gegenstand der gegenwärtigen Literatur ist. Die untersuchte Strömung ist vollständig gesteuert durch Trägheitseffekte, Phasenübergang, sowie Wellendynamik. Es wird gezeigt, dass der verwendete reibungsfreie Ansatz ausreichend ist, um alle Strömungsphänomene, die für diese Konfiguration relevant sind, zu betrachten. Mit dem im zweiten Teil untersuchten Modell-Propeller wird der Potsdam Propeller Test Case (PPTC) nachvollzogen. Zusätzlich zu reibungsfreien Rechnungen werden dazu auch implizite Grob-Struktur-Simulationen (implicit large-eddy simulations, ILES) durchgeführt. Die Ergebnisse beider numerischer Ansätze werden für zehn verschiedene Betriebspunkte vergleichend analysiert. Dies umfasst die Untersuchung der Freifahrt-Charakteristik des Propellers, den Propeller-Nachlauf, die Druckverteilung über dem Schaufelblatt, eine eingehende Analyse der Strömungstopologie unter kavitierenden Bedingungen, sowie eine qualitative und quantitative Bewertung der Strömungsaggressivität. Für die Untersuchungen ohne Phasenübergang werden wichtige Unterschiede in der Vorhersage festgestellt. Es wird jedoch gezeigt, dass beide Methoden für Strömungen mit Phasenübergang gleichwertige Ergebnisse erzielen, insbesondere auch hinsichtlich der Strömungsaggressivität. Soweit dem Autor bekannt, stellt die durchgeführte Studie die erste voll-kompressible Betrachtung der kavitierenden Umströmung einer Schiffsschraube dar.

Publications

The subjects considered in this thesis have been contributed continuously to the scientific community during the course of this PhD project. The present thesis is based on the publications listed below.

Peer-Reviewed Journal Papers

1. B. Budich, S. J. Schmidt, N. A. Adams (2018). „Numerical Simulation and Analysis of Condensation Shocks in Cavitating Flow“. In: *Journal of Fluid Mechanics* 838, pp. 759–813. DOI: 10.1017/jfm.2017.882

Peer-Reviewed Conference Proceedings

1. B. Budich, S. J. Schmidt, N. A. Adams (2015a). „Numerical Investigation of a Cavitating Model Propeller Including Compressible Shock Wave Dynamics“. In: *Proceedings of the 4th International Symposium on Marine Propulsors*. Austin, TX, USA

2. B. Budich, S. J. Schmidt, N. A. Adams (2015b). „Numerical Simulation of Cavitating Ship Propeller Flow and Assessment of Erosion Aggressiveness“. In: *Proceedings of the 6th International Conference on Computational Methods in Marine Engineering*. Rome, Italy

3. B. Budich, F. Borrmann, S. J. Schmidt, and N. A. Adams (2015c). „Assessment of Erosion Aggressiveness for the Cavitating Model Propeller VP1304 by Fully Compressible Numerical Simulation“. In: *Proceedings of the 18th Numerical Towing Tank Symposium*. Cortona, Italy

4. B. Budich, S. Neuner, S. J. Schmidt, and N. A. Adams (2015d). „Numerical investigation of shedding partial cavities over a sharp wedge“. In: *Proceedings of the 9th International Symposium on Cavitation*. Lausanne, Switzerland

5. B. Budich, S. J. Schmidt, N. A. Adams (2016a). „Numerical Investigation of Condensation Shocks in Cavitating Flow“. In: *Proceedings of the 31st Symposium on Naval Hydrodynamics*. Monterey, CA, USA

6. B. Budich, S. J. Schmidt, N. A. Adams (2016b). „Implicit Large Eddy Simulation of the Cavitating Model Propeller VP1304 using a Compressible Homogeneous Mixture Model“. In: *Proceedings of the 31st Symposium on Naval Hydrodynamics*. Monterey, CA, USA

The following publication has been prepared by the author while being a Research Associate at the TUM Institute of Aerodynamics and Fluid Dynamics. The subject, however, is not covered in this thesis.

7. B. Budich, V. Pasquariello, M. Grilli, and S. Hickel (2013). „Passive Flow Control of Shock-Wave/Turbulent-Boundary-Layer-Interactions Using Micro Vortex Generators“. In: *Proceedings of the 8th International Conference on Turbulence and Shear Flow*. Poitiers, France

Contributions to Scientific Conferences without a Written Paper

1. B. Budich, S. J. Schmidt, N. A. Adams (2014). „Numerical Investigation of a Cavitating Ship Propeller Including Collapse-Induced Wave Dynamics“. In: *Kolloquium Kavitation und Kavitationserosion*. Bochum, Germany

2. B. Budich, S. J. Schmidt, N. A. Adams (2017). „Compressible Implicit Large-Eddy Simulation of the Cavitating Model Propeller VP1304“. In: *7th International Conference on Computational Methods on Marine Engineering*. Nantes, France

Table of Contents

List of Figures

List of Tables

CHAPTER 1

Introduction

1.1 Motivation & Scope

Cavitation, i.e., the local evaporation of liquid due to a static pressure drop, the subsequent formation of cavities, and the successive re-condensation of the latter, is ubiquitous in fluid engineering. In some areas of application, cavitating flow can be leveraged in an advantageous manner. For example, it can be utilized for surface cleaning (Ohl *et al.*, 2006a), or to enhance medical drug delivery via sonoporation (Ohl *et al.*, 2006b; Lentacker *et al.*, 2014). In shock-wave lithotripsy, cavitation is employed for the destruction of kidney or gall stones (Johnsen and Colonius, 2008). Furthermore, cavitation enhances jet break-up, and subsequent spray formation of nozzle flow (Lin and Reitz, 1998; Örley *et al.*, 2015), or is used for homogenization of emulsions in processing industry (Innings *et al.*, 2011). For most hydraulic systems, on the other hand, negative effects originating from cavitating flow prevail. As reviewed by Arndt (1981), affected systems encompass turbo-pumps, hydro-turbines, and ship propellers, equally as hydraulic ducting or spillways of embankment dams. Typically, cavitation leads to a degradation of system efficiency, e.g., by deteriorating deliverable power output, or increasing drag resistance. Moreover, collapsing vapor structures cause radiated noise, and may further induce excitation and vibration of nearby structures (Franc and Michel, 2005). When exposed to cavitating flow over a sustained amount of time, most materials will be damaged (Kim *et al.*, 2014). Cavitation erosion thus may eventually lead to failure of the affected components, or the system as a whole.

In most situations, avoiding cavitation in its entirety is not feasible, or practical (Franc and Michel, 2005). However, due its detrimental effects on most engineering applications, it should be minimized, or controlled as much as possible. It is thus essential to assess the susceptibility of a system to the occurrence of cavitating flow, as well as to predict the location, extent, and dynamics of cavitation. For this purpose, Computational Fluid Dynamics (CFD) represents a valuable tool in the design process. Already at an early stage, it can give important insights into the flow, and flow physics, by providing a spatial and temporal resolution which is often difficult to achieve when relying solely on experiments. Furthermore, numerical models enable the development of quantitative measures for the flow aggressiveness (Li, 2012; Mihatsch *et al.*, 2015), which is not easily deducible from experiments for full- or model-scale geometries.

Various approaches for the numerical modeling of cavitation are available, a good review is provided by Egerer *et al.* (2014a) and Schmidt (2015). The majority of the studies focusing on industrial applications rely on the assumption of liquid incompressibility, or assume pseudo-compressibility. However, from investigations of collapse mechanisms for single isolated bubbles, e.g., by Philipp and Lauterborn (1998) and Lindau and Lauterborn (2003), evidence for collapse-induced shock generation is provided. Experimental observations indicate that similar phenomena occur in cloud cavitation, while additional bubble interactions considerably increase complexity. For collapsing isolated vapor bubbles, the maximum instantaneous pressure is observed to reach several GPa (Philipp and Lauterborn, 1998), while likely being even higher for collapsing clouds. From these findings one can conclude that for a quantitative prediction of cavitation erosion, the resolution of collapse-induced pressure peaks is critical. Furthermore, the coupled behavior between phase transition and wave dynamics may lead to an alteration of system dynamics (Arndt *et al.*, 2000; Leroux *et al.*, 2004).

A promising approach thus is the fully-compressible model pioneered by Schnerr *et al.* (2008) and Schmidt (2015), relying on the assumption of a homogeneous mixture, and the use of thermodynamic closures for modeling phase transfer. It captures all time-scales of cavitating flow, including compressible shock waves emitted upon cavity collapse events. While accounting for the interaction between phase transition and acoustics, the inherently transient nature of cavitating flow is resolved, and collapse-induced pressure peaks are only subject to the spatial resolution. The method thus allows to derive quantitative measures for the flow aggressiveness, as done by Mihatsch *et al.* (2015).

Capturing compressible wave dynamics requires explicit time integration, which yields time-steps on the order of nano-seconds, or below. In order to cover convective time-scales, at least tens of millions of iterations are necessary, and the

compressible approach is hence associated with a high computational cost. Cavitating flow in most configurations is predominantly governed by inertial effects and wave dynamics. Therefore, molecular viscosity is often deliberately omitted from the model, with the additional benefit of reducing the computational burden.

In order to further assess and review the role of the inviscid assumption in the scope of this thesis, the compressible approach is applied to two complementary subjects. The first investigation examines the canonical cavitating flow of a shedding partial cavity. The second considers cavitating ship propeller flow, which has not been investigated in the literature using a compressible method before.

In the first study, sheet-to-cloud transition of a partial cavity within a channel flow characterized by a well-defined line of separation is analyzed. The computations are validated with time-resolved x-ray densitometry measurements by Ganesh *et al.* (2016a), and results are in close agreement with the experimental references. It is shown that the inviscid flow model captures cavity dynamics across all relevant scales, and that the process is predominantly driven by phase-change, inertial effects, and wave-dynamics. This leads to the conclusion that viscous effects play only a subordinate role, while compressibility is crucial for this type of flow. A further focus of this investigation lies on the comprehensive discussion of condensation-shock phenomena. Dominating the sheet-to-cloud transition as well as cavity dynamics, condensation shocks differ fundamentally from hydrodynamic shock waves emitted during cavity collapse events. The work thus provides new insights into the physics governing the dynamics of partial cavities. It confirms the experimental observation that, alongside the re-entrant jet mechanism, which is classically associated with sheet cavitation, condensation shocks feed an additional intrinsic instability mechanism for partial cavities.

With the second part, the capabilities of the fully compressible method in the context of ship propeller flow are evaluated. This extends previous investigations on planar and non-planar but non-rotating hydrofoils (Schmidt *et al.*, 2007; Schnerr *et al.*, 2008; Schmidt *et al.*, 2009) to rotating propeller blades, including also effects of the propeller hub, and secondary flow. Due to the moderate Reynolds-numbers of the considered model propeller, the flow may be subject to scaling effects. A goal of this study thus is the assessment of the model uncertainty stemming from the inviscid assumption. Therefore, the inviscid model used for the previous analysis is juxtaposed to a more elaborate numerical scheme, based on filtering the governing equations and an implicit large eddy simulation (ILES) approach, which incorporates viscous effects. The propeller is studied for both wetted as well as cavitating flow conditions, and results are validated with experimental and alternative numerical studies conducted in the scope of the Potsdam Propeller Test Case (PPTC, see Schiffbau-Versuchsanstalt Potsdam, 2017). When no phase

change is present, the inviscid model shows important constraints in its applicability, as expected, while the ILES performs well for the entire range of investigated operating points. Under cavitating conditions, however, both approaches again yield comparable results regarding the location and extent of cavitation. Although the ILES resolves more cavity dynamics, the flow aggressiveness of the investigated operating points is equally rated by both methods. The investigation thus provides further evidence that the inviscid assumption is sufficient when the flow is governed by the occurrence and dynamics of cavitation.

1.2 Outline

The outline of this thesis is as follows. First, some fundamentals on cavitation and cavitating flow are introduced in chapter 2. Furthermore, a short discussion of approaches for the assessment of flow aggressiveness, relying on both experimental as well as numerical methods, is given. Subsequently, chapter 3 introduces the underlying physical model, fundamental assumptions, and the governing equations. Two thermodynamic closures are discussed, including two approaches for modeling the two-phase speed of sound. The numerical method is presented, and a brief description of the flow solver is provided. The following two chapters cover the main studies conducted in the scope of this thesis. In chapter 4, the canonical flow configuration of partial cavitation exhibiting sheet-to-cloud transition and the condensation shock phenomenon is analyzed. Subsequently, the model ship propeller *VP1304* is investigated for both wetted and cavitating flow conditions in chapter 5. A review covering the aspects relevant for the individual subjects and related literature is provided within both chapters, respectively. At the end of each chapter, major findings and conclusions are summarized. Finally, concluding remarks, an outlook, and recommendations for future work are given in chapter 6.

CHAPTER 2

Fundamentals

This chapter briefly introduces some fundamental aspects of cavitation and cavitating flow. First, inception mechanisms, common flow topologies, and the intrinsic dynamics of cavitating flow are presented in §2.1. Subsequently, several approaches for the assessment of flow aggressiveness are briefly reviewed in §2.2. The survey covers methods relying on both experimental and numerical investigations.

Focusing only on basic concepts, the following discussion is by no means meant to be exhaustive. For a comprehensive and more detailed presentation of these subjects, see, e.g., the textbooks by Brennen (1995), Franc and Michel (2005), and Kim *et al.* (2014).

2.1 Cavitation

Preliminary Considerations *Cavitation* denotes the formation of vapor within a liquid medium, caused by a change in the local static pressure p. This can be illustrated with a phase diagram of a one-component liquid, such as, e.g., water, shown in figure 2.1. The diagram includes the regions of the solid, liquid, and vapor phase. Connecting triple and critical point, the line of coexistence of liquid and vapor phase is denoted as the saturation pressure p_{sat}, which is dependent on the temperature T, only. Liquid evaporation can be categorized into two processes, (a) an increase in temperature while keeping an essentially constant pressure, denoted as *boiling*, or (b) by decreasing the pressure at almost constant temperature, i.e., *cavitation*. Due to the latent heat of evaporation, a slight decrease in temperature is observed in the surrounding liquid, denoted as *thermal delay*.

A further discrimination can be conducted regarding the driving mechanism for the pressure drop. In *acoustic cavitation*, it is induced by pressure waves, as, e.g., generated by an ultrasonic sonotrode. Alternatively, the decrease in pressure can be realized by the flow, e.g., by accelerating the liquid, low-pressure regions near flow obstacles, or within vortex cores. This process is termed *hydrodynamic cavitation*, and is found in many applications, such as diesel or gasoline injection components, hydraulic ducts or the liquid film of bearings. Hydraulic turbo-machinery, such as water turbines, turbo-pumps, or, as investigated in this thesis, ship propellers, are affected by cavitation as well.

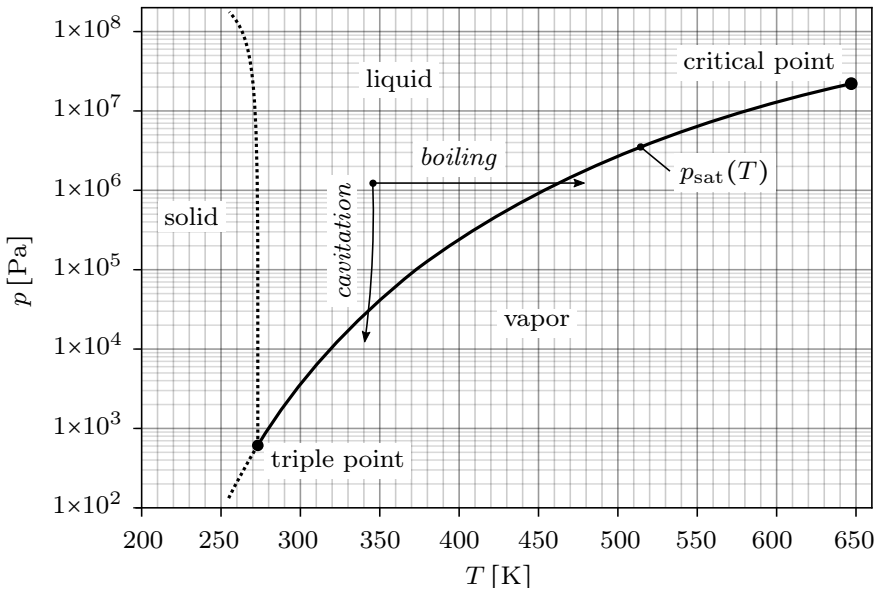

Figure 2.1: Phase diagram of water, for a pressure range of $1 \times 10^2\,\mathrm{Pa} \leq p \leq 1 \times 10^8\,\mathrm{Pa}$, and a temperature range of $200\,\mathrm{K} \leq T \leq 650\,\mathrm{K}$.

The vapor pockets, or *cavities*, are typically advected with the liquid flow. When subjected again to an increase in pressure, a sudden, implosion-like re-condensation takes place. This is typically associated with the generation of intense pressure peaks upon collapse, inducing shock waves that subsequently propagate through the surrounding liquid. The pressure peaks are maximal for symmetric collapse events, which may occur in the bulk of the liquid. In the vicinity of material walls, however, collapses occur asymmetrically, and a so-called *micro-jet* is formed, directed towards the wall.

Cavitation Inception The first initiation of cavitation when decreasing the minimum pressure within the liquid is denoted as *cavitation inception*. Two fundamental mechanisms of cavitation inception can be discriminated. *Homogeneous cavitation* describes the formation of vapor structures within the bulk of a pure liquid. For *heterogeneous cavitation*, in contrast, impurities in the liquid act as nucleation sites, thereby facilitating cavitation. These impurities, e.g., immersed solid particles, micro bubbles of non-condensable gas, gas trapped in crevices of rough walls, or other particles and contaminations, are ubiquitous for untreated substances. In consequence, "homogeneous nucleation [...] becomes virtually irrelevant in water at normal temperatures" (Brennen, 1995).

Heterogeneous cavitation is hence the predominant mechanism in most technical applications. The susceptibility to cavitation may depend on the number of nucleation sites (Franc and Michel, 2005). Cavitation hence does not necessarily take place immediately when crossing the saturation line. Instead, the pressure can drop below the saturation pressure, until a certain critical threshold pressure p_{th} is reached, before inception occurs. The pressure difference $p_{\mathrm{th}} - p_{\mathrm{sat}}$ is denoted as *(static) cavitation delay*.

For highly purified liquids, the threshold pressure p_{th} can be well below the vapor pressure p_{sat}, i.e., the liquid may attain meta-stable, non-equilibrium states. Depending on "the contamination of the liquid and the character of the containing surface" (Brennen, 1995), liquids can withstand even negative pressures, i.e., tension. A comprehensive list of experimental studies on the cavitation delay is provided by Brennen (1995), and Franc and Michel (2005), reporting values on the order of tens to hundreds of bars.

Cavitation Index The main non-dimensional parameter utilized for the characterization of cavitating flow is the *cavitation index*, or *cavitation number*, σ. Following Franc and Michel (2005), it is defined as

$$\sigma = \frac{p_{\mathrm{ref}} - p_{\mathrm{sat}}}{\Delta p} \ , \tag{2.1}$$

relating the difference between a reference pressure and the vapor pressure to a pressure difference, which characterizes the system under consideration. The cavitation number is thus a problem-dependent parameter. Frequently, reference conditions at a specified upstream location are chosen, and the pressure difference is given by the dynamic pressure at that location, such that

$$\sigma = \frac{p_{\mathrm{ref}} - p_{\mathrm{sat}}}{\frac{1}{2}\rho_{\mathrm{ref}} u_{\mathrm{ref}}^2} \ , \tag{2.2}$$

with ρ_{ref} denoting a reference density, which is typically chosen as equal to the liquid density at the reference station. Commonly, for ship propellers as considered with chapter 5, the rotational speed is taken as the characteristic velocity. This yields the cavitation number σ_n

$$\sigma_n = \frac{p_{\mathrm{ref}} - p_{\mathrm{sat}}}{\frac{1}{2}\rho_{\mathrm{ref}} (nD)^2} \ , \tag{2.3}$$

with n being the rate of revolution, and D the diameter of the propeller.

Cavitation Topologies Cavitating flow can attain various topologies. Franc and Michel (2005) in this respect discern three "main forms" of cavitation. *Bubble cavitation* exhibits single, isolated vapor bubbles. Typically, these originate from nuclei present in the free-stream, or from wall roughnesses, and are advected along with the flow. Depending on their size and shear forces in the flow, bubble cavities are not necessarily of spherical shape. *Attached* or *sheet cavitation* form within low-pressure regions. In contrast to bubble cavitation, these cavities remain essentially fixed in space. Yet, they can still undergo large variations in volume. Examples are cavities attached at nozzle inlets, or to low-pressure regions, such as the leading edge, or the suction side, of a hydrofoil. A further candidate region for cavitation are the low-pressure cores of vortices. Provided that the pressure drop is large enough, *vortex cavitation* can appear in small-scale turbulent eddies, as well as in large-scale vortical structures. Examples for the latter are the tip vortex of a finite wing, or the hub vortex of a turbine runner.

Not covered by the above classification is *cloud cavitation*. Sometimes regarded as an additional topology, cloud cavities are an agglomeration of vapor bubbles of various length-scales. Furthermore, when a sheet cavity covers only a portion of the geometry it is attached to, this type of cavitation is also termed *partial cavitation*. The extent of *super-cavitation*, in contrast, is comparable, or exceeds the length of the affected object.

Especially for hydrodynamic cavitation occurring in most technical system, some, or all of the above "main forms" may co-exist. Frequently, a clear spatial or

temporal distinction is difficult, as transition between these topologies occur. An example is the case of sheet-to-cloud transition, as discussed in chapter 4.

Cavitation Dynamics Close to cavity inception, when the extent of cavitating regions is still small, the dynamics are largely dictated by the surrounding (wetted) flow pattern (Franc and Michel, 2005). At lower cavitation numbers, the extent of cavitation increases, and the cavities start to interfere with the flow. This feed-back loop renders cavitating flow inherently unstable. Two fundamental mechanisms of intrinsic instability are the *re-entrant jet*, and *condensation shocks*, see chapter 4 for a closer discussion of these phenomena. These mechanism will lead to periodic oscillation of partial or sheet cavities, causing a sheet-to-cloud transition, and hence, shedding.

The shedding frequency f can be non-dimensionalized by a characteristic velocity u_{ref} and length L_{ref}, to give a Strouhal-number

$$St = \frac{f L_{\text{ref}}}{u_{\text{ref}}} \ . \tag{2.4}$$

Alternative definitions of the Strouhal-number are possible, see, e.g., the discussion of Dular and Bachert (2009). For shedding partial cavities, the Strouhal-number typically falls into the range $0.25 \leq St \leq 0.35$ (Franc and Michel, 2005). Note, however, that perfect repeatability of the shedding is rarely observed. Rayleigh-Taylor and Kelvin-Helmholtz instabilities, as discussed in chapter 4, contribute to a stochastic behavior of the flow. Therefore, frequency spectra typically do not exhibit a single isolated peak, but elevated amplitudes in a certain band around the shedding frequency.

2.2 Erosion Assessment

Cavitation typically imposes a constraint on the operation envelope through the discussed detrimental effects on the system efficiency, induced noise, as well as vibration levels. However, material erosion is often of major concern for technical systems affected by cavitation, and "perhaps the most ubiquitous engineering problem caused by cavitation is the material damage" (Brennen, 1995). Important design variables are the locations prone to cavitation erosion, incubation times, i.e., the time when material removal is first detected, and damage rates.

A comprehensive overview of experimental techniques used for assessing cavitating erosion is provided by Chahine *et al.* (2014). A direct observation of material erosion by experiments is very challenging. Often, full-scale experiments with realistic

geometries can only be carried out with the final product, during normal operation. While providing valuable data, this only enables an *a posteriori* evaluation of the design. Furthermore, the investigations are subject to operating conditions and an environment which are difficult to control, and assess. On the other hand, within the controllable environment of a laboratory, often only simplified, or scaled specimen can be utilized. Furthermore, it is rarely possible, or feasible, to observe erosion within the time frames available for observation.

In order to lower the required exposure times in model-scale, the cavitation intensity needs to be increased. The American Society for Testing and Materials (ASTM, see American Society for Testing and Materials, 2017) standardized two of these accelerated erosion experiments, i.e., submerged cavitating jets (*ASTM GS134*), and tests using ultrasonic horns (sonotrodes, *ASTM GS32*), see Chahine *et al.* (2014) for further references to these techniques. Another example of accelerated erosion experiments is the flow within the radially divergent gap investigated by Franc (2009). While the cavitation jet exhibits cavitating shear layers and vortices, the latter example is characterized by sheet-to-cloud transition. While these cavitation topologies are commonly encountered in technical devices, the flow in the aforementioned studies is only representative for the full complexity found in a realistic geometry. These tests are therefore primarily utilized for evaluating the (relative) resistance of different materials, or coatings, against cavitation erosion.

When geometric similarity to the actual technical system is required, a common technique for the assessment of flow aggressiveness is the visual inspection of high-speed videos in model- or full-scale tests. Several attempts of (a) systematizing the physical mechanisms responsible for material erosion, and (b) estimating the erosiveness for individual events from direct visualization of the flow evolution are discussed in the literature. Kawanami *et al.* (2002) use laser holography for a three-dimensional reconstruction of the flow field. The authors identify cavitating horse-shoe structures, commonly found in cloud cavitation, as highly erosive events. The erosiveness of these flow features is attributed by the authors to a focusing of bubbles towards the wall in the "legs" of the vortex. A comprehensive framework for the identification of potentially damaging cavitation structures is proposed by Bark *et al.* (2004). Distinguishing "global", "local", "focusing", and "micro" cavities, the authors provide a taxonomy, which supports the designer for relating the observation of several hydrodynamic processes to potential material erosion. The authors find that in most cases, cloudy structures are the cause of erosive cavitation. Dular and Petkovšek (2015) categorize flow structures that cause material erosion as well, discriminating five fundamental mechanisms: "spherical cloud collapse", "horse-shoe cavitation cloud collapse", "twister cloud collapse", "cloud separation", and "cavity closure". The authors also conclude that cloud-related collapse events account for 80% of the observed damage in their study.

In addition to the visual assessment of flow features, several other techniques can be applied. Boorsma and Fitzsimmons (2009), e.g., demonstrate how acoustic emissions can be leveraged to determine operating conditions leading to erosive cavitation for a ship propeller. For ship propellers, paint removal tests, see, e.g., Carlton (2012) and the references therein, are recommended by the International Towing Tank Conference (see International Towing Tank Conference, 2017) for an assessment of expected material erosion (International Towing Tank Conference, 2008). The results can, however, only be indicative, as they help to locate regions of high flow aggressiveness, but do not provide information about erosion severity (Kuiper, 1997).

All of the aforementioned studies require sound experience regarding their calibration, the correct interpretation of the results, as well as their appropriate extrapolation to the full-scale product. This leads Kuiper (1997) to the conclusion that "cavitation research has not given the designer a reliable method to measure the erosivity of cavitation".

It is advantageous to supplement experimental work by numerical analysis methods, as the flow evolution can be observed, in principle, at arbitrary time and spatial resolution. As such, e.g., flow phenomena internal to cavities can be investigated, which are difficult to observe with experimental visualization techniques. As discussed by Bensow *et al.* (2013), this can be used complementary to experimental high-speed videos for a visual evaluation of flow aggressiveness. Terwisga *et al.* (2009) reviews various erosion models which can be used for a more quantitative assessment of flow aggressiveness using numerical methods. In a related work, Li (2012) surveys some of these methods, e.g., by Nohmi *et al.* (2008), and proposes a new erosion intensity function, based on the summation of the rate of pressure change $\partial p/\partial t$, when exceeding a certain threshold. The authors observe a general improvement in their predictions over previous methods, but also find some points of disagreement for the investigated configurations of a NACA 0015 and a NACA 0018-45.

Although good results are obtained for the analyzed cases, some difficulties with the above methods remain. Often they involve threshold values, which cannot be determined *a priori*, and are case-dependent in general. Furthermore, the derived "erosion intensity" is a scalar value, and thus does not provide time- or rate information. However, cavitating flow exposes a solid boundary to a collective load of collapse events of different strengths, occurring with different rates. In general, the most violent events appear least often, while lower-intensity events occur at a higher frequency. Thus, a more suitable characterization of the "erosive potential" (Franc, 2009) of a flow can be achieved by incorporating rate and strength information, as, e.g., provided by (impact) load spectra, see also Franc *et al.* (2011).

A natural choice for the assessment of flow aggressiveness relies on the static pressure p. However, when employing a numerical method using an incompressible treatment of the flow, the pressure is a result of fulfilling the requirement of a divergence-free flow field, and thus is not directly related to cavity collapse events. A possible rectification is the usage of discrete bubble models, coupled to the incompressible solver, see, e.g., Ma *et al.* (2016). Through this approach, collapse peak pressures can be computed and utilized for the erosion assessment, as, e.g., done by Nohmi *et al.* (2008). However, these methods require further assumptions, e.g., regarding the modeling of bubble deformation, bubble-bubble and bubble-flow interactions, as well as bubble break-up and coalescence mechanisms, in order to capture the full dynamics of cavitating flow.

A fully compressible method can be utilized to remedy these aspects, as it captures collapse-induced pressure peaks and resolves the associated propagating shock waves structures. Computed pressure fluctuations, which are subject only to the spatial resolution, can be leveraged for a direct assessment of flow aggressiveness. As motivated initially, the latter approach of a fully compressible model is chosen in this thesis. For assessing the flow aggressiveness, two indicators based on the resolved pressure peaks are utilized. These are discussed in more detail in §3.3, after a presentation of the numerical method with the next chapter.

CHAPTER 3

Numerical Modeling of Cavitating Flow

This chapter introduces the physical modeling and the numerical method employed for the studies throughout this thesis. In the first part, §3.1, underlying assumptions and the governing equations are examined with §3.1.1 and §3.1.2, respectively. Following, two thermodynamic closures are presented in §3.1.3, including a discussion of modeling the two-phase speed of sound in cavitating flow. The second part, §3.2, presents the numerical method. The time-integration scheme is briefly considered in §3.2.1, and §3.2.2 introduces the employed Arbitrary-Lagrangian-Eulerian approach for describing a moving numerical grid. Subsequently, two discretization schemes for the evaluation of the numerical flux are presented in §3.2.3. In the third part, §3.3, two methods used in this thesis for the qualitative and quantitative assessment of flow aggressiveness are presented. A short description of the employed flow solver CATUM, and its extension in the scope of this thesis are given in §3.4, before a summary in §3.5 concludes this chapter.

This chapter is partially based on previous publications of the author, see Budich *et al.* (2016b), and Budich *et al.* (2018).

3.1 Physical Model

3.1.1 Fundamental Assumptions

In this thesis, the homogeneous equilibrium cavitation model developed by Schmidt (2015) is utilized, which bases on the assumptions of phase, thermal and mechanical equilibrium. In the following, these and additional assumptions employed for the subsequent analyses are briefly reviewed. For a more detailed examination, see, e.g., the work of Schnerr *et al.* (2008), Sezal (2009), and Schmidt (2015).

Compressibility and the associated shock wave phenomena play a dominant role for cavitating flow. Reisman *et al.* (1998) identify several isolated flow phenomena and relate them to propagating shock waves, e.g., "leading-edge structures" and "crescent-shaped regions". In addition, the interplay between collapse dynamics, wave dynamics, and phase transition may lead to a change of the dynamics of the system as a whole. This is, e.g., demonstrated by Arndt *et al.* (2000), and more recently by Ganesh *et al.* (2016b), by investigating sheet-to-cloud transition for a 2D NACA 0015 hydrofoil. Both groups find a "multi-modal behavior" (Ganesh *et al.*, 2016b) of the shedding Strouhal-number, caused by the formation of propagating shock waves. Induced by the downstream collapse of vapor clouds, these act on the upstream attached sheet cavity, thereby affecting the behavior of the system itself. Finally, pressure peak loads generated during cavity collapse events have a significant contribution to the flow aggressiveness and generated noise. Reisman *et al.* (1998) conclude that "shock wave dynamics rather than the collapse dynamics of single bubbles determine the damage and noise in many cavitating flows". These pressure peaks can only be properly captured when accounting for the compressibility of the liquid. Therefore, full two-phase compressibility is retained in the model developed in the following.

For technical applications, the cavitation delay discussed in §2.1 is usually negligible when compared with typical pressure gradients, since the level of contamination in untreated substances such as tap or sea water is extremely high. Thus, for the problems considered in this thesis, it can be assumed that immediate evaporation takes place when the static pressure falls below the vapor pressure, i.e., $p_{\mathrm{th}} = p_{\mathrm{sat}}$. Liquid and vapor phases hence remain in equilibrium, and the specific Gibbs free energy of the phases is equal, $g_{\mathrm{l}} = g_{\mathrm{v}}$. Furthermore, heat transfer between phases is assumed to occur sufficiently fast, such that thermal equilibrium holds. Temperatures are hence equal at phase interfaces as well, $T_{\mathrm{l}} = T_{\mathrm{v}}$.

The influence of surface tension σ acting on phase boundaries can be assessed with the Weber number $\mathrm{We} = (\rho_{\mathrm{l}} L U^2)/\sigma$. Relating inertial forces to forces due to surface tension, the latter becomes important when $\mathrm{We} = \mathcal{O}(1)$. Here, ρ_{l} denotes the liquid density, while L and U are characteristic length and velocity scales, respectively. For water at $T \approx 20\,^{\circ}\mathrm{C}$, $\sigma \approx 0.072\,\mathrm{N/m}$. The characteristic velocity for

the problems considered in the following is $U = \mathcal{O}(10\ \mathrm{m/s})$. With $\rho_\mathrm{l} \approx 998\,\mathrm{kg/m^3}$, this yields a length scale of $L = \mathcal{O}(1 \times 10^{-7}\,\mathrm{m})$ where surface tension effects need to be considered. This is in agreement with Franc and Michel (2005), who conclude that surface tension is predominant only during the last stages of cavity collapse events. This length scale, however, is not resolved by the grids utilized in the subsequent studies. Surface tension can therefore be neglected, and mechanical equilibrium $p_\mathrm{v} = p_\mathrm{l}$ is assumed at phase boundaries.

By consideration of the Froude-number $\mathrm{Fr} = U/\sqrt{gL}$ with $g = 9.81\mathrm{m/s^2}$, the relative importance of buoyant to inertial forces can be assessed. Using $U = \mathcal{O}(10\,\mathrm{m/s})$ and $L = \mathcal{O}(1 \times 10^{-1}\,\mathrm{m})$ for the characteristic length of the considered problems, $\mathrm{Fr} = \mathcal{O}(10)$. It is concluded that buoyant forces can be neglected as well.

For the present studies, also the effect of solved and non-condensable gas content is neglected. In addition, it is assumed that both phases share a common velocity field. Together with the above assumptions of phase, thermal and mechanical equilibria, this allows to regard the two-phase flow as a homogeneous mixture of water and water-vapor, and a single-fluid cavitation model can be applied. The appropriateness of these assumptions, and of the derived homogeneous mixture approach, is demonstrated by a variety of studies, see, e.g., Schmidt (2015), Örley (2016), Egerer (2016), and Mihatsch (2017).

The dynamics of cavitating flow is often dominated by the large discrepancy in momentum between the liquid and gaseous phase. This includes the primary mechanisms of instability, e.g., re-entrant jets, and, as demonstrated in this thesis, condensation shocks. It is thus often justified to assume that the flow is inertia-dominated, and to apply inviscid modeling. The effects of viscous and thermal diffusion processes are related via the non-dimensional Prandtl-number $\mathrm{Pr} = c_p\mu/\kappa$ with the specific heat capacity c_p, dynamic viscosity μ, and thermal conductivity κ. For water at $0\,^\circ\mathrm{C} \leq T \leq 25\,^\circ\mathrm{C}$, $6 \lesssim \mathrm{Pr} \lesssim 14$. Viscous diffusivity hence dominates thermal conductivity, justifying to neglect the latter as well when assuming inviscid flow. The suitability of the inviscid assumption has been demonstrated for a range of applications, e.g., two-dimensional hydrofoils (Schmidt *et al.*, 2009), twisted hydrofoils (Schnerr *et al.*, 2008), diesel-injector components (Sezal *et al.*, 2009), or flow in a radial-diverging gap (Mihatsch *et al.*, 2015).

The applied homogeneous mixture approach, however, is not restricted to the inviscid assumption. Recently, Egerer *et al.* (2016) incorporated viscous effects into the modeling and investigated the mutual interaction of turbulence and cavitation, using an implicit, large-eddy simulation (ILES) approach. A similar method is used by Örley *et al.* (2015) for investigating cavitating nozzle flow and the subsequent primary jet break-up.

In this thesis, both inviscid and viscous modeling approaches are employed, and results are juxtaposed.

3.1.2 Governing Equations

Based on the above assumptions, the governing equations are the time-dependent, three-dimensional, compressible Navier-Stokes equations. For the assumed homogeneous mixture, only a single set of balance laws for mass, momentum, and total energy is required. In order to allow for discontinuities such as shocks and phase interfaces, the fluid domain Ω is divided into disjunct control volumes Ω_i with boundaries $\partial\Omega_i$, and the integral (weak) form of the equations is considered:

$$\frac{\partial}{\partial t}\int_{\Omega_i} \boldsymbol{U}\,\mathrm{d}V + \int_{\partial\Omega_i} \boldsymbol{F}\left(\boldsymbol{U}\right)\,\mathrm{d}\boldsymbol{S} = 0\ , \tag{3.1}$$

with the vector of conserved quantities $\boldsymbol{U}$, the physical flux $\boldsymbol{F}$, the volume element $\mathrm{d}V$ and the surface element $\mathrm{d}\boldsymbol{S} = \boldsymbol{n}\,\mathrm{d}S$, where $\boldsymbol{n}$ denotes the outward-pointing unit normal vector on $\partial\Omega_i$.

All fluid quantities discussed in the following either characterize a pure substance, or, in the case of two-phase flow present in Ω_i, denote properties of the homogeneous mixture. For this purpose, the volume-averaging operator is introduced:

$$\widehat{\bullet} \equiv \left(\int_{\Omega_i} \bullet\,\mathrm{d}V\right) / \left(\int_{\Omega_i} \mathrm{d}V\right)\ . \tag{3.2}$$

The vector of conserved quantities in equation (3.1) is then given by $\boldsymbol{U} = [\widehat{\rho}, \widehat{\rho u}_1, \widehat{\rho u}_2, \widehat{\rho u}_3, \widehat{\rho E}]^T$, with the mixture density $\widehat{\rho}$, the momentum flux of the mixture $\widehat{\rho\boldsymbol{u}} = [\widehat{\rho u}_1, \widehat{\rho u}_2, \widehat{\rho u}_3]^T$, and the total specific energy of the mixture $\widehat{E} = \left(\widehat{e} + \frac{1}{2}\widehat{\boldsymbol{u}}\cdot\widehat{\boldsymbol{u}}\right)$. The vector $\widehat{\boldsymbol{u}} = [\widehat{u}_1, \widehat{u}_2, \widehat{u}_3]^T$ denotes the fluid velocity, while $\widehat{e}$ is the specific internal energy of the mixture.

The physical flux $\boldsymbol{F}\left(\boldsymbol{U}\right)$ can be split in three parts, $\boldsymbol{F}\left(\boldsymbol{U}\right) = \boldsymbol{F}^c + \boldsymbol{F}^p + \boldsymbol{F}^v$, where $\boldsymbol{F}^c$, $\boldsymbol{F}^p$, and $\boldsymbol{F}^v$ denote the convective, pressure, and viscous flux contributions, respectively. Across $\mathrm{d}\boldsymbol{S}$, these are given as follows:

$$\boldsymbol{F}^c = \left(\boldsymbol{n}\cdot\widehat{\boldsymbol{u}}\right)\boldsymbol{U}\ ,\quad \boldsymbol{F}^p = \widehat{p}\begin{bmatrix}0\\ \boldsymbol{n}\\ \boldsymbol{n}\cdot\widehat{\boldsymbol{u}}\end{bmatrix}\ ,\quad \boldsymbol{F}^v = -\begin{bmatrix}0\\ \boldsymbol{n}\cdot\widehat{\boldsymbol{\tau}}\\ \boldsymbol{n}\cdot\left(\widehat{\boldsymbol{u}}\cdot\widehat{\boldsymbol{\tau}} - \widehat{\boldsymbol{q}}\right)\end{bmatrix}. \tag{3.3a, b, c}$$

Here, $\widehat{p}$ denotes the static pressure in the mixture, $\widehat{\boldsymbol{\tau}}$ the viscous shear stress tensor, and $\widehat{\boldsymbol{q}}$ the heat flux. With the dynamic viscosity of the mixture $\widehat{\mu}$, and the unit tensor $\boldsymbol{I}$, $\widehat{\boldsymbol{\tau}}$ is given by the assumption of a Newtonian fluid as:

$$\widehat{\boldsymbol{\tau}} = \widehat{\mu}\left(\left(\nabla\widehat{\boldsymbol{u}}\right) + \left(\nabla\widehat{\boldsymbol{u}}\right)^T - \frac{2}{3}\left(\nabla\cdot\widehat{\boldsymbol{u}}\right)\boldsymbol{I}\right)\ . \tag{3.4}$$

For obtaining the heat flux $\widehat{\boldsymbol{q}}$, Fourier's law of heat conduction is applied:

$$\widehat{\boldsymbol{q}} = -\widehat{\kappa}\,\nabla\widehat{T} \ , \tag{3.5}$$

with the thermal conductivity of the mixture $\widehat{\kappa}$, and the static temperature $\widehat{T}$.

The vapor volume or void fraction α can be expressed as:

$$\alpha = \frac{\widehat{\rho} - \rho_{\mathrm{l,sat}}}{\rho_{\mathrm{v,sat}} - \rho_{\mathrm{l,sat}}} \ , \tag{3.6}$$

where $\rho_{\mathrm{l,sat}}$ and $\rho_{\mathrm{v,sat}}$ denote the densities of saturated liquid and vapor, respectively. Furthermore, the mass fractions of liquid ε_{l} and vapor ε_{v} are:

$$\varepsilon_{\mathrm{l}} = (1-\alpha)\,\rho_{\mathrm{l,sat}}/\widehat{\rho} \quad , \qquad \varepsilon_{\mathrm{v}} = \alpha\rho_{\mathrm{v,sat}}/\widehat{\rho} \ . \tag{3.7a, b}$$

For the mixture properties $\widehat{\mu}$ and $\widehat{\kappa}$, model assumptions are necessary. Following Beattie and Whalley (1982), a quadratic law is applied for $\widehat{\mu}$ in mixture regions:

$$\widehat{\mu} = (1-\alpha)\left(1 + \frac{5}{2}\alpha\right)\mu_{\mathrm{l,sat}} + \alpha\mu_{\mathrm{v,sat}} \ , \tag{3.8}$$

with $\mu_{\mathrm{l,sat}}$ and $\mu_{\mathrm{v,sat}}$ the dynamic viscosities of liquid and vapor, respectively. For $\widehat{\kappa}$, a linear relation between the thermal conductivities of saturated water $\kappa_{\mathrm{l,sat}}$ and vapor $\kappa_{\mathrm{v,sat}}$, is assumed:

$$\widehat{\kappa} = (1-\alpha)\,\kappa_{\mathrm{l,sat}} + \alpha\kappa_{\mathrm{v,sat}} \ . \tag{3.9}$$

The quantities $\rho_{\mathrm{l,sat}}$, $\rho_{\mathrm{v,sat}}$, $\mu_{\mathrm{l,sat}}$, $\mu_{\mathrm{v,sat}}$, $\kappa_{\mathrm{l,sat}}$, and $\kappa_{\mathrm{v,sat}}$, are either modeled by temperature-dependent relations, or assumed constant, depending on the applied thermodynamic model, as discussed in §3.1.3.

As motivated above, cavitating flow can often be regarded as inertia-dominated, and the effects of molecular viscosity as well as thermal conductivity can be neglected, i.e., using $\widehat{\mu} \equiv 0$ and $\widehat{\kappa} \equiv 0$ in above equations. In consequence, the viscous flux $\boldsymbol{F}^{v}$ can be canceled from the governing equations under these assumptions, yielding the compressible Euler-equations.

A suitable thermodynamic closure for the above system of equations (3.1)–(3.9) is necessary. In the next section, the two thermodynamic models applied in the scope of this thesis are presented.

3.1.3 Thermodynamic Closures

The working fluid for all studies presented in this thesis is the system consisting of water and water-vapor. Throughout this work, two thermodynamic modeling approaches are utilized. The first approach considers temperature-dependent fluid properties, and requires to solve for the energy equation. The second, simplified model, assuming isentropic phase change in the two-phase region, is based on a barotropic equation of state. The subsequent discussion bases on the presentation given in Budich *et al.* (2018).

3.1.3*a* Full Thermodynamic Modeling of Water

The density $\widehat{\rho}$ and specific internal energy $\widehat{e}$ uniquely define the thermodynamic state of the mixture. The temperature $\widehat{T}$ is computed from the specific internal energy using the caloric equation of state $\widehat{e}(\widehat{\rho},\widehat{T})$, which follows a piecewise definition in the pure liquid, pure vapor, and the mixture region, respectively. All fluid properties utilized for the full thermodynamic model discussed subsequently are summarized in table 3.1.

Phase boundaries are given by the temperature-dependent properties of the saturated mixture, i.e., the saturation pressure $p_{\mathrm{sat}}(\widehat{T})$ and the densities of saturated vapor and liquid, $\rho_{\mathrm{v,sat}}(\widehat{T})$ and $\rho_{\mathrm{l,sat}}(\widehat{T})$, respectively. Following Schmidt and Grigull (1989), these are calculated with the following relations:

$$\ln\left(p_{\mathrm{sat}}(\widehat{T})/p_{\mathrm{c}}\right) = \frac{1}{\Theta}\sum_{i=1}^{6} a_i\,(1-\Theta)^{l_i} \quad , \tag{3.10}$$

$$\ln\left(\rho_{\mathrm{v,sat}}(\widehat{T})/\rho_{\mathrm{c}}\right) = \sum_{i=1}^{6} b_i\,(1-\Theta)^{m_i} \quad , \tag{3.11}$$

$$\rho_{\mathrm{l,sat}}\left(\widehat{T}\right)/\rho_{\mathrm{c}} = 1+\sum_{i=1}^{6} c_i\,(1-\Theta)^{n_i} \quad . \tag{3.12}$$

The polynomials (3.10)–(3.12), with coefficients a_i, b_i, c_i and exponents l_i, m_i, n_i as given in table 3.2, are expressed in terms of the non-dimensional reduced state variables, i.e., the reduced temperature $\Theta = \widehat{T}/T_{\mathrm{c}}$, reduced pressure $\widehat{p}/p_{\mathrm{c}}$ and reduced density $\widehat{\rho}/\rho_{\mathrm{c}}$. The critical point of water is defined by the critical temperature $T_{\mathrm{c}} = 647.096\,\mathrm{K}$, the critical pressure $p_{\mathrm{c}} = 22.064\times10^{6}\,\mathrm{Pa}$, and the critical density $\rho_{\mathrm{c}} = 322.0\,\mathrm{kg/m^3}$. Equations (3.10)–(3.12) fit to the database established by the International Association for the Properties of Water and Steam (IAPWS, see Wagner and Pruß, 2002). A comparison of the employed analytical relations with IAPWS data from Lemmon *et al.* (n.d.) is shown in figure 3.1 for the range $273.15\,\mathrm{K} \le T \le 313.15\,\mathrm{K}$.

Table 3.1: Reference values utilized for the full thermodynamic model.

property	symbol		value
critical temperature water	T_c	[K]	647.096
critical pressure water	p_c	[Pa]	22.064×10^6
critical density water	ρ_c	[kg/m^3]	322.0
reference temperature	T_0	[K]	273.15
liquid specific heat capacity at constant volume†	$c_{\mathrm{v,l}}$	[J/kgK]	4180.0
vapor specific heat capacity at constant volume†	$c_{\mathrm{v,v}}$	[J/kgK]	1410.8
liquid specific energy†	$e_{l,0}$	[J/kg]	617
latent heat of evaporation†	$l_{\mathrm{v},0}$	[J/kg]	2501.3×10^3
parameter in Tait-equation	B	[Pa]	3300×10^5
exponent in Tait-equation	N	[-]	7.15
specific gas constant for vapor	R_{vap}	[J/kg]	461.5

† evaluated at the stated reference temperature for the full thermodynamic model T_{ref} T_0

The temperature-dependent viscosity and thermal conductivity of the saturated liquid and gas phase are computed from correlations recommended by IAPWS neglecting critical enhancement (omitted here for brevity, see The International Association for the Properties of Water and Steam, 2011; Egerer *et al.*, 2014b). Figure 3.2 compares the employed equations with IAPWS data from Lemmon *et al.* (n.d.) for the same temperature range as above.

In the pure liquid region, $\widehat{\rho} > \rho_{\mathrm{l,sat}}(\widehat{T})$, the specific internal energy is given as

$$\widehat{e} = c_{\mathrm{v,l}}(\widehat{T} - T_0) + e_{\mathrm{l},0} \ , \tag{3.13}$$

with the specific heat at constant volume of the liquid $c_{\mathrm{v,l}} = 4180.0\,\mathrm{J/kgK}$, and the

Table 3.2: Polynomial coefficients for the temperature-dependent saturation properties of the two-phase system of water and water-vapor, equations (3.10)–(3.12), after Schmidt and Grigull (1989).

	p_{sat}		$\rho_{\mathrm{v,sat}}$		$\rho_{\mathrm{l,sat}}$	
i	a_i	l_i	b_i	m_i	c_i	n_i
1	-7.85823	1.0	-2.02957	2/6	1.992060	1/3
2	1.83991	1.5	-2.68781	4/6	1.101230	2/3
3	-11.78110	3.0	-5.38107	8/6	-0.512506	5/3
4	22.67050	3.5	17.31510	18/6	-1.752630	16/3
5	-15.93930	4.0	44.63840	37/6	-45.448500	43/3
6	1.77516	7.5	64.34860	71/6	-6.756150×10^5	110/3

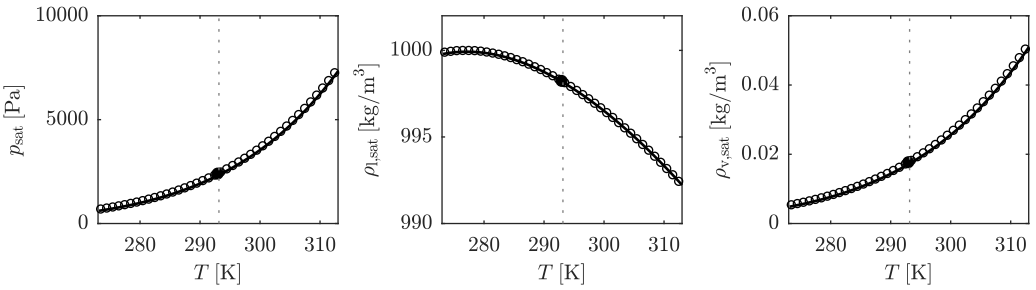

Figure 3.1: Saturation pressure $p_{\mathrm{sat}}(T)$, density of saturated liquid $\rho_{\mathrm{l,sat}}(T)$, and of saturated vapor $\rho_{\mathrm{l,sat}}(T)$, for the range $273.15\,\mathrm{K} \leq T \leq 313.15\,\mathrm{K}$. Comparison between analytical relations employed for the full-thermodynamic model according to equations (3.10)–(3.12) (—), and IAPWS data from Lemmon *et al.* (n.d.) (∘). The dashed line indicates the barotropic reference temperature $T_{\mathrm{ref}} = 293.15\,\mathrm{K}$.

reference energy $e_{\mathrm{l},0} = 617\,\mathrm{J/kg}$, taken at the reference temperature $T_0 = 273.15\,\mathrm{K}$. The pressure in the liquid $\widehat{p}$ is computed using the Tait-equation (Saurel *et al.*, 1999), with parameters $B = 3300 \times 10^5\,\mathrm{Pa}$, and $N = 7.15$:

$$\frac{\widehat{p} + B}{p_{\mathrm{sat}}(\widehat{T}) + B} = \left(\frac{\widehat{\rho}}{\rho_{\mathrm{l,sat}}(\widehat{T})} \right)^N \quad . \tag{3.14}$$

In the pure vapor region, $\widehat{\rho} < \rho_{\mathrm{v,sat}}(\widehat{T})$, the caloric equation of state reads

$$\widehat{e} = c_{\mathrm{v,v}}(\widehat{T} - T_0) + l_{\mathrm{v},0} + e_{\mathrm{l},0} \quad , \tag{3.15}$$

with the specific heat at constant volume for vapor $c_{\mathrm{v,v}} = 1410.8\,\mathrm{J/kgK}$, and the contribution due to latent heat $l_{\mathrm{v},0} = 2501.3 \times 10^3\,\mathrm{J/kg}$. The pressure is obtained by applying the ideal gas law for water-vapor, with specific gas constant $R_{\mathrm{vap}} = 461.5\,\mathrm{J/kg}$:

$$\widehat{p} = \widehat{\rho} R_{\mathrm{v}} \widehat{T} \quad . \tag{3.16}$$

In mixture regions, $\rho_{\mathrm{l,sat}}(\widehat{T}) \geq \widehat{\rho} \geq \rho_{\mathrm{v,sat}}(\widehat{T})$, the pressure is equal to the vapor pressure $\widehat{p} = p_{\mathrm{sat}}(\widehat{T})$ and the specific internal energy is given by:

$$\widehat{e} = \left(\varepsilon_{\mathrm{v}} c_{\mathrm{v,v}} + \varepsilon_{\mathrm{l}} c_{\mathrm{v,l}}\right)(\widehat{T} - T_0) + \varepsilon_{\mathrm{v}} l_{\mathrm{v},0} + e_{\mathrm{l},0} \quad . \tag{3.17}$$

In order to obtain the thermodynamic state of the mixture, equations (3.13)–(3.17) need to be solved iteratively for α, $\widehat{T}$, and $\widehat{p}$.

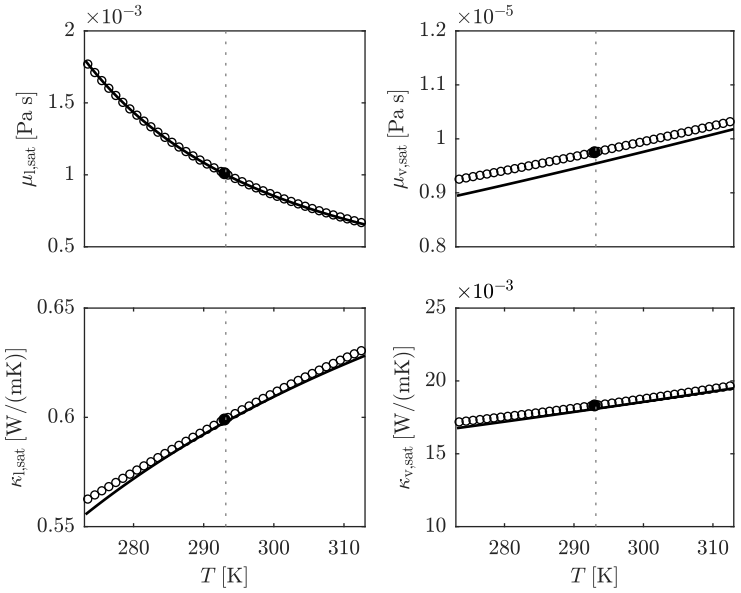

Figure 3.2: Dynamic viscosity and thermal conductivity of saturated liquid, $\mu_{\mathrm{l,sat}}(T)$ and $\kappa_{\mathrm{l,sat}}(T)$, and saturated vapor, $\mu_{\mathrm{v,sat}}(T)$ and $\kappa_{\mathrm{v,sat}}(T)$, for the range $273.15\,\mathrm{K} \leq T \leq 313.15\,\mathrm{K}$. Comparison between analytical relations employed for the full-thermodynamic model (—), and IAPWS data from Lemmon *et al.* (n.d.) (∘). The dashed line indicates the barotropic reference temperature $T_{\mathrm{ref}} = 293.15\,\mathrm{K}$.

3.1.3*b* Barotropic Thermodynamic Model for Water

Modeling the full thermodynamic behavior for the system of water-vapor by analytical relations as discussed above is computationally expensive. Moreover, temperature fluctuations are typically small, due to the larger heat capacity of water. This motivates a barotropic model, where it is not necessary to solve for the energy equation explicitly, thereby reducing the computational cost significantly. In the following, a barotropic equation of state $\widehat{p}(\widehat{\rho})$ is obtained upon assuming isentropic phase change in the mixture region. To this extent, the barotropic equation of state is continuously extended by a modified Tait-equation for the pure liquid, and all fluid properties are evaluated at a constant reference temperature T_{ref}. This assumption is strictly not valid along isentropes. However, due to the high specific heat capacity of water, temperature variations are small and can be neglected. The reference temperature is chosen here as $T_{\mathrm{ref}} = 293.15\,\mathrm{K}$. Table 3.3 summarizes the fluid properties employed in this model. A similar barotropic model involving a Diesel-like test fluid is used by Egerer *et al.* (2014a).

In pure liquid regions, $\widehat{\rho} > \rho_{\mathrm{l,sat}}(T_{\mathrm{ref}})$, the pressure is computed from the density via a modified Tait-equation, see equation (3.14), with $\rho_{\mathrm{l,sat}} = \rho_{\mathrm{l,sat}}(T_{\mathrm{ref}})$ and $p_{\mathrm{sat}} = p_{\mathrm{sat}}(T_{\mathrm{ref}})$. In case of two-phase flow, $\rho_{\mathrm{l,sat}}(T_{\mathrm{ref}}) \geq \widehat{\rho} \geq \rho_{\mathrm{v,sat}}(T_{\mathrm{ref}})$, the vapor

Table 3.3: Reference values utilized for the barotropic thermodynamic model.

property	symbol		value
reference temperature for barotropic model	T_{ref}	[K]	293.15
density of saturated liquid†	$\rho_{\mathrm{l,sat}}$	[kg/m^3]	998.16
density of saturated vapor†	$\rho_{\mathrm{v,sat}}$	[kg/m^3]	0.017214
saturation pressure†	p_{sat}	[Pa]	2339.3
specific heat capacity of the liquid†	$c_{\mathrm{p,l}}$	[J/kgK]	4184.4
latent heat of evaporation†	$l_{\mathrm{v,ref}}$	[J/kg]	2453.5×10^3

† evaluated at the stated reference temperature for the barotropic model T_{ref}

volume fraction α is computed according to equation (3.6), with $\rho_{\mathrm{l,sat}} = \rho_{\mathrm{l,sat}}(T_{\mathrm{ref}})$ and $\rho_{\mathrm{v,sat}} = \rho_{\mathrm{v,sat}}(T_{\mathrm{ref}})$.

The pressure of a saturated mixture in the barotropic model can be computed by integrating the speed of sound along an isentrope

$$\widehat{c}^2 = \left.\frac{\partial\widehat{p}}{\partial\widehat{\rho}}\right|_{s=const.} \quad\Rightarrow\quad \widehat{p}(\widehat{\rho}) - p_{\mathrm{sat}}(T_{\mathrm{ref}}) = \int_{\rho_{\mathrm{l,sat}}}^{\widehat{\rho}} \widehat{c}^2 \,\mathrm{d}\tilde{\rho} \ . \tag{3.18}$$

In order to obtain $\widehat{p}(\widehat{\rho})$, a functional dependence $\widehat{c}(\tilde{\rho})$ for the speed of sound in the mixture region is required. For this purpose, the next section discusses two alternative approaches.

3.1.3*c* Analytical Relations for the Two-Phase Speed of Sound

Assuming a homogeneous mixture, Brennen (1995), and Franc and Michel (2005) derive analytical relations for the speed of sound in mixture regions $\widehat{c}$. The authors discuss two limiting cases, which denote an upper and lower estimate for $\widehat{c}$.

For the case of infinitely slow phase change, the speed of sound can be modeled with the *frozen speed of sound* $\widehat{c}_{\mathrm{fr}}$:

$$\frac{1}{\widehat{\rho}\,\widehat{c}_{\mathrm{fr}}^2} = \frac{\alpha}{\rho_{\mathrm{v,sat}} c_{\mathrm{v}}^2} + \frac{1-\alpha}{\rho_{\mathrm{l,sat}} c_{\mathrm{l}}^2} \ , \tag{3.19}$$

with the speed of sound in the pure liquid and pure vapor c_{l} and c_{v}, respectively.

When both phases are in thermodynamic equilibrium, i.e., in the case of infinitely fast heat exchange between phases and thus phase change, the latent heat of vaporization has to be taken into account on the right hand side of equation (3.19),

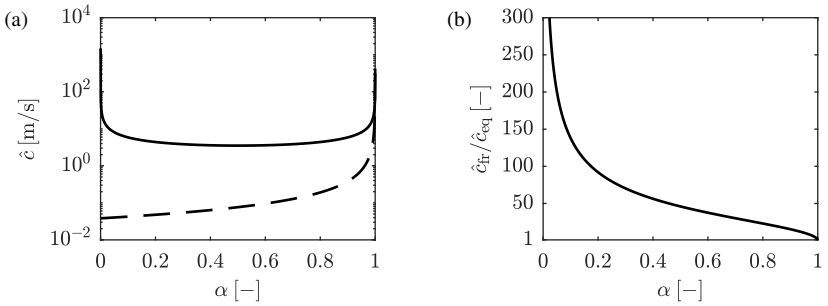

Figure 3.3: (a) Comparison between frozen speed of sound $\widehat{c}_{\mathrm{fr}}$ (equation (3.19), ——), and equilibrium speed of sound $\widehat{c}_{\mathrm{eq}}$ (equation (3.20), – –) in the two-phase region, $0 \leq \alpha \leq 1$. (b) Ratio $\widehat{c}_{\mathrm{fr}}/\widehat{c}_{\mathrm{eq}}$ in the two-phase region.

such that the *equilibrium speed of sound* $\widehat{c}_{\mathrm{eq}}$ becomes:

$$\frac{1}{\widehat{\rho}\,\widehat{c}_{\mathrm{eq}}^2} = \frac{\alpha}{\rho_{\mathrm{v,sat}} c_{\mathrm{v}}^2} + \frac{1-\alpha}{\rho_{\mathrm{l,sat}} c_{\mathrm{l}}^2} + \frac{(1-\alpha)\rho_{\mathrm{l,sat}} c_{\mathrm{p,l}} \widehat{T}}{(\rho_{\mathrm{v}} L)^2} \quad . \tag{3.20}$$

In the barotropic model, the specific heat capacity of the liquid $c_{\mathrm{p,l}} = 4184.4\,\mathrm{J/kgK}$, and latent heat of evaporation $L = 2453.5 \times 10^3\,\mathrm{J/kg}$ are assumed to be constant at the constant reference temperature T_{ref}.

A comparison of these two analytical relations for $\widehat{c}$ as a function of the void fraction α is given in figure 3.3. As shown in figure 3.3*a*, both yield a strong decrease for the speed of sound in the mixture region, being at least two orders of magnitude lower than the speed of the sound in either the pure liquid, $c_{\mathrm{l}} \approx 1482\mathrm{m/s}$, or pure vapor, $c_{\mathrm{v}} \approx 423\,\mathrm{m/s}$. The frozen speed of sound exhibits a global minimum of $\min(\widehat{c}_{\mathrm{fr}}) = 3.51\,\mathrm{m/s}$ at $\alpha = 0.5$, while the equilibrium speed of sound is minimal for $\alpha \to 0^+$ with $\min(\widehat{c}_{\mathrm{eq}}) = 0.038\,\mathrm{m/s}$.

Figure 3.3*b* illustrates the ratio $\widehat{c}_{\mathrm{fr}}/\widehat{c}_{\mathrm{eq}}$. In the region of relevant void fractions, both approaches differ by a factor ranging between 10 ($\alpha = 0.95$) and 140 ($\alpha = 0.1$). Brennen (1995) discusses that the behavior of a real two-phase medium lies in between these two extremes. The actual physical value is mainly controlled by the "degree of thermal exchange between the phases" (Brennen, 1995). While perfect thermal exchange is assumed for the equilibrium speed of sound, the frozen speed of sound derives from the assumption of no exchange between the phases. However, the actual value of $\widehat{c}$ is difficult to measure experimentally, and may be problem-dependent. In either case, the mixture speed of sound may easily attain values smaller than the convective flow velocity in a technical system. Resulting in locally supersonic flow, this supports the occurrence of compressible shock wave phenomena in the two-phase flow, as discussed in chapter 4.

3.1.3*d* Barotropic Equation of State for Water

In the barotropic model, the assumed analytical relation for the mixture speed of sound directly influences the level of vaporisation. With the definition of the isentropic speed of sound, equation (3.18), and the mixture density, $\rho = \alpha\rho_{\mathrm{v,sat}} + (1-\alpha)\rho_{\mathrm{l,sat}}$, see equation (3.6), it immediately follows:

$$\partial\alpha = -\frac{1}{\widehat{c}^2}\frac{\partial\widehat{p}}{\rho_{\mathrm{l,sat}} - \rho_{\mathrm{v,sat}}} \ . \tag{3.21}$$

Any change in pressure thus leads to a change in the vapor volume fraction, which is proportional to the inverse square of the speed of sound.

Recognizing that $\widehat{c}_{\mathrm{fr}} \to c_{\mathrm{l}}$ for $\alpha \to 0^+$, the integration of (3.21) with the frozen speed of sound shows that essentially no vapor is produced. This is in agreement with the assumption of the frozen model, but can thus not be used in the simulations. Still relying on the frozen speed of sound, an upper estimate for the produced vapor is obtained by assuming a constant mixture speed of sound equal to the global minimum, $\min(\widehat{c}_{\mathrm{fr}}) = 3.51\ \mathrm{m/s}$. The maximum pressure difference is achieved when hypothetically expanding the mixture from vapor pressure p_{sat} to the triple line p_{triple}. Even under these assumptions, the maximum attainable vapor volume fraction is 14%. In contrast, the maximum void fraction observed for the problems investigated in the scope of this thesis frequently exceeds 90%. From these considerations, it is concluded that the frozen speed of sound is not suitable for the employed barotropic model and the presented configurations.

Alternatively, an intermediate model yielding a mixture speed of sound in between the values given by the frozen and equilibrium assumption is conceivable. However, for such a model, additional information, such as bubble size distributions, interfacial areas between liquid and vapor phase, or approximations for the degree of thermal exchange between the phases, is required. Reliable estimates for the relevant parameters, either from experiments or from scale-resolved simulations, are not available in the open literature. Thus, to avoid the need for further assumptions, the equilibrium speed of sound $\widehat{c}_{\mathrm{eq}}$ is chosen for integrating equation (3.18).

The resulting barotropic equation of state $\widehat{p}(\widehat{\rho})$ is depicted in figure 3.4 in the $\widehat{p} - \widehat{v}$ phase diagram, with $\widehat{v} = 1/\widehat{\rho}$ denoting the specific volume of the mixture. Figure 3.4 shows that the pressure within mixture regions deviates from the saturation pressure $p_{\mathrm{sat}}(T_{\mathrm{ref}})$, due to the assumption of isentropic phase change. However, the deviation of the isentrope from the isotherm is only noticeable at very high void fractions of $\alpha \gtrsim 99.9\%$.

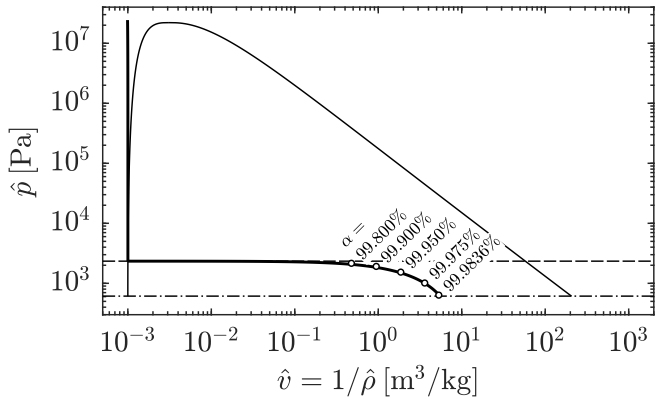

Figure 3.4: $\widehat{p} - \widehat{v}$ phase diagram for the two-phase system of water and water-vapor, including the closed-form barotropic equation of state $\widehat{p}(\widehat{\rho})$ (—). Lines denote the saturation lines of liquid and vapor, $p_{\mathrm{l,sat}}$ and $p_{\mathrm{v,sat}}$ (—), the saturation pressure $p_{\mathrm{sat}}(T_{\mathrm{ref}})$ (– –), and the triple line p_{triple} (–·–).

In this barotropic model the evaporation rate is directly linked to the mixture speed of sound, see again equation (3.21). As discussed, lower values of $\widehat{c}$ are associated with a stronger vapor production. It is to be noted, however, that complete evaporation, i.e., pure vapor ($\alpha = 1$), cannot be reached in this model. As indicated in figure 3.4, the assumed isentropic phase change leads in the limit of $\alpha \to 1$ to a crossing of the triple line p_{triple}. Hence, the triple line represents a constraint of the physical model, where the thermodynamic closures become invalid. This aspect is discussed in more detail by Mihatsch *et al.* (2015). The maximum admissible amount of the vapor void fraction is $\alpha = 99.9836\%$. Due to the low characteristic velocities in the analyzed configurations, this value is, however, not reached in the computations.

3.2 Numerical Method

The numerical method employed in this thesis is based on previous work at the TUM Institute of Aerodynamics and Fluid Mechanics. A detailed presentation and discussion of the numerical scheme is given in Sezal (2009), Schmidt (2015), and Egerer (2016). In the following, only the main building blocks are summarized.

The finite volume method is adopted, i.e., the computational domain $\tilde{\Omega}$ is a discretized representation of the fluid domain Ω. For the spatial discretization, N disjunct control volumes $\tilde{\Omega}_i$ are used, such that $\tilde{\Omega} = \bigcup \tilde{\Omega}_i$, $i = 1, \ldots, N$. Throughout this thesis, body-fitted, block-structured grids with hexahedral elements are employed.

The discrete form of the volume-averaging operator for the computational cell $\tilde{\Omega}_i$, replacing equation (3.2), reads:

$$\overline{\bullet} \equiv \left(\int_{\tilde{\Omega}_i} \bullet \, \mathrm{d}V \right) / \tilde{V}_i \ , \tag{3.22}$$

with the volume $\tilde{V}_i$ of the cell i.

The Navier-Stokes equations (3.1), applied to $\tilde{\Omega}_i$, and re-arranged into enthalpy notion, read in semi-discrete from:

$$\forall\, i: \quad \frac{\partial}{\partial t}\left(\overline{\boldsymbol{Q}}\right) + \frac{1}{\tilde{V}_i} \sum_{j=1}^{6} \left(\tilde{\boldsymbol{F}}_{i,j} \right) = 0 \ , \tag{3.23}$$

where $\overline{\boldsymbol{Q}} = [\bar{\rho}, \overline{\rho u}_1, \overline{\rho u}_2, \overline{\rho u}_3, \overline{\rho H}]^T$ denotes the vector of transported quantities, volume-averaged within $\tilde{\Omega}_i$, with the total specific enthalpy $\overline{H} = \overline{E} + \bar{p}/\bar{\rho}$. The vector $\tilde{\boldsymbol{F}}_{i,j}$ is the numerical flux across the cell face $j = 1, \ldots, 6$ of cell i. Summing over all cell faces yields the total numerical flux for cell i, $\tilde{\boldsymbol{F}}_i = \sum_{j=1}^{6} \tilde{\boldsymbol{F}}_{i,j}$.

Integration of equation (3.23) in time is shown in §3.2.1. Subsequently, §3.2.2 discusses a method for treating moving geometries in the developed framework. Finally, two different approaches for the evaluation of $\tilde{\boldsymbol{F}}_i$ are outlined in §3.2.3.

3.2.1 Time Integration

In order to capture compressible shock-wave dynamics, explicit time integration of equation (3.23) is performed. The time step $\Delta t = t^{n+1} - t^n$ is thus limited by the Courant-Friedrichs-Lewy (*CFL*) criterion. For this purpose, first a local time-step Δt_i is computed for each cell i. The global time step Δt is then given by the minimum of all local time steps:

$$\forall\, i: \quad \Delta t_i = CFL \cdot \left[\frac{|\overline{\boldsymbol{u}}| + \bar{c}}{l_i / n_d} + \frac{2\nu_{tot}}{(l_i/n_d)^2} \right]^{-1} \quad , \qquad \Delta t = \min_i \Delta t_i \ . \tag{3.24a, b}$$

The first and second term in square brackets of equation (3.24*a*) limit the time step due to convection and diffusion, respectively, see Ferziger and Peric (2002). *CFL* denotes the constant *CFL*-number, l_i a characteristic length scale of the cell, n_d the number of physical dimensions of the problem, and ν_{tot} the total dynamic viscosity, which is the sum of resolved, ν, and modeled viscosity, ν_{SGS}, i.e., $\nu_{\mathrm{tot}} = \nu + \nu_{\mathrm{SGS}}$. For all problems considered in the following, $n_d = 3$, except where otherwise stated. The length l_i is estimated from the cell volume $\tilde{V}_i$, and the largest cell face $S_i^{\max} = \max_{j=1}^{6} \tilde{S}_{i,j}$, as $l_i = \tilde{V}_i / \tilde{S}_i^{\max}$.

3.2.1*a* Runge-Kutta scheme

For all investigations carried out in the following, a low-storage Runge-Kutta scheme is selected, see Schmidt (2015). Based on a partial differential equation in time for the quantity φ, and an arbitrary right-hand side $f(\varphi)$, this can be formalized as follows:

$$\frac{\partial \varphi}{\partial t} = f(\varphi) \quad \Rightarrow \quad \varphi^{n+1,r} = \varphi^{n+1,0} + \xi_r \Delta t \, f(\varphi^{n+1,r-1}), \quad r = 1, \ldots, N_r \tag{3.25}$$

$$\varphi^{n+1,0} = \varphi^n, \quad \varphi^{n+1} = \varphi^{n+1,N_r} \ . \tag{3.26}$$

The time step Δt is thus split in N_r sub-steps, with the coefficients ξ_r for the sub-step r. The realization of φ at instant $t = t^n$ is denoted with φ^n, at $t = t^{n+1}$ by φ^{n+1}, and at sub-step r by $\varphi^{n+1,r}$.

In this thesis, a 4-step, low-storage Runge-Kutta (LS RK4) method with enlarged stability region of 2^{nd}-order is utilized, with coefficients ξ_r given by table 3.4. A constant *CFL*-number of $CFL = 1.4$ is used in equation (3.24*a*) for all presented computations.

3.2.1*b* Time-Operator Preconditioning

With an estimate of the speed of sound in liquid water of $c_\text{l} \approx 1500\text{m/s}$, the time step computed with equation (3.24) is $\Delta t = \mathcal{O}(1 \times 10^{-9}\,\text{s})$ for the investigated problems. In contrast, using $L = \mathcal{O}(1 \times 10^{-1}\,\text{m})$ and $U = \mathcal{O}(10\,\text{m/s})$ for the characteristic scales of length and velocity, the convective time scale is $L/U = \mathcal{O}(1 \times 10^{-2}\,\text{s})$. In consequence, at least $\mathcal{O}(1 \times 10^7)$ iterations are required in order to cover a relevant time span, using the compressible approach. To save computational time, it is thus crucial to shorten the initial simulation startup to a minimum. As wave dynamics are not of interest during this transient phase, preconditioning is an effective way to accelerate the solution. For an overview of possible preconditioning techniques, see, e.g., the review by Turkel (1999).

Due to its effectiveness and practicability, the simplest differential preconditioner given by Turkel (1999) is selected. Its application can be demonstrated using the one-dimensional, linearized gas dynamics equations (see Toro, 2009), in analogy

Table 3.4: Coefficients ξ_r for the employed Runge-Kutta method LS RK4.

r	1	2	3	4
ξ_r	11/100	5/18	1/2	1/1

with the full Navier-Stokes equations. In matrix notation:

$$\frac{\partial}{\partial t}\boldsymbol{U} + \boldsymbol{A}\frac{\partial}{\partial x}\boldsymbol{U} = 0 \quad , \qquad \boldsymbol{A} = \begin{bmatrix} 0 & \rho_{\mathrm{ref}} \\ c_{\mathrm{ref}}^2/\rho_{\mathrm{ref}} & 0 \end{bmatrix} , \tag{3.27}$$

with the vector of conserved quantities $\boldsymbol{U} = [\rho, u]^T$, and $\boldsymbol{A} = \partial\boldsymbol{F}/\partial\boldsymbol{U}$ as the Jacobian of the flux $\boldsymbol{F}(\boldsymbol{U}) = [\rho_{\mathrm{ref}}\, u, c_{\mathrm{ref}}^2/\rho_{\mathrm{ref}}\, \rho]^T$. Here, ρ_{ref} and c_{ref} denote the reference density and the velocity of wave propagation used for the linearization. The latter is equal to the speed of sound in the medium. The system is numerically stiff due to the large spectral radius of $\boldsymbol{A}$, $\sigma(\boldsymbol{A}) = c_{\mathrm{ref}}$, caused by the high speed of sound of liquid water.

The system can be preconditioned by $\boldsymbol{P}$:

$$\boldsymbol{P}^{-1}\frac{\partial}{\partial t}\boldsymbol{U} + \boldsymbol{A}\frac{\partial}{\partial x}\boldsymbol{U} = 0 \quad , \qquad \boldsymbol{P} = \begin{bmatrix} \zeta^2 & 0 \\ 0 & 1 \end{bmatrix} , \tag{3.28}$$

with the preconditioning factor ζ. The steady-state solutions of equation (3.28) are identical to that of equation (3.27). According to Turkel (1999), it is an effective preconditioner if $\zeta = \mathcal{O}(\mathrm{Ma}) << 1$, with the characteristic Mach-number Ma of the problem, while no preconditioning is performed for $\zeta = 1$. Equation (3.28) can be re-cast in the form of equation (3.27):

$$\frac{\partial}{\partial t}\boldsymbol{U} + \tilde{\boldsymbol{A}}\frac{\partial}{\partial x}\boldsymbol{U} = 0 \quad , \qquad \tilde{\boldsymbol{A}} = \boldsymbol{P}\boldsymbol{A} = \begin{bmatrix} 0 & \zeta^2\rho_{\mathrm{ref}} \\ c_{\mathrm{ref}}^2/\rho_{\mathrm{ref}} & 0 \end{bmatrix} . \tag{3.29}$$

The spectral radius of $\tilde{\boldsymbol{A}}$ becomes $\sigma(\tilde{\boldsymbol{A}}) = \zeta c_{\mathrm{ref}}$. Choosing $\zeta < 1$ thus reduces the effective wave propagation velocity and, correspondingly, the stiffness of the system. Referring to equation (3.24), this allows to increase the time step size almost proportionally by the factor ζ^{-1}.

This acceleration approach is strictly only applicable when the solution of equation (3.29) converges to a steady-state solution. Therefore, it is only applied during the simulation startup phase with the cavitation model disabled. Typically, a value of $\zeta^{-1} = \mathcal{O}(10)$ is chosen for the problems considered in this work.

3.2.2 Arbitrary-Lagrangian-Eulerian Approach

For an overview and in-depth discussion of Arbitrary-Lagrangian-Eulerian (ALE) methods, see, e.g., the review by Donea *et al.* (2004). Only fundamental concepts of the utilized approach are examined here.

Using an ALE description, a continuum, e.g., solid or fluid, is considered within an inertial frame of reference, and, in general, the numerical grid can move independently and arbitrarily. Depending on the application, the mesh may be translated along with the continuum (Lagrangian description), stay fixed in inertial space (Eulerian description), or describe an appropriately defined movement, which may be guided by the continuum's movement. ALE methods are widely used for problems involving fluid-structure interactions (FSI), where the mesh of the fluid domain is coupled to some degree to the displacement of a solid object bounding the flow.

Extension of an existing finite volume method by an ALE approach is straightforward. The modification of the governing equations is restricted to (a) account for potential volume changes of the computational cells in equation (3.23), and (b) the introduction of the convective velocity into the convective fluxes, see §3.2.3. For this purpose, first a mesh-update function ψ is introduced:

$$\psi : \boldsymbol{x}^n \longmapsto \boldsymbol{x}^{n+1} \quad , \qquad \psi = \psi\left(\boldsymbol{x}^n, \overline{\boldsymbol{u}}, t, \Delta t, \ldots\right) \quad , \tag{3.30}$$

with the location of the mesh vertices $\boldsymbol{x}$. Due to the small size of the time step Δt, the mesh displacement is small within a single iteration. It is thus sufficient to evaluate ψ at the beginning of each iteration, instead of updating the mesh within each Runge-Kutta sub-step, which reduces the computational effort. The velocity of the vertices can then be computed as:

$$\boldsymbol{u}^m = \frac{1}{\Delta t} \cdot \left(\boldsymbol{x}^{n+1} - \boldsymbol{x}^n\right) \quad . \tag{3.31}$$

The mesh velocity at cell centers $\boldsymbol{u}_i^m$ and at the centers of each cell face $\boldsymbol{u}_{i,j}^m$ are then approximated as the average velocity of the adjacent vertices, respectively.

In the case of arbitrary mesh movements, the governing equations need to be supplemented by a geometric conservation law (GCL), ensuring that the change in cell volume is compatible with the movement of the cell faces. In semi-discrete notion:

$$\frac{\partial}{\partial t}\left(\tilde{V}_i\right) - \sum_j \left(\boldsymbol{u}_{i,j}^m \cdot \boldsymbol{n}_{i,j}\, S_{i,j}\right) = 0 \quad . \tag{3.32}$$

Using the approach sketched above, three basic mesh movements are implemented in the scope of this work: (a) non-uniform translation in one coordinate direction, (b) non-uniform stretching in one coordinate direction, and (c) solid body rotation with constant rotational velocity around a coordinate axis. For the studies in this thesis, namely the ship propeller analyzed with chapter 5, only the latter is applied.

3.2.3 Numerical Flux Function

As mentioned above, two different schemes are used in this thesis for the evaluation of $\tilde{\boldsymbol{F}}_{i,j}$, the numerical flux across face j of cell i. It can again be split into convective, pressure, and viscous fluxes, $\tilde{\boldsymbol{F}}_{i,j} = \tilde{\boldsymbol{F}}^c_{i,j} + \tilde{\boldsymbol{F}}^p_{i,j} + \tilde{\boldsymbol{F}}^c_{i,j}$. The primary difference between the two schemes lies in the convective contribution $\tilde{\boldsymbol{F}}^c_{i,j}$, and whether the viscous flux $\tilde{\boldsymbol{F}}^v_{i,j}$ is included in the model. First, the *baseline scheme*, proposed by Schmidt (2015), is discussed. Afterwards, the *ILES scheme*, recently developed by Egerer *et al.* (2016), is presented.

3.2.3*a* Baseline Scheme

The baseline scheme is proposed by Schmidt (2015), and discussed in further detail, e.g., by Sezal (2009) and Mihatsch (2017). It is used for Euler computations, i.e., when neglecting viscous fluxes $\tilde{\boldsymbol{F}}^v$ in the model. Only the main components are briefly summarized here by exemplarily discussing the evaluation of $\tilde{\boldsymbol{F}}_{i,j}$ in one direction of the logical block coordinate system, sketched in figure 3.5. The unit-normal vector of the considered cell face is given by $\boldsymbol{n}_{i,j} \equiv \boldsymbol{n}^i$, and the cell face area by $S_{i,j} \equiv S^i$. The scheme uses a compact 4-point stencil. The involved adjacent cells are indicated by superscripts $^{--}$, $^{-}$, $^{+}$, and $^{++}$.

The fluid velocity is computed as $\overline{\boldsymbol{u}} = \overline{\rho\boldsymbol{u}}/\overline{\rho}$ from the vector of transported quantities $\overline{\boldsymbol{Q}}$. It is decomposed into its normal component $\overline{u}_\perp = \overline{\boldsymbol{u}} \cdot \boldsymbol{n}^i$, and the vector parallel to the cell face $\overline{\boldsymbol{u}}_\parallel = \overline{\boldsymbol{u}} - u_\perp \boldsymbol{n}^i$. Velocity reconstruction at the interface is based on the total-variation-diminishing (TVD) limiter of Koren (1993), which is formally 3^{rd}-order accurate for smooth fields:

$$\phi(r) = \max\left[0, \min\left(2r, \frac{1+2r}{3}, 2\right)\right] , \tag{3.33}$$

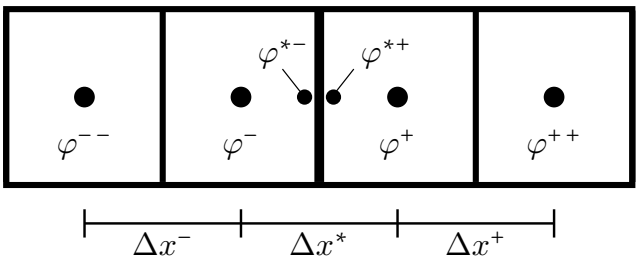

Figure 3.5: Sketch of the 4-point stencil for the evaluation of numerical flux function $\tilde{\boldsymbol{F}}_{i,j}$, exhibiting the employed nomenclature.

acting on the left and right gradient $r = \{r^-, r^+\}$ of quantity φ:

$$r^- = \frac{\Delta x^*}{\Delta x^-}\frac{\varphi^- - \varphi^{--}}{\varphi^+ - \varphi^-} \quad , \qquad r^+ = \frac{\Delta x^*}{\Delta x^+}\frac{\varphi^+ - \varphi^{++}}{\varphi^- - \varphi^+} \ , \tag{3.34a, b}$$

where the distances between the cell centers are $\Delta x^- = x^- - x^{--}, \Delta x^* = x^+ - x^-$, and $\Delta x^+ = x^{++} - x^+$, as indicated in figure 3.5. Reconstruction of $u_\perp$ and the components of $\boldsymbol{u}_\parallel$ at the interface is then given as follows, with $\varphi = \{\overline{u}_\perp, \overline{\boldsymbol{u}}_\parallel\}$:

$$\varphi^{*-} = \varphi^- + \frac{1}{2}\phi\left(r^-\right)\left(\varphi^+ - \varphi^-\right) \quad , \qquad \varphi^{*+} = \varphi^+ - \frac{1}{2}\phi\left(r^+\right)\left(\varphi^+ - \varphi^-\right) \tag{3.34a, b}$$

The advection velocity u^* is computed from:

$$u^* = \frac{Z^+ u_\perp^{*+} + Z^- u_\perp^{*-}}{Z^+ + Z^-} - \frac{p^+ - p^-}{Z^+ + Z^-} - u_\perp^i \ , \tag{3.35}$$

with the magnitude of the face-normal velocity of the cell face itself, $u_\perp^i = \boldsymbol{u}^i \cdot \boldsymbol{n}^i$, where $\boldsymbol{u}_{i,j}^m \equiv \boldsymbol{u}^i$, computed as the average velocity of the four adjacent mesh vertices, see equation (3.31). The velocity $u_\perp^i$ is non-zero only when using moving meshes with ALE.

$Z^\pm$ in equation (3.35) denote weighted estimates for the left and right acoustic impedances:

$$Z^- = \frac{1}{4}\left(3\rho^- + \rho^+\right) c_{\max} \quad , \qquad Z^+ = \frac{1}{4}\left(\rho^- + 3\rho^+\right) c_{\max} \ , \tag{3.36a, b}$$

where $c_{\max}$ is an upper approximation for the speed of sound within the adjacent cells, $c_{\max} = \max(c^{--}, c^-, c^+, c^{++})$. In order to enhance the numerical stability of the scheme, the frozen speed of sound is chosen here. Note that $c_{\max}$ is purely motivated by considerations regarding the stability of the scheme. It does not affect the acoustic propagation velocity, as discussed in detail by Sezal (2009).

The reconstructed velocities are selected, based on the sign of the advection velocity $\mathrm{sgn}(u^*)$, with $\varphi = \{\overline{u}_\perp, \overline{\boldsymbol{u}}_\parallel\}$:

$$\varphi^* = \frac{1}{2}\left[\left(1 + \mathrm{sgn}(u^*)\right)\varphi^{*-} + \left(1 - \mathrm{sgn}(u^*)\right)\varphi^{*+}\right] \ , \tag{3.37}$$

in order to give an upwind-biased reconstruction of the fluid velocity $u_\perp^* \boldsymbol{n}^i + \boldsymbol{u}_\parallel^*$ at the interface. Furthermore, 1st-order upwind-reconstruction is applied to density, internal energy and enthalpy, i.e., with $\varphi = \left\{\bar{\rho}, \bar{e}, \bar{h}\right\}$:

$$\varphi^* = \frac{1}{2}\left[\left(1 + \mathrm{sgn}(u^*)\right)\varphi^- + \left(1 - \mathrm{sgn}(u^*)\right)\varphi^+\right] \ . \tag{3.38}$$

Low-mach consistency (Schmidt, 2015) is ensured by employing a 2nd-order central approximation for the interface pressure p^*:

$$p^* = \frac{1}{2}\left(\bar{p}^+ + \bar{p}^-\right) \ . \tag{3.39}$$

Preliminary tests of the ALE method for describing rotating systems exhibited oscillations in the pressure. These occurred, e.g., in the case of pure solid body rotation, with a pressure gradient in the radial direction and a vanishing gradient of radial velocity. These "checkerboard patterns" are caused by a lack of cross-diffusion in the original baseline method. Thus, when considering moving meshes, the interface pressure is modified by a low-Mach consistent regularization term, which introduces additional cross-diffusion to the scheme:

$$p^* = \frac{1}{2}\left(\bar{p}^+ + \bar{p}^-\right) - \frac{1}{4}\frac{Z^+ + Z^-}{c_{\max}}\left(\bar{u}_\perp^+ - \bar{u}_\perp^-\right)\cdot u_{\text{ref}} \ , \tag{3.40}$$

with the reference velocity equal to the magnitude of the face-normal interface velocity $u_{\text{ref}} = |u_\perp^i|$.

Summarizing, the numerical flux across the face j of cell i is given by the baseline scheme as the sum of convective and pressure flux, $\tilde{\boldsymbol{F}}_{i,j} = \tilde{\boldsymbol{F}}^c_{i,j} + \tilde{\boldsymbol{F}}^p_{i,j}$, with:

$$\tilde{\boldsymbol{F}}^c_{i,j} = \rho^* u^* \begin{bmatrix} 1 \\ u_\perp^* \boldsymbol{n}^i + \boldsymbol{u}_\parallel^* \\ h^* \end{bmatrix} S_{i,j} \quad , \qquad \tilde{\boldsymbol{F}}^p_{i,j} = p^* \begin{bmatrix} 0 \\ \boldsymbol{n}_{i,j} \\ 0 \end{bmatrix} S_{i,j} \ . \tag{3.41a, b}$$

3.2.3*b* ILES scheme

Due to an excessive amount of numerical dissipation (Egerer *et al.*, 2016), the upwind-biased *baseline scheme* is not suitable for performing large-eddy simulations of cavitating flow. Thus, Egerer *et al.* (2016) recently developed the *ILES scheme*, which operates on the same compact 4-point stencil as the previous method.

Computation of the convective fluxes $\tilde{\boldsymbol{F}}^c_{i,j}$ involve a sensor functional ς, combining the vorticity-dilatation sensor $\beta^{\boldsymbol{u}}$ of Ducros *et al.* (1999), and a sensor based on the variation of the void fraction β^α (Egerer *et al.*, 2016):

$$\varsigma(\beta^{\boldsymbol{u}}, \beta^\alpha) = \begin{cases} 1 \ , & \text{if } \beta^{\boldsymbol{u}} > \beta^{\boldsymbol{u}}_{\text{th}} \ \vee \ \beta^\alpha > \beta^\alpha_{\text{th}} \\ 0 \ , & \text{else} \end{cases} \quad , \tag{3.42}$$

$$\beta^{\boldsymbol{u}} = \frac{\left| \nabla \cdot \overline{\boldsymbol{u}} \right|^2}{\left| \nabla \cdot \overline{\boldsymbol{u}} \right|^2 + \left| \nabla \times \overline{\boldsymbol{u}} \right|^2 + \varepsilon} \quad , \qquad \beta^\alpha = \Delta_i \alpha + \Delta_j \alpha + \Delta_k \alpha \ , \tag{3.43a, b}$$

with ε a small number in order to avoid division by zero, and $\Delta_i\alpha = |\alpha^- - \alpha^{--}| + |\alpha^{++} - \alpha^+|$ the variance of α in the stencil cells along the logical block direction i. The sensor threshold values are chosen as $\beta^{\boldsymbol{u}}_{\text{th}} = 0.95$ and $\beta^{\alpha}_{\text{th}} = 0.9$, adhering to recommendations of Egerer (2016).

Designating the upwind-biased convective flux according to equation (3.41 *a*) of the baseline scheme with $\tilde{\boldsymbol{F}}^{c,U}_{i,j}$, and a higher-order central reconstruction with $\tilde{\boldsymbol{F}}^{c,C}_{i,j}$, the convective flux is then given as:

$$\tilde{\boldsymbol{F}}^{c}_{i,j} = \varsigma\, \tilde{\boldsymbol{F}}^{c,U}_{i,j} + (1-\varsigma)\, \tilde{\boldsymbol{F}}^{c,C}_{i,j} \quad . \tag{3.44}$$

Thus, the numerical dissipation of the upwind-biased reconstruction scheme $\tilde{\boldsymbol{F}}^{c,U}_{i,j}$ described above is localized at detected flow discontinuities, i.e., shock waves and pseudo-phase boundaries. In smooth regions of the flow, convective fluxes are given by $\tilde{\boldsymbol{F}}^{c,C}_{i,j}$. As discussed in detail by Egerer *et al.* (2016), these are computed using a 2^{nd}-order approximation of the density, while velocities are discretized by a linear 4^{th}-order central scheme. ALE capabilities are introduced similarly as for the baseline scheme, i.e., by taking the interface velocity into account when computing the advection velocity u^*.

Computation of the interface pressure p^* for the pressure flux $\tilde{\boldsymbol{F}}^{p}_{i,j}$ also employs the sensor functional. At discontinuities, for providing low-Mach consistency, again analogously to the baseline scheme, the arithmetic mean of the left and right pressure reconstructed with Roe's minmod-limiter (Roe, 1986) is utilized. In smooth regions, a linear 4^{th}-order central discretization is employed. No additional regularization of the interface pressure is necessary for moving meshes with ALE. The viscous flux $\tilde{\boldsymbol{F}}^{v}_{i,j}$ is discretized by a linear 2^{nd}-order centered scheme.

In this ILES approach, no explicit modeling of unresolved subgrid-scales (SGS) is performed. Instead, following the idea of the Adaptive Local Deconvolution Method (ALDM, see Hickel *et al.*, 2006, 2014), the truncation error of the scheme implicitly acts as a physically consistent SGS model for turbulence. This is achieved by calibrating free parameters in the scheme introduced via a regularization term in the numerical flux function, as demonstrated by Egerer *et al.* (2016).

3.2.3*c* Near-wall treatment

For wall-bounded flow, a van-Driest-type wall damping (Van Driest, 1956) is applied to the convective part of the regularization term:

$$\beta^{\text{vD}} = \left[1 - \exp\left(-\left(\frac{y^+}{A^+}\right)^n\right)\right]^m \quad . \tag{3.45}$$

Here, $y^+ = y/l^+$ designates the dimensionless wall-distance, with the wall-unit $l^+ = \bar{\mu}/(\bar{\rho}u_\tau)$, the friction velocity $u_\tau = \sqrt{\tau_w/\bar{\rho}}$, and the wall-shear stress $\tau_w = \bar{\mu}\,|\partial\overline{\boldsymbol{u}}/\partial\boldsymbol{n}_w|$ along the wall-normal direction indicated by the unit vector $\boldsymbol{n}_w$. Parameters $A^+ = 50$, $n = 3$ and $m = 1/3$ in equation (3.45) are taken from the original ALDM (Hickel *et al.*, 2006). This damping is active essentially only in the near wall region within a distance $y^+ < 80$ (Hickel and Adams, 2007).

The wall-normal velocity gradient magnitude $|\partial\overline{\boldsymbol{u}}\,/\partial\overline{\boldsymbol{n}}|$ can be obtained either directly, or by using a wall-function. The latter yields, in general, a better approximation of the above wall-quantities, denoted by $\breve{l}^+$, $\breve{u}_\tau$, and $\breve{\tau}_w$.

It is emphasized that, although under-resolving the near-wall region, no wall-model is applied when using the ILES scheme. Wall-models are widely used for under-resolved ILES. However, most studies employing a density-based approach use canonical thermodynamic models such as ideal gas (see, e.g., the recent review by Larsson *et al.*, 2016) and thus do not involve phase change, or, when considering two-phase flow such as cavitation, rely on the incompressible description of the fluid (see, e.g., Bensow and Bark, 2010). The application of a wall-model is omitted in the presented computations, as the interference with the fully compressible treatment of two-phase cavitating flow still requires dedicated research, which is beyond the scope of this thesis. A variety of aspects, e.g., the impact on flow separation, near-wall cavity regions and their associated dynamics, as well as the interference with collapse-induced pressure gradients are not sufficiently investigated yet. Due to these uncertainties, no wall-model is employed for two-phase computation. In order to ensure model consistency with the two-phase simulations, it is refrained from using a wall-model in the single-phase computations as well.

Hence, wall-functions are evaluated only *a posteriori*, without a direct feedback in the simulation. In the presented studies, the generalized wall-function without considering pressure gradients of Shih *et al.* (1999) is used for obtaining estimates of the near-wall quantities.

3.3 Assessment of Flow Aggressiveness

In this thesis, two methods for evaluating the erosiveness of cavitating flow are employed. Both rely on the resolution of collapse-induced pressure fluctuations, which is enabled by the compressible approach. As presented subsequently, these are the *maximum pressure criterion*, and the *collapse detection algorithm*.

3.3.1 Maximum Pressure Criterion

For this criterion, the highest pressure encountered during the analysis interval of the computation is recorded within each computational cell. Pressure maxima within the field allow to qualitatively locate regions in the flow where the most violent collapses occur. Restricting the analysis to solid boundaries, this enables to identify erosion-sensitive areas of the technical system under investigation.

The maximum pressure criterion quickly provides an overview and first estimate of the flow aggressiveness. However, several shortcomings inherent to the method have to be kept in mind. As such, it does not differentiate with respect to the origin of peak pressures, which are not necessarily associated with erosion risk, such as stagnation points. Furthermore, it provides only a scalar value, and does not include any information on the rate of occurrence of collapse events. Finally, the method emphasizes solely the strongest event at a given position, which might be heavily subjected to the stochastic nature of the flow. As discussed in §2.2, the collective load of cavitating flow is more appropriately characterized by a load spectrum. Thus, the significance of the maximum pressure criterion is inherently limited.

3.3.2 Collapse Detection Algorithm

The collapse detector, developed by Mihatsch *et al.* (2015), allows to compute *collapse spectra*, which are closely related to impact load spectra, as shown by the authors. It enables a quantitative assessment of the flow aggressiveness. In a later study, based on numerically determined impact load spectra, Mihatsch (2017) is further able to calculate estimates for the incubation time, which are in reasonable agreement with experimentally determined values.

The collapse detection algorithm identifies isolated collapse events in space and time, including an estimation of the collapse strength by recording the collapse pressure. For more details of the implemented algorithm, refer to Mihatsch *et al.* (2015). It first identifies isolated regions of computational cells, where complete condensation occurs. A collapse event is then characterized by a change of sign of local velocity divergence. The time, location, instantaneous collapse pressure, and maximum condensation rate of thus detected events is recorded.

As shown by Schmidt *et al.* (2014), maximum collapse pressures are resolution-dependent, i.e., peak pressures are inversely proportional to the cell size at the collapse center. This is reminiscent of the decay of a spherical, linear pressure wave with $p(r) \sim 1/r$. As discussed by Mihatsch *et al.* (2015), this grid influence

can be removed by introducing a reference length d_{ref} as a calibration parameter, as discussed below, and computing a scaled collapse pressure

$$p_{\text{collapse}}^{\text{scaled}} \sim p_{\text{collapse}} \sqrt[3]{V_{\text{cell}}}/d_{\text{ref}} \ . \tag{3.46}$$

It is assumed that the focal point of the emitted pressure wave is equal to the center of the detected computation cell, and that the radius of the initial wave front is proportional to $\sqrt[3]{V_{\text{cell}}}$, i.e., the equivalent cell length, based on the cell volume V_{cell}.

In addition to its influence on the peak pressure, the spatial resolution also dictates the scale of the smallest spatial structures that can be represented on a given mesh, since an increasing number of smaller vapor structures is generated on finer grid levels. As each vapor structure potentially can cause a collapse, the rate of collapse events N is also resolution-dependent. This holds for Euler computations, where no theoretical limit on the smallest scale exists, due to the absence of molecular viscosity. For ILES computations, this is true as long as the Kolmogorov scale η is not resolved, which is typically not the case for the investigated systems. Thus, a scaling law for obtaining a scaled collapse rate N_{scaled} is proposed by Mihatsch *et al.* (2015):

$$N_{\text{scaled}} \sim N \cdot \chi^{\kappa} \quad , \qquad \text{with } \chi = d_{\text{grid}}/d_{\text{ref}} \ . \tag{3.47}$$

The authors utilize the equivalent cell length $d_{\text{grid}} = \sqrt[3]{V_{\text{cell}}}$ to compute an individual length ratio for each collapse event. Based on experiments of cavitating flow within a radial divergent gap by Franc (2009), Mihatsch *et al.* (2015) calibrated d_{ref} and κ in equations (3.46) and (3.46), yielding $d_{\text{ref}} = 181\ \mu\text{m}, \kappa = 3/2$.

It is conjectured that these parameters are case-dependent, although this is still subject of future investigations. Furthermore, as shown in this thesis, they also dependent on the employed numerical scheme. In order to obtain a calibration for a technical system, it is necessary to quantify the impact load spectrum experimentally, analogously to Mihatsch *et al.* (2015) relying on the work of Franc (2009). For the investigated ship propeller analyzed in chapter 5 this has not been conducted, yet. However, these scalings are mandatory when comparing results from different grid levels, as well as when employing a numerical grid with a strong inhomogeneous distribution of the spatial resolution. Therefore, the cited values for d_{ref} and κ are adopted here as well. Equations (3.46) and (3.46) in this context do not provide absolute values for the collapse rates and pressures levels, that can be compared, e.g., to the material yield strength.

3.4 Flow Solver

For all studies conducted in the scope of this thesis, the solver CATUM is employed. Developed at the TUM Institute of Aerodynamics and Fluid Mechanics, it is a finite-volume flow solver, integrating the compressible Navier-Stokes or Euler equations on block-structured grids. It is written in Fortran, and parallelized using Massage Passing Interface (MPI, see MPI Forum, 2017) directives, for massively-parallel computations on Intel x86 architectures.

Previously, CATUM relied directly on the block-topology of the multi-block mesh for parallel domain decomposition. Assignment of individual blocks of the domain to MPI processes followed a 1-to-1 mapping, i.e., each process integrates the governing equations in space and time over exactly one block. Necessarily, load balancing aspects had to be taken into account already during mesh generation.

While being well-suited for many applications, complex geometries, e.g., the ship propeller considered in chapter 5, often require a more elaborate block topology with a large number of blocks. For these configurations, where mesh generation and appropriate blocking is a challenging task by itself, it is non-trivial to achieve an optimal distribution of cells among the processes by manual load balancing strategies. Since this aspect is crucial for the parallel performance of the code, CATUM was re-structured in the course of this thesis to overcome the 1-to-1 block-to-process restriction. Block assignment to processes can be handled by an external algorithm, e.g., METIS (see Karypis and Kumar, 1998), in order determine the optimal load balancing for a given block topology. This leads to a more efficient computation at simulation-time, and added flexibility during mesh generation, especially for large-scale multi-block configurations. While placing emphasis on backward compatibility, a new code structure and corresponding data layouts were designed in order to achieve this goal.

Moreover, the entire CATUM workflow is re-designed and centered around the CFD General Notation Standard (CGNS, see CFD General Notation System Steering Committee, 2017), an American Institute of Aeronautics and Astronautics (AIAA, see American Institute of Aeronautics and Astronautics, 2017) recommended practice. In this context, a library of mid-level CGNS routines, and a range of supportive pre- and post-processing tools have been newly developed, partly together with supervised students. This includes a tool for domain splitting as a pre-processor to parallel partitioning, computing the wall-distance field for arbitrary geometries, analyzing boundary conditions, or the placement of numerical probes. The solver is further extended by the time-operator preconditioning shown in §3.2.1*b*, and the ALE approach discussed in §3.2.2.

3.5 Summary

All studies presented in this thesis employ the homogeneous mixture approach developed by Schmidt (2015). It is based on the assumptions of mechanical, thermodynamic, and phase equilibrium. Thus, by neglecting surface tension effects, equal pressures $p_\mathrm{l} = p_\mathrm{v}$ are assumed at phase boundaries, as well as equal temperatures $T_\mathrm{l} = T_\mathrm{v}$, and equal Gibbs free energy $g_\mathrm{l} = g_\mathrm{v}$ for the involved phases. Phase change hence happens under equilibrium conditions, such that the cavitation delay vanishes, i.e., $\Delta p = p_\mathrm{th} - p_\mathrm{sat} = 0$, which is equivalent to the assumption of a sufficiently high nuclei content. Furthermore, the influence due to non-condensable gas is neglected for the subsequent studies.

Thermodynamic properties of the system of water and water-vapor are either described by analytical relations modeling the full temperature-dependent behavior, or with a barotropic equation of state. The latter is based on the assumption of isentropic phase change in the two-phase region, and fluid properties are evaluated at a constant reference temperature. Furthermore, an analytical description of the two-phase speed of sound is required. For this purpose, the equilibrium and frozen speed of sound are discussed. It is shown, that the latter is unsuitable for the problems under investigation, and thus the equilibrium speed of sound is chosen for the model.

In summary, the above assumptions yield a parameter-free cavitation model, allowing to describe the two-phase flow as a single fluid. Hence, only a single set of governing equations needs to be solved. These are either the three-dimensional, compressible Euler-equations, or the compressible Navier-Stokes equations. For solving the system, two alternative numerical flux functions are applied. For inviscid Euler-equations, the upwind-biased baseline scheme is employed, which uses 1^{st}-order upwind reconstruction of density and internal energy, and the TVD-limiter of Koren (1993) for reconstructing the velocity, which is formally of 3^{rd}-order in smooth regions. For ensuring low-Mach consistency of the scheme, a 2^{nd}-order approximation of interface pressure is used. When considering Navier-Stokes equations, the ILES scheme of Egerer *et al.* (2016) is utilized. A sensor functional switches between the baseline scheme at shock and phase discontinuities, and a higher-order reconstruction for smooth regions. The latter employs 2^{nd}-order reconstruction of density and internal energy, while velocity and pressure are reconstructed by a linear 4^{th}-order scheme. Viscous fluxes are discretized by a linear 2^{nd}-order central scheme. The truncation error of the scheme is controlled with free parameters introduced via a regularization term, which acts as an physically consistent, implicit model for turbulence.

The full two-phase compressibility is retained in the model. In order to resolve wave dynamics, explicit time-integration of the equations is performed, using a 2^{nd}-order, 4-step Runge-Kutta scheme. In this work, it is extended by time-operator preconditioning, allowing to artificially decrease the stiffness of the problem. Applicable during the initial transient phase, this allows to accelerate the solution, and hence to save computational time. The numerical method is further extended by capabilities to treat moving meshes. Relying on the ALE approach, this includes translational movements, grid stretching, and solid body rotation.

This fully compressible treatment of cavitating flow allows to leverage the captured pressure fluctuations for the evaluation of the flow aggressiveness. In this work, the maximum pressure criterion and the collapse detection algorithm are utilized for both a qualitative and quantitative assessment.

CHAPTER 4

Condensation Shock Phenomena in Cavitating Flow

In this chapter, fully compressible computations of the cavitating flow past a sharp corner, reproducing a recent reference experiment by Ganesh *et al.* (2016a), are discussed. On one hand, the analysis serves as a validation study for the inviscid modeling approach, and the employed single fluid cavitation model. On the other hand, new insights into the dynamics of partial cavitation and condensation shock phenomena are provided. The introduction, §4.1, reviews the significance of partial cavitation for technical systems, discusses flow features that govern the system dynamics, and relevant mechanisms of instability. Thereafter, a description of the problem under consideration, the reference experiment, and the derived computational setup is provided in §4.2. Preparatory studies in §4.3 examine the employed thermodynamic model, and the influence of the spatial resolution. The main findings are then discussed in §4.4, by consideration of the instantaneous and mean flow topology, a spectral analysis of the system dynamics, and an in-depth discussion of the shedding mechanism is carried out. Focus is put on validating the results by comparison with transient x-ray densitometry, and an examination of the condensation shock phenomenon. Concluding thoughts are provided in §4.5.

The contents of this chapter have been published by the author in the Journal of Fluid Mechanics (Budich *et al.*, 2018).

4.1 Introduction

Many hydrodynamic applications, such as turbo-pumps, ship propellers, hydro-turbines, or diesel injectors, are required to operate in regimes where cavitation cannot be avoided. Frequently, it is encountered as partial cavitation, i.e., when the cavity closes on the surfaces of a flow obstacle. In general, partial cavitation is a highly unsteady phenomenon. As Callenaere *et al.* (2001) point out, two fundamental sources of unsteadiness can be distinguished. First, "system instabilities" denote unsteady behavior due to the interaction of the cavity volume with the surrounding system. Second, "intrinsic instabilities" render the cavity inherently unsteady, even under steady operating conditions.

In its most violent form, partial cavitation is associated with the periodic shedding of large vapor clouds. A comprehensive discussion of this flow regime is given for example by Reisman *et al.* (1998), and Laberteaux and Ceccio (2001). It is characterized by a variety of cavitation topologies, including sheet, cloud, as well as vortex cavitation, and involves various length- and time-scales. Cavitating vortices range from small-scale turbulent eddies, larger streamwise-oriented structures, known as "streamers" (Laberteaux and Ceccio, 2001), to cavitating horse-shoe vortices, which can reach the extent of the original sheet cavity itself, or fractions thereof. Further characteristic patterns are "crescent-shaped regions" and "leading-edge structures" (Reisman *et al.*, 1998). While the length-scale of global cavity structures is on the order of the characteristic scales of the flow obstacle, cavity clouds consist of numerous bubbles of various sizes. By performing off-axis laser holography of cloud cavitation on a two-dimensional hydrofoil, Kato *et al.* (1999) were able to detect bubbles down to a radius of 10 μm. The authors report that the number density for bubbles with radii of 35 μm or larger is on the order of 10^3 bubbles/cm^3.

Cloud cavitation results in large fluctuations of cavity volume, causing strong variations in lift and drag forces. Wade and Acosta (1966), studying unsteady cloud cavitation on a plano-convex hydrofoil, report on lift oscillations reaching up to ±10% of the steady mean. For the case of a two-dimensional NACA 0015 hydrofoil, Arndt *et al.* (2000) later find variations in the lift exceeding the mean by 100%. Consequently, cloud cavitation may also lead to substantial structural vibrations. Moreover, many researches have shown that surface pressure loads are extremely high for this regime, refer, e.g., to Le *et al.* (1993) and Kawanami *et al.* (1997). Reisman *et al.* (1998) identify propagating shock waves emitted during "local" and "global events" as the fundamental reason for these pressure fluctuations. Due to the violent nature of the collapses, cloud cavitation is not only associated with severe levels of noise, but is also considered as one of the most aggressive forms of cavitation (Gopalan and Katz, 2000).

Due to these detrimental implications, it is of primary interest (a) to investigate the transition from stable cavities to the unsteady shedding of clouds, (b) to identify relevant mechanisms governing the dynamics of cloud cavitation, and, possibly, (c) to deduce effective means for flow control. In the classical view, cloud cavitation is associated with the occurrence of a re-entrant jet. Feeding an intrinsic instability mechanism, it develops at the cavity closure. Regarded as a thin, upstream-propagating flow of liquid underneath the original sheet cavity, it displaces the cavity away from the wall. When intersecting again with the vapor-liquid interface close to the leading edge, it pinches off the sheet, thereby generating a newly detached cloud. One of the earliest experimental observation of re-entrant jets is reported by Knapp (1955). The authors use high-speed videos for investigating the cavitating flow over two-dimensional and axisymmetric bodies. Furness and Hutton (1975), utilizing two-dimensional unsteady potential flow analysis, are among the first who predict the re-entrant jet phenomenon by analytical models. Later, many experimental studies followed, which identify the re-entrant jet as the driving mechanism for sheet-to-cloud transition, see, e.g., the works of Wade and Acosta (1966), Lush and Skipp (1986), and Foeth *et al.* (2008). Kawanami *et al.* (1997), studying re-entrant jet-induced cloud cavitation over an elliptic-nose hydrofoil, demonstrate an effective means of passive flow control. By placing a small obstacle perpendicular to the direction of the flow, the re-entrant jet can be stopped, thereby suppressing the associated cloud cavitation. The same conclusion is drawn by Pham *et al.* (1999) in a similar study for a plano-convex hydrofoil. Preventing the shedding of large-scale vapor clouds, it allows to mitigate effectively flow aggressiveness, and, thus, cavitation erosion. As a positive side effect, Kawanami *et al.* (1997) also report on the reduction of emitted noise and hydrofoil drag.

As early as 1964, Jakobsen (1964) speculates that the observed violent head breakdown in cavitating inducers is caused by a different mechanism. He conjectures that the two-phase mixture locally reaches a supersonic state such that shock phenomena occur in the cavitating flow. However, no direct experimental observation is made by the author. Similarly, Kawanami *et al.* (1997) also report on a condensation shock phenomenon, but eventually conclude that cloud shedding is related to a re-entrant jet.

Shocks can appear in bubbly flow, since the mixture speed of sound is significantly lower than for any of the two pure constituents. Mallock (1910), assuming a homogeneous mixture, is the first who derives an analytical expression for the speed of sound in a two-phase medium. One of the earliest work on the subject of propagating shock waves in bubbly flow is presented by Campbell and Pitcher (1958), studying planar waves in gas-liquid mixtures. The authors also assume a homogeneous mixture, and derive Rankine-Hugoniot jump conditions, thereby

relating the propagation velocity of the shock to its strength. This work is later extended by Crespo (1969), and Noordzij and Wijngaarden (1974) by also taking the relative bubble motion into account. The principal mechanisms of compressible wave propagation, e.g., steepening of compression waves, frequency-dependency, and oscillations in the wave structure, are identified. However, the authors consider bubbles of air immersed in liquid, and thereby exclude phase transfer. For cavitating flow, in contrast, phase transfer between the vapor and liquid needs to be taken into account. Brennen (1995), and Franc and Michel (2005) derive analytical relations for the speed of sound in a two-phase flow. For intermediate void fractions, the speed of sound of the mixture can be up to two orders of magnitude smaller than without phase transfer. A two-phase flow with phase transition is thus more susceptible to the occurrence of shocks, and, as a consequence, the dynamics of the mixture can be significantly affected.

It is important to recall that so-called condensation shocks are distinct from shock waves emitted by collapsing cavity structures, such as bubbles or clouds. The pressure rise of collapse-induced shocks is of short duration and high amplitude, potentially reaching the order of several GPa (Philipp and Lauterborn, 1998). In contrast, condensation shocks, associated with a retracting partial cavity, act on longer time-scales, and involve phase change. Furthermore, with amplitudes of only a few kPa as in the investigated case, the associated pressure rise can be very weak. Propagating through the liquid medium, collapse-induced shock waves have the potential to affect a shedding process. By abruptly stopping cavity growth when impinging on an attached sheet, as described by Arndt *et al.* (2000) and Leroux *et al.* (2004), this represents an external forcing of the cavity. On the other hand, condensation fronts propagate within a partial cavity. Comparable to a re-entrant jet, these fronts travel upstream through the sheet, having a velocity of the same order as the convective velocity, and cause pinch-off and subsequent shedding of vapor clouds. Yet, also condensation shocks and re-entrant jets are distinct entities, as the former involve phase change and may span the complete height of the cavity, while the latter are typically a thin layer of upstream-propagating liquid underneath the sheet.

Experimental observation of condensation shocks dictating sheet-to-cloud shedding has been described only recently in the literature. Ganesh *et al.* (2016a) use x-ray densitometry for visualizing the instantaneous vapor volume fraction of the cavitating flow over a convergent-divergent wedge. Investigating a range of cavitation numbers, the authors discern three regimes termed “incipient”, “transitory”, and “periodic”. In the first case, the shedding is dominated by a re-entrant jet, while for the latter an upstream-propagating condensation shock is found. In the transitory regime, both phenomena alternate intermittently. The authors show that, depending on the operation point, the time-averaged flow attains a

void fraction of 5 – 50%, while instantaneous values of 80 – 90% or higher can be reached within the sheet cavity, in a spanwise-averaged sense. Due to the low speed of sound at these void fractions, the two-phase flow supports compressible wave phenomena. Interestingly, the authors demonstrate in a subsequent study (Ganesh *et al.*, 2015), that cloud shedding in the case of condensation shocks cannot be controlled with an obstacle located on the wedge surface.

Numerical investigations for this configurations have been recently performed by Gnanaskandan and Mahesh (2016a). Utilizing compressible large-eddy simulation, the authors study the system at a cavitation number $\sigma_1 = (p_1 - p_{\text{vap}})/(\frac{1}{2}\rho_{\text{ref}} u_1^2) = 2.1$, with the upstream pressure p_1, the upstream velocity u_1, the vapor pressure p_{vap}, and the reference density ρ_{ref}. In accordance with the experiments at this operating point, corresponding to the "transitory" regime, the authors observe re-entrant flow, and obtain a good agreement for the shedding Strouhal-number. Moreover, detailed examinations of velocity and void fraction fluctuations for the sheet and cloud are provided. However, the condensation front phenomenon is not discussed by the authors.

One of the first numerical studies examining cloud cavitation in conjunction with condensation shocks is conducted by Schmidt *et al.* (2009). The authors use a fully compressible, homogeneous mixture approach and equilibrium thermodynamics for investigating the cavitating flow past a two-dimensional NACA 0015 hydrofoil. By neglecting physical viscosity in the model, the authors discuss the condensation shock phenomenon, and demonstrate that the observed cavity dynamics are essentially inertia-driven. For the same configuration, Eskilsson and Bensow (2012) also employ a compressible cavitation model. Comparing results obtained with Euler, Reynolds-Averaged Navier-Stokes and large-eddy simulations, the authors also remark the occurrence of such shocks.

With no direct experimental observation of condensation shocks available until recently, the authors of the aforementioned numerical studies make no attempt for a detailed inspection. The goal of the present contribution is thus to re-visit this phenomenon. Relying on the numerical method developed by Schmidt *et al.* (2009), the primary focus is the in-depth analysis of condensation shocks, and a validation with the available experiments of Ganesh *et al.* (2016a).

With the present study, an experimental cavitation number of $\sigma_1 = 1.96$ is considered, i.e., the "periodic" regime. The computational domain closely follows the experimental set-up. All variations of cross-sections within the up- and downstream duct, as well as the presence of the lateral walls of the test-section is account for, which is omitted in the previous studies by Gnanaskandan and Mahesh (2016a). Using the experimental references of Ganesh *et al.* (2016a), typical flow features, the global dynamics of the system, and the time-evolution of the shedding process

are compared. Furthermore, time-averaged and RMS void fraction profiles, as well as instantaneous vapor volume fractions are juxtaposed.

For this study, following the methodology of Schmidt *et al.* (2009), a continuum approach for modeling the cavitating flow as a homogeneous mixture is employed. Unresolved flow features, such as bubbles, nuclei, as well as the effect of surface tension are omitted. Furthermore, after affirming that temperature variations can be neglected, barotropic thermodynamic closures are utilized. While retaining full two-phase compressibility in the method, molecular viscosity is deliberately omitted from the model. For the case of a cavitating nozzle-target flow exhibiting sheet and cloud cavitation, it has been shown previously by Mihatsch *et al.* (2015) that inviscid modeling is sufficient to capture relevant features of cavitating flow. In the present study, it is demonstrated that this is also valid when cavity dynamics are dominated by condensation shock phenomena. The results further provide an indication that condensation shocks, additionally to re-entrant jets, feed an intrinsic instability mechanism of partial cavities.

4.2 Problem Description

4.2.1 Experimental Set-up

The experimental work of Ganesh *et al.* (2016a) is reproduced. A schematic of the experimental set-up is shown in figure 4.1. The test-section, figure 4.1*a*, possesses a quadratic cross-section with an area of 76.2 mm × 76.2 mm, with h_{ch} = 76.2 mm denoting the channel height. A quasi two-dimensional wedge profile, shown in detail in figure 4.1*b*, with a contraction angle of φ_1 = 22.1°, a diffuser angle of φ_2 = 8.13°, and a height h_{w} = 25.4 mm, is mounted on the bottom wall of the test-section. The origin of the coordinate system coincides with the location of the wedge apex at mid-span. The x-, y- and z-directions denote the streamwise, transverse and spanwise direction, respectively. In the following, the test-section walls in the lower/upper transverse direction are denoted as bottom/top walls, and for the lower/upper spanwise direction as left/right lateral or side-walls. The directions parallel and normal to the back-side of the wedge are denoted by s and n, respectively.

The test-section is embedded into a circular feeding line with a diameter of 244.4 mm. At 464.4 mm upstream of the wedge apex, a double contraction connects the test-section to the feeding line. Across this contraction, the cross-section changes from circular through an octagonal section to quadratic, as indicated in figure 4.1*a*. At 571.5 mm downstream of the wedge apex, a mount discontinuously

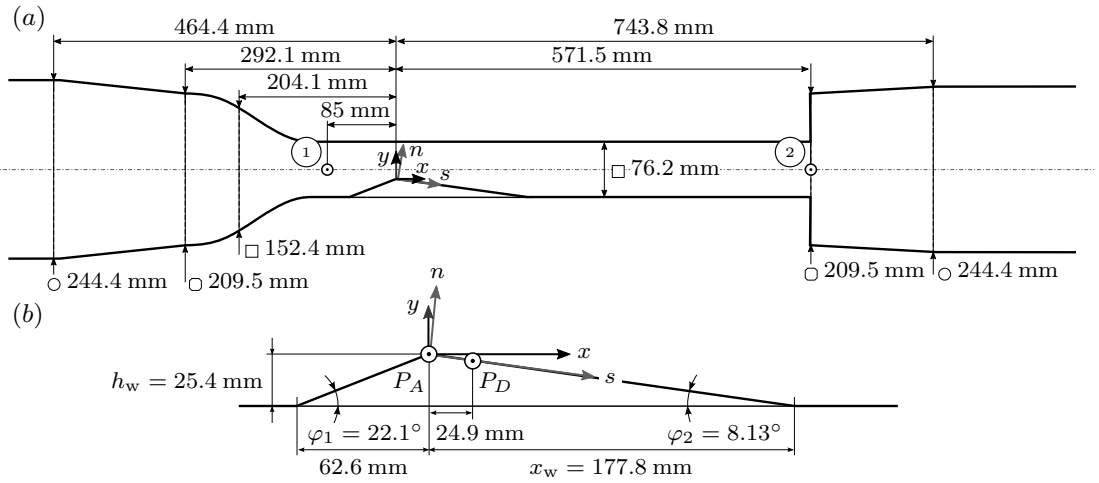

Figure 4.1: Experimental set-up for the investigation of partial cavitation, showing (a) the test-section, and (b) the convergent-divergent wedge. Sketches include the coordinate systems $(x - y)$ and $(s - n)$, and locations 1, 2, P_A and P_D employed for numerical probes.

connects the test-section back to the feeding line, with an additional variation in cross-section shape through an octagonal section.

Optical access to the region of the wedge is provided from the top, and from either side of the test-section. Positions 1 and 2 in figure 4.1*a* indicate the location of static pressure transducers P_1 and P_2, which are utilized to specify the operating point in the experiment. In addition, as shown in figure 4.1*b*, the pressure above the wedge is measured in the experiments by using the static pressure transducers P_A and P_D. These are located below the wedge surface, and connected to a circular opening of diameter 0.8 mm at mid-span of the wedge surface, see Ganesh *et al.* (2016a). This locally modifies the geometry of the wedge apex in the experiments, potentially acting as a nucleation site for cavitation. However, due to the small physical dimension of the probe, the effect on the overall system behavior is expected to be negligible.

4.2.2 Computational Domain and Grid

The computational domain, depicted in figure 4.2, reproduces the nominal experimental set-up. A feeding line with a length of about 1 m ahead of the double contraction is considered. The double contraction, the test-section and the rear mount back to the feeding line are identical to the experimental set-up, including all changes in cross-section shape and size. About 1 m downstream of the test-section, the feeding line connects to an additional large circular tube with a diameter of 800 mm and a length of 500 mm. Although this tube is not part

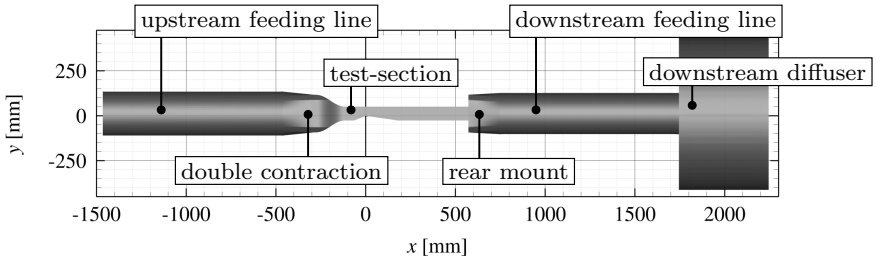

Figure 4.2: Side-view ($x - y$ plane) of the numerical domain employed for the investigations of partial cavitation, including the duct up- and downstream of the test-section, and the large diffuser near the outlet boundary.

of the experimental facility, it allows for improved specification of the boundary conditions. In the experiment, pressure waves originating from, e.g., cavity collapse events in the vicinity of the wedge are able to travel through the whole facility, where a damping due to large increases in cross-sections occurs. The additional tube in the computational set-up causes a comparable effect. However, adjusting the pressure at the end of the additional tube is required in order to recover the experimentally measured pressure at position 2 in the test-section.

Three grid levels, denoted as lvl_0, lvl_1 and lvl_2, are created, see table 4.1 for details. All grids are body-fitted block-structured hexahedral grids. The finest grid level is comprised of 24 million elements for the complete domain, with 17.5 million cells located within the test-section excluding the double contraction. In the vicinity of the wedge, as visualized in figure 4.3, the grid is aligned parallel to the wedge surface, in order to increase the spatial resolution of the sheet cavity. Cubic control volumes with a constant cell edge length up to $n = 30\,\text{mm}$ above the wedge are utilized in this region. Minimum grid spacing on the finest grid level is $l_s = l_n = l_z = 0.5\,\text{mm}$.

Table 4.1: Parameters of the numerical grids employed for the investigations of partial cavitation.

grid level	number of cells (total)	number of cells (test-section)	cell size (wedge vicinity)
lvl_0	0.87×10^6	0.28×10^6	2 mm
lvl_1	4.30×10^6	2.36×10^6	1 mm
lvl_2	24.47×10^6	17.55×10^6	0.5 mm

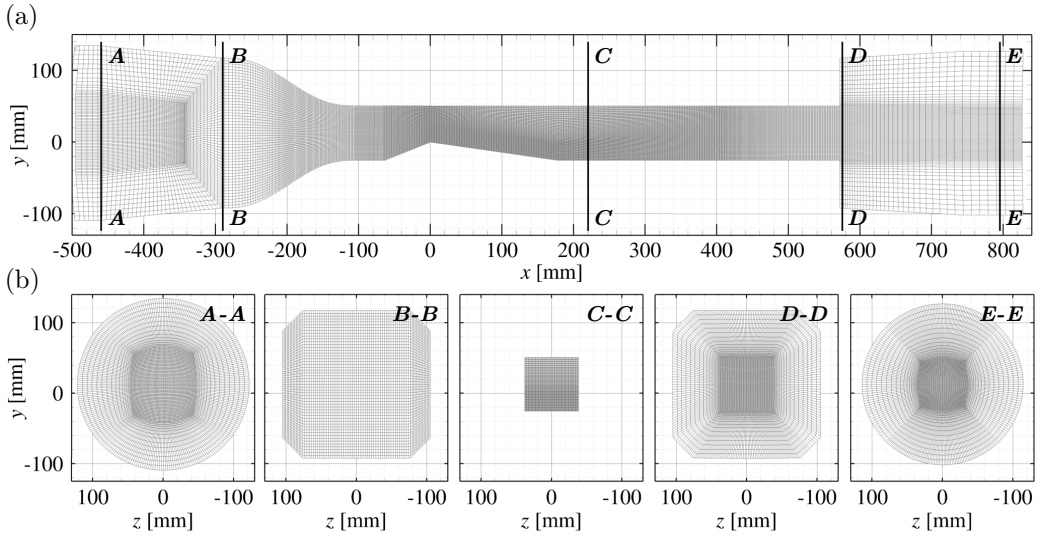

Figure 4.3: Numerical mesh employed for the investigations of partial cavitation, showing the lvl_1 grid in the region of the test-section. (a) Side-view on $x-y$ plane, (b) variation of cross-sections $A-A$ through $E-E$ in the $y-z$ plane.

4.2.3 Boundary Conditions

At the inlet plane of the upstream feeding line, a homogeneous inflow velocity u_0 is specified, while an asymptotic boundary condition on the static outlet pressure p_3 is utilized at the outlet plane of the large downstream diffuser. All walls are modeled as slip-walls, as viscous effects are neglected.

Ganesh *et al.* (2016a) specifies the operating point of the experiment by measuring the static pressure at points 1 and 2 in figure 4.1. The bulk velocity u_1 at position 1 is derived by the authors by measuring the pressure drop between two upstream locations and their corresponding area ratios, and then applying Bernoulli's law. In the experiments, $p_1 = 63\,\text{kPa}$, giving an upstream cavitation number $\sigma_1 = (p_1 - p_{\text{vap}})/(\frac{1}{2}\rho_{\text{ref}}u_1^2) = 1.95$. Ganesh *et al.* (2016a) state an uncertainty of $\pm 0.1\,\text{m/s}$ for the computed upstream velocity, and $\pm 2\,\text{kPa}$ for the pressure measurements. This leads to an overall uncertainty in σ of ± 0.11.

In order to reproduce the experimental operation point in the computations, both u_0 and p_3 are adjusted iteratively, until the velocity $u_1 = 7.9\,\text{m/s}$ at position 1, and the static pressure $p_2 = 55\,\text{kPa}$ at position 2 match with the experimental values. The matching is performed on grid lvl_0. For the subsequent levels lvl_1 and lvl_2, identical boundary conditions are used.

Since the pressure p_2 is controlled with the downstream boundary condition, the pressure p_1 depends on the pressure drop in the test-section. It is hence part of the solution. Consequently, the upstream cavitation number σ_1 in the simulation

cannot be independently prescribed. A definition of the operating point in the computations through the imposed boundary conditions motivates the cavitation number $\sigma_2 = (p_2 - p_{\text{vap}})/(\frac{1}{2}\rho_{\text{ref}}u_1^2)$. As will be shown subsequently, $\sigma_2 = 1.7$, which is a perfect match between simulation and experiment.

4.2.4 Conducted Simulations

With preparatory studies, discussed in §4.3, the influence of the thermodynamic model is assessed. It is found that, first, the high specific heat capacity of the liquid medium causes only minor temperature fluctuations. The temperature-dependency of fluid properties is hence negligible. Second, the present case is characterized by a low convective flow velocity. The occurring condensation shocks, and associated entropy losses are thus weak. Third, baroclinic vorticity production is negligible for the dynamics of the considered system. It is concluded that the influence of the thermodynamic model is insignificant. The subsequent discussion hence focuses on results obtained with the barotropic model, due to its considerably lower computational cost.

A grid sequencing method is employed, consisting of consecutive computations with increasing resolution in space and time. Statistically converged solutions from a coarse grid are thereby interpolated to the next finer grid. This significantly shortens transients on the finer grid levels, and thus reduces the computational cost. Three grid levels, denoted as lvl_0, lvl_1, and lvl_2 are employed. Table 4.2 summarizes the conducted simulations, showing the average time step, the interval used for statistical sampling, and the total run time in terms of physical as well as computational time. Transients associated with simulation start-up and after interpolation are excluded from this evaluation.

Table 4.2: Overview of simulations conducted with the barotropic model for the investigation of partial cavitation.

grid level	average time step [s]	sampling interval [s]	total run time [s]	CPU time [CPUhrs]
lvl_0	3.91×10^{-7}	1.95×10^{-6}	5.20	0.03×10^{6}
lvl_1	1.64×10^{-7}	0.82×10^{-6}	3.16	0.18×10^{6}
lvl_2	0.79×10^{-7}	0.39×10^{-6}	1.66	1.25×10^{6}

4.3 Preparatory Studies

4.3.1 Assessment of Thermodynamic Model

In the following, the influence of the thermodynamic modeling on the global system behavior is reviewed. The importance of temperature-dependency of the fluid properties in the modeling, the role of the barotropic assumption, and the need to evolve the energy equation is assessed.

4.3.1*a* Isolated condensation shock

The dynamics of the sheet-to-cloud cavitation for the problem at hand are dominated by the repeated occurrence of condensation shocks. Capturing the associated entropy losses requires to solve for the energy equation. In contrast, not accounting for these influences may cause an alteration of the shock speed or strength, and, hence, may affect the overall shedding dynamics.

The influence of the thermodynamic model is first studied with regard to isolated, propagating condensation shocks, represented by simplified cases of one-dimensional Riemann-problems. The computational domain utilized for this study is shown in figure 4.4. A total of 1000 homogeneously spaced cells is used for discretizing the region of interest, $|x| \leq 1\,\mathrm{m}$. For decoupling the boundaries from the interior, the flow is extrapolated at the boundaries, located at $|x| = 10\,\mathrm{m}$, and a very coarse mesh is used for the region $1\,\mathrm{m} \leq |x| \leq 10\,\mathrm{m}$. Here, $n = 80$ cells are used, which are spaced according to an exponential bunching law, $Sp_i = Sp_1 \cdot i \cdot \exp(R(i-1))$. Sp_i denotes the distance from the starting to node i, $1 \leq i \leq n$, and the ratio $R = -\log\lfloor (n-1)Sp_1 \rfloor/(n-2)$.

For initialization, "left" and "right" states are extracted from representative pre- and post-shock states at discrete locations in the full three-dimensional simulations presented below. In general, the flow direction is reversed across the shock, while only a weak jump in pressure occurs. The vapor volume fraction upstream of the

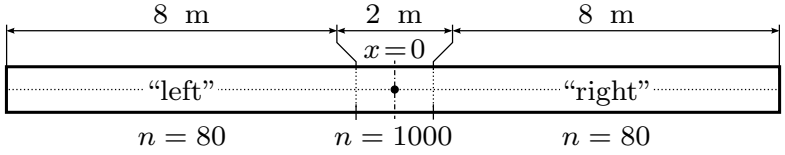

Figure 4.4: Computational domain employed fort the Riemann-problem study, with n denoting the number of cells along the respective edge.

Table 4.3: Initial states at $t = 0$ for the representatively considered Riemann-problem, extracted from three-dimensional simulation.

	ρ [kg/m^3]	u [m/s]	α [-]	p [Pa]	T [K]†
$x < 0$ (*left*, pre-shock)	130	2.9	0.87	2335	(293.11)
$x > 0$ (*right*, post-shock)	998	-4.1	0.00	4367	(293.13)

† Initial temperature is computed from internal energy, and applies only for the full-thermodynamic simulation.

shock attains values between 80% and 97%, while complete condensation occurs after the front has passed.

Results of this study are exemplified here by one set of "left" and "right" states, given in table 4.3. For the full thermodynamic simulation, additional specification of the internal energy is necessary. It is chosen such that the "left" and "right" pressure and density match for the two models. The chosen initialization yields a left-running condensation front. Figure 4.5 shows a comparison of the results obtained with the barotropic and the full thermodynamic model, after integrating until $t = 0.14\,\mathrm{s}$. Results are provided in terms of the density ρ, velocity u, and void fraction α. For the full thermodynamic simulation, also the temperature difference $T - T_0$ is provided, with T_0 being the initial temperature of the "left" state.

For ρ, u, and α, both models yield identical results, and the left-running shock is located at the same position. The front propagation velocity can be evaluated equally as $u_{\mathrm{shock}} = -5.18\,\mathrm{m/s}$. The obtained value for u_{shock} is in good agreement with the result of the full three-dimensional computations. Temperature variations predicted with the full thermodynamic model are small. The temperature increase across the shock amounts to $\max(T - T_0) = 0.077\,\mathrm{K}$, as the observed condensation shock is very weak. The associated entropy production can be neglected.

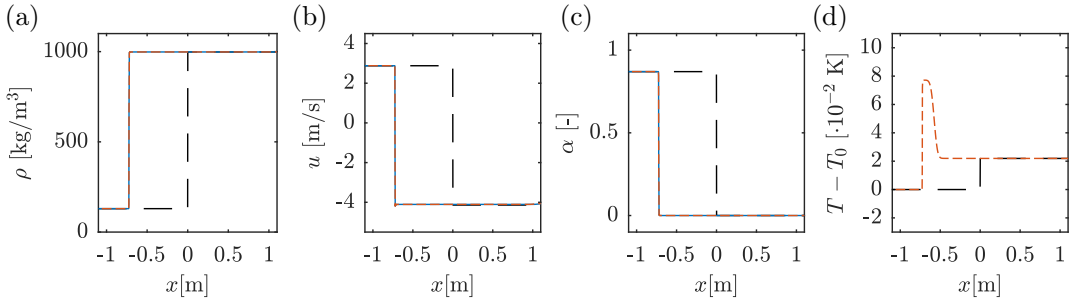

Figure 4.5: Results of the representatively considered Riemann-problem, with initial states given in table 4.3, showing (a) density ρ, (b) velocity u, (c) void fraction α, and (d) temperature difference $T - T_0$. Comparison between the initial state at $t = 0\,\mathrm{s}$ (– – –), and $t = 0.14\,\mathrm{s}$, obtained with the barotropic (——), and full thermodynamic model (– –).

The presented analysis is repeated with various pre- and post-shock states, extracted from the full three-dimensional simulations. From these investigations, it is deduced that the thermodynamic model has no measurable influence regarding the computed velocity and strength for the considered low-speed condensation fronts occurring in the present case. This provides an indication that the barotropic model is able to correctly predict the shock-dominated cavitating flow dynamics for the problem at hand.

4.3.1*b* Full-thermodynamic simulation

A second aspect that has to be assessed is the role of baroclinic torque, acting predominantly at liquid-vapor interfaces, as it cannot represented with a barotropic model. For this purpose, three-dimensional simulations are carried out using both thermodynamic approaches. Only marginal differences are found for the global system dynamics and statistics calculated with both thermodynamic models. Furthermore, temperature fluctuations predicted with the full thermodynamic model are below 5 K.

From these preparatory studies, it is concluded that the influence of the thermodynamic model is insignificant.

4.3.2 Grid Convergence

Figure 4.6 shows the time-evolution of the total amount of vapor volume in the complete domain, $V_\alpha = \int_\Omega \alpha \, \mathrm{d}V$, together with an indication of the temporal mean $\overline{V}_\alpha$, for all three grid levels lvl_0, lvl_1 and lvl_2. Compared to the two finer grid levels, the mean vapor volume predicted on lvl_0 is larger, and the dynamics differ noticeably. In contrast, grid levels lvl_1 and lvl_2 yield nearly the same mean integral vapor volume, and also show a comparable time-evolution. With $\langle \bullet \rangle_z$ denoting averaging in spanwise direction, figure 4.7 shows the mean void fraction $\langle \overline{\alpha} \rangle_z$, and the root mean square (RMS) of the vapor fluctuations $\langle \overline{\alpha' \alpha'} \rangle_z^{1/2}$. In agreement with above findings for $\overline{V}_\alpha$, the spatial extent of mean vapor structures, figures 4.7*a-c*, is largest on lvl_0. Also the RMS level of vapor fluctuations, figures 4.7*d-f*, predicted on lvl_0 is higher, compared to the two finer grid levels. On the other hand, the shape and extent of $\langle \overline{\alpha} \rangle_z$ and $\langle \overline{\alpha' \alpha'} \rangle_z^{1/2}$ are almost identical for grids lvl_1 and lvl_2.

Furthermore, the three grid levels are analyzed with regard to the dominant frequencies present in the flow. For this purpose, Welch's method for estimating the spectral density is applied to the operating point-defining quantities u_1, p_1, p_2

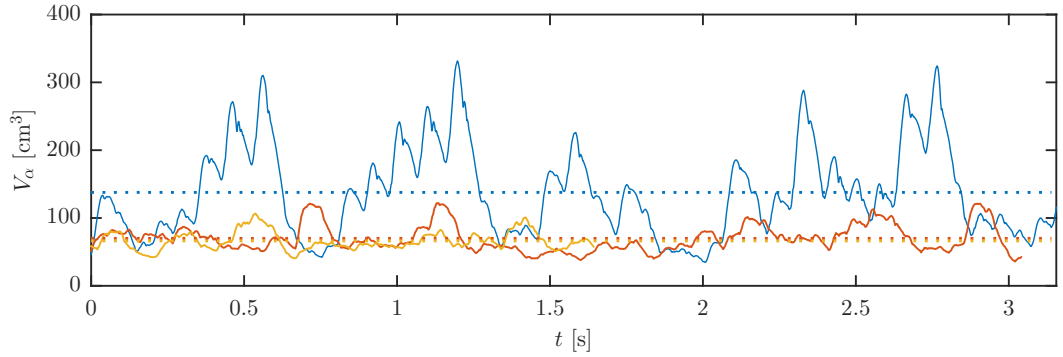

Figure 4.6: Time-evolution of the integral vapor volume V_α (lvl_0 —, lvl_1 —, lvl_2 —), including the respective time-average (···).

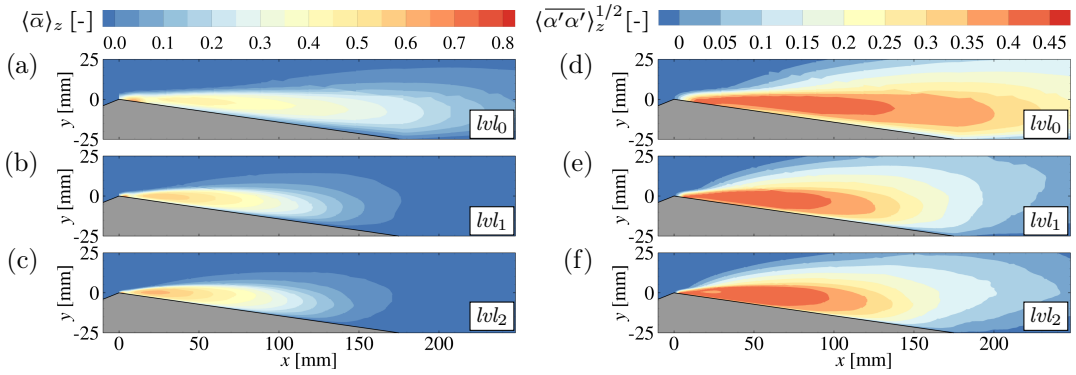

Figure 4.7: Grid convergence of (a-c) time-averaged void fraction field $\langle\bar{\alpha}\rangle_z$, and (d-f) time-averaged RMS of void fraction field $\langle\overline{\alpha'\alpha'}\rangle_z^{1/2}$. Comparison between numerical prediction on (a,d) lvl_0, (b,e) lvl_1, and (c,f)lvl_2.

at locations 1 and 2, as well as the pressure p_{P_D} and local void fraction α_{P_D} at probing position P_D. The signals are sampled with a time-resolution as given in table 4.1, and then linearly interpolated on a constant time step of 2×10^{-6} s (lvl_0), and 1×10^{-6} s (lvl_1 and lvl_2). The spectra are estimated using Hanning window segments with equal window length in time domain of 0.2 s, and 50% overlap between subsequent segments. The resulting spectra are given in figure 4.8.

Signals recorded in the vicinity of the wedge, namely p_1, p_{P_D}, and α_{P_D}, exhibit a dominant low frequency f_1 on all three grid levels. This frequency can be identified as the shedding frequency of the sheet cavity. For lvl_0, $f_1^{lvl_0} \approx 11.4$ Hz, which is lower than on the two finer grids. This in accordance with the larger extent of the sheet cavity on this grid level, as seen above. For lvl_1 and lvl_2, the computed shedding frequency are in excellent agreement with $f_1^{lvl_1} \approx 19.1$ Hz $\approx f_1^{lvl_2}$. The dominant frequencies for the signals of u_1 and p_2 also agree for lvl_1 and lvl_2. In contrast, grid lvl_0 shows discrepancies, both in the dominant frequencies as well as in the integral power of the spectrum, indicating that the cavity dynamics are not sufficiently resolved on this level.

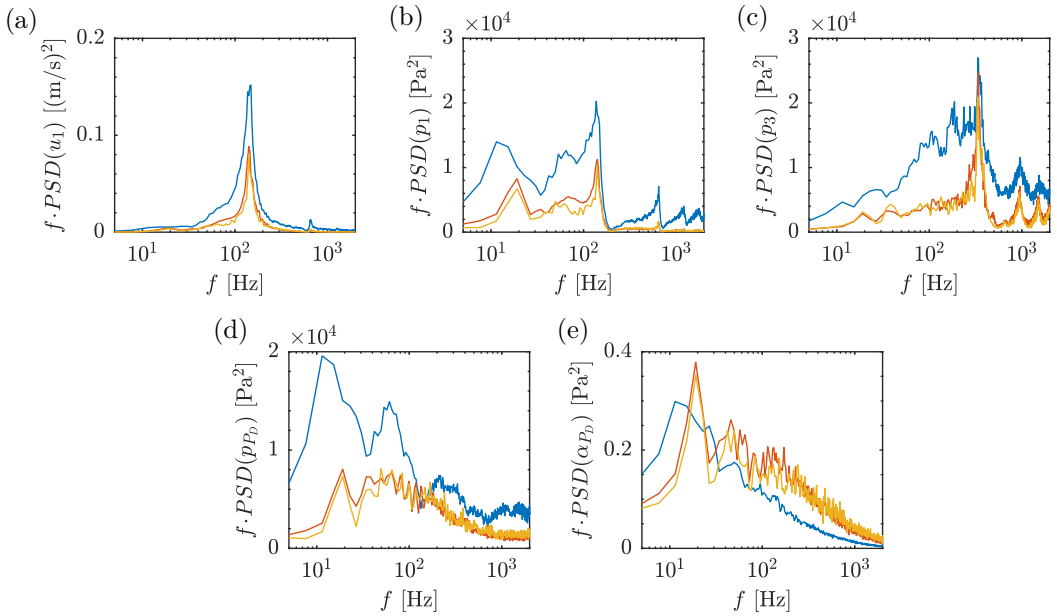

Figure 4.8: Frequency spectra of time-signals of (a) upstream velocity u_1, (b) upstream pressure p_1, (c) downstream pressure p_2, (d) pressure at P_D, and (e) local void fraction at P_D (lvl_0 —, lvl_1 —, lvl_2 —).

Minor deviations in the spectral power can be observed also between lvl_1 and lvl_2. This is associated with a higher level of fragmentation of vapor structures on finer grid levels when using a formally inviscid modeling approach. This fragmentation leads to a grid-dependence of peak-pressures and cavity collapse rates, which in turn affects the level of recorded pressure fluctuations, and thus spectra, see the in-depth discussion by Mihatsch *et al.* (2015). As seen from figure 4.8, this does not alter the predicted low-frequent shedding of the sheet cavity. This mechanism is governed by the intrinsic instability of the cavity and the occurrence of the condensation shock phenomenon, which is of primary interest for the current contribution.

Regarding the operating point and the associated global dynamics of the system, the presented analysis confirms grid convergence on grid lvl_2. The following discussion hence focuses on results obtained with the finest mesh.

4.4 Results

4.4.1 Operating Point

In the following, the agreement with the experimental operating point is assessed by evaluating the temporal mean, denoted by an over-bar $\overline{\bullet}$, of quantities recorded at probing locations 1 and 2, and by comparison of the velocity profile upstream of the wedge.

Table 4.4 shows the obtained mean velocity $\bar{u}_1$, and pressures $\bar{p}_1$, $\bar{p}_2$. Additionally, the mean cavitation numbers $\bar{\sigma}_1$ and $\bar{\sigma}_2$ are given. Quantities $\bar{u}_1$ and $\bar{p}_2$, controlled with the boundary conditions, match the experimental references, and vary only little for the different grid levels. Correspondingly, an almost exact agreement is obtained for the cavitation number $\bar{\sigma}_2$. In contrast, the mean upstream pressure $\bar{p}_1$ is consistently higher in the simulations for all three grid levels. As already discussed, the upstream pressure and thus also the upstream cavitation number is part of the solution. Compared to the experiments, $\bar{p}_1$ and $\bar{\sigma}_1$ are larger by approximately 10%, indicating that the pressure loss $\Delta p = p_1 - p_2$ in the test-section is higher in the simulation.

The following two sections further investigate the agreement with the experimental operating point. In §4.4.1*a*, an analytical model is derived which can be used to explain the observed differences to the experimental references in the pressure drop. Subsequently, the velocity profile upstream of the wedge is analyzed in §4.4.1*b*.

Table 4.4: Operating point-defining flow properties up- and downstream of the test-section, comparison between numerical results on grids lvl_0, lvl_1 and lvl_2, and experimental reference.

grid level	$\bar{u}_1$ [m/s]	$\bar{p}_1$ [Pa]	$\bar{p}_2$ [Pa]	$\bar{\sigma}_1$ [–]	$\bar{\sigma}_2$ [–]
lvl_0	7.9	$71{\times}10^3$	$55{\times}10^3$	2.21	1.69
lvl_1	7.9	$69{\times}10^3$	$55{\times}10^3$	2.16	1.71
lvl_2	7.9	$69{\times}10^3$	$55{\times}10^3$	2.16	1.72
exp.	7.9	$63{\times}10^3 \pm 2\times10^3$	$55{\times}10^3 \pm 2\times10^3$	1.95 ± 0.11	1.73 ± 0.11

4.4.1*a* Pressure Drop

In order to assess the influences contributing to a larger pressure loss across the test-section in the simulation compared to the experiment, an analytical model for Δp between stations 1 and 2 is derived in the following. Figure 4.9 provides a sketch of the considered simplified configuration. The flow in the test-section is assumed inviscid, stationary, and two-dimensional. Furthermore, the inflow and outflow velocities are taken as equal, $u_1 \approx u_2$. This can be readily obtained by considering the continuity equation within the test-section, and assuming complete re-condensation before the flow exits the test-section at station 2. Finally, it is assumed that the quantities u_1, u_2, p_1 and p_2 act across the entire inflow and outflow plane of the test-section, which is reasonable accurate enough for the following derivation. Under these assumptions, the pressure drop is solely caused by pressure contributions along walls with a non-vanishing normal vector in the direction of the flow:

$$\Delta p = \frac{1}{A_{\mathrm{ch}}} \int_A p \left([1,0,0]^T \cdot \boldsymbol{n} \right) \, \mathrm{d}S \tag{4.1}$$

Here, A_{ch} denotes the channel cross-section, while $\boldsymbol{n}$ is the inward-pointing unit normal vector on the integration surfaces. Only the upstream and downstream shoulder of the wedge hence contribute to the pressure drop.

By assuming a pressure distribution along the wedge surface, equation (4.1) can be solved analytically. The total pressure of the flow entering the test-section is given by the upstream station 1 as $p_t = p_1 + \frac{1}{2}\rho_1 u_1^2$. The pressure at the edge between the bottom wall and the upstream shoulder of the wedge is assumed to be $\zeta_1 p_t$. An inviscid flow model requires a stagnation point at this location, i.e. $\zeta_1 = 1$. Under the presence of a viscous boundary layer, however, no stagnation point is present, such that the total pressure is only partly recovered, and thus $0 < \zeta_1 < 1$. Originating at the apex and extending over a fraction ξ of the back-side of the wedge with length L_w, a cavity is present in the temporal mean. Accounting for the fact that, intermittently, both wetted and cavitating flow exists, the pressure in this region can be modeled as constant and equal to a multiple of the vapor pressure, i.e., $\zeta_2 p_{\mathrm{sat}}$, with $\zeta_2 \geq 1$. For the upstream shoulder, a linear decrease from $\zeta_1 p_t$ to $\zeta_2 p_{\mathrm{sat}}$ at the apex is assumed. The pressure recovery downstream of the cavity is also assumed linear, from $\zeta_2 p_{\mathrm{sat}}$ to $\zeta_3 p_t$, with $0 < \zeta_3 < 1$. Note that even for inviscid flow, no stagnation point can be assumed here, as the region downstream of the cavity is largely affected by the passage of clouds shedding from the sheet cavity.

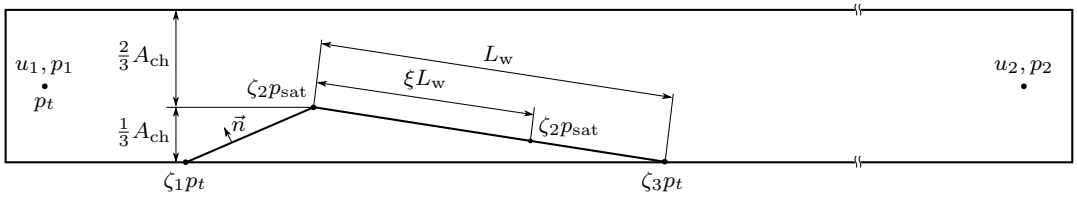

Figure 4.9: Sketch of the simplified test-section geometry, utilized for the analytical pressure loss model, including an indication for the parameters ζ_1, ζ_2, ζ_3, and ξ.

Integration of equation (4.1) with the assumed analytical pressure profile yields

$$\Delta p = \frac{1}{6}\Big[p_t\big(\zeta_1 - (1-\xi)\zeta_3\big) - \zeta_2 \xi p_{\mathrm{sat}}\Big]. \tag{4.2}$$

Under inviscid assumptions, i.e., with $\zeta_1 = 1$, and, for simplicity, assuming a stationary cavity which covers the entire back-side of the wedge, i.e., $\zeta_2 = 1, \xi = 1$, equation (4.2) reduces to

$$\Delta p = \frac{1}{6}\Big[\ p_t - p_{\mathrm{sat}}\Big] \tag{4.3}$$

This predicts a pressure loss of $\approx 15\,\mathrm{kPa}$, which clearly exceeds the experimentally observed value of 8.2 kPa. These considerations substantiate that the present configuration generates a pressure drop, disregarding any other loss mechanisms, including losses due to viscosity. It is thus comparable with the formation of wave drag in super-sonic flow. It is caused solely by the presence of two-phase flow, which prevents a pressure recovery on the back-side of the wedge.

In order to calibrate the parameters ζ_1, ζ_2, ζ_3, and ξ, the assumed analytical pressure profile along the wedge surface is compared with the result obtained by the inviscid computations presented in the remainder of this paper. As shown in figure 4.10, the parameters $\zeta_1 = 1$, $\zeta_2 = 4$, $\zeta_3 = 0.53$, and $\xi = 0.6$ give a good agreement with the numerical result. The thus computed analytical pressure drop (12.3 kPa) compares well with a numeric integration of the profile shown in figure 4.10 (12.7 kPa). Despite the simplifying assumptions of the presented analysis, the computed Δp also compares reasonable well with the pressure loss given by the two point-probes at locations 1 and 2, as stated in table 4.4 (14 kPa).

Due to the boundary layer in the experiments, no stagnation point is present at the upstream edge between wedge and bottom wall, and thus $0 < \zeta_1 < 1$. No experimental data is available which would allow for an estimation of ζ_1. Thus, using the ANSYS CFX simulation package, incompressible, single-phase simulations solving the RANS equations are carried out. For this purpose, the same geometry, including all changes in the upstream and downstream ducting, as discussed in §4.2, is utilized. Viscous walls are resolved with a wall-unit $y^+ \lesssim 10$

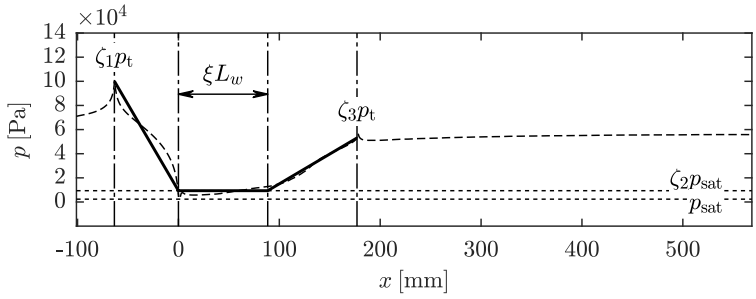

Figure 4.10: Pressure along the bottom wall for the analytical pressure loss model. Comparison between assumed analytical shape (—) with parameters $\zeta_1 = 1$, $\zeta_2 = 4$, $\zeta_3 = 0.53$, $\xi = 0.6$, and time-averaged pressure $\bar{p}_{\text{bottom}}$, as recorded from full three-dimensional simulation at mid-span along the bottom wall (– –).

in the vicinity of the wedge, turbulence modeling is carried out with the k–ω SST model. Inflow and outflow boundary conditions are chosen identical to the compressible simulation. These computations yield a value of $\zeta_1/p_t \approx 0.81$. Using this parameter in equation (4.2), in conjunction with the previously determined value of $\zeta_3 = 0.53$, and the experimental value for the cavity length of $\xi = 0.53$, this gives $\Delta p = 7.9\,\text{kPa}$. This result is in good correspondence with the experimentally obtained pressure drop of 8.2 kPa.

From this analytical model, two factors contributing to an over-estimation of the pressure loss can be identified: First, in the case of a partial cavity, i.e., for $0 < \xi < 1$, a larger cavity length, correlating with a larger cavity extent, causes an increase of Δp. A second factor is the pressure $\zeta_1 p_t$ at the upstream edge between the wedge and the bottom-wall. The significance of these two aspects is assessed with figure 4.11. Keeping the parameters $\zeta_2 = 4$, $\zeta_3 = 0.53$ fixed, the cavity length is studied with figure 4.11*a* via the parameter ξ. The investigation is carried out for two upstream pressures $\zeta_1 = (0.81, 1)$, corresponding to the cases without and with a stagnation point upstream, respectively. A variation in the cavity length between $0.5 \leq \xi \leq 1$ leads to a change in Δp of at most 3.6 kPa. In figure 4.11*b*, the parameter ζ_1 for the upstream pressure is varied, with the same parameters $\zeta_2 = 4$, $\zeta_3 = 0.53$, and a fixed cavity length $\xi = 0.6$. With an influence of at most 8.3 kPa on Δp when considering $0.5 \leq \zeta_1 \leq 1$, the pressure $\zeta_1 p_t$ also has a substantial influence on the overall pressure drop.

The simulations give a cavity extent which is larger by ca. 12%, compared to the experiments. As deduced from figure 4.11, this corresponds to an additional increase in the pressure drop by $\approx 0.5\,\text{kPa}$. Furthermore, a stagnation point in the upstream edge of the wedge is predicted by the simulations, which is not present in the experiments. This latter aspect accounts for an additional pressure loss by ca. 2.8 kPa. Combined, the model thus estimates a deviation in the pressure loss by

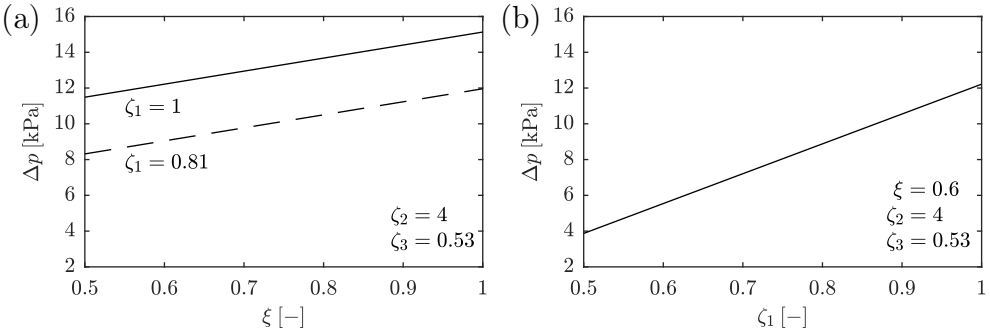

Figure 4.11: Sensitivity study for pressure loss estimated with equation (4.2), regarding (a) the cavity length, and (b) the upstream pressure.

ca. 3.3 kPa, relying entirely on inviscid assumptions. Regarding the simplifications in the derivations, most notably the assumption of two-dimensional, stationary flow and neglect of viscous losses in the tunnel, this corresponds reasonable well with the observed difference of 6 kPa between the predicted and experimental pressure loss.

It is concluded from this study, that the stagnation point, resulting from the inviscid flow assumption, has a larger influence on the pressure drop than the overestimation of the cavity extent. Regarding the uncertainty in the measurements of quantities $\bar{p}_1$ and $\bar{\sigma}_1$ in table 4.4, the agreement with the experimental operating point can still be considered satisfactory.

4.4.1*b* Upstream Velocity

Due to the inviscid assumption, viscous effects, such as boundary layers or corner vortices within the channel, are not captured by the numerics. This could potentially alter the effective inflow conditions to the cavitating region. In order to assess this aspect, the upstream velocity profile at $x = -82$ mm is analyzed in the following.

For this purpose, figure 4.12 shows the profile of the axial velocity component within the test-section along the transverse direction at mid-span. The velocity is normalized by the upstream velocity at position 1 as $\bar{u}/\bar{u}_1$, and the y–coordinate by the channel height as y/h_{ch}. The plot compares LDV measurements by Ganesh *et al.* (2016a), including an indication of the experimental uncertainty, to numerical predictions. Ganesh *et al.* (2016a) conducted two sets of measurements, i.e. in the bulk, and, with a higher spatial resolution, in the near-wall region. The measured velocity of both sets do not exactly match in the overlapping region $0.02 \leq y/h_{\mathrm{ch}} \leq 0.06$, which is attributed to uncertainties in the measurements. The difference, however, amounts to $\lesssim 2\%$, and can thus be regarded as negligible.

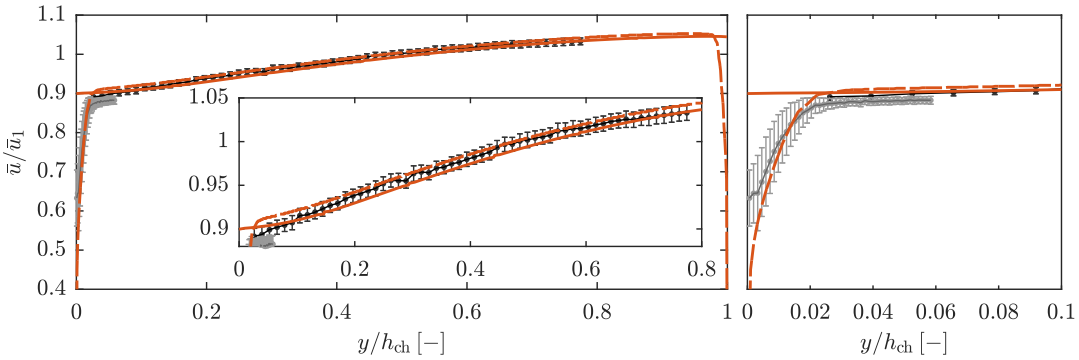

Figure 4.12: Validation of upstream velocity profile at $x = -82\,\mathrm{mm}$. Comparison between experimental data by Ganesh *et al.* (2016a) (measurements in the bulk —, and near-wall profile —, including experimental uncertainty) and numerical predictions (compressible, inviscid simulation —, and incompressible, viscous simulation – –).

Numerical data included in figure 4.12 encompasses the inviscid computations discussed in the remainder of this paper, as well as the viscous, but incompressible RANS computation conducted with ANSYS CFX, introduced in the previous section. The RANS represents steady, single-phase computations, while the inviscid computations are transient, and include phase-change. Results of the latter are thus time-averaged. The presence of cavitation developing downstream of the wedge apex does not influence the investigated upstream velocity profile, as can be seen from the visualization.

In the bulk, a very good agreement with the references is found, with both numerical predictions being located within the experimental error bars for the large majority of the profile. The viscous computations show a slightly higher velocity, compared to the inviscid simulation. This is due to the displacement effect of the boundary layer while keeping the total mass-flux through the velocity inlet boundary condition identical. With a deviation of $\lesssim 1.5\%$ between the predictions, this effect is, however, negligible. The RANS computations exhibit good agreement with the experimental references also in the near-wall region. As expected from the employed slip boundary condition, the inviscid simulation shows no boundary layer. However, the differences are restricted to a region of less than 2% of the channel height, corresponding to 1.5 mm. Due to the acceleration of the flow on the convergent part of the wedge, the boundary layer is expected to be even thinner when reaching the wedge apex. From this investigation, it is concluded that the incoming boundary layer does not have a significant influence on the sheet cavity, and that the assumption of a slip boundary condition in the two-phase computations is acceptable.

4.4.2 Instantaneous Flow Topology

Figure 4.13 compares instantaneous simulation results with snapshots from experimental high-speed videos in top-view. For a visualization of the numerical results, iso-surfaces of the 10% void fraction are chosen. Furthermore, instantaneous vortical structures are shown with iso-surfaces of $\lambda_2 = -2 \times 10^6\ 1/\mathrm{s}^2$, colored by axial vorticity ω_x. Here, λ_2 denotes the second eigenvalue of $\boldsymbol{S}^2 + \boldsymbol{\Omega}^2$, with $\boldsymbol{S}$ and $\boldsymbol{\Omega}$ being the symmetric and asymmetric part of the velocity gradient tensor $\nabla \boldsymbol{u}$, respectively. Dash-dotted lines indicate the location of the apex ($x = 0$) and rear edge ($x = x_\mathrm{w}$) of the wedge. For illustration of the shedding process, five representative time instants are selected in figures 4.13*a-e*, exhibiting typical topological features and coherent flow structures.

Frame (a) shows the time-instant of maximum attached sheet cavity length. The sheet, curved towards both side-walls, attains its largest streamwise extent at mid-span. The experimental picture shows small-scale streamwise-oriented cavitating vortices ("streamers"), trailing from the attached sheet at mid-span. Furthermore, cavitating vortices are situated along both side-walls. Close to the left side-wall, a stream-wise oriented vortex is located and connected to the sheet. Another vortex, oriented normal to the bottom wall and propagating downstream, is located close to the lower side-wall. Side-views provided by Ganesh *et al.* (2016a) show that the stream-wise oriented vortices in the vicinity of the lateral walls are typically located at some distance from the bottom wall. They are hence distinct from corner vortices found in turbulent channel flow. Instead, they are characteristic features of the cavitating flow. The simulations equally exhibit these flow structures. Furthermore, the iso-surface show perturbations of the attached sheet along the side-walls, developing downstream of the apex, which is also found in the experimental picture.

Instant (b) depicts the situation of a condensation shock propagating through the attached sheet towards the wedge apex. As indicated by the dashed line, the progression of the shock is faster at mid-span, while it is slightly slower close to the walls. Simultaneously, a large cavitating horse-shoe vortex develops at the downstream part of the vapor structure. Just upstream of the horse-shoe vortex, a so-called crescent-shaped region is found, a typical flow phenomenon of cavitating flow, see, e.g., Reisman *et al.* (1998). The simulations also predict the occurrence of the condensation shock phenomenon, with a non-uniform rate of progression across the spanwise direction. Likewise, large cavitating horse-shoe vortices, as well as crescent-shaped regions can be found.

At instant (c), the condensation front touches the wedge apex. For most shedding cycles, this does not occur simultaneously across the complete span. Instead, the shock reaches the apex first close to mid-span, while it lags slightly behind near

the lateral walls. A similar behavior is found in the simulation. When the shock reaches the apex, a detached cloud is generated, concentrating strong vorticity along the spanwise direction. Typically, streamers, as shown by the experimental picture, or horse-shoe vortices, as depicted in the numerical visualization, develop at the trailing part of the cloud.

Time-instant (d) shows the situation just after the detachment along the entire spanwise direction, and development of a fully separated cloud further downstream. The region just downstream of the apex is characterized by complex flow patterns.

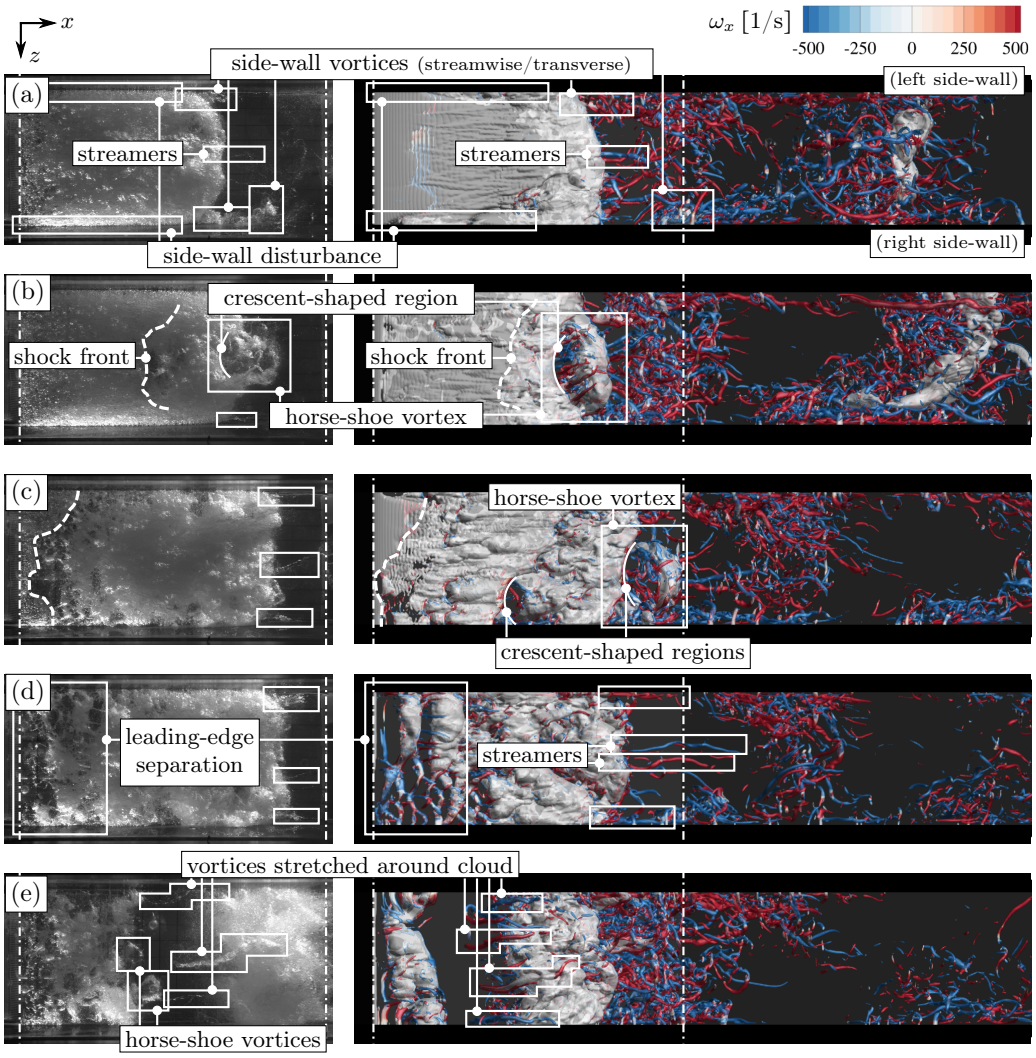

Figure 4.13: Illustration of shedding cycle and coherent flow structures (top-view). Comparison between experiment (*left*) and simulation on lvl_2 grid (*right*). Numerical results show vapor structures with iso-surface of $\alpha = 0.1$ (gray), and vortical structures with iso-surface of $\lambda_2 = -2{\times}10^6 1/\mathrm{s}^2$, colored by axial vorticity ω_x. White boxes indicate coherent flow structures, dash-dotted lines denote the wedge apex ($x = 0$) and the wedge rear point ($x = x_\mathrm{w}$).

Cavitating vortices are mainly oriented along the spanwise direction, partially forming horse-shoe-type structures. Streamwise-oriented vortices connect these patches of cavitation. The flow topology predicted by the simulation resembles the experimental picture.

Finally, at instant (e), the separated cloud is convected further downstream, while a new cavity sheet develops. Typical for this situation is the observation of large cavitating vortices wrapping around the cloud, oriented primarily in streamwise direction. Again, the simulation exhibits comparable structures.

Comparing experimental and numerical frames (a-e), it can be observed that the simulation exhibits slightly less small-scale cavitation. Yet, the λ_2-criterion illustrates the existence of complex vortical structures. For example, smaller streamwise-oriented vortices can be found at the downstream part of the cloud as well as concentrated close to tunnel side-walls. This indicates that the pressure drop in these vortex cores is not sufficient for cavitation to occur. Resolving vortex cavitation within these small-scales structures would require a much finer numerical grid. However, the larger cavitating structures (e.g., horse-shoe cavitation on a variety of length scales, crescent-shaped regions, streamers, vortices along the side-walls in streamwise direction as well as normal to the bottom wall) are predicted in close agreement to the experiments. From this qualitative comparison, it can be concluded that the selected numerical model is able to capture the primary features present in the cavitating flow of sheet-to-cloud transition.

The shedding process can also be visualized with the spanwise average. For this purpose, figure 4.14 shows a series of 6 consecutive time instants by virtue of the instantaneous, spanwise-averaged void fraction $\langle\alpha\rangle_z$, streamwise velocity $\langle u\rangle_z$, and pressure $\langle p\rangle_z$ in the vicinity of the wedge. The plots of velocity and pressure include iso-contours of $\langle\alpha\rangle_z$ for relating these fields with the occurrence of cavitation.

The first instant, $t = t_0$, depicts the instant when the attached sheet reaches its maximum length in streamwise direction, here $s_L \approx 100\text{mm}$. The spanwise-averaged void fraction attains values close to $\langle\alpha\rangle_z \approx 0.8$. Within the sheet, the local flow velocity is small and directed downstream, while the spanwise-averaged pressure attains values close to the vapor pressure. Shortly thereafter, a condensation shock forms at the rear part of the attached sheet. In the subsequent time instants, $t = t_0 + 6\text{ms}$ and $t = t_0 + 12\text{ms}$, the condensation shock propagates upstream through the sheet. Simultaneously, the spanwise-averaged void fraction in the attached part of the sheet increases, reaching values of $\langle\alpha\rangle_z \approx 0.9$. The condensation front spans almost the complete height of the attached sheet, and causes condensation. Across the shock, the direction of flow is reversed and the static pressure increases. A shear layer forms between the free-stream and the upstream-directed flow behind the shock, exhibiting classical Kelvin-Helmholtz instabilities. Within the low-pressure

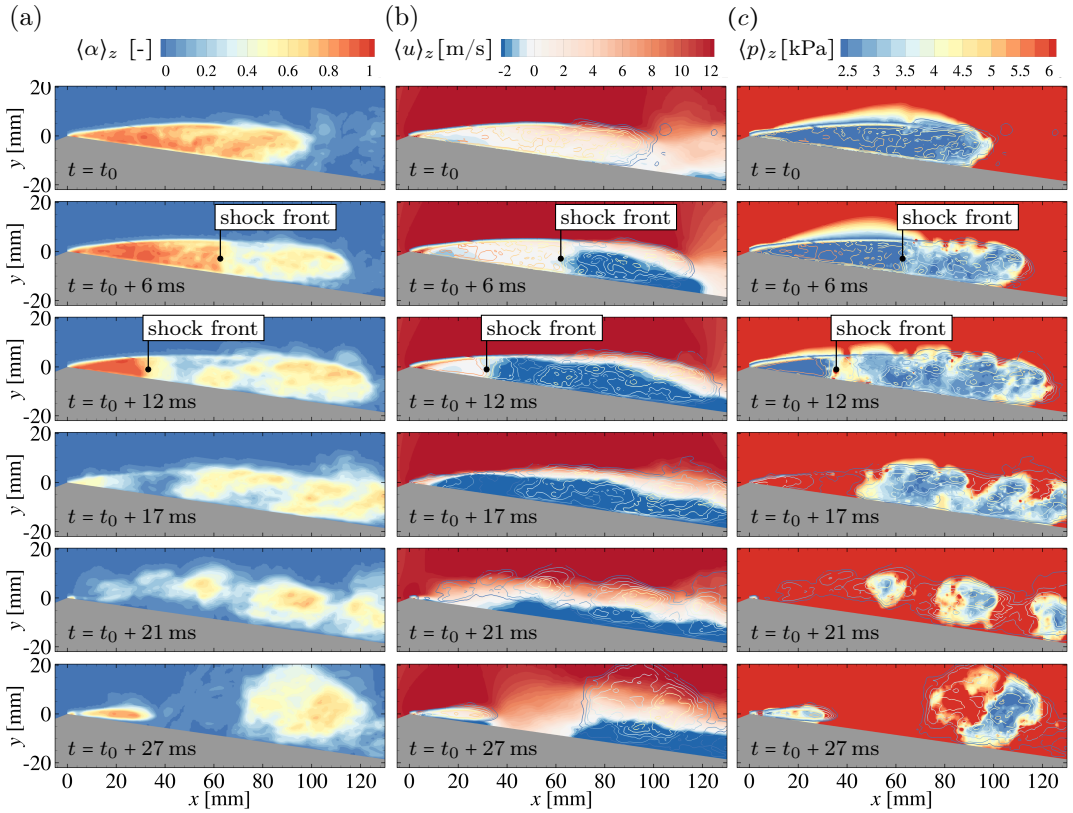

Figure 4.14: Spanwise-averaged, instantaneous flow field during shock-dominated shedding cycle for 6 consecutive time instants, numerical prediction on lvl_2 grid. Comparison between (a) void fraction $\langle\alpha\rangle_z$, (b) streamwise velocity $\langle u\rangle_z$, and (c) pressure $\langle p\rangle_z$. Iso-contours of $\langle\alpha\rangle_z$ superimposed on $\langle u\rangle_z$ and $\langle p\rangle_z$.

vortex cores, evaporation takes place. This leads to the formation of new cavity structures behind the shock, subsequently rolling up into a cloud. Across the condensation front, the more dense liquid displaces the lighter mixture region within the sheet. As a consequence, Rayleigh-Taylor instabilities develop along the interface. In addition to the non-uniform rate of progression noted above, the resulting perturbations of the interface contribute to the fact that it does not appear as a sharp front in the spanwise average. At $t = t_0 + 17\,\text{ms}$, the shock touches the wedge apex. Again, caused by variations in spanwise direction, this does not happen uniformly across the wedge and the spanwise-averaged void fraction is non-zero close to the apex for this instant. Simultaneously, the downstream cloud is continuously fed by the shear layer. Due to the upstream-directed flow following behind the shock front, the cloud is not yet detached. Detachment across the complete spanwise direction is shown with the next frame, $t = t_0 + 21\,\text{ms}$. The upstream-directed flow breaks down, the cloud separates, and starts to propagate downstream. With the cloud being convected downstream, the growth of a new sheet is initiated, as shown in the last frame, $t = t_0 + 27\,\text{ms}$.

For a total of 27 shedding cycles, the maximum attached sheet length s_L is determined from the spanwise-averaged void fraction. The average yields a mean attached sheet length of $\bar{s}_L = 108.4\,\text{mm}$. A measure for the cycle-to-cycle variation is given by the standard deviation of $\bar{s}_L$, which amounts to $\pm 13\,\text{mm}$.

4.4.3 Temporal evolution of shedding process

The shedding process across multiple cycles can be further analyzed by recording the temporal evolution of the spanwise-averaged flow on a plane at a normal distance $n = n_p$ parallel to the wedge surface. Choosing $n_p = 5.2\,\text{mm}$, figure 4.15 shows the thus obtained variation in time for the void fraction $\langle\alpha\rangle_z|_{n_p}$ and axial velocity $\langle u\rangle_z|_{n_p}$, plotted along the s-direction for a time-span of 1 s.

Individual shedding cycles can be identified by the triangular shape in the plot of $\langle\alpha\rangle_z|_{n_p}$. Black solid lines exemplarily highlight several cycles. Positive slopes denote processes of cavity growth, i.e., the formation of a new attached sheet. For most cycles, typical void fractions in the attached sheet exceed 70%, with a tendency to increase during the growth process and towards the wedge apex, as already noted above. In general, the flow is directed downstream within the sheets, and the velocity magnitude is small. After reaching a maximum sheet length, a new process of cavity collapse is initiated, indicated by negative slopes in figure 4.15. Due to the restriction to the plane $n = n_p$, the structures observed here are slightly shorter than the maximum attached sheet length $\bar{s}_L$ computed above. The majority of collapse processes are associated with the occurrence of a condensation shock. Behind the shock, the flow is directed upstream, and the magnitude of flow velocity is significantly increased. In most cycles, the void fraction drops across the shock to values close to zero, as expected. For some cycles, however, non-zero vapor content is present just downstream of the condensation shock. On one hand, this is associated with the cavitating shear layer following immediately behind the shock. On the other hand, the front propagation velocity may be inhomogeneous along the spanwise-direction, as mentioned above. During the collapse process, the cloud, still being connected with the sheet, moves downstream only moderately. For most cycles it does not pass behind $s \approx 150\,\text{mm}$. At the time instant when the shock touches the apex, the cloud completely separates and is convected further downstream.

The slopes in figure 4.15 can be used to estimate the characteristic velocities for the cavity growth and collapse process. The cavity growth velocity, on average $\bar{u}_{\text{growth}} = 5.5\,\text{m/s}$, is approximately constant during a given shedding cycle. The velocity of cavity collapse, corresponding to the propagation velocity of the condensation

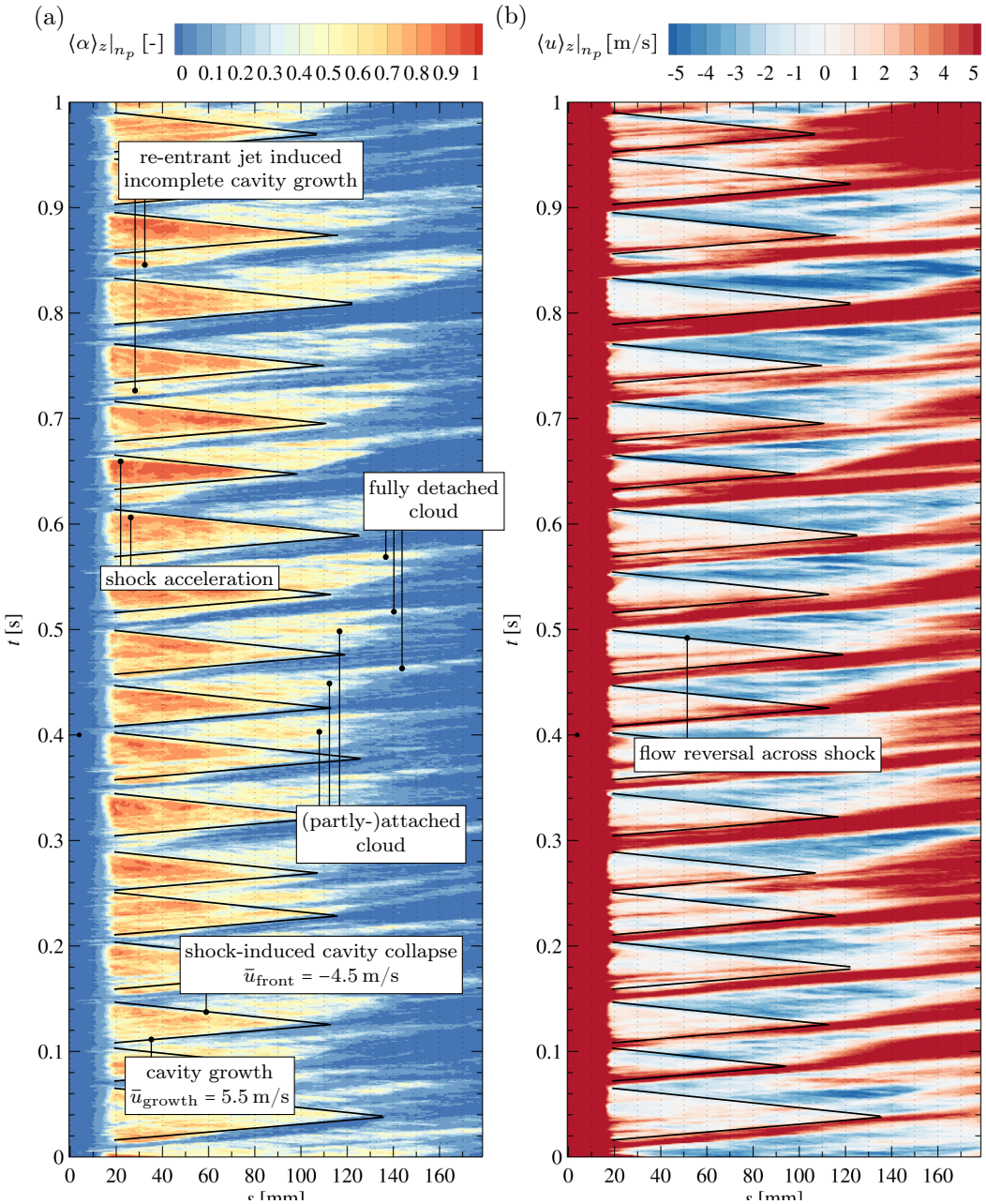

Figure 4.15: Time-evolution of the shedding process over a period of 1 s, numerical prediction on lvl_2 grid. Spanwise-averaged quantities are extracted from a wedge-parallel plane at a normal distance $n = n_p = 5.2$mm and plotted along s. Comparison of (a) void fraction $\langle\alpha\rangle_z|_{n_p}$, and (b) axial velocity component $\langle u\rangle_z|_{n_p}$. Slopes indicated by black lines denote processes of cavity growth ($\bar{u}_{\text{growth}} = 5.5\,\text{m/s}$), and cavity collapse ($\bar{u}_{\text{shock}} = -4.5\,\text{m/s}$).

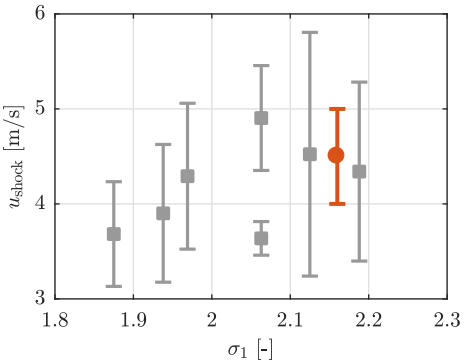

Figure 4.16: Validation of average propagation velocity of condensation shocks $\bar{u}_{\text{shock}}$. Comparison between simulation (—●—), and experiments of Ganesh *et al.* (2016a) (—■—). Error bars indicate cycle-to-cycle variation.

shock front $\bar{u}_{\text{shock}}$, is found to be $\bar{u}_{\text{shock}} \approx -4.5\,\text{m/s}$ on average. The front undergoes a slight acceleration when it approaches the wedge apex. Figure 4.16 compares the value of $\bar{u}_{\text{shock}}$ obtained numerically with experimental measurements for upstream cavitation numbers $1.88 \leq \sigma_1 \leq 2.19$. The computed value for the front propagation velocity is in close agreement with the experimentally reported values.

The acceleration of the condensation shock towards the wedge apex is caused by the fact that the void fraction in the sheet close to the apex increases during the process of cavity collapse, as seen from figures 4.14 and 4.15. This is in agreement with the findings of Brennen (1995), who, neglecting bubbly dynamics, surface tension and phase change, derives the following equation for the front propagation velocity relative to the upstream fluid $u_{\text{shock,rel}}$ in a bubbly flow

$$u^2_{\text{shock,rel}} = \frac{p_2 - p_1}{\rho_L} \cdot \frac{1 - \alpha_2}{(1 - \alpha_1)(\alpha_1 - \alpha_2)} \,. \tag{4.4}$$

States upstream and downstream of the shock are denoted by subscripts "1" and "2", respectively. Assuming the pressure drop $p_2 - p_1$ being almost constant across the front, $u_{\text{shock,rel}}$ increases when $\alpha_1 \to 1$. As seen from figure 4.15, the velocity of the flow upstream of the front also remains approximately constant. Thus, the absolute velocity of the condensation front u_{shock} increases as well.

Figure 4.15 shows that the predicted shedding process does not undergo perfect repeatability. This is documented for the current configuration by Ganesh *et al.* (2016a). It is also a general feature of sheet-to-cloud shedding, as, e.g., described by Reisman *et al.* (1998). For the present case, irregular processes of cavity growth in between two main sheddings can be found in figure 4.15, e.g., around $t = 0.08\,\text{s}$, $t = 0.61\,\text{s}$, $t = 0.79\,\text{s}$ and $t = 0.82\,\text{s}$. These are associated with the occurrence of a classical re-entrant jet instability. According to Ganesh *et al.* (2016a), this is more

frequent at higher cavitation numbers. As reported by the authors, however, it can also appear for the chosen operating point. Furthermore, it is observed in the simulations that a large, coherent collapse of a cloudy structure can prematurely stop the sheet before it reaches its "natural" maximum sheet length, as dictated by the adverse pressure gradient. Thereby initiating a condensation front, this downstream cloud collapse depends, e.g., on the previous cycle, neighboring cavity structures, etc. Furthermore, a cloud collapse does not necessarily occur at mid-span. This can initiate sheet retraction on primarily one side, while the opposite side lacks a bit behind. This in turn affects the next cycle, and may promote variations in the spanwise direction. The entire shedding process is thus stochastic. This contributes to the cycle-to-cycle variations noticed in figure 4.15, e.g., regarding the maximum void fraction reached in the sheets, internal structures in the sheets, and the attached sheet length. This is analyzed in more detail and compared with the experiments in §4.4.6.

4.4.4 Mean Flow Topology

For analyzing the time-averaged flow field in this section, the results obtained on the lvl_2 grid are sampled for a time-span of 1.66 s, comprising approximately 30 shedding cycles. Figure 4.17 depicts the two-dimensional flow field obtained by averaging in time and the spanwise direction. The contour plots show the mean pressure $\langle\bar{p}\rangle_z$, axial velocity $\langle\bar{u}\rangle_z$, and void fraction $\langle\bar{\alpha}\rangle_z$ in the vicinity of the wedge. The direction of the mean flow is indicated by streamlines, a contour line of $\langle\bar{u}\rangle_z = 0\,\mathrm{m/s}$ highlights a region of reversed mean flow. Due to the convergent shape of the channel, the mean flow is accelerated above the wedge. Correspondingly, the local static pressure drops, reaching values close to the vapor pressure on the back side of the wedge. Accordingly, a contiguous region of cavitation is present in the temporal mean. Located above the back-side of the wedge, it originates from the sharp wedge apex. A narrow region of reversed flow exists just above the wedge in the mean flow, spanning less than half of the cavity height.

The mean flow is not homogeneous in the spanwise direction. This is illustrated by figure 4.18 showing the time-averaged three-dimensional flow field. The mean cavitation pattern is visualized by an iso-surface of the 20% void fraction. Slices perpendicular to the spanwise direction show the local time-averaged void fraction $\bar{\alpha}$ above the wedge, with a cut-off at $\bar{\alpha} < 0.1$. On the bottom- and left side-wall of the channel, the contour of mean velocity in streamwise-direction $\bar{u}$ is given. An iso-contour of $\bar{u} = 0\,\mathrm{m/s}$ denotes a region of reversed flow present in the time-averaged flow field. Vortical structures are shown by iso-surfaces of $\overline{Q} = 1 \times 10^5\,1/\mathrm{s}^2$, with $\overline{Q}$ denoting the time-average of the instantaneous Q-criterion, $Q = 1/2(\|\boldsymbol{S}\|^2 - \|\boldsymbol{\Omega}\|^2)$. The orientation of the vortices is given by coloring the iso-surface by the local mean

axial vorticity $\overline{\omega}_x$. Despite the long time-span of the temporal average containing many shedding cycles, fluctuations in the iso-surface of the vapor volume fraction can be observed. However, these deviations can be regarded as small, and the statistics are considered as sufficiently converged.

The streamwise extent of the time-averaged vapor structure is largest at mid-span. Simultaneously, the region of reversed flow extents further downstream close to the side-walls. Two counter-rotating vortices along the streamwise direction are present in the temporal mean. These vortices originate from the corner between the side-walls and the bottom wall of the test-section, just downstream of the

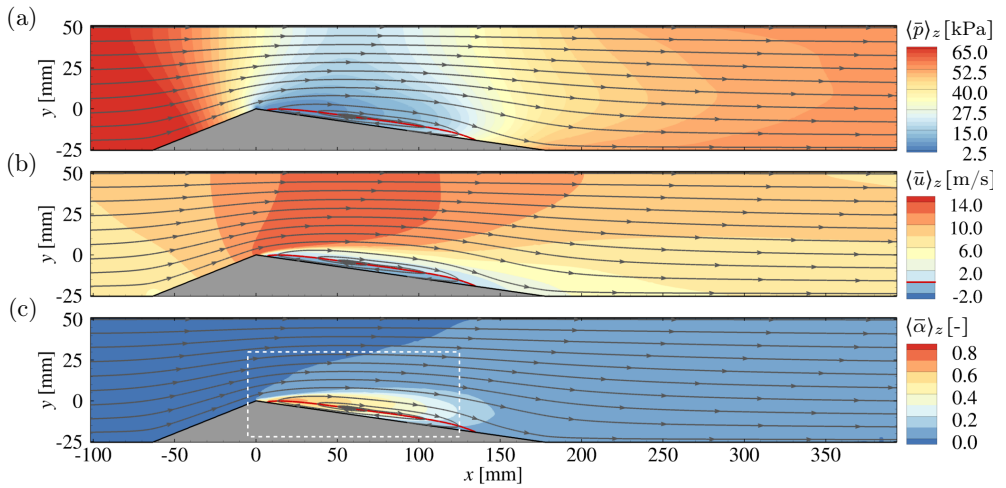

Figure 4.17: Time- and spanwise-averaged flow field in the test-section, numerical prediction on lvl_2 grid. Comparison of (a) pressure $\langle\bar{p}\rangle_z$, (b) axial velocity $\langle\bar{u}\rangle_z$, and (c) void fraction $\langle\bar{\alpha}\rangle_z$. Direction of flow indicated by stream-lines, the red solid line indicates a region of reversed flow $\langle\bar{u}\rangle_z = 0$, the white dashed frame highlights the field-of-view for the experimental x-ray densitometry of Ganesh *et al.* (2016a).

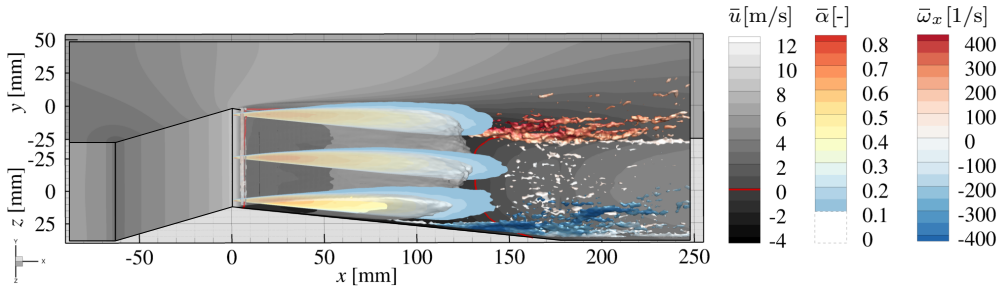

Figure 4.18: Time-averaged flow field in the vicinity of the wedge, numerical prediction on lvl_2 grid. Vapor structures are shown by iso-surfaces of $\overline{\alpha} = 0.2$, and vortical structures by iso-surfaces of $\overline{Q} = 1 \times 10^5\ 1/s^2$, colored by axial vorticity $\overline{\omega}_x$. Contours of $\overline{\alpha}$ given in three slices perpendicular to the spanwise direction, with a cut-off at $\overline{\alpha} < 0.1$. Tunnel walls show contours of axial velocity $\overline{u}$. The red solid line indicates a region of reversed flow $\overline{u} = 0$.

contiguous mean vapor structure. They are slightly inclined away from the bottom wall, and oriented such that fluid is transported along the lateral walls in positive y-direction, converging towards mid-span.

The spanwise inhomogeneity of the time-averaged flow is caused by the presence of the side-walls. A direct verification of the three-dimensional mean flow structure with the experiments is not possible, as no corresponding data is available. However, it is in alignment with the observations made in context of figure 4.13 above. All presented instantaneous images exhibit noticeable variations along the spanwise direction, e.g., the development of horse-shoe vortices in the center of the channel, vortices along the side-walls, and show that the extent of attached sheets is largest at mid-span. Thus, the presence of the side-walls cannot be neglected in the simulations. It is concluded that the global flow topology is correctly captured, even though slip boundary condition due to the inviscid modeling are used in the present study.

4.4.5 Spectral Analysis

In order to identify dominant frequencies and their spatial distribution in the system, a spectral analysis for signals recorded within the entire test-section is carried out. For this purpose, the local axial velocity component u and pressure p is recorded along the bottom wall of the test-section by a total of 55 numerical probes. The probes are located at mid-span, and distributed evenly in streamwise direction with a spacing of $\Delta x \approx 11\,\mathrm{mm}$ between two consecutive probes. For the spectral analysis, Welch's method is applied. The signals are sampled with a time-resolution as given in table 4.2, and then linearly interpolated on a constant time step of $1 \times 10^{-6}\,\mathrm{s}$. The spectra are estimated using Hanning window segments with equal window length in time domain of 0.2 s, and 50% overlap between subsequent segments.

The frequency content is displayed in figure 4.19. The plots show the square root of the pre-multiplied power spectral density, $\sqrt{f\,PSD(\bullet)}$, as a function of the streamwise position. The computed spectra for the axial velocity u, figure 4.19*a*, and the pressure p, figure 4.19*b*, can thus be interpreted as the RMS amplitude at a given frequency. A non-dimensional representation of the spectra is obtained using the local mean quantities for normalization, $\sqrt{f\,PSD(\bullet)/\bar{\bullet}^2}$. Figure 4.20 shows the time-averaged axial velocity, figure 4.20*a*, and pressure, figure 4.20*b*, at mid-span along the bottom wall, which are used for the non-dimensionalization. The resulting dimensionless frequency spectra are given in figure 4.21 for the velocity signals, figure 4.21*a*, and pressure signals, figure 4.21*b*. The location of the wedge apex, $x = 0$, and rear edge, $x_\mathrm{w} = 177\,\mathrm{mm}$, are indicated by dashed lines, while the projection of the maximum attached sheet length on the x-axis, $\bar{x}_L = cos(\varphi_2)\bar{s}_L = 107.3\,\mathrm{mm}$, is shown with a dash-dotted line in the figures.

The spectrum for the axial velocity, figure 4.19*a*, shows a dominant peak (global maximum) in the region $\bar{x}_L \lesssim x \lesssim x_\mathrm{w}$. The associated frequency $f_1 \approx 19.1\,\mathrm{Hz}$ corresponds to the frequency of cloud shedding. It is also found in the spectra of discrete probes, as discussed in §4.3.2. With an RMS amplitude of approximately 6.4 m/s, substantial variations are found for the axial velocity component. These are caused by the flow reversal following behind the propagating condensation front, and are comparable to the upstream velocity u_1. The normalized spectrum, figure 4.21*a*, shows that the fluctuations exceed the local mean velocity significantly. The amplification locally exceeds a factor of > 15, and remains high within the entire region of attached sheets.

Due to the stochastic nature of the shedding process, the spectra do not show a sharp peak at a single frequency. Instead, the fluctuations appear as smeared over a range of frequencies: taking 80% of the peak RMS amplitude, the shedding occurs in a frequency band of approximately $f_1 \pm 2\,\mathrm{Hz}$. The spectrum further shows the existence of harmonics of the shedding frequency.

The spatial region with noticeable variations in the velocity signals extends downstream of the attached sheet and behind the wedge. This is caused by downstream propagating clouds that lead to a perturbation of the near-wall velocity, recurring coherently with the shedding frequency. Furthermore, RMS amplitudes exceeding approximately 2 m/s can be found in the frequency band $10 \leq f \leq 100\,\mathrm{Hz}$ throughout the test-section, but are concentrated around the maximum attached sheet length and the wedge apex.

As expected, the pressure spectrum, figure 4.19*b*, equally exhibits the strongest fluctuations at the shedding frequency f_1, and harmonics thereof. In contrast to the velocity, where the largest RMS amplitudes are found within a single spatial region, two distinctive peaks can be identified in the pressure spectrum at f_1. At the first location, just upstream of the maximum attached sheet length $x \lesssim \bar{x}_L$, the RMS amplitude amounts to approximately 15 kPa. This corresponds to the region where the condensation shock is formed, connected to a pressure rise, within each cycle. In addition, a second maximum can be found centered around $x \approx x_\mathrm{w}$. Here, the majority of shed clouds collapse coherently. Intense pressure peaks emitted by these collapses cause RMS amplitudes which are approximately 40% higher than for the first peak. In between these two regions, a contribution at a lower frequency is visible, which might be caused by an interference between these two mechanism. The normalized pressure spectrum, figure 4.21*b*, shows that the variations caused by the condensation shock are on the same order as the local mean pressure, which is essentially equal to the vapor pressure. The relative pressure fluctuations are hence smaller by about one order of magnitude than variations in the velocity, as seen above.

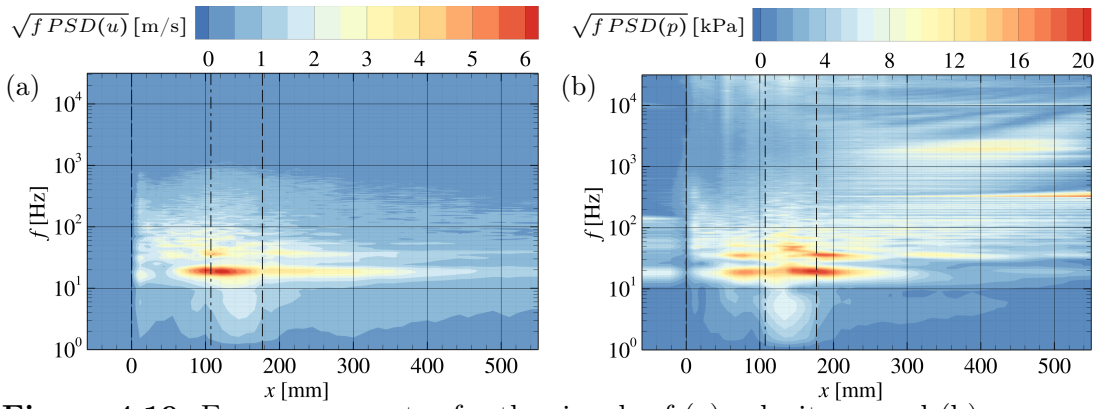

Figure 4.19: Frequency spectra for the signals of (a) velocity u, and (b) pressure p, recorded by probes distributed within the test-section along the bottom wall at mid-span. Dashed lines indicate the locations of the wedge apex ($x = 0$) and the rear point ($x = x_w$), dash-dotted lines indicate the mean of the maximum attached sheet length ($x = \bar{x}_L$).

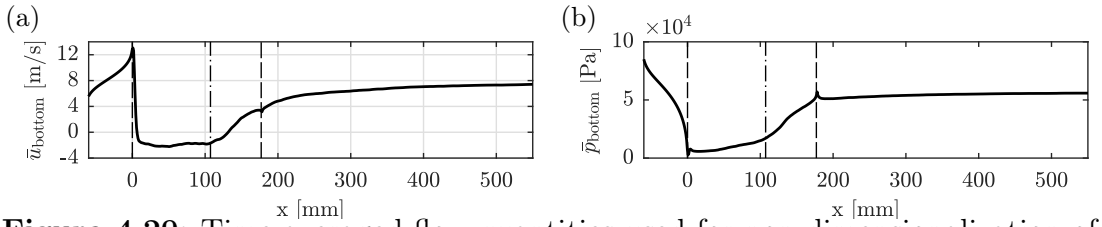

Figure 4.20: Time-averaged flow quantities used for non-dimensionalization of the frequency spectra plotted in figure 4.19. Juxtaposition of (a) mean velocity $\bar{u}_{bottom}$, and (b) pressure $\bar{p}_{bottom}$, recorded at mid-span along the bottom wall.

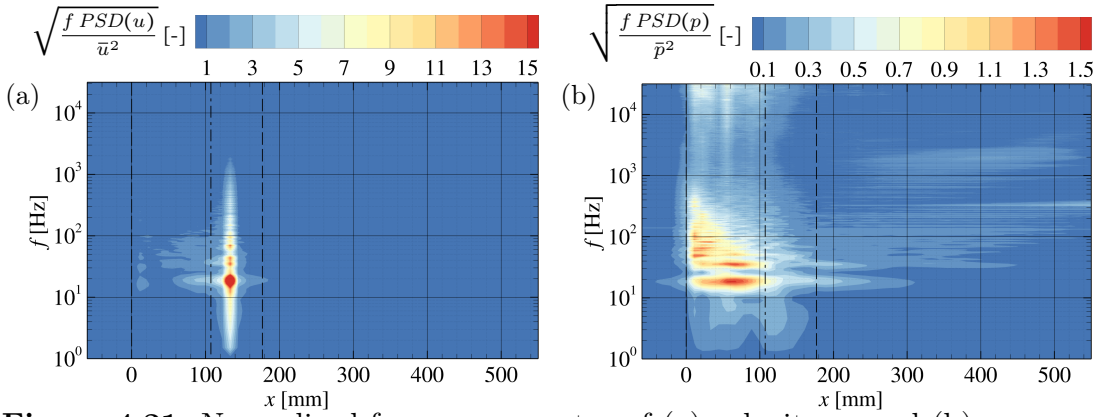

Figure 4.21: Normalized frequency spectra of (a) velocity u, and (b) pressure p, recorded by probes distributed within the test-section along the bottom wall at mid-span. The spectra are normalized by the local mean of velocity and pressure, respectively. Dashed lines indicate the locations of the wedge apex ($x = 0$) and the rear point ($x = x_w$), dash-dotted lines indicate the mean of the maximum attached sheet length ($x = \bar{x}_L$).

While no significant velocity fluctuations are present upstream of the wedge ($x < 0$), noticeable levels of pressure fluctuations are found in this region. These are caused by shocks, originating from coherent cloud collapses, that propagate upstream through the liquid medium. Downstream, in the region $300 \leq x \leq 500$ mm, the pressure spectrum shows significant contributions at frequencies $f \geq 1$ kHz. These are generated by high-frequent, incoherent collapse events created during the disintegration of downstream propagating clouds into smaller vapor structures.

Two artifacts in the pressure spectrum can be found. First, in the vicinity of the wedge, the amplitude rises when approaching the upper bound of the spectrum, i.e., at frequencies $f > 10$ kHz. Due to the intermittent presence of vapor directly adjacent to the wedge surface, the pressure signals recorded in this area are clipped at the vapor pressure. This leads to the observed ringing artifacts. Second, the spectrum gives a sharp peak at $f \approx 300$ Hz when approaching the exit of the test-section. This is caused by interactions between cavity collapse acoustics and the free-stream jet exiting the test-section into the larger downstream tubing. The normalized pressure spectrum however shows that the relative amplitude of this phenomenon is small.

The shedding process can be characterized by a non-dimensional Strouhal-number. In agreement with Ganesh *et al.* (2016a), it is computed here as $St = f_1 \bar{s}_L / u_1$, using the shedding frequency f_1, the mean attached sheet length $\bar{s}_L$, and the upstream velocity u_1. With $f_1 = 19.1 \pm 2$ Hz and $\bar{s}_L = 108.4 \pm 13$ mm, it amounts to $St = 0.262 \pm 0.03$. The frequency f_1 is obtained equally by the presented spectral analysis of the pressure and velocity signal record along the bottom wall, as well as by pressure and void fraction signals recorded with discrete numerical probes at position 1 and P_D, as discussed in §4.3.2. On the other

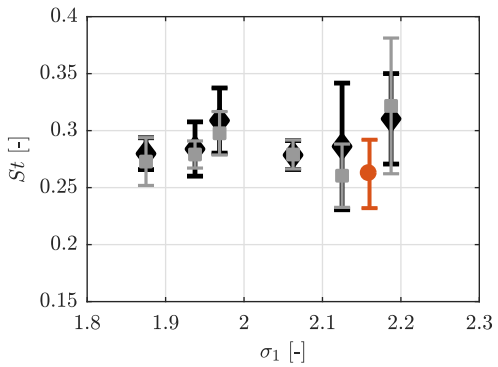

Figure 4.22: Validation of shedding Strouhal-number St. Comparison between simulation (—●—), and experiments of Ganesh *et al.* (2016a) (frequency obtained from pressure transducer signals —◆—, and void fraction measurements —■—). Error bars indicate cycle-to-cycle variation.

hand, in order to determine the shedding frequency experimentally, Ganesh *et al.* (2016a) uses pressure probes as well as transient, spanwise-averaged void fraction measurements obtained by x-ray densitometry. Figure 4.22 shows the comparison with the experimental references for upstream cavitation numbers $1.88 \leq \sigma_1 \leq 2.19$. The computed Strouhal-number is in close agreement with the experimentally reported values for periodic shedding cavities, which is given by Ganesh *et al.* (2016a) as $St = 0.26 \pm 0.02$.

4.4.6 Comparison with x-ray densitometry

4.4.6*a* Time-averaged void fraction

The dashed rectangle drawn in figure 4.17*c* indicates the field-of-view for the x-ray densitometry conducted by Ganesh *et al.* (2016a). A zoom into this view is given in figure 4.23*a*, juxtaposing the temporal mean of the experimentally obtained void fraction, with the corresponding numerical result of $\langle \overline{\alpha} \rangle_z$. Figure 4.23*b* compares profiles of the experimentally and numerically obtained void fraction, plotted as a function of the normal coordinate n. These profiles are extracted along the y-direction, at locations spaced evenly in spanwise direction for $10\,\text{mm} \leq x \leq 120\,\text{mm}$, with $\Delta x = 10\,\text{mm}$, as indicated by dashed lines in figure 4.23*a*.

The simulation exhibits a larger vapor production in the temporal and spanwise mean. The extent of the mean vapor structure in streamwise direction, as, e.g., measured by the 20% void fraction, is larger than for the experiments. The local maximum average void fraction in the simulation is up to 25% higher compared to the experiments. The agreement in the front part of the wedge, $0 \lesssim x \lesssim 50\,\text{mm}$, corresponding to the location of the sheet cavity, is better than in the region further downstream. As shown by the vapor profiles, the local mean void fraction attains an almost constant value of 50% across the height of the sheet, being consistently higher in the simulation. The void fraction then abruptly drops to $\alpha \approx 0$, with a good agreement for the cavity thickness and the sharpness of the liquid-vapor interface. Further downstream, $x \gtrsim 50\,\text{mm}$, the agreement is deteriorated. In this region, the liquid-vapor transition occurs more gradually.

Four factors may contribute to the larger mean amount of vapor in the simulation. First, the shape of the wedge apex influences the local vapor production. As no information about the actual manufactured apex geometry is available, it is modeled as a sharp corner in the simulation. A finite apex radius would mitigate the suction peak in the pressure, which contributes to an attenuating of cavitation. Second, the equilibrium speed of sound c_{eq} is used for obtaining the barotropic equation of state. As discussed in §3.1.3*c*, this is a lower estimate of the true

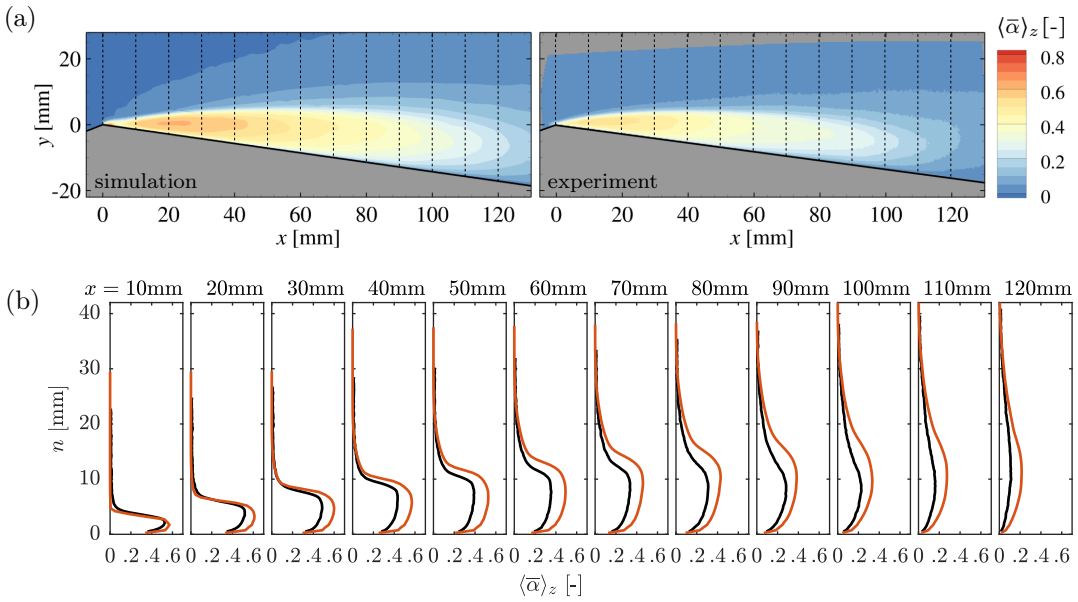

Figure 4.23: Validation of time- and spanwise-averaged void fraction field $\langle\overline{\alpha}\rangle_z$. (a) Comparison of contour plots obtained numerically (*left*), and with x-ray densitometry by Ganesh *et al.* (2016a) (*right*). (b) Void fraction profiles $\langle\overline{\alpha}\rangle_z(n)$ extracted along dashed lines indicated in (a) (simulation —, experiment —).

speed of sound in mixture regions. With lower values of c being connected to stronger evaporation, this may cause a higher vapor content. Third, in the region $x \gtrsim 50$ mm, the main contribution to the mean void fraction originates from cloudy structures, periodically detaching from the sheet cavity. It is believed that the spatial resolution in this region is insufficient to capture the complete three-dimensionality and granularity of the vapor structures. As mentioned initially, Kato *et al.* (1999) find that the bubble number density in clouds can be on the order of 10^3 bubbles/cm^3 or higher. The necessary spatial resolution is beyond what is currently computationally feasible when considering a large-scale system such as the one under investigation. A larger vapor content for the shed clouds causes prolonged structures observed in the temporal mean. Finally, neglecting the effect of gas content in the simulations may also contribute to a higher mean amount of vapor, although an exact quantification is difficult. Qualitatively, the presence of free gas increases the compressibility of the bulk. For the present configuration, it is expected that the suction peak at the wedge apex is mitigated, thereby reducing the local rate of vapor production. Furthermore, acoustics in the bulk are damped, which leads also to an attenuation of expansion waves. As these in turn may induce cavitation, this can further contribute to less vapor content.

The mean amount of vapor produced may further be affected by viscous lateral boundary layers present in the experiments, by introducing additional three-

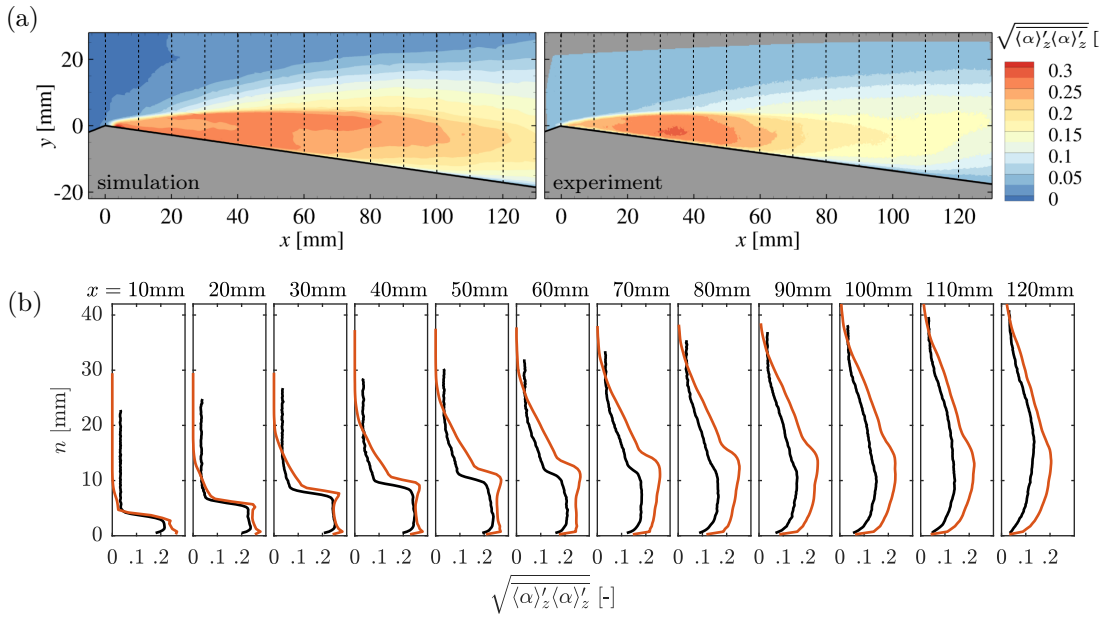

Figure 4.24: Validation of RMS of time- and spanwise-averaged void fraction field $(\overline{\langle\alpha\rangle'_z\langle\alpha\rangle'_z})^{1/2}$. (a) Comparison of contour plots obtained numerically (*left*), and with x-ray densitometry by Ganesh *et al.* (2016a) (*right*). (b) Profiles of $(\overline{\langle\alpha\rangle'_z\langle\alpha\rangle'_z})^{1/2}$ extracted along dashed lines indicated in (a) (simulation —, experiment —).

dimensionality. As demonstrated in the context of figure 4.18, the presence of the tunnel side-walls causes spanwise inhomogeneities in the simulation as well. Since the walls are modeled with slip boundary conditions, this is however purely attributed to the effect of flow restriction.

Subsequently, the fluctuations of the spanwise-averaged void field $\langle\alpha\rangle_z$ are analyzed in terms of their RMS level, and compared to the experiments. For this purpose, figure 4.24*a* shows a contour plot of $(\overline{\langle\alpha\rangle'_z\langle\alpha\rangle'_z})^{1/2}$, and figure 4.24*b* the corresponding profiles along the y-direction, evaluated at identical locations as before. Note that the definition of the RMS used here differs from that utilized in the context of the grid convergence study in §4.3.2, $\langle\overline{\alpha'\alpha'}\rangle_z^{1/2}$, as it is not possible to measure the true fluctuations of the three-dimensional void fraction field with the available experimental measurement techniques. As such, peak RMS fluctuations documented here are smaller by a factor of approximately 1.6, compared to the actual fluctuations of the void fraction given in figure 4.7 in §4.3.2.

Similar conclusions as with figure 4.23 can be drawn. Simulation and experiment agree best in the upstream part, $0 \lesssim x \lesssim 50$ mm. Here, the RMS level matches with an almost constant plateau in the center of the attached sheet. Across the liquid-vapor interface, the RMS level drops abruptly. At slightly larger wall-normal distances, the computed fluctuations follow a nearly linear trend before

they vanish in the free-stream. This can be ascribed to periodic perturbations of the sheet interface. A similar trend is also observed for the experiments, albeit weaker. The fluctuations recorded in the experiments do not vanish in the free-stream, presumably due to noise in the measurements. In the downstream region, $x \gtrsim 50\,\mathrm{mm}$, dominated by the existence of detached clouds, the characteristics of the RMS fluctuations agree qualitatively between computation and experiment. As already discussed, the utilized grid is insufficient for resolving the full fine-scale complexity of the detached clouds, which may affect the predicted fluctuations.

4.4.6*b* Instantaneous void fraction

In the previous section, it is discussed that the agreement between the computed and the experimental void fraction depends on whether cavitation occurs as attached sheets or as cloudy structures. As both mechanisms may alternate in time at a specific location, a clear differentiation is difficult when considering time-averaged data. In order to better assess the representation of different regimes of cavitating flow, the instantaneous void fraction is analyzed in the following.

For this purpose, two consecutive time instants are selected. Situation A, $t = t_0$ corresponds to the presence of an attached sheet reaching its maximum streamwise extent. For situation B, the instant $t = t_0 + 12\,\mathrm{ms}$ is chosen, with a condensation shock being propagated midway through the sheet. Instants A and B are depicted in figure 4.25, comparing the instantaneous, spanwise-averaged void fraction field $\langle\alpha\rangle_z$ from the simulation with the experimental result obtained by x-ray densitometry. In addition, the comparison is carried out in terms of instantaneous, spanwise-averaged void profiles along the y-direction, extracted at identical locations as above.

At instant A, simulation and experiment show an attached sheet attaining an almost identical length $s_L \approx 90\mathrm{mm}$. Profiles show that the sheet thickness predicted by the simulation matches the experiment up to $x \approx 40\,\mathrm{mm}$. In the rear part, $x \gtrsim 40\,\mathrm{mm}$, the sheet is slightly thicker in the simulation, due to a disturbance of the liquid-vapor interface propagating through the cavity for the selected cycle. Despite this difference, excellent agreement is obtained for the void fraction within the attached sheet, reaching values of $\gtrsim 80\%$. In addition, the downstream profiles within the sheet correctly capture the trend of increasing void fraction at larger normal distances to the wedge.

At instant B, the condensation shock reaches the position $x \approx 40\mathrm{mm}$. The numerical void fraction profiles extracted upstream of the shock position, i.e., within the attached sheet, again match excellently with the experimental references. In close agreement, the void fraction decreases for both the simulation and the experiment

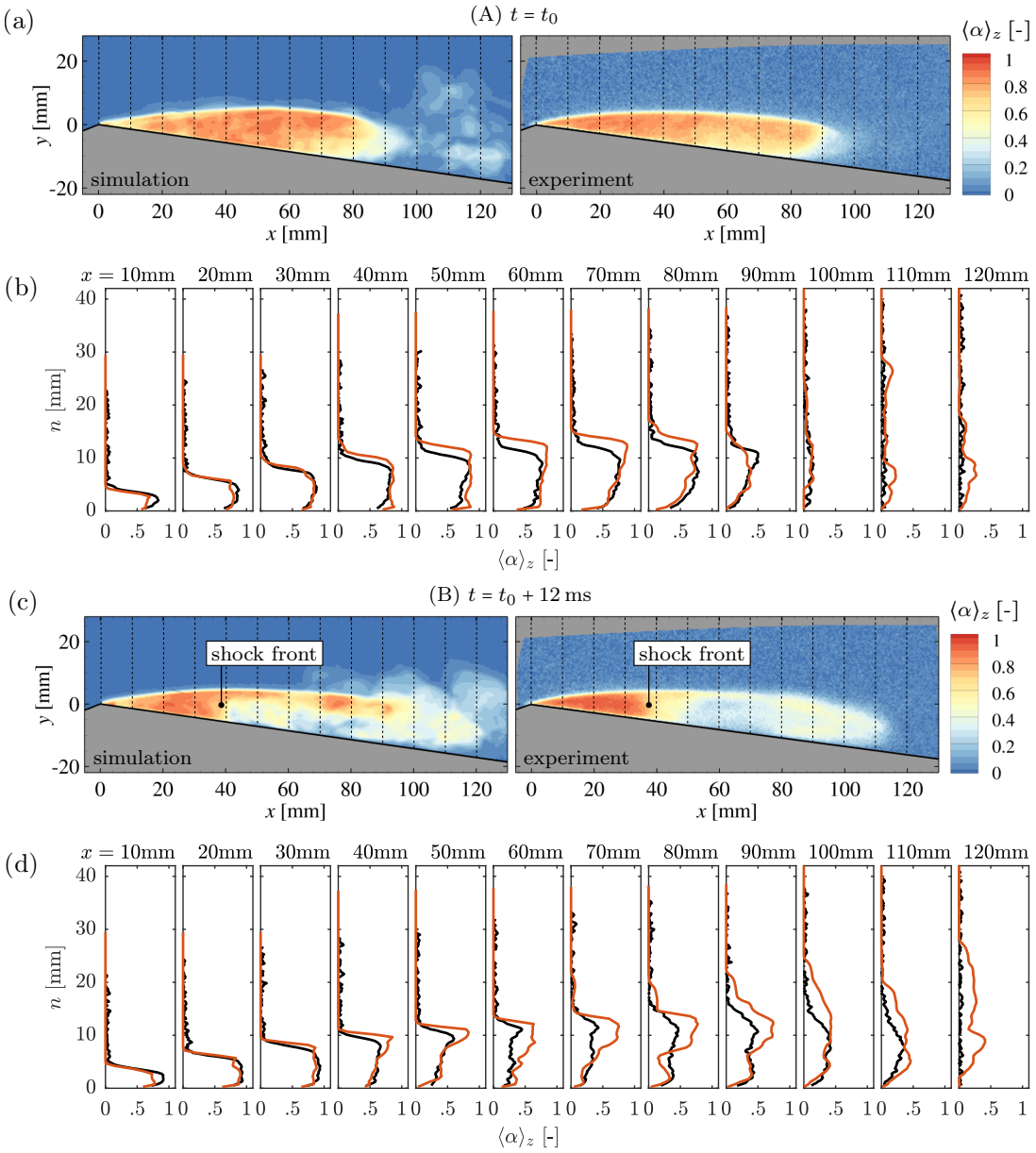

Figure 4.25: Validation of instantaneous, spanwise-averaged void fraction field $\langle\alpha\rangle_z$ at the instant of maximum attached sheet length $(A, t = t_0)$, and with the condensation shock at $x \approx 40$ mm, $(B, t = t_0 + 12$ ms$)$. (a,c) Comparison of contour plots obtained numerically (*left*), and with x-ray densitometry by Ganesh *et al.* (2016a) (*right*). (b,d) Void fraction profiles $\langle\alpha\rangle_z(n)$ extracted along dashed lines indicated in (a,c) (simulation —, experiment —).

from $\langle\alpha\rangle_z \gtrsim 0.85$ just upstream to $\langle\alpha\rangle_z \approx 0.4$ across the shock. Compared to the simulation, the decrease of the void fraction in streamwise direction appears more gradually in the experiments. It is believed that this is caused by a larger variation of the condensation shock front in the spanwise direction for the selected time-instant. Larger deviations in the void fraction can be found downstream of the condensation shock. In this region, cloudy vapor structures develop. These originate from the shear layer located at a distance of $n \approx 10\,\mathrm{mm}$ above the wedge, i.e., between the free-stream and the upstream-directed flow following behind the shock. The amount of vapor produced in the shear layer is higher in the simulation than in the experiment, and, correspondingly, also in the cloud downstream.

From this analysis, it can be concluded that the agreement in the local, instantaneous void fraction depends on the topology of the cavitating flow. In a sheet cavity, the model closely agrees with the experimental references, yielding equivalent values of $0.80 \lesssim \langle\alpha\rangle_z \lesssim 0.95$. The agreement is less good when cloudy or foamy cavitation structures exist. In this case, the amount of vapor tends to be larger in the simulation than in the experiment. From the aspects mentioned in the discussions of figure 4.23, it is believed that the main contributing reason for this discrepancy is the lack of spatial resolution, which is insufficient for representing the full complexity of a bubbly cloud.

4.4.6*c* Individual shedding cycle

Over the period of a shedding cycle, figure 4.26 juxtaposes the vapor volume obtained from x-ray densitometry and the computed instantaneous spanwise-averaged void fraction field $\langle\alpha\rangle_z$. In addition, the void fraction extracted at mid-span $\alpha|_{z=0\,\mathrm{mm}}$ is provided. The shedding process is exemplified by 6 consecutive time instants, beginning with the instant $t = t_0$, when an attached sheet reaches its largest streamwise extent. The time intervals for experiment and numerics are identical.

The spanwise-averaged field compares well with the experimental references. During the existence of an attached sheet, the amount of volume fraction within the attached part of the cavity matches well. Comparing $t = t_0$, $t = t_0 + 6\,\mathrm{ms}$ and $t = t_0 + 12\,\mathrm{ms}$, the spanwise-averaged void fraction increases, as noted before, exhibiting values of $\langle\alpha\rangle_z \gtrsim 0.8$. With good agreement of the propagation velocity u_{shock}, as discussed above, the position of the condensation shock is almost identical for simulation and experiment for the presented frames. The void fraction in the downstream developing cloud differs, as discussed. Nevertheless, location and spatial extent of downstream cloudy structures, e.g., cavitation in the shear layer and their subsequent roll-up, match reasonably well with the experiment.

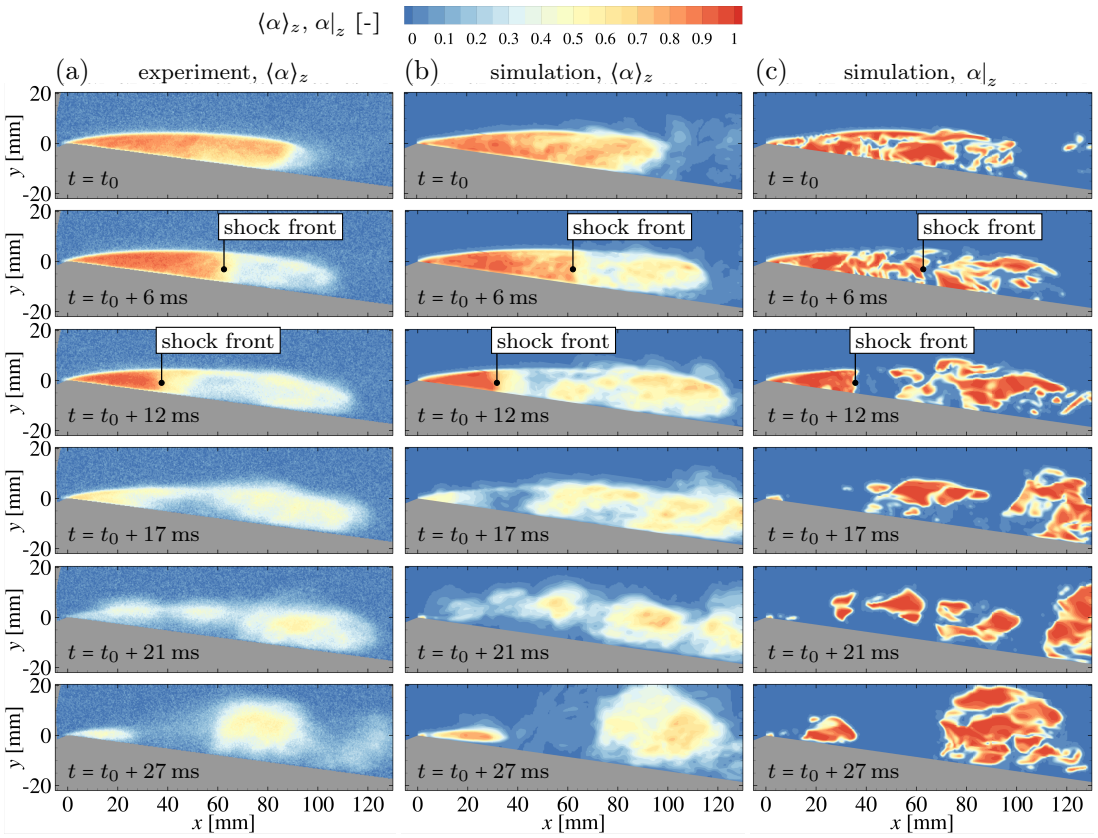

Figure 4.26: Instantaneous vapor void fraction during shedding cycle for 6 consecutive time instants. Comparison between (a) x-ray densitometry by Ganesh *et al.* (2016a), and numerical void fraction (b) spanwise-averaged, as well as (c) in the mid-plane slice.

Further insight can be gained from the void fraction field extracted in the mid-span slice. At the beginning of the shedding cycle, $t = t_0$ and $t = t_0 + 6\,\text{ms}$, the sheet is not a contiguous region of constant vapor volume fraction. Rather, its internal structure exhibits local patches of low and high void fractions. In addition, the void fraction in slices parallel to the mid-span show a noticeable variation in the spanwise direction, especially at the beginning of a shedding cycle. Correspondingly, the condensation front is difficult to identify during the early stages of a shedding cycle in individual slices. This finding cannot be compared directly with the x-ray densitometry as it is an integral measurement in spanwise direction. However, experimental high-speed videos, see figure 4.13, do not show a clear sheet either, but inhomogeneous cavity structures. Furthermore, the propagation velocity of the condensation front, being a function of the local void fraction as shown by equation (4.4) is inhomogeneous as well.

When the shock progresses towards the wedge apex, i.e., at $t = t_0 + 12\,\text{ms}$, the void fraction in the mid-span slice attains an almost constant value throughout the remaining part of the sheet, accompanied by the occurrence of the condensation

shock. This observation agrees with the fact that the spanwise-average of the void fraction increases over the period of a shedding cycle, leading to an acceleration of the condensation front. As already noted above, this observation can also be made for the experimental measurements. Void fractions $\langle\alpha\rangle_z \gtrsim 0.9$ imply that for these time instants the flow transitions to a contiguous vapor sheet.

4.4.6*d* Shedding Process

The temporal evolution of the shedding process, in conjunction with the cycle-to-cycle variation of the void fraction and velocity in the simulation has been discussed in figure 4.15 in §4.4.3. In order to further assess the numerical results, an equivalent analysis is repeated here also for the experimental data. Figure 4.27 compares the variation in time of $\langle\alpha\rangle_z|_{n=n_p}$ in simulation and experiment over a period of 1 s.

Similar features are observed in the time-evolution of the void fraction, for both the experiment and the simulation. Growth and collapse processes are clearly present. Experiment and simulation equally show a noticeable level of cycle-to-cycle variation, e.g., regarding the maximum attained cavity sheet lengths. Also the maximum level of vapor volume fraction within the sheets varies. For the experiment, the void fraction varies from $\langle\alpha\rangle_z \approx 0.55$ at $t \approx 0.68$ s to $\langle\alpha\rangle_z \approx 0.95$ at $t \approx 0.4$ s. Furthermore, irregular processes of cavity growth, presumably due to the occurrence of re-entrant jets, are observed experimentally as well, e.g., at $t = 0.08$ s, $t = 0.47$ s, $t = 0.71$ s.

Growth and collapse behavior predicted by the simulation tends to be slightly more irregular. Furthermore, the internal structures in the sheets appear more scattered in the simulation. As mentioned in §4.4.6, free gas content, which is neglected in the computation, may have a damping effect on the acoustics in the bulk, and thus could cause a reduction of such scatter.

4.4.7 Condensation Shock Phenomenon

In the following, the propagating condensation front is analyzed with the help of Rankine-Hugoniot jump conditions. These relations hold for any hyperbolic conservation law. For one-dimensional flow, this can be written in the generic form

$$\frac{\partial}{\partial t}\boldsymbol{U} + \frac{\partial}{\partial x}\boldsymbol{F}(\boldsymbol{U}) = 0 \ , \tag{4.5}$$

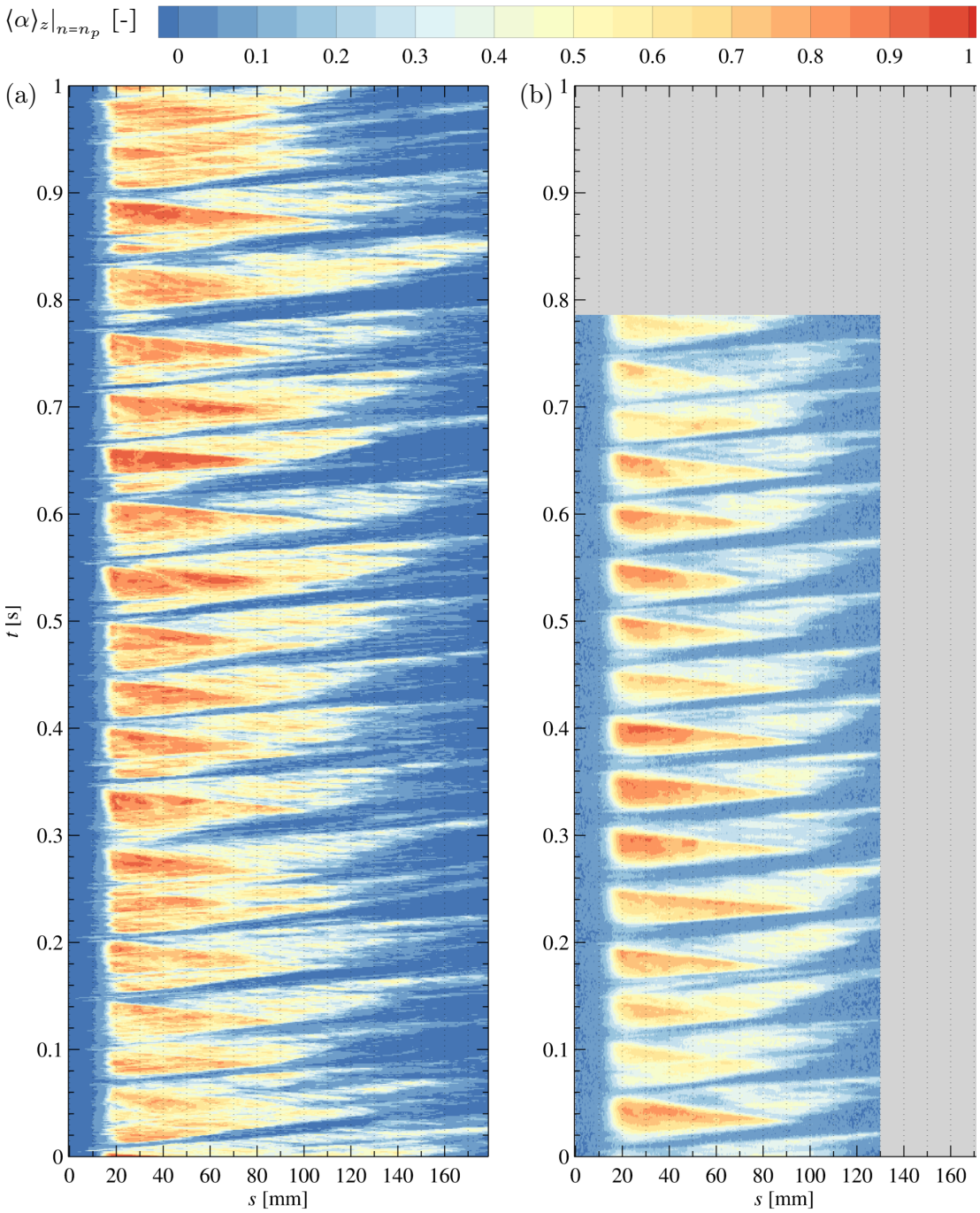

Figure 4.27: Time-evolution of the shedding process over a period of 1s. Spanwise-averaged void fraction $\langle\alpha\rangle_z|_{n_p}$ extracted from a wedge-parallel plane at a normal distance $n = n_p = 5.2$ mm and plotted along s. Comparison of (a) numerical prediction on lvl_2 grid, and (b) experimental x-ray densitometry of Ganesh *et al.* (2016a).

with the state vector $\boldsymbol{U}$ and flux $\boldsymbol{F}$. The solution supports the existence of discontinuities, i.e., shocks. These must satisfy the Rankine-Hugoniot relations

$$[\boldsymbol{F}(\boldsymbol{U})]_{L,R} = s \cdot [\boldsymbol{U}]_{L,R} \quad , \tag{4.6}$$

with the subscripts L and R denoting the left- and right flow states, $[\bullet]_{L,R} = (\bullet)_L - (\bullet)_R$, and s being the constant propagation velocity of the discontinuity. Equations (4.6) can be utilized (a) for assessing whether the observed condensation fronts fulfill the Rankine-Hugoniot conditions and thus represent a compressible shock wave phenomenon, and (b) to compute the shock strength or propagation velocity s. Note that this is a simplified analysis, assuming a planar, one-dimensional front, propagating with constant velocity within a homogeneous medium.

Neglecting bubble dynamics, surface tension and viscosity, the system can be modeled by the compressible Euler equations, with the vector of conserved quantities and flux given by $\boldsymbol{U} = [\rho, \rho u, \rho E]^T$ and $\boldsymbol{F}(\boldsymbol{U}) = [\rho u, \rho u^2 + p, \rho u \left(e + \frac{1}{2}u^2\right) + p]^T$, respectively. The Rankine-Hugoniot conditions then read

$$\begin{bmatrix} \rho u \\ \rho u^2 + p \\ \rho u \left(e + \frac{1}{2}u^2 + p/\rho\right) \end{bmatrix}_{L,R} = s \cdot \begin{bmatrix} \rho \\ \rho u \\ \rho E \end{bmatrix}_{L,R} \quad . \tag{4.7a, b, c}$$

For this analysis, pre- and post-shock states are extracted from the simulations at several stages during the shedding cycles. The subsequent discussion considers a suitable time instant, depicted in figure 4.28. The visualization shows the void fraction and streamwise velocity at mid-span, figures 4.28*a,b*, and the respective spanwise average, figures 4.28*c,d*. The pre- and post-shock states are extracted at the locations indicated in the figure. Table 4.5 summarizes the obtained velocity perpendicular to the front $u_\perp$, density ρ, void fraction α, and the pressure p. For reference, the pre- and post-shock speed of sound, under the assumption of frozen and equilibrium conditions, equations (3.19) and (3.20), is also provided in table 4.5. Due to the non-linearity of these relations, applying equations (3.19) and (3.20) is not commutative with the averaging operation. The speed of sound is thus first computed locally within each computational cell, and then spatially averaged.

Upstream of the discontinuity, the local flow velocity is small, and mainly oriented downstream. The sheet is characterized by a void fraction exceeding 95% in the slice, and a spanwise average of 84%. Across the shock, the direction of flow is reversed, with a significant increase in magnitude. Complete condensation to $\alpha = 0$ occurs behind the front in the slice. In contrast, the shock appears smeared for the spanwise average, and the post-shock void fraction is non-zero. The pressure rise across the front for the chosen instant is 1.7 kPa on the spanwise average,

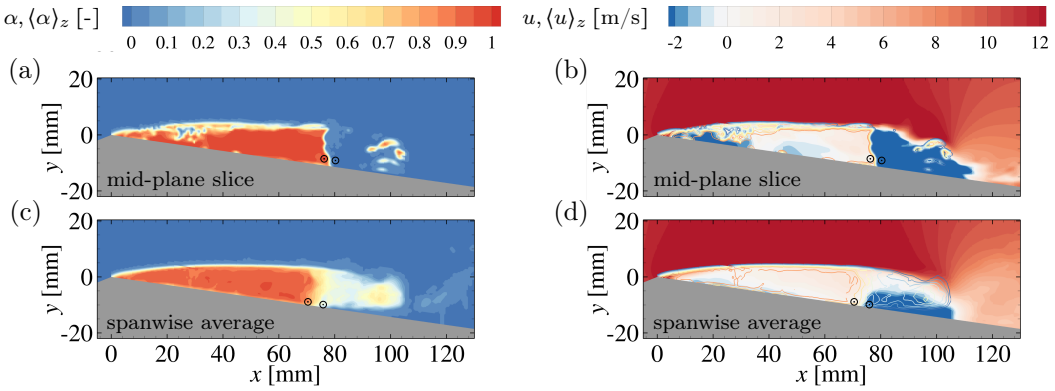

Figure 4.28: Instantaneous flow field exhibiting a condensation shock at $x \approx 75\,\mathrm{mm}$. Comparison of flow field (a,b) in the mid-span slice, and (c,d) as spanwise-average, showing (a,c) vapor volume fraction, and (b,d) axial velocity, with iso-contours of void fraction superimposed. Indicated locations are used for extracting pre- and post-shock quantities shown in table 4.5.

and only slightly larger in the slice. In general, values between 1 and 5 kPa are observed. The compression is thus very weak, which is in close agreement with the values reported by Ganesh *et al.* (2016a).

Utilizing the quantities extracted at discrete locations for various time instants in equations (4.7a,b), it is found that the discontinuities indeed satisfy the Rankine-Hugoniot conditions, with an error of $\lesssim 1\%$. In contrast, errors of 10-15% are obtained with the spanwise-averaged values. The reason lies in the fact that the jump conditions are strictly applicable only at discrete locations, while being not necessarily valid for spanwise-averaged flow states. Interestingly, this approach still yields a good approximation of the bulk front propagation velocity: With the values from table 4.5 for the chosen example, a value of $\langle s \rangle_z = -5.43\,\mathrm{m/s}$ can be computed for the spanwise average. This is in reasonable agreement with the

Table 4.5: Representatively chosen pre- and post-shock flow states for Rankine-Hugoniot analysis, extracted from the time-instant depicted in figure 4.28. Comparison between quantities in the mid-span slice and spanwise average.

		$\rho\,[\frac{\mathrm{kg}}{\mathrm{m}^3}]$	$u_\perp\,[\frac{\mathrm{m}}{\mathrm{s}}]$	$p\,[\mathrm{Pa}]$	$\alpha\,[-]$	$c_{\mathrm{fr}}\,[\frac{\mathrm{m}}{\mathrm{s}}]$	$c_{\mathrm{eq}}\,[\frac{\mathrm{m}}{\mathrm{s}}]$
mid-span slice	pre-shock	31	0.7	2319	0.97	10	1.2
	post-shock	998	-5.5	4381	0.00	1482	1482
spanwise average	pre-shock	162	0.5	2358	0.84	67	573
	post-shock	739	-4.5	4129	0.41	60	566

average value of $s \approx -4.5 \pm 0.5\,\mathrm{m/s}$ obtained from the s-t diagram, figure 4.15.

The propagation velocity computed in the slice for the chosen example is $s = -5.75\,\mathrm{m/s}$. Ranging, in general, between -4.5 and $-8\,\mathrm{m/s}$, it tends to be higher than the bulk propagation velocity. This can be explained with the assumption of one-dimensional flow, thereby disregarding any existing perturbations of the interface and inhomogeneities in the pre- and post-shock states. As discussed, the actual front experiences Kelvin-Helmholtz- and Rayleigh-Taylor-instabilities. It is thus strongly non-planar, and has a non-uniform propagation velocity.

Note that the Rankine-Hugoniot condition for the conservation of energy, equation (4.7c), can be utilized for computing the temperature variation associated with the condensation shock. In the present example, assuming that the liquid behind the shock is at reference temperature T_{ref}, this variation can be evaluated as $\Delta T \approx 0.3\,\mathrm{K}$. Although this is larger in magnitude than for the example chosen in §4.3.1, the temperature variation across the shock is still negligibly small.

Using the quantities in the slice, the shock Mach number $\mathrm{Ma_s}$, relating the front propagation velocity, relative to the pre-shock flow, to the pre-shock speed of sound can be computed. As already mentioned, estimates for the upper and lower bounds of the thermodynamic speed of sound are given by equations (3.19) and (3.20). By excluding any phase transfer from the estimation, i.e., using the frozen speed of sound c_{fr}, the Mach number evaluates to $\mathrm{Ma_s^{fr}} = 0.63$ for the current example, and hence a condensation shock could not exist. In contrast, with the equilibrium speed of sound c_{eq}, $\mathrm{Ma_s^{eq}} = 5.2$ for the chosen instant. In the simulation, $\mathrm{Ma_s} = \mathrm{Ma_s^{eq}} > 1$, because the equilibrium speed of sound is utilized in the thermodynamic model. The local speed of sound in the experiments is unknown. However, since a propagating shock wave is observed by Ganesh *et al.* (2016a), it is concluded that in the experiments $\mathrm{Ma_s} > 1$, too.

4.5 Conclusions

The formation of cloud cavitation, classically associated with re-entrant jets, can also be caused by the occurrence of condensation shocks. This has been predicted previously by numerical simulations (Schmidt *et al.*, 2009; Eskilsson and Bensow, 2012). However, a direct observation by experimental studies, see Ganesh *et al.* (2016a), has become available only recently. The authors suggest that condensation shocks represent an additional instability mechanism of partial cavitation. The motivation for the presented research is to obtain further insight into the physics of condensation shock phenomena, with the help of numerical simulations.

Based on the experiments by Ganesh *et al.* (2016a), a validation of the numerical results is carried out. Focus is put on an operating point where periodic cloud shedding, and the formation of upstream-traveling condensation shocks occur. The computational set-up reproduces the nominal definition of the experiments, including all variations of cross-section within the up- and downstream duct. The assumption of spanwise periodicity within the test-section is avoided. The physical model is based on the homogeneous mixture approach, equilibrium thermodynamics, and a barotropic equation of state. By neglecting physical viscosity, the study concentrates on inertia-dominated flow physics. Compressibility of the two-phase flow is retained in the numerical method. Utilizing explicit integration in time, all relevant time-scales of cavitating flow are resolved. The method captures cavitation-induced shock-wave dynamics, and its interaction with phase transition.

The computations are in good agreement with most of the experimental results. Typical flow patterns occurring during the shedding process are well reproduced. Especially sheet and cloud cavitation, inhomogeneous flow topology in the spanwise direction, cavitating horse-shoe and hairpin vortices, as well as crescent-shaped regions are found in the simulations. Furthermore, growth and collapse speeds of the partial cavity are well matched. The comparison of the shedding Strouhal-number and the evolution of the shedding process indicates that global system dynamics are in good agreement.

Excellent match is observed for the spanwise-average vapor volume fraction within cavity sheets, reaching values of $>80\%$. In individual slices, void fractions may locally exceed $>90\%$, suggesting that the sheets consist of large contiguous regions of vapor, instead of individual bubbles. Within the downstream-propagating clouds, however, the predicted void fraction is larger compared to the measurements. This is attributed to the spatial resolution being insufficient for reproducing the full range of scales for cloud cavitation. Slight deviations are found in the overall regularity of the shedding cycles. It is suggested that stabilizing mechanisms, such as viscous layers and free gas content, may lead to a reduction of scatter for individual shedding cycles. The observed intermittency of irregular growth-phases, and, less frequently, re-entrant jets, is also noted experimentally.

From this study, it is concluded that the investigated configuration is dominated by inertial effects, phase transfer, and wave dynamics. By virtue of an analytical model relying on the assumption of steady, inviscid flow, it is shown that the pressure drop in the test-section is dominated by the occurrence of cavitation. Surpassing all other loss mechanisms, including viscous losses, this further justifies the usage of an inviscid flow model.

In agreement with the experiments, the simulations identify a recurring condensation shock phenomenon as the main mechanism for cloud shedding. The predictions closely correspond to the experimentally observed behavior. The fronts span almost the entire height of the cavity, and only a weak pressure increase across the front is detected. The computed propagation velocity closely agrees with the experimentally determined value. It is further found that the direction of flow is reversed behind the front, similar to re-entrant jets. In contrast to the latter, however, upstream-directed flow is induced across most of the cavity height. It thus is not possible to stop the front by a small obstacle and suppress the associated cloud shedding, as already found experimentally by Ganesh *et al.* (2015). Associated with the condensation front is the development of Rayleigh-Taylor and Kelvin-Helmholtz instabilities. These contribute to a thickening of the front in the spanwise average, while appearing sharp in individual slices.

The simulations show that condensation shocks are, just like re-entrant jets, an inertia-dominated feature of partial cavities. It is demonstrated that pre- and post-shock flow states fulfill Rankine-Hugoniot jump conditions. The front thus represents a compressible shock wave, and analytical relations can be used for predicting the shock strength and propagation velocity. It is found that these fronts can be triggered by shocks emanating from a downstream collapsing cloud. However, they are also observed under the absence of such events. This implies that the adverse pressure gradient is sufficient for inducing a shock front. In addition to re-entrant jets, condensation shock phenomena thus feed an intrinsic instability mechanism of partial cavities.

CHAPTER 5

Cavitating Ship Propeller Flow

In this chapter, numerical simulations of the model-propeller *VP1304* are presented. Experimental reference investigations are provided by the Schiffbau-Versuchsanstalt Potsdam (Potsdam Model Basin, SVA). Furthermore, the propeller is investigated numerically by several research groups with the Workshop on Cavitation and Propeller Performance, in the scope of the 2nd Symposium on Marine Propellers 2011 (SMP'11). The ensemble of these studies are published as the Potsdam Propeller Test Case (PPTC). The propeller is thus extensively covered in the literature, and well-suited for a validation of the chosen numerical approach.

After a short introduction to ship propeller cavitation, and a review on the state-of-the-art for their numerical simulation in §5.1, the test case is presented in §5.2, while §5.3 outlines the employed solution strategy. Thereafter, the results of this study are presented in §5.4. The analysis includes the propeller open-water performance, a study of the propeller wake velocity field, and a more detailed discussion of the flow field at the nominal design point of the propeller, for both wetted and cavitating flow conditions. Emphasis is put on a juxtaposition of results obtained with the baseline and the ILES scheme outlined in §3.2.3, and validation against the experimental and numerical work published in the scope of the PPTC. Furthermore, a comparative assessment of the flow aggressiveness is conducted for three operating points. Relying on the methods discussed in §3.3, i.e., recorded maximum surface pressure loads and the collapse detection algorithm, erosion-endangered areas on the propeller are identified for three different operating points. Concluding remarks are summarized in §5.5.

This chapter is partly based on previous publications of the subject at international conferences, see Budich *et al.* (2015a,b,c, 2016b, 2017).

5.1 Introduction

For marine propulsion systems cavitation occurs already at moderate loading conditions, and is thus encountered on almost all modern ship propellers (Carlton, 2012). Propeller cavitation is associated with a range of adverse effects. In this respect, Kuiper (1997) identifies three primary factors, i.e., "erosion, noise and vibrations", which continue to be relevant today (Terwisga *et al.*, 2007). Being subjected over a sustained time to cavitation, most metal materials deployed for ship propellers will erode (Kim *et al.*, 2014). This may eventually lead to failure of affected components, such as the propeller itself, and appendages, causing increased cost for inspection, maintenance, and overhaul. Collapsing vapor structures generate severe pressure fluctuations, which contribute to the erosiveness of the flow. In conjunction with variations in the integral cavity volume, these are also major sources for structural vibrations induced on the ship hull, and underwater radiated noise. Finally, cavitation-induced thrust break-down, and degradation of propeller efficiency limits the achievable propeller performance, albeit being of less importance, compared to the aforementioned aspects, according to Kuiper (1997).

Cavitation phenomena hence impose numerous limitations on ship propeller design. These detrimental effects are caused by the inherently unstable, and thus transient behavior of cavitating flow. Therefore, in addition to controlling the location and extent of vapor regions, cavity dynamics need to be taken into account. For propeller design, an in-depth understanding of the unsteadiness of cavitating flow, a prediction of flow aggressiveness due to cavitation, as well as an estimate of the locations prone to, and, possibly, the rate of expected material erosion are of primary interest.

Despite recent advancements in CFD, above aspects of propeller cavitation are preferably assessed by model-scale experiments (Terwisga *et al.*, 2007). Experimental analysis of ship propellers, however, is often complicated by accessibility constraints, and the spatial and temporal resolution of available (optical) measurement techniques. Difficulties arise especially for detailed investigations of internal flow features in cavitating regions, and the observation of small-scale vapor structures, which are usually responsible for the most erosive collapse events. Furthermore, experiments within the controllable environments of towing tanks or cavitation tunnels are often preferred over full-scale tests. Yet, questions concerning scale effects and repeatability need to be addressed (Terwisga *et al.*, 2007). The situation is complicated further by the fact that direct observation of material erosion is not possible within the time frames typically available in the laboratory. Instead, alternative to expensive long-term field tests at full-scale, erosion risk is commonly inferred from paint tests, or by visual inspection of cavity dynamics

using high-speed videos, as discussed in §2.2. Above aspects can only properly be assessed with expert knowledge about the individual testing facilities and measurement techniques, requiring sound experience.

Due to these difficulties, it is advantageous to complement experimental work by numerical studies. Already at an early stage of propeller design, these are capable of providing detailed insights into the flow at a considerably higher spatial and temporal resolution. In addition, they provide the potential to derive quantitative means of assessing erosion risk. The majority of numerical methods utilized for analyzing cavitating ship propellers are (a) potential-based Boundary Element Methods (BEM, see, e.g., Mueller and Kinnas, 1999; Pereira and Salvatore, 2004; Kinnas and Fine, 2006), (b) (Unsteady) Reynolds-Averaged Navier-Stokes approaches (URANS, see, e.g., Ji *et al.*, 2011; Morgut and Nobile, 2012; Ahn and Kwon, 2013; Li *et al.*, 2014), or (c) coupled BEM-URANS approaches (e.g. Tian and Kinnas, 2015; Gaggero *et al.*, 2017). The methods are also deployed in the industrial development cycle. In order to survey the capabilities of current numerical methods, several workshops on propeller cavitation were conducted in the recent past.

In the scope of the Virtual Tank Utility in Europe (VIRTUE) 2008 "Workshop on Cavitating Propeller Modeling", (see Salvatore and Streckwall, 2009), the model propeller *INSEAN E779A* (Pereira and Salvatore, 2004; Pereira *et al.*, 2004) is studied, for both homogeneous and in-behind conditions. Reviewing BEM, RANS as well as Large-eddy simulation (LES) models, it is found that the open-water performance in homogeneous inflow conditions can be predicted typically within 5% accuracy. While, qualitatively, a good agreement can be achieved regarding the location and extent of cavitation, large quantitative deviations are observed among the computations. Salvatore and Streckwall (2009) attribute these uncertainties in the numerical methods to an excessive amount of numerical dissipation, as well as the employed turbulence and cavitation models.

The model propeller *VP1304* is investigated with the Potsdam Propeller Test Case (PPTC, see Schiffbau-Versuchsanstalt Potsdam, 2017). During the "Workshop on Cavitation and Propeller Performance" in 2011 (see Hoekstra *et al.*, 2011), and 2015 (Kinnas *et al.*, 2015), the device is studied for homogeneous inflow and inclined shaft conditions, respectively. For the situation of uniform inflow considered with the PPTC 2011, similar conclusions as for the VIRTUE test case are drawn. The propeller thrust under cavitating conditions, e.g., is predicted again by the majority of contributions within 5% accuracy, and, despite some deviation in the predicted integral cavity extent, the qualitative location of cavitation on the blade is well-captured (Heinke, 2011b). Under inclined-shaft conditions considered with the PPTC 2015, however, the agreement is deteriorated: taking the median of all participants, cavitating thrust predictions deviate by $\approx 13\%$, and cavity

extent is, in general, over-estimated. While pressure pulses at the blade passing frequency (BPF) are satisfactorily computed, it is identified that the prediction quality at higher frequencies still needs to be improved (Kinnas *et al.*, 2015).

The turbulence modeling in RANS approaches represents a major source of uncertainty, having a large influence on the predicted cavity extent and dynamics, see, e.g. Coutier-Delgosha *et al.* (2003). Frequently, it is found that most of cavity dynamics observed in the experiments is suppressed when using RANS turbulence models (Reboud *et al.*, 1998; Coutier-Delgosha *et al.*, 2003; Goncalves *et al.*, 2010). Reboud *et al.* (1998) traced this to an excessive amount of eddy viscosity, which prevents, e.g., the development of a re-entrant jet instability, rendering a shedding sheet cavity as stable in the computations. An ad-hoc fix is the correction proposed by Reboud *et al.* (1998), which artificially reduces the eddy viscosity in the region of cavitation. While this can lead to improved results by including more cavity dynamics, a physical justification is difficult. Furthermore, due to the Reynolds-averaging of the governing equations in (U)RANS methods, a detailed analysis of the inherent transient nature of cavitating flow remains limited. Consequently, Salvatore and Streckwall (2009) conclude from the VIRTUE workshop that reliable predictions of radiated pressure fluctuations as well as erosion predictions for ship propellers are challenging with RANS models.

Thus, large-eddy simulations represent a promising advancement in the field (Gnanaskandan and Mahesh, 2016b). Resolving energy-carrying transient flow structures, LES enables a better resolution of cavity dynamics, and their interaction with flow turbulence. Bensow and Bark (2010) investigate the *E779A* in both homogeneous as well as artificial wake conditions, performing implicit large-eddy simulations (ILES), in conjunction with an incompressible flow model. The authors find that delicate flow features such as internal jets, upstream desinance, and leading-edge vortices are well captured by the method. Some discrepancies, such as an over-estimation of the cavity extent, are also discussed. The authors conjecture that this might be accredited in parts to the negligence of compressibility effects in the employed model.

While compressibility is disregarded in all of the current studies of cavitating ship propellers, it plays an essential role due to a variety of aspects. As addressed in §3.1, the intrinsic coupling between collapse-induced shock-wave dynamics and phase change may impact cavity dynamics. Transient cavitating flow, such as, e.g., the sheet-to-cloud transition of partial cavities investigated in §4, may be dictated by compressible condensation shock phenomena. In addition, predicting pressure peaks associated with cavity collapse events requires to account for the two-phase compressibility. As demonstrated by Mihatsch *et al.* (2015), this information can be utilized for a quantitative evaluation of flow aggressiveness.

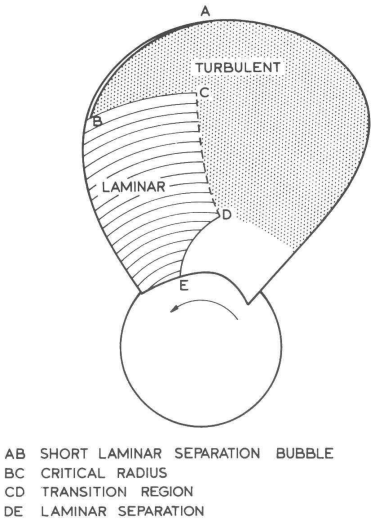

Figure 5.1: Schematic of the boundary layer on the suction side of a model propeller, from Kuiper (1981).

A–B short laminar separation bubble
B–C critical radius
C–D transition region
D–E laminar separation

Compressible simulation hence represents a promising tool, by capturing the cavity dynamics across all relevant scales, and, furthermore, by providing a framework for estimating the erosiveness of propeller designs quantitatively. The present work thus aims at assessing the capabilities of a fully compressible numerical method for analyzing cavitating ship propellers. For this purpose, the model propeller *VP1304* is selected, as it is comprehensively covered in the literature through the PPTC.

It is important to review that model propellers, with Reynolds numbers being at least two orders of magnitude smaller than in full-scale, can be subjected to strong scaling effects. Without the application of roughness elements along the leading edge, the boundary layer on the suction side of a model propeller typically exhibits both laminar as well as turbulent regions, and Carlton (2012) states that "laminar flow can prevail over significant parts of the blade". Following Kuiper (1981), who investigates boundary layer characteristics on model propellers using paint tests, the suction side boundary layer can be schematized as shown in figure 5.1. Downstream of a laminar separation bubble along the leading edge *A–B*, and above a critical radius *B–C*, the boundary layer is turbulent close to the tip. Below the critical radius, typically, an extensive region of laminar flow exists on the suction side, undergoing transition to turbulence within the region *C–D*. Due to thick blade profiles close to the hub, and lower local Reynolds numbers, a laminar separation *D–E* terminates the laminar flow region at smaller radii. According to Kuiper (1981), "the position of the points *B*, *C*, and *D* can vary strongly with the shape of the propeller sections, the propeller loading and the propeller Reynolds number". The pressure side boundary layer is usually less intricate, compared to the situation on the suction side. Typically, it exhibits a "significant laminar region" (Kuiper, 1981) as well, and transition occurs more gradually, due to favorable pressure gradients.

For assessing scale effects, the sectional Reynolds number $\mathrm{Re}_{0.7} = (c_{0.7}u_{0.7})/\nu$, based on the blade section $r/R = 0.7$, at 70% of the propeller radius R, is commonly selected as the relevant parameter (Carlton, 2012). Here, $c_{0.7}$ denote the chord length of the section, and $u_{0.7} = \sqrt{V_\mathrm{a}^2 + (0.7\omega R)^2}$ the section advance speed, with inflow velocity V_a and rate of revolution ω. Kuiper (1981) states that "a common criterion for the absence of a strong Reynolds dependency is a minimum sectional Reynolds number of 2×10^5 at $0.7R$". However, the flow is not necessarily turbulent over the entire blade. According to Funeno (2002), and Rhee and Joshi (2005), a region of laminar flow may cover 50%–60% of the blade surface for model propellers with diameters $D \approx 200 \ldots 300\,\mathrm{mm}$. This is in agreement with findings of Kuiper (1981), studying three different model propellers subjected to homogeneous inflow conditions. Even for a sectional Reynold number of $\mathrm{Re}_{0.7} \approx 1 \times 10^6$, the author finds laminar regions covering at least 50% and up to the majority of the blade, depending on the loading, and the type of propeller. Although the effect on the thrust and torque is attenuated with increasing the Reynolds number, Kuiper (1981) points out that laminar boundary layers can persist up to much higher Reynolds numbers, considerably exceeding 1×10^6.

5.2 Problem Description

The considered five-bladed, controllable-pitch model propeller *VP1304* is depicted in figure 5.2, mounted in push arrangement within the cavitation tunnel at SVA. Views on the propeller pressure and suction side are given in figures 5.2*a* and 5.2*b*, respectively, while figure 5.2*c* depicts the experimental setup with a dummy hub, only. The geometric properties of *VP1304* are summarized in table 5.1. The pitch of the propeller is held constant at the specified design pitch (pitch ratio $P_{0.7}/D = 1.635$ at $r/R = 0.7$) for all subsequent investigations.

Figure 5.3 shows a schematic of the propeller, including the definition of the coordinate system employed throughout this study. The propeller coordinate system (PCS) with the x-axis directed downstream is utilized. The origin of the

Figure 5.2: Model propeller *VP1304* within the cavitation tunnel at SVA, (a) view on suction side, (b) view on pressure side, (c) dummy hub only. Taken from Heinke (2011b).

Table 5.1: Main geometric characteristics of *VP1304*.

property	symbol	unit	value
number of blades	Z	[-]	5
diameter	D	[mm]	250
chord length[a]	$c_{0.7}$	[mm]	104.17
design pitch ratio[a]	$P_{0.7}/D$	[-]	1.635
hub ratio	d_h/D	[-]	0.3
area ratio	A_E/A_0	[-]	0.77896
skew angle extent[b]	Φ_{ext}	[°]	18.837

[a] at $r/R = 0.7$ [b] difference between maximum and minimum skew angle

PCS (x = 0 m) corresponds to the propeller plane, as specified by SVA. The z-axis points along the 0°-position of the blade, which coincides with the propeller generator line. In this coordinate system, the propeller rotates in the negative sense of rotation around the x-axis, with angular velocity $\boldsymbol{\omega} = [-\omega, 0, 0]^T$. The angle θ is taken in the direction of propeller rotation.

Experimental reference data used for this study is provided by SVA reports published in the scope of the PPTC. These cover the propeller open-water performance (Barkmann, 2011a), LDV measurements in the propeller wake (Mach, 2011), and cavitation tunnel tests (Heinke, 2011a). Numerical reference data bases on studies of workshop participants, see the summaries by Barkmann (2011b), Lübke (2011), and Heinke (2011b)[1].

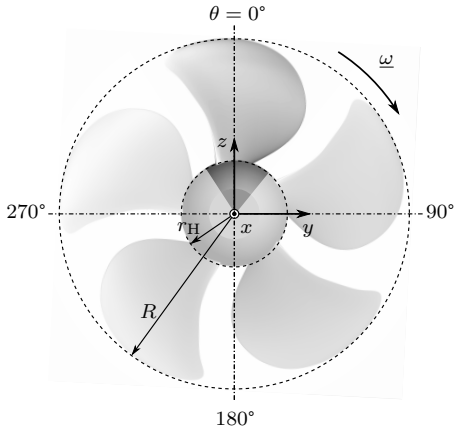

Figure 5.3: Coordinate system definition for *VP1304* (view from behind).

[1]For further reference on the numerical studies conducted within the scope of the PPTC 2011, refer also to the following individual publications of PPTC participants: Caldas *et al.* (2011), Fujiyama *et al.* (2011), Gaggero *et al.* (2011), Gatchell *et al.* (2011), Klasson and Huuva (2011), Li (2011), Liu and Hong (2011), Morgut and Nobile (2011), Salvatore and Greco (2011), Sipilä *et al.* (2011), and Yakubov *et al.* (2011).

For all operation points considered in the following, the propeller is subjected to homogeneous inflow conditions. The operation points can be characterized by the advance coefficient $J = V_a/(nD)$, and the cavitation number $\sigma_n = (p_\infty - p_{vap})/(\frac{1}{2}\rho_0 n^2 D^2)$. Here, V_a denotes the constant inflow velocity, $n = \omega/(2\pi)$ the constant rate of revolution, p_∞ the reference upstream pressure, p_{vap} the reference vapor pressure, and ρ_0 the reference liquid density. The properties p_{vap} and ρ_0 are determined by SVA for each experimental run individually. For defining the operating point in the simulations, these properties are assumed constant. Taken from the barotropic thermodynamic model for water at the reference temperature $T_{ref} = 293.15\,\mathrm{K}$, the values $p_{vap} = 2339.3\,\mathrm{Pa}$ and $\rho_0 = 998.16\,\mathrm{kg/m^3}$ are used, see §3.1.3*b*. As these values differ only slightly from the SVA measurements, the deviation from the experimental operating point caused by this approach are small (e.g., $< 2\%$ for σ_n), and can be regarded as negligible.

The propeller performance is given by the non-dimensional thrust coefficient, $K_T = T/(\rho_0 n^2 D^4)$, and the torque coefficient, $K_Q = Q/(\rho_0 n^2 D^5)$. The propeller efficiency can be computed by $\eta_0 = (J/2\pi) \cdot (K_T/K_Q)$, and the blade loading coefficient by $C_{th} = (8/\pi) \cdot (K_T/J^2)$. Here, T and Q denote the delivered propeller thrust and the required torque, respectively. Experimental measurements of T and Q are corrected by the contributions of the bearings, hub and nose cap, and the gap between shaft and hub. These measurements are thus understood as being generated solely by the propeller blades, see Barkmann (2011a). Correspondingly, for evaluating the thrust and torque in the simulations, the local fluid forces are integrated over the propeller blade surface, only.

For designating the operating points used for the analysis, the nomenclature proposed by SVA is adopted. A total of 12 operating points is specified for the PPTC. The open-water performance is investigated with towing-tank experiments at five different J, denoted as cases *2.1a-e*. In the experiments, the propeller is mounted in pull arrangement, and a nose cap designed to avoid pressure build-up at the downstream end is utilized, see Barkmann (2011a). With case *2.2*, the propeller wake field under wetted conditions is studied by means of LDV measurements. For this case, contrary to cases *2.1*, the propeller is operated in a cavitation tunnel, see Mach (2011). It is mounted in push arrangement, and a different hub cap geometry is utilized. Further analysis within the cavitation tunnel is carried out at three additional advance ratios, denoted as cases *2.3.1*, *2.3.2*, and *2.3.3*, and reported by Heinke (2011b). This includes both wetted flow conditions, cases *2.3.1-3a*, and cavitating flow conditions, cases *2.3.1-3b*. The nominal design point of the propeller ($J = 1.019$) is identified by case *2.3.2*.

Table 5.2 provides an overview of the characteristic parameters n, σ_n, J, and K_T for each operating point. Furthermore, estimates of the propeller Reynolds-number $\mathrm{Re}_n = nD^2/\nu$, and the sectional Reynolds-number at $r/R = 0.7$, $\mathrm{Re}_{0.7} = (c_{0.7}u_{0.7})/\nu$,

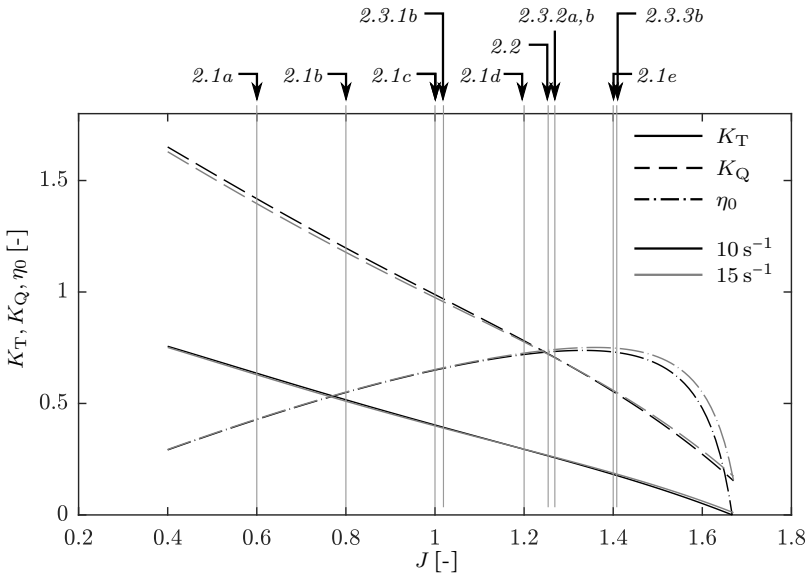

Figure 5.4: Propeller open-water performance from Barkmann (2011a), with indication of specified operating points.

are given. For this purpose, the dynamic viscosity ν of water is assumed constant at T_{ref}, yielding $\nu = 1.004 \times 10^{-6}$ m^2/s.

With values ranging between 8.9×10^5 (case *2.1a*) and 1.7×10^6 (case *2.3.3*), the sectional Reynolds-numbers $\text{Re}_{0.7}$ are in the lower regime, which is typical for model propellers, as discussed in §5.1. The character of the boundary layer on the model propeller is, however, unknown, as no information is provided from the experiments in this regard. Since no tripping of the boundary layer is applied, it can be conjectured that laminar regions exist on the blade surface, and that Reynolds-effects are present.

Figure 5.4 shows the open-water performance map of the propeller as measured by Barkmann (2011a). In order to assess a possible Reynolds number effect, the open-water performance is experimentally determined at two different numbers of revolution, $n = 10$ s^{-1} and $n = 15$ s^{-1}. Barkmann (2011a) concludes from this study that a weak influence of the Reynolds number is present. As seen in figure 5.4, the slopes of K_T and K_Q are smaller at the higher Reynolds number, while the maximum open-water efficiency is reached at a higher advance coefficient, compared to the lower Reynolds number.

As summarized in table 5.2 and indicated in figure 5.4, 10 out of 12 operating points are investigated with the present study. These comprise the open-water performance of the propeller, cases *2.1a-e*, wake velocity analyses, case *2.2*, the design point at both wetted and cavitating conditions, cases *2.3.2a,b*, and the cavitating cases *2.3.1b* and *2.3.3b*.

Table 5.2: Operating points, as specified by PPTC, and considered in this study.

PPTC case	n [rev/s]	σ_n [-] †	J [-]	K_T [-]	Re_n [-]	$Re_{0.7}$ [-]
2.1a‡	15	∞	0.6	0.629	9.34×10^5	8.87×10^5
b‡			0.8	0.510	9.34×10^5	9.10×10^5
c‡			1.0	0.399	9.34×10^5	9.40×10^5
d‡			1.2	0.295	9.34×10^5	9.75×10^5
e‡			1.4	0.188	9.34×10^5	1.01×10^6
2.2‡	23	∞	1.254	0.25	1.43×10^6	1.51×10^6
2.3.1a	24.987	∞	1.019	0.3870	1.56×10^6	1.57×10^6
b‡		2.024	1.019	0.3725	1.56×10^6	1.57×10^6
2.3.2a‡	24.986	∞	1.269	0.2450	1.56×10^6	1.65×10^6
b‡		1.424	1.269	0.2064	1.56×10^6	1.65×10^6
2.3.3a	25.014	∞	1.408	0.167	1.56×10^6	1.69×10^6
b‡		2.000	1.408	0.1362	1.56×10^6	1.69×10^6

† wetted conditions denoted by $\sigma_n = \infty$ ‡ operating point considered in this study

5.3 Numerical Strategy

5.3.1 Computational Domain

For all specified operating points, the propeller is subjected to a homogeneous inflow condition. In the context of the PPTC workshop, the cavitation tunnel is thus allowed to be idealized as a cylinder with a cross-sectional area equal to the real tunnel geometry. The same approach is followed for this study. In order to reduce the computational effort, the numerical domain comprises a single blade passage with opening angle 72°, and periodic lateral boundary conditions.

Since *VP1304* is a controllable-pitch propeller, a small gap of approximately 3 mm height between blade and hub is present near the leading and trailing edge. Furthermore, an additional gap exists between the shaft and the hub. These gaps, as well as the small radius between blade and hub are omitted from the numerical model, as their influence on the overall flow field is regarded as negligible. For all computations, the propeller is mounted in push arrangement, and the cavitation tunnel hub cap, as specified by the PPTC, is utilized. For the experimental open-water tests a different set-up is used, i.e., pull arrangement and an altered hub cap geometry. However, the influence of these factors is regarded

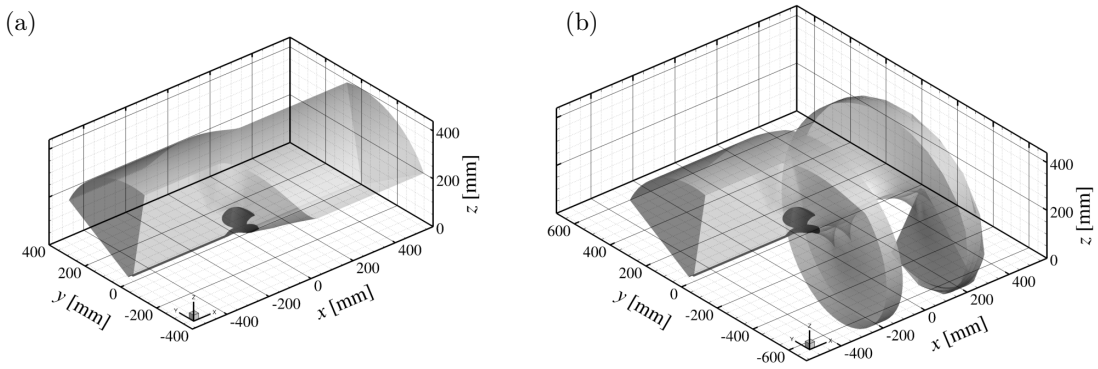

Figure 5.5: Visualization of the numerical domain for the investigation of *VP1304*, in (a) reference, and (b) tip-vortex configuration.

as negligible considering the open-water performance of the propeller, since the integral measurements of K_T and K_Q include contributions of the propeller blades only, as explained.

The computational domain is depicted in figure 5.5. The distances from the blade generator line to the inlet and outlet boundary are $l_\mathrm{in} = l_\mathrm{out} = 2D$. For modeling the towing tank environment of the open-water computations, and to minimize blockage effects, the boundaries in radial directions are located at $l_\mathrm{rad} = 10D$ from the propeller axis for case *2.1*. For the assessment of the wake-velocity (case *2.2*) and the cavitation tunnel tests (cases *2.3*), the radial boundaries are located at $l_\mathrm{rad} = 2.71R$, yielding a blockage ratio identical to the cavitation tunnel.

Block-structured, body-fitted numerical grids are utilized in order to discretize the domain. The mesh consists of an O-topology around the blade, which covers a region of approximately 8 mm perpendicular to the blade surface. It is embedded into an H-topology for the remaining passage. For case *2.1*, the whole computational domain is oriented along the propeller axis, see figure 5.5*a*. In order to improve the spatial resolution of the propeller wake flow for cases *2.2* and *2.3*, in contrast, the downstream portion of the domain is projected into a helical shape, as shown in figure 5.5*b*. This procedure is illustrated in figure 5.6 showing a schematic of the block topology in the vicinity of the propeller blade at constant radius. The passage of the reference grid, depicted in figure 5.6*a*, is oriented parallel to the x-axis downstream of the blade. As a consequence, the mesh is not aligned with the trailing tip vortex, which crosses the periodic boundaries. In a first step, figure 5.6*b*, the passage is transformed into a helix, in order to align it to the trailing vortex structure. The location of the tip vortex, and thus also the helix pitch-angle $\Theta(x)$, depends on the advance coefficient J. In a final step, the grid lines perpendicular to the vortex are adjusted, as shown in figure 5.6*c*, in order to avoid excessively sheared cells, and to further improve the mesh quality in the downstream region.

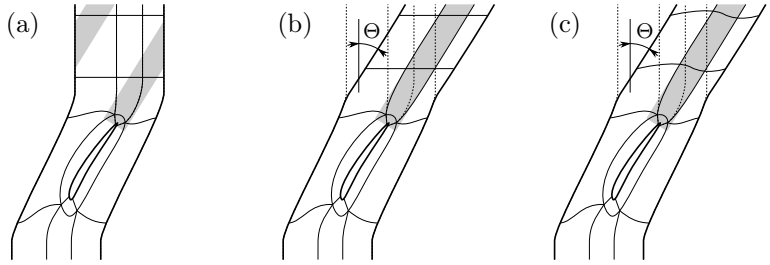

Figure 5.6: Sketch of the numerical domain (thick lines) and blocking (thin lines) on a cross section of constant radius for visualizing the tip-vortex alignment procedure, (a) reference configuration, (b) helical transformation, and (c) final tip-vortex alignment with correction of the cross-section. The trailing tip vortex is indicated by the shaded area, the helix pitch angle is denoted by Θ.

5.3.2 Numerical Grid and Wall-Resolution

Three grid levels, denoted as lvl_0, lvl_1, and lvl_2, are created. These are required for the grid sequencing procedure, as explained below, and can be further utilized for investigating the influence of the spatial discretization. In order to isolate and better assess the role of the discretization scheme, identical grids are utilized for both baseline and ILES computations.

To better judge the resolution requirements for the finest grid level, the viscous length scale $l^+ = u_\tau/\nu$ needs to be approximated by estimating the skin friction coefficient $c_f = \tau_w/(\frac{1}{2}\rho_0 u_{\text{ref}}^2)$ with $u_\tau = \sqrt{\tau_w/\rho_0}$. This requires a suitable correlation of the skin friction with the Reynolds-number Re, e.g., $c_f = 0.075\,[\log_{10}(\text{Re}) - 2]^{-2}$, as recommended by the International Towing Tank Conference (see International Towing Tank Conference, 2011). Using the already-computed sectional Reynolds-numbers $\text{Re}_{0.7}$ for the considered operating points from table 5.2, this yields estimates for the viscous length scale of $1.3 \times 10^{-6}\,\text{m} \lesssim l^+ \lesssim 2.4 \times 10^{-6}\,\text{m}$.

The time-step Δt of the explicit time integration is directly linked to the spatial resolution via the CFL-criterion, equation (3.24). Thus, to fully resolve the viscous length scale l^+, the time-step needs to be $1.3 \times 10^{-9}\text{s} \lesssim \Delta t \lesssim 2.2 \times 10^{-9}\text{s}$. Independent of the operating point shown in table 5.2, more than 3×10^7 iterations are required for covering a single revolution of the propeller with this time-resolution.

From these considerations, and given the number of operating points targeted in this study, no attempt is made to fully resolve the viscous boundary layer on the blade surface, as the required computational resources are beyond what is available to the author. The minimum grid size in wall-normal direction Δy on the the finest grid is thus designed to yield $y^+ = \Delta y/l^+ \approx 4$. For the wall-tangential direction with grid size Δs, $s^+ = \Delta s/l^+ \approx 25$. The finest grid consists of 5.63×10^6 cells in total for the blade passage (corresponding to 28×10^6 cells for the entire propeller), with

Table 5.3: Properties of the employed grid levels for *VP1304*.

		lvl_0			lvl_1			lvl_2	
cells[a]		1.42×10^5			6.92×10^5			5.63×10^6	
cells[b]		1.74×10^4			4.83×10^4			3.88×10^5	
$y^{+\dagger}$	13	69	37	9	62	33	4	42	21
$\breve{y}^{+\dagger}$	16	259	88	10	211	74	3	108	37
$s^{+\dagger}$	83	441	1346	55	323	240	25	36	89
$\breve{s}^{+\dagger}$	222	1433	3263	137	985	542	47	84	148
Δt		3.04×10^{-8} s			2.33×10^{-8} s			6.42×10^{-9} s	

[a] for the entire domain
[b] within the blade vicinity, given by the blocks constituting the O-topology
[†] given as minimum, maximum, and average value

3.9×10^5 cells used for the blocks constituting the O-topology in the vicinity of the blade. Refer to table 5.3 for further grid characteristics for all three grid levels. The resolution of the near-wall region is provided in terms of the minimum, maximum and average of the grid size in wall-normal, and wall-tangential direction. In order to obtain these properties, computations of case *2.1c* using the ILES scheme are employed, and the near-wall velocity gradient is either (a) directly computed, yielding y^+, s^+, or (b) estimated with the wall-function of Shih *et al.* (1999) as described in §3.2.3*c*, denoted by $\breve{y}^+, \breve{s}^+$. Figure 5.7 visualizes the lvl_2 grid. A view of the discretized blade surface is provided in figure 5.7*a* and figure 5.7*b*, showing the blade suction and pressure side, respectively. A contour plot of $\breve{y}^+$ as obtained with the ILES computation of case *2.1c* on either side of the blade is given in figures 5.7*c,d*.

The influence of the spatial resolution on the predicted propeller performance and cavitation patterns is investigated in more detail for the design point of the propeller, see §5.4.3.

5.3.3 Boundary Conditions

For the lateral boundaries, circumferential periodicity is utilized. At the radial boundary, a far-field condition is imposed, and the grids are coarsened, in order to damp wave reflections. Walls are modeled as slip-walls for the baseline computations, while a no-slip boundary condition is applied in the ILES. Despite the under-resolution of the near-wall region with the finest grid in the ILES, it is again emphasized that no wall-function is applied, see the discussion in §3.2.3*c*.

The propeller rotational speed ω is prescribed via the mesh movement using the ALE approach, as introduced in §3.2.2. The constant inflow velocity V_a is imposed at the inlet, and an asymptotic boundary condition for the static pressure

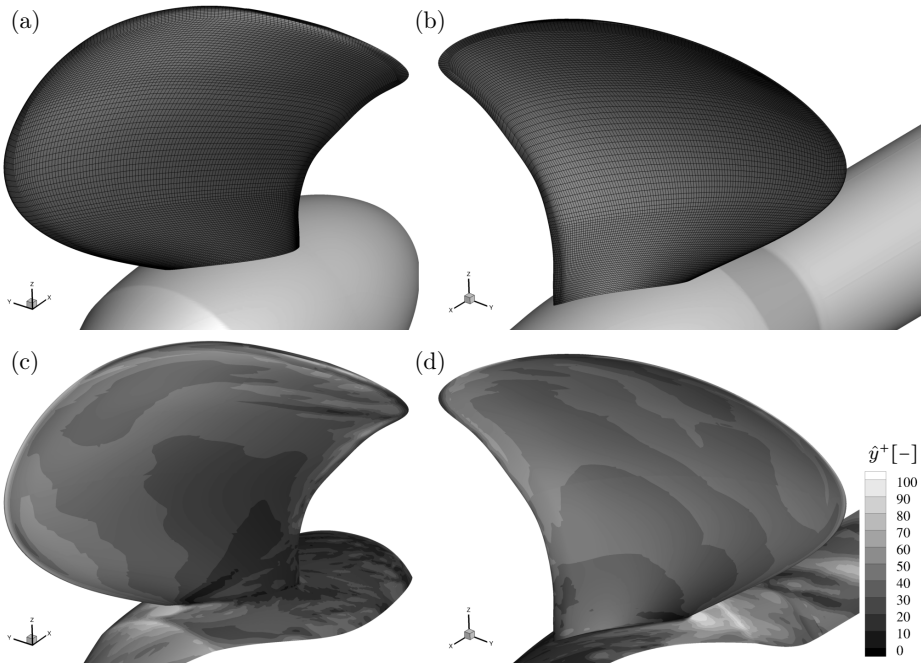

Figure 5.7: Visualization of the *lvl*$_2$ grid, showing (a,b) the blade surface mesh, and (c,d) the near-wall resolution in terms of $\breve{y}^+$, on the propeller suction and pressure side, respectively.

p_∞ is utilized at the outlet. All quantities are chosen such that computations are performed at J- and σ_n-identity, with respect to the experiments. Note that this differs from the PPTC problem specification, which requested K_T-identity. This approach is chosen here instead, in order to achieve better comparability of baseline and ILES computations, due to otherwise changed boundary conditions, stemming from different levels of the predicted thrust.

Note that inflow and outflow conditions are identical for baseline and ILES computations, i.e., a block profile is utilized for the inflow velocity. Again aiming at maximizing the comparability of both numerical approaches, no additional free-stream turbulence is imposed at the inlet for the ILES. Furthermore, no information about the turbulence level is provided for the experiments, and the coarser mesh used for the upstream region would lead to a dissipation of any free-stream turbulence.

5.3.4 Thermodynamic Model

In order to assess the role of the thermodynamic model, preparatory simulations of case *2.1c* and *2.3.2a,b* using the full thermodynamic model and the barotropic approach, as introduced in §3.1.3, are carried out. Similarly to the results obtained for the configuration presented in the previous chapter 4, only marginal differences are found in the statistics, e.g., when considering the propeller performance (K_T,

K_Q, η_0) and mean cavitation patterns, as well as for the global system dynamics. The temperature fluctuations predicted with the full thermodynamic model are negligible as well. This is due to the large heat capacity of water, and the fact that the characteristic velocities with $U = \mathcal{O}(10\,\mathrm{m/s})$ are equally low as for the previous configuration.

From these preparatory studies, it is concluded that the influence of the thermodynamic model is insignificant, and the barotropic model is employed for all studies presented in the following.

5.3.5 Simulation Start-up and Conducted Simulations

In order to initialize the computations, an impulse start is carried out, i.e., the propeller is immediately operated at the rotational speed ω designated for the considered operation point. Due to the fully compressible treatment of the working fluid, pressure waves originate from the propeller blade. Statistical sampling can only be started when these waves are sufficiently decayed. In order to reduce this initial transient phase and the required computational resources, two strategies are pursued, (a) time-operator preconditioning, see §3.2.1, and (b) grid sequencing. The initialization strategy is depicted schematically in figure 5.8.

All computations are initialized on the coarsest grid lvl_0. Once a quasi-steady solution is established on one level, it is interpolated to the next finer grid level, until the target grid is reached. The simulation start-up on the coarser levels is always conducted with the cavitation model disabled. This allows to use time-operator preconditioning in order to accelerate convergence, which is carried out in two steps. First, on, the coarser grid levels, a preconditioning factor of $\zeta^{-1} = 30$ is used. When reaching the target grid, an intermediate preconditioning factor $\zeta^{-1} = 10$ is used, before preconditioning is disabled, i.e., setting $\zeta^{-1} = 1$. When statistical sampling is required, the step-wise reduction of the preconditioning is performed also on coarse grid levels, otherwise it is only carried out for the finest grid level. Similarly, the cavitation model is activated only for the required grid level(s), and after the flow has developed with preconditioning disabled.

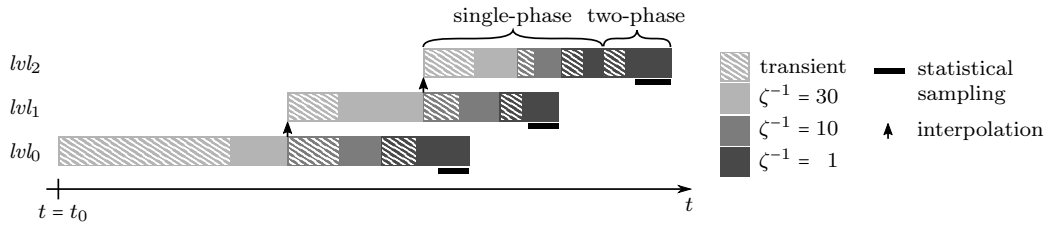

Figure 5.8: Start-up strategy for cavitating ship propeller analysis, relying on time-operator preconditioning and grid sequencing.

5.4 Results

5.4.1 Case *2.1* – Open-Water Performance

First, integral performance characteristics of *VP1304* are investigated utilizing the baseline and ILES method, and validated against PPTC references. For this purpose, the open-water performance is analyzed in the range $0.6 \leq J \leq 1.4$, following the specifications of PPTC case *2.1*. Results of this study are summarized for baseline and ILES computations in figures 5.9*a* and 5.9*b*, respectively. The plots show the thrust coefficient K_T, the torque coefficient K_Q, the propeller efficiency η_0, and the thrust loading coefficient C_th over the entire range of investigated advance coefficients.

Figures 5.9*a,b* include PPTC reference data, encompassing experimental studies by SVA, and simulations conducted by PPTC workshop participants. Two sets of experiments were performed by SVA, i.e., tests in the towing tank (Barkmann, 2011a), and in the cavitation tunnel (Heinke, 2011a). In the towing tank, as already mentioned, the propeller is operated in pull configuration with an adapted hub cap geometry. For the cavitation tunnel tests, in contrast, the propeller was operated in push configuration, and a different hub cap is used. In order to obtain comparable data sets, thrust and torque measurements consider the contributions of the propeller blades, only. Furthermore, the correction of Glauert (1933) can be applied to account for the blockage effect due to the tunnel side-walls. Results from the towing-tank tests are shown in figures 5.9*a,b* by black dashed lines. Gray dotted lines and gray dash-dotted lines indicate results obtained in the cavitation tunnel, with and without application of the Glauert-correction, respectively. In addition, numerical data submitted to the PPTC workshop is included in figures 5.9*a,b* as well, comprising a total of 19 simulations from 14 groups, refer to Barkmann (2011b). Table 5.4 gives an overview of all considered references. The contributions are categorized in potential flow methods (3 out of 19), included in figure 5.9*a*, and viscous flow methods (16 out of 19), shown in figure 5.9*b*. Data from these studies is summarized as box plots, showing the minimum, maximum, median, the 25th and the 75th percentile at each investigated advance coefficient J.

For the present study, both baseline and ILES computations are conducted at advance coefficients $J = (0.6, 0.8, 1.0, 1.2, 1.4)$. The cavitation tunnel configuration is utilized, i.e., push arrangement and the cavitation tunnel hub geometry. In order to compute the thrust and torque, the fluid forces are evaluated on the blade surface only, in correspondence with the experiments. For the baseline computations, only pressure forces are considered, while pressure and viscous forces are taken into account with the ILES approach. In order to compute viscous forces in the ILES, the wall-normal velocity gradient magnitude $|\partial \boldsymbol{u}/\partial \boldsymbol{n}|$ can be

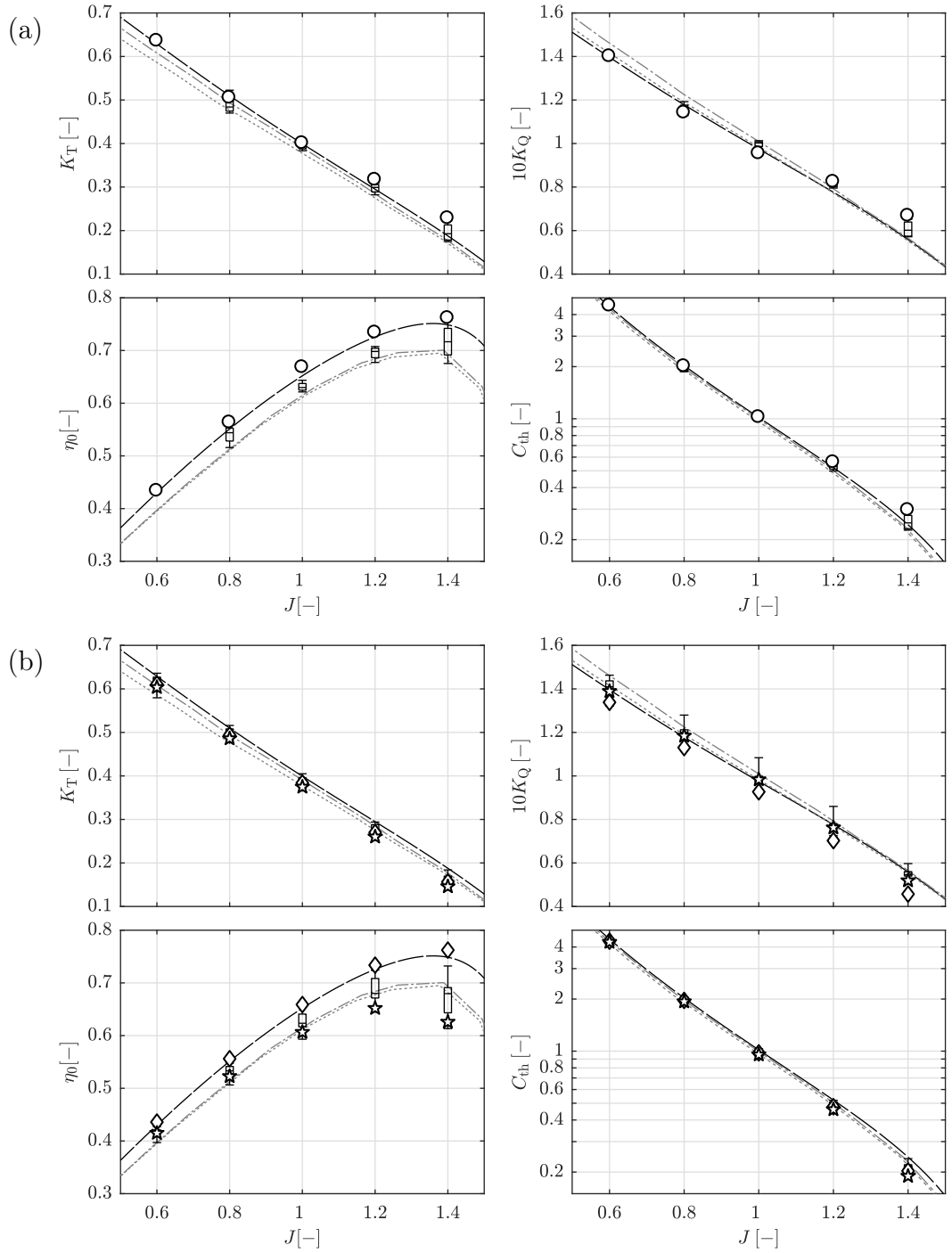

Figure 5.9: Validation of propeller open-water performance for *VP1304* in the range $0.6 \leq J \leq 1.2$. Comparison of K_T, K_Q, η_0, and C_{th}. Juxtaposition of PPTC references (towing tank ▬▬, cavitation tunnel without ▬·▬ and with ····· Glauert correction; numerical references ⊢□⊣), and numerical results obtained with (a) the baseline scheme (∘) and (b) the ILES scheme (direct evaluation of wall-normal velocity gradient ⋄, estimated using wall-function of Shih *et al.* (1999) ☆).

evaluated either directly, or by virtue of a wall-function, as explained in §3.2.3*c*. Results from both methods are included in figure 5.9*b*.

The baseline simulations, see figure 5.9*a*, show good agreement with PPTC references in the thrust coefficient for $J \leq 1$. Similarly, the agreement for the torque coefficient is best at lower J, with a tendency of predicting slightly smaller values. In combination, this leads to a larger propeller efficiency, compared to the experiments. At higher J, larger deviations are noticeable, and the predicted coefficients for the thrust and torque as well as the thrust loading are higher with respect to the experimental references. It can be observed that potential flow methods submitted to the PPTC workshop show similar tendencies at larger J for all investigated quantities in figure 5.9*a*. It is thus conjectured that this departure from the experiments are primarily caused by neglecting viscous effects in these models. The baseline results show a stronger pressure recovery near the trailing edge, compared to the ILES. Analyzing the flow topology in more detail in §5.4.4, this is connected with the occurrence of a zone of separated flow along the trailing

Table 5.4: Numerical references from PPTC workshop for open-water performance, see Barkmann (2011b).

	acronym	$J = 0.6$	0.8	1.0	1.2	1.4
potential	HSVA-PPB		×	×	×	×
methods	HSVA-QCM		×	×	×	×
	INSEAN-PFC	×	×	×	×	×
viscous	Berg-OpenFOAM	×	×	×	×	×
methods	Cradle-SC/Tetra	×	×	×	×	×
	CSSRC-Fluent	×	×	×	×	×
	MARIC-Fluent	×	×	×	×	×
	SSPA-Fluent	×	×	×	×	×
	SVA-Vortex	×	×	×	×	×
	TUHH-Fresco+	×	×	×	×	×
	UniGenua-Panel	×	×	×	×	×
	UniGenua-OpenFOAM	×	×	×	×	×
	UniGenua-StarCCM(kw)	×	×	×	×	×
	UniGenua-StarCCM(ke)	×	×	×	×	×
	UniTriest	×	×	×	×	×
	ViscusDT-StarCCM	×	×	×	×	×
	VOITH-Comet	×	×	×	×	×
	VOITH-OpenFOAM	×	×	×	×	×
	VTT-FinFlo	×	×	×	×	×

edge of blade in the ILES. This is not found with the baseline computations, where the flow remains attached. It is believed that this is the main cause for the observed deviations in the propeller performance between the two methods.

As shown in figure 5.9*b*, the ILES computations yield improved results for the predicted propeller performance over the entire range of investigated advance coefficients. Very good agreement with the experimental and numerical references is obtained for the thrust coefficient K_{T}. The torque K_{Q}, in contrast, exhibits an almost constant negative offset from the experimental references. Combined, the efficiency η_0 again is slightly over-predicted compared to the experiments, but improved with respect to PPTC contributions. The loading coefficient C_{th} deviates only slightly from the experimental references at larger J for the ILES, but compares well with results from other PPTC participants.

It is conjectured that the observed deviations, especially in the computed torque coefficient, are connected to the systematic prediction of a smaller value for the local wall shear stress τ_{w} when performing under-resolved ILES without the application of a wall-function. In order to test for this assumption, τ_{w} is re-evaluated using the *a posteriori* usage of the generalized wall function of Shih *et al.* (1999), yielding an improved estimated wall shear stress $\breve{\tau}_w$. Using the approximation $\breve{\tau}_w$ for computing the integral viscous drag forces slightly lowers the thrust, while the predicted torque is increased. The thus computed torque coefficient shows an improved agreement with the references in figure 5.9*b*.

In order to assess the difference between both evaluation approaches for the wall-normal velocity gradient, figure 5.10 visualizes the ratio $\breve{\tau}_w/\tau_{\mathrm{w}}$ on the propeller blade and hub surfaces for case *2.1c* (J = 1.0). By using the wall-function, the wall shear stress is higher on average by a factor of 3.5, while reaching locally at most a factor of 10. As expected, the largest change is found in the region of strong velocity gradients near the leading edge.

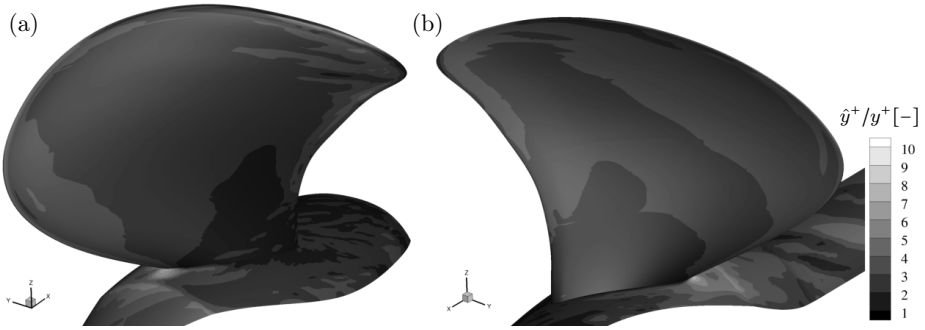

Figure 5.10: Ratio $\breve{\tau}_w/\tau_{\mathrm{w}}$, relating the directly computed wall-shear stress τ_{w} to $\breve{\tau}_w$, approximated using the wall-function of Shih *et al.* (1999), as computed with the ILES scheme for case *2.1c*. Visualization of the (a) blade suction side, and (b) blade pressure side.

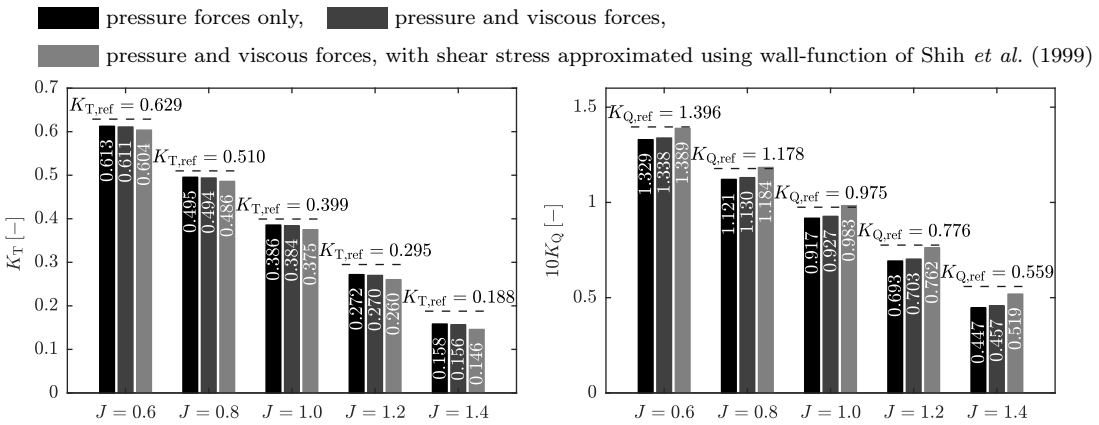

Figure 5.11: K_T and K_Q predicted by ILES for the investigated operating points *2.1a-e*, including experimental references from towing-tank tests, Barkmann (2011a). Comparison of contributions due to pressure forces, as well as pressure and viscous forces. The latter are computed either with directly obtained wall-shear stress τ_w, or with $\breve{\tau}_w$, approximated using the wall-function of Shih *et al.* (1999).

A more detailed analysis of pressure and viscous contributions to K_T and K_Q as predicted by the ILES for the investigated open-water operating points are shown in figure 5.11. It is found that the increased prediction of the wall shear stress influences the torque to a larger degree compared to the thrust. At $J = 1.4$, e.g., the viscous contributions to the torque account for up to 16%. In contrast, the thrust is lowered by only 5%. Therefore, an increase of $\breve{\tau}_w$ over τ_w causes only a slight divergence in K_T from the references, while improving the prediction of K_Q.

From these considerations, it is concluded that the observed deviations in the torque coefficient for the ILES are caused by under-estimating the viscous forces. This is due to the under-resolution of the near wall region, without the application of a wall-function. It should be noted that the presented approach can provide only an approximation of the viscous contributions to the thrust and torque, and hence only gives an explanation for the observed deviations. It cannot immediately be compared with a direct application of a wall-function, as this will cause a feed-back to the flow by altering the near-wall behavior. The propeller efficiency computed by this procedure, see figure 5.9*b*, albeit being still in reasonable agreement with the numerical reference data, illustrates its limitation.

The ILES approach without an active usage of a wall-function has been selected in the present study for correspondence with the established numerical method for cavitating conditions, as discussed in §3.2.3*c*. It is concluded that the integral open-water performance predicted with the ILES is in good agreement with the available references, and, in the frame of the PPTC, yields satisfactory results.

5.4.2 Case *2.2* – Propeller Wake Velocity

With case *2.2*, the propeller wake field for non-cavitating conditions is investigated. Experimental reference is provided by LDV measurements performed within the propeller wake, see Mach (2011).

The wake field is evaluated on two planes perpendicular to the propeller axes, in a distance of $x/D = 0.1$ and $x/D = 0.2$ behind the propeller. Statistical sampling of the numerical results is performed for 1 propeller revolution on the lvl_2 grid. The axial u_{ax}, radial u_{r} and azimuthal u_θ components of the velocity are non-dimensionalized with the inflow velocity V_{a}, as $1 - u_{\mathrm{ax}}/V_{\mathrm{a}}$, $u_{\mathrm{r}}/V_{\mathrm{a}}$, and u_θ/V_{a}, respectively. Azimuthal velocities are positive in the direction of propeller rotation, while the radial velocity is taken positive in the direction of increasing radius.

Contour plots of the axial deficit velocity $1-u_{\mathrm{ax}}/V_{\mathrm{a}}$ in the propeller wake are shown in figure 5.12, with the planes $x/D = 0.1$ and $x/D = 0.2$ given in figures 5.12*a-c* and 5.12*d-f*, respectively. The numerical predictions, obtained with the baseline and ILES scheme, are compared to the LDV measurements. Both numerical results qualitatively compare well with the experimental references. At lower radii, $r/R \leq 0.97$, the flow is accelerated, noticeably behind the suction side, as expected. The tip vortex structure at $0.97 \lesssim r/R \lesssim 1$ is captured by the simulations, with a region of highly accelerated (decelerated) flow at radii smaller (larger) than the location of vortex core, respectively. Overall, the ILES resolves smaller structures in the wake field and yields larger velocity gradients. In contrast, the tip vortex region appears more smeared in the baseline computations, and the agreement is deteriorated at the downstream plane $x/D = 0.2$. Since identical meshes are used for both methods, this can be attributed to the higher level of numerical dissipation present in the baseline discretization scheme. Furthermore, the deficit in the wake of the propeller blade is under-estimated with the baseline approach. This is to be expected, considering the absence of a physical boundary layer on the blade surface due to the employed slip boundary condition. In contrast, the velocity deficit in the wake of the blade is larger in the ILES compared to the experiments. Similar observations can be made for most of the PPTC contributions, see Lübke (2011), and might be due to the under-resolution of the near-wall region. The core of the trailing tip vortex is better captured with the ILES on both evaluation planes. Due to the higher order of the spatial discretization, it de-correlates less quickly, compared to the baseline scheme. However, comparing with the experiments, the strength of the vortex is predicted slightly larger in both its extent and magnitude with the ILES scheme. Additionally, the location of the tip vortex is shifted to a lower radius by ca. 3 mm at $x/D = 0.2$ in the simulations. This is connected to a stronger contraction of the stream tube passing through the propeller disc, which is obtained consistently with both discretization schemes. This might be caused

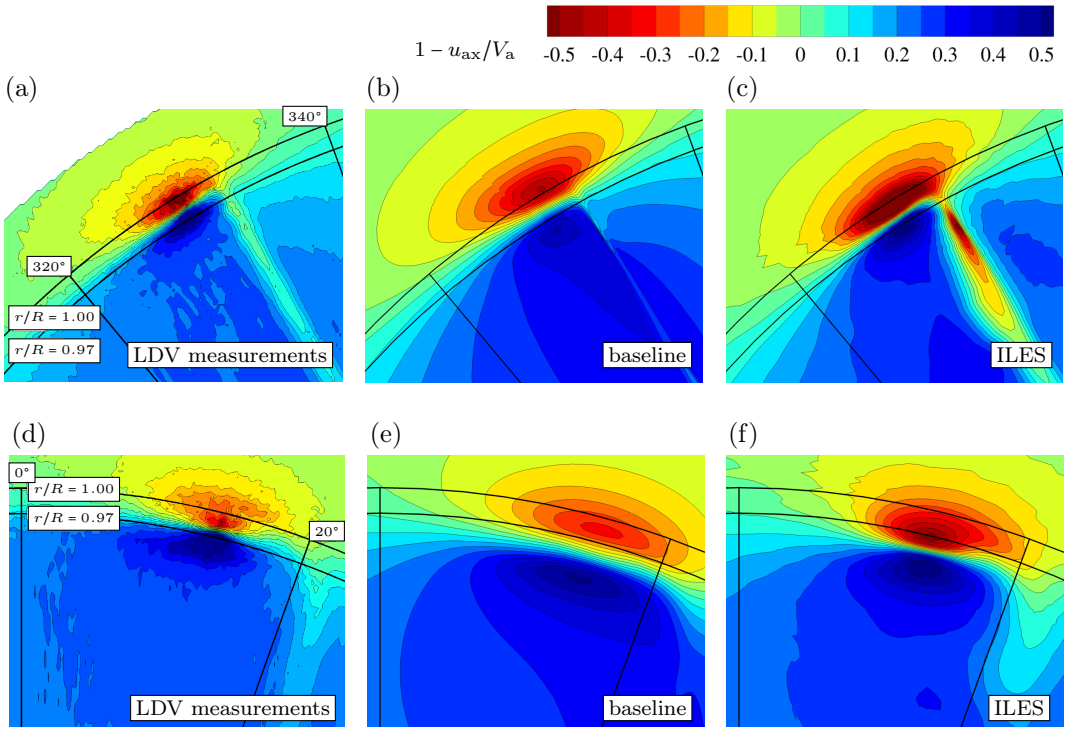

Figure 5.12: Contour plot of the deficit velocity $1 - u_{ax}/V_a$ on planes (a-c) $x/D = 0.1$, and (d-f) $x/D = 0.2$. Juxtaposition of (a,d) LDV measurements, and numerical results obtained with the (b,e) baseline, and (c,f) ILES scheme, with indication of the radii $r/R = (0.97, 1.0)$, and azimuthal positions $\theta = (0°, 20°, 320°, 340°)$.

by representing the tunnel geometry by a cylindrical domain. Despite an equal cross-sectional area yielding an identical blockage ratio, the effect of the square shape of the tunnel is disregarded using this approach.

For a quantitative comparison of the wake, profiles of the velocity components $1 - u_{ax}/V_a$, u_θ/V_a, and u_r/V_a on constant radii $r/R = (0.7, 0.9, 0.95, 0.97, 1.0)$ are analyzed. The results for both evaluation planes $x/D = (0.1, 0.2)$ are juxtaposed in figures 5.13 and 5.14, respectively. The plots provide a view on a single blade passage, with a 72° sector indicated by the dashed-dotted lines. Black dashed and solid lines show the time-averaged baseline and ILES results, respectively. Experimental references are taken from Mach (2011). The measurements are performed within the entire plane behind the propeller, computing a time-average over a period of up to 2070 propeller revolutions. For the comparison in figures 5.13 and 5.14, the reference data provided for the five blade passages is ensemble-averaged, in order to reduce it to a single 72° sector, and for decreasing the measurement noise. The thus obtained ensemble mean is shown by the gray solid line. The gray shaded area indicates the minimum and maximum in the reference data at a given angular position of each sector.

Figure 5.13: Profiles of the non-dimensionalized velocity in the propeller wake, components $1-u_{ax}/V_a$, u_θ/V_a, and u_r/V_a, at $x/D = 0.1$ along constant radii $r/R = (0.7, 0.9, 0.95, 0.97, 1.0)$. Juxtaposition of numerical results (baseline scheme – –, ILES scheme —) and LDV measurements (ensemble average of five blade sectors —, shaded area: minimum and maximum).

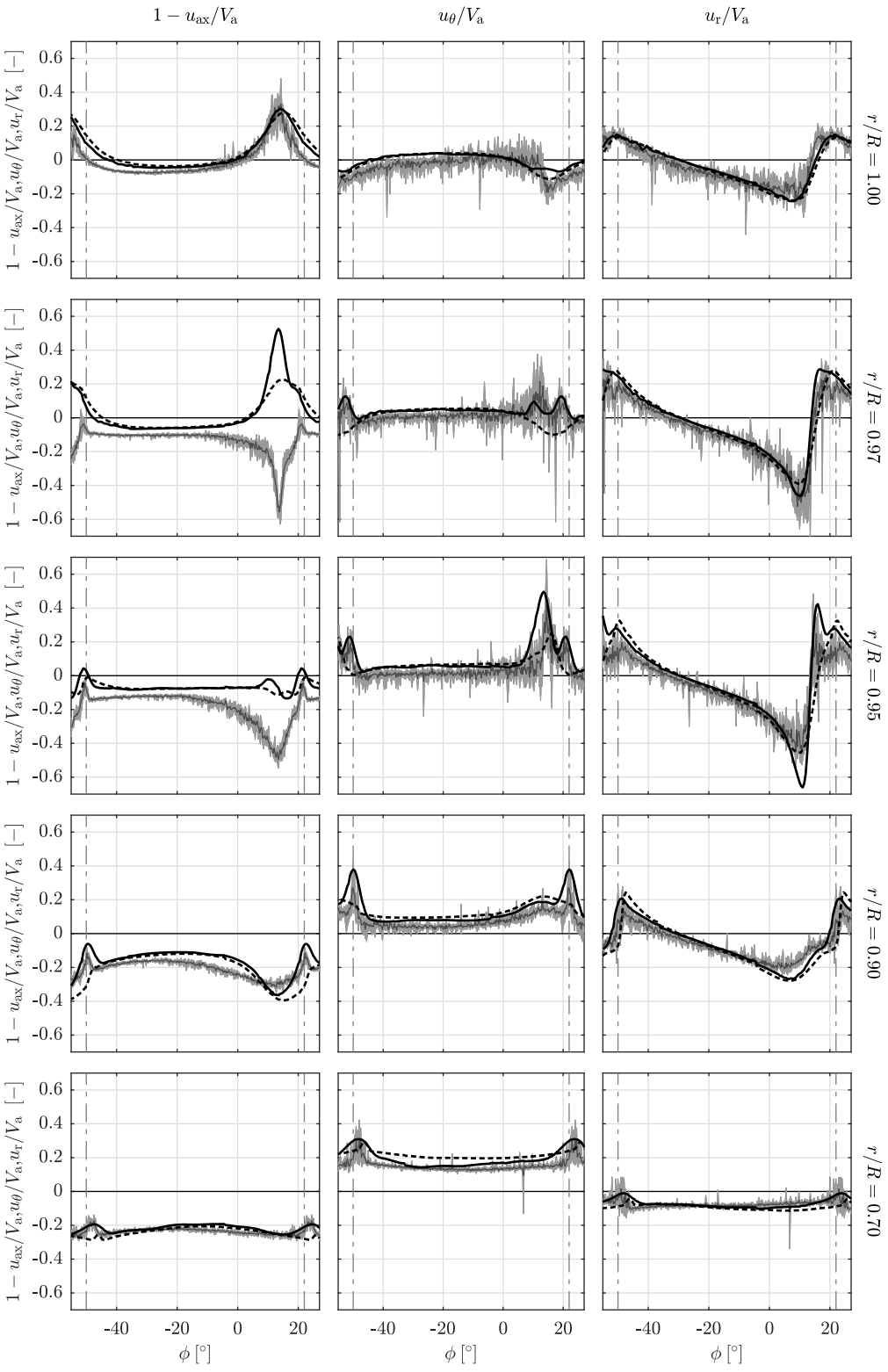

Figure 5.14: Profiles of the non-dimensionalized velocity in the propeller wake, components $1-u_{ax}/V_a$, u_θ/V_a, and u_r/V_a, at $x/D = 0.2$ along constant radii $r/R = (0.7, 0.9, 0.95, 0.97, 1.0)$. Juxtaposition of numerical results (baseline scheme **– –**, ILES scheme **——**) and LDV measurements (ensemble average of five blade sectors ——, shaded area: minimum and maximum).

Results obtained with the baseline scheme exhibit a good agreement, resolving the overall flow topology for all velocity components satisfactorily well. However, as expected, the prediction quality is noticeably improved using the ILES scheme. The baseline method fails to resolve small-scale structures, while the ILES captures most of these features, compare, e.g., the radial component on $x/D = 0.1$, and the azimuthal component at $x/D = 0.2, r/R = 0.97$. Furthermore, as shown by the axial velocity component at $x/D = 0.1, r/R = (0.7, 0.9)$, the velocity deficit behind the blade is not predicted by the baseline method. As already explained, this is caused by the slip boundary condition for the blade. The ILES yields a better agreement, albeit predicting a stronger deficit for $0.7 < r/R \leq 0.97$, as discussed.

Topological differences in the current predictions worth mentioning are observed for the axial component at position $x/D = 0.2$ and $r/R = (0.95, 0.97)$. Here, the experiments show an excess velocity, while both simulations equally predict a velocity deficit. This is related to the stronger contraction of the slip-stream in the simulation, as explained in the context of figure 5.12. As a consequence, the radii $r/R = (0.95, 0.97)$ cut the tip vortex above its core, where a deceleration of the flow is induced in the numerical results. For the experiments, in contrast, $r/R = (0.95, 0.97)$ lies beneath the core, passing through the region of flow acceleration.

Despite this difference, the best match is obtained with both schemes for the axial and radial components. Comparing the azimuthal component to the experiments, a systematically larger value is predicted. The current study, however, is in alignment with other numerical PPTC references regarding this aspect, where this observation is made for most of the contributed results, see Lübke (2011).

5.4.3 Case *2.3.2* – Influence of Spatial Resolution at the Design Point

In order to assess the influence of the spatial resolution, the propeller flow for the nominal design point, case *2.3.2* ($J = 1.269$), is analyzed in more detail. For this purpose, instantaneous and statistical results obtained with the ILES scheme for the three grid levels lvl_0, lvl_1, and lvl_2 are compared.

The simulations are conducted for non-cavitating conditions, case *2.3.2a*, as well as cavitating conditions with a cavitation number $\sigma_n = 1.424$, case *2.3.2b*. The propeller is operated in push configuration and the corresponding hub cap is utilized, in accordance with the cavitation tunnel experiments conducted at SVA, see Heinke (2011b). In order to obtain statistical data, the numerical results are sampled over a period of at least two propeller revolutions. An overview of the sampling time for the individual computations is given in table 5.5.

Table 5.5: Time-span used for statistical sampling of ILES for case *2.3.2*.

grid level	lvl_0		lvl_1		lvl_2	
condition[†]	*2.3.2a*	*2.3.2b*	*2.3.2a*	*2.3.2b*	*2.3.2a*	*2.3.2b*
$\Delta T_{\text{sampling}}$ [rev]	11.6	12.9	5.9	5.4	2.1	3.6

[†] *2.3.2a*: non-cavitating conditions, *2.3.2b*: cavitating conditions

5.4.3*a* Time-Averaged Flow Topology

First, a qualitative comparison of the time-averaged flow topology obtained with ILES on the three grid levels is carried out.

Limiting Streamlines Time-averaged limiting streamlines on both the blade suction and pressure side are shown in figures 5.15 and 5.16 for non-cavitating and cavitating conditions, respectively. In addition, contours of the mean void fraction $\overline{\alpha} \geq 0.1$ on the surface are shown for cavitating conditions.

On the coarse grid, the streamlines on either side of the blade are mainly oriented along constant radii (i.e., tangentially). For wetted conditions, only a narrow zone of flow separation is found along the trailing edge. Under cavitating conditions, it is situated downstream of the suction side root cavity. This is opposite to the flow topology on lvl_1 and lvl_2 grids. Here, the flow is oriented towards the blade tip for the largest part of the blade. Tangentially-oriented streamlines can be found above $r/R \gtrsim 0.8$, starting from the leading edge, and extending towards the blade tip. Both for wetted and cavitating conditions, a large region of separated flow is located on the suction side along the trailing edge. It is of comparable extent for lvl_1 and lvl_2 grids, but noticeably larger compared to lvl_0. Under wetted conditions, the onset of flow separation is slightly delayed on the lvl_2 grid, compared to lvl_1.

Besides that, only minor differences are found between the two finer grids, and, overall, the surface flow topology is in good agreement. Aside from the region close to the leading edge above $r/R \gtrsim 0.8$, it resembles the flow pattern of laminar flow, which can be obtained for model propellers (see, e.g., plate 3.12 of Kuiper, 1981). Since no tripping of the boundary layer is utilized in the experiments, it can be indeed expected that laminar regions do exist on the propeller, as discussed initially. Despite the small Reynolds-number for the current configuration, it is likely not low enough to exhibit the same extent of laminar flow in the experiments, as predicted by the simulations. Unfortunately, this cannot be verified due to the lack of experimental data.

It is noted that the tangentially-oriented streamlines of the lvl_0 grid, in contrast, rather resemble a fully turbulent flow topology. With the coarse resolution of the

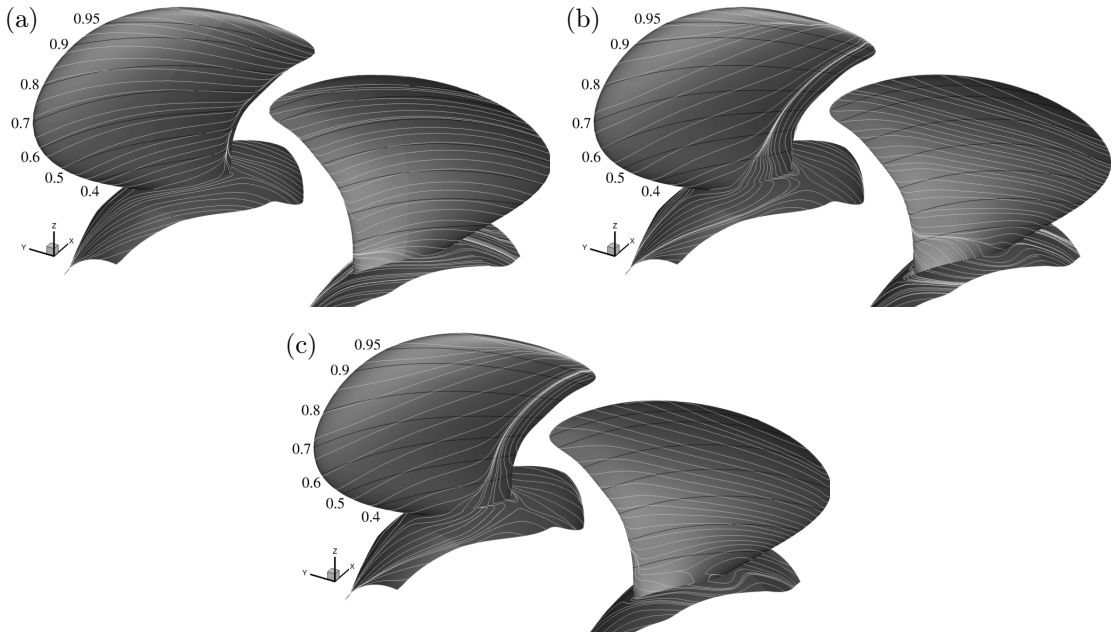

Figure 5.15: Limiting streamlines on blade and hub, predicted by ILES for the design point *2.3.2a* (non-cavitating conditions), juxtaposing results obtained for (a) lvl_0, (b) lvl_1, and (c) lvl_2 grids.

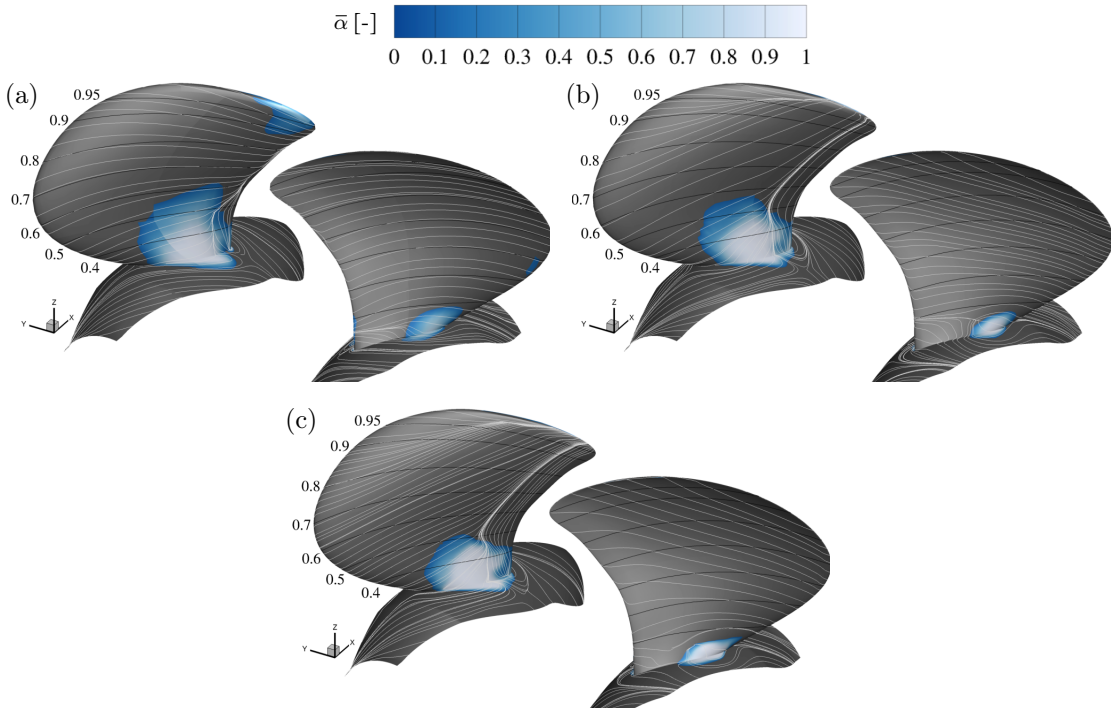

Figure 5.16: Limiting streamlines on blade and hub, predicted by ILES for the design point *2.3.2b* (cavitating conditions), juxtaposing results obtained for (a) lvl_0, (b) lvl_1, and (c) lvl_2 grids.

near-wall region, however, no near-wall turbulence is resolved. Instead, compared to the finer grids, viscous forces are under-, and the near-wall momentum is over-estimated, causing the flow to remain attached.

Propeller-Slipstream The time-averaged slip-stream for cavitating conditions is provided in figure 5.17, juxtaposing the three grid levels. The flow is visualized by contours of the non-dimensional axial excess velocity $\overline{u}_{ax}/V_a - 1$ in the slice $y = 0$. Mean vortical structures are shown with iso-surfaces of $\overline{\lambda}_2 = -1 \times 10^5\ 1/s^2$ colored by axial vorticity $\overline{\omega}_x$ in figures 5.17*a,c,e*, and juxtaposed to mean vapor structures, given by iso-surfaces of $\overline{\alpha} = 0.1$ in figures 5.17*b,d,f*.

Grid lvl_0 exhibits a stronger mean flow acceleration behind the propeller, implying a larger thrust compared to the two finer grids, caused by predicting lower drag forces due to the coarse spatial resolution. Accordingly, the tip vortex is stronger

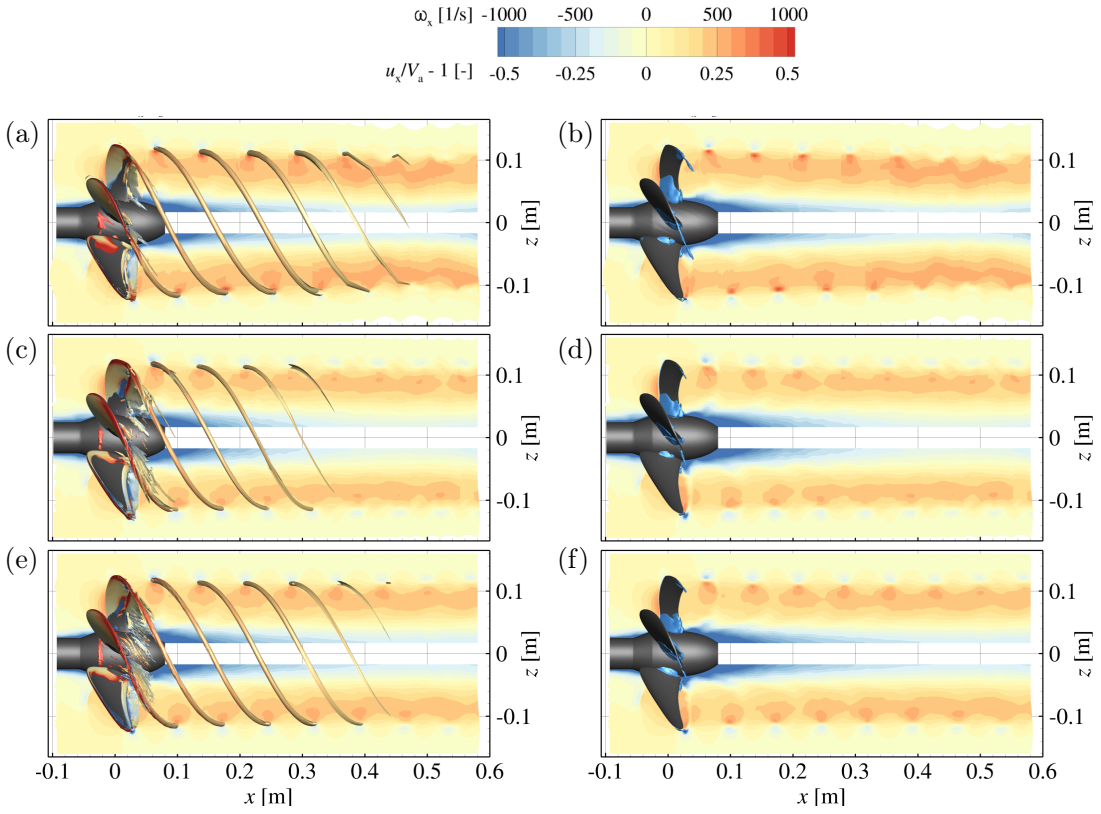

Figure 5.17: Time-averaged propeller slip-stream predicted by ILES for the design point *2.3.2b* (cavitating conditions), showing contours of non-dimensional axial velocity $\overline{u}_{ax}/V_a - 1$ on the slice $y = 0$, and (a,c,e) vortical structures by iso-surfaces of $\overline{\lambda}_2 = -1 \times 10^5\ 1/s^2$ colored by axial vorticity $\overline{\omega}_x$, or (b,d,f) vapor structures by iso-surfaces of $\overline{\alpha} = 0.1$. Juxtaposition of results obtained on (a,b) lvl_0, (c,d) lvl_1, and (e,f) lvl_2 grids, respectively.

on the coarsest grid. Compared to the results on lvl_1 and lvl_2, the cavitating portion of the vortex reaches further behind the blade on lvl_0, while the trailing tip vortex structure remains correlated over a larger distance within the propeller wake. Regarding the flow acceleration, as well as tip vortex strength and axial extent, the time-averaged results on lvl_1 and lvl_2 are nearly identical, while the flow topology for the coarse grid deviates. Furthermore, the cavitating portion of the trailing tip vortex is also comparable, which is further investigated below.

5.4.3*b* Propeller Performance

Subsequently, the integral propeller performance is analyzed. For this purpose, time-averaged values of K_T, K_Q, and η_0, as computed on the three grid levels, are given in figure 5.18. Figures 5.18*a,b* show the results for non-cavitating and cavitating conditions, respectively. Experimental references from Heinke (2011b) are included as well. For completeness, the time-signals used for the sampling are provided in the appendix figure A.1.

As discussed in the context of case *2.1*, the open-water performance predicted with the ILES yields lower values for the thrust and torque in comparison with the references, while the propeller efficiency agrees well with the experiments, refer again to figure 5.9*b*. Similar trends are also observed for the design point cases

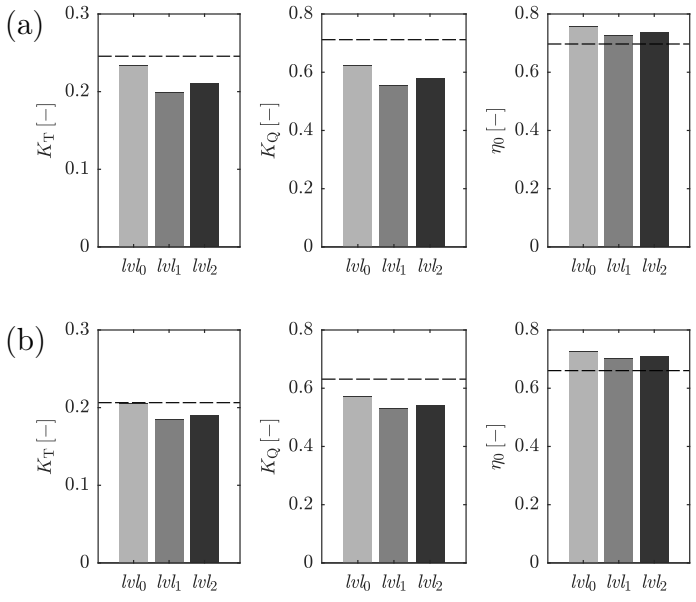

Figure 5.18: Time-averaged propeller performance at the design point case *2.3.2*, predicted by ILES (lvl_0 —, lvl_1 —, and lvl_2 —), under (a) non-cavitating, and (b) cavitating conditions. Including experimental references (– –, see Heinke, 2011a)

2.3.2a,b. Comparing non-cavitating and cavitating flow conditions, the agreement with the references is improved for the latter. This is to be expected, since, as soon as cavitation occurs, it dominates viscous contributions to the propeller performance. Viscous forces, whose prediction is affected by the under-resolution of the near-wall region as discussed, are hence of less importance.

Comparing the numerical prediction for the three grid levels, the coarsest grid predicts the largest value for the thrust, as already conjectured in the previous section. While the results of lvl_0 deviate noticeably, a good match in the propeller performance is observed between the lvl_1 and lvl_2 meshes. Under non-cavitating conditions, figure 5.18*a*, the differences between the medium and fine mesh in the thrust and torque coefficient amount to $\lesssim 5\%$, and $\approx 2\%$ for the efficiency. For cavitating conditions, figure 5.18*b*, the deviations are less than 2% in K_T and K_Q, and $< 1\%$ in η_0. Thus, the agreement between the two finer grids is improved, with respect to non-cavitating conditions. Summarizing, in addition to a better match with the experimental references, also the effect of spatial resolution is slightly attenuated when the flow is governed by the occurrence of cavitation.

5.4.3*c* Blade Pressure Coefficient

In the following, the grid-dependence of the blade surface pressure, as computed by the ILES, is investigated. A validation of the surface pressure with numerical references is provided in the next section.

First, a qualitative comparison of the non-dimensional pressure coefficient $c_\mathrm{p} = (p - p_\mathrm{ref})/(\frac{1}{2}\rho_\mathrm{ref} n^2 D^2)$ is carried out. For this purpose, contours of c_p on the blade and hub surfaces are given by figures 5.19 and 5.20 for non-cavitating and cavitating conditions, respectively. For the latter, the contour is clipped at the level of the vapor pressure $c_\mathrm{p} = -\sigma_\mathrm{n}$. Results for the three grid levels lvl_0, lvl_1, and lvl_2, are shown in figures 5.19*a,b,c* and 5.20*a,b,c*, respectively. Views on both the suction and pressure side of the blade are provided.

The visualizations again indicate a good overall agreement between lvl_1 and lvl_2 results, for both non-cavitating as well as cavitating conditions. The coarsest grid lvl_0, in contrast, shows some topological differences, e.g., a strong area of pressure recovery on the suction side along the trailing edge for $0.7 \leq r/R \leq 0.9$. This is not observed in this strength for the two finer grids, where a region of separated flow is situated along the trailing edge, as seen above. Under cavitating conditions, the extent of the region $c_\mathrm{p} = -\sigma_\mathrm{n}$ is in good agreement for all three grid levels for the suction side. Only minor differences can be noted for the pressure side.

A quantitative comparison of the blade surface pressure is carried out for five discrete radii $r/R = (0.4, 0.5, 0.7, 0.9, 0.95)$, as provided by figure 5.21. Here,

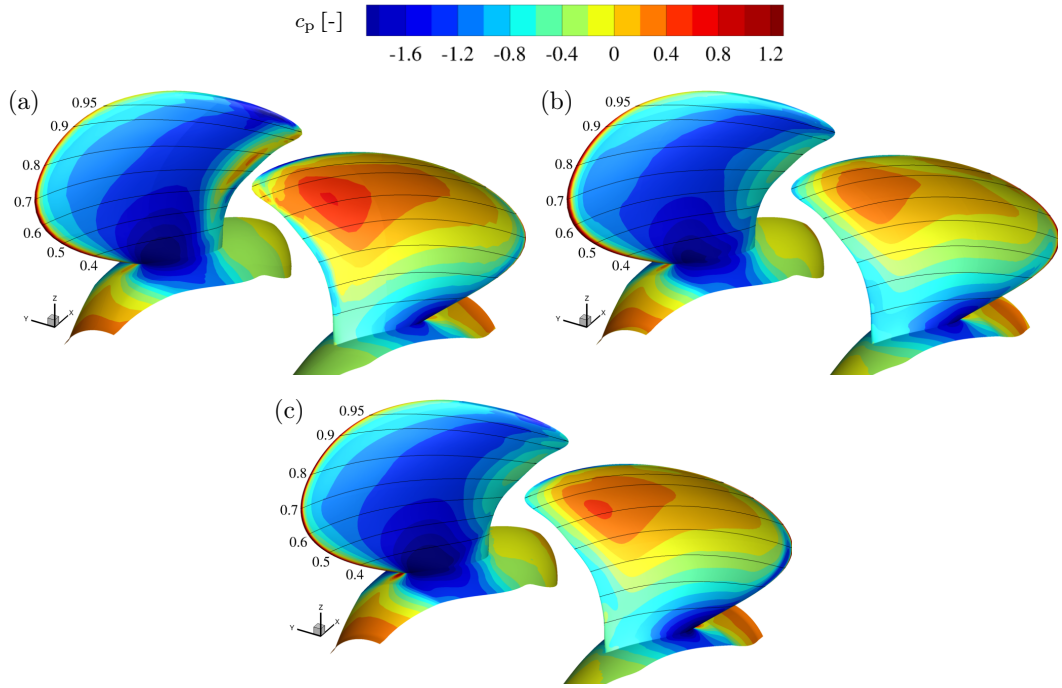

Figure 5.19: Contour of the surface pressure coefficient c_p on blade and hub, predicted by ILES for the design point case *2.3.2a* (non-cavitating conditions), juxtaposing (a) lvl_0, (b) lvl_1, and (c) lvl_2 grids.

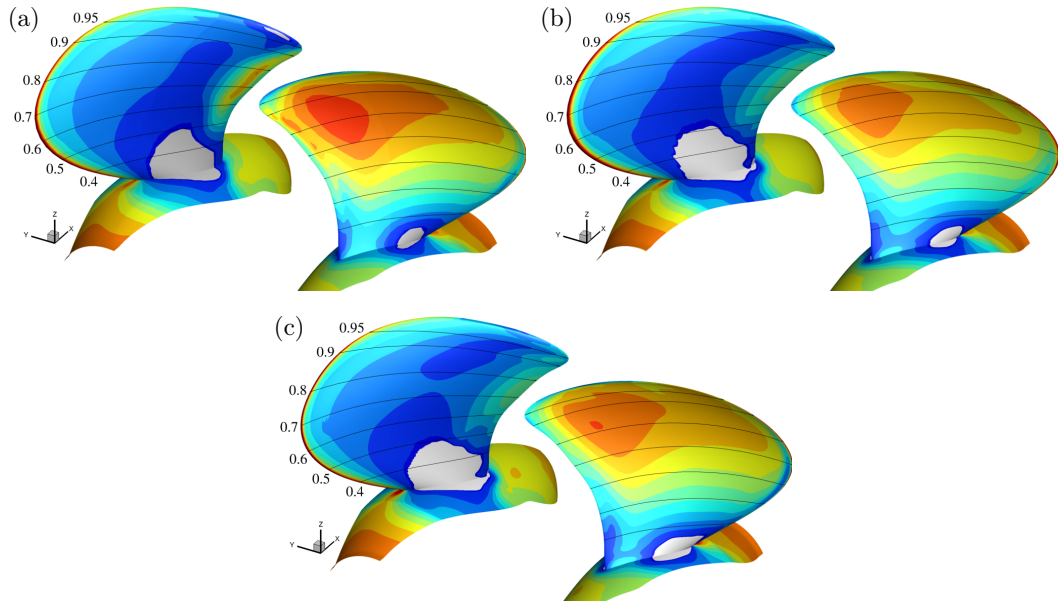

Figure 5.20: Contour of the surface pressure coefficient c_p on blade and hub, predicted by ILES for the design point case *2.3.2b* (cavitating conditions), juxtaposing (a) lvl_0, (b) lvl_1, and (c) lvl_2 grids (see above for legend).

the pressure is non-dimensionalized with the local section advance speed as $c_{p,r} = (p - p_{ref})/(\frac{1}{2}\rho_{ref}(V_a^2 + \omega^2 r^2))$, and plotted along the normalized axial position x/c_r, with c_r the local chord length of the section. For each investigated radius, the level of the vapor pressure is indicated by a dashed line.

Overall, the agreement between lvl_1 and lvl_2 grids is again improved when comparing them with the coarsest mesh lvl_0. The largest differences between the results are found for both non-cavitating and cavitating conditions near the leading and trailing edges. This is caused not only by the different geometric representation of the surface curvature in these regions, but also in the capability of resolving the strong local gradients with the different grids, and discrepancies in predicting flow separation along the trailing edge, as discussed. At mid-chord, the deviations between the meshes is higher at the smallest radius $r/R = 0.4$. As shown above, this is caused by a difference in the onset location of flow separation near the suction side root. Under cavitating conditions, however, the agreement between lvl_1 and lvl_2 grids is noticeably increased, as already observed with the investigations carried out above. This also holds for the lower radii, although the chordwise-extent of cavitation slightly differs, see, e.g., $r/R = 0.5$. Going to the larger radii $r/R = (0.7, 0.9, 0.95)$, the results for lvl_1 and lvl_2 grids are again nearly identical, for both non-cavitating as well as cavitating conditions. Constituting the largest part of the blade surface, this explains the good agreement between lvl_1 and lvl_2 regarding the integral performance parameters, as discussed previously.

5.4.3*d* Cavitation Patterns

In this section, the cavitation predictions for case *2.3.2b* are investigated in more detail. Here, only the difference between the different grids is assessed. Refer to the next section for a validation of the computations with experimental references.

Figure 5.22 shows the evolution of integral vapor volume within the entire computational domain, $V_\alpha = \int_{\tilde{\Omega}} \alpha \, \mathrm{d}V$ for the three grid levels. Additionally, the mean amount of integral vapor volume $\overline{V}_\alpha$, together with the standard deviation $\sigma(\overline{V}_\alpha)$ is provided. Furthermore, mean and instantaneous vapor structures in the vicinity of the propeller are shown in figures 5.23 and 5.24, by means of $\overline{\alpha} = 0.1$ and $\alpha = 0.1$, respectively. Again, a view on the suction and pressure side is provided for each grid level.

From these investigations, similar conclusions as already presented above can be drawn. The integral amount of vapor for grid lvl_0 is higher than for the two finer meshes, while the latter two agree satisfactorily well. Comparing the mean cavity patterns shown in figure 5.23, the spatial extent of cavitation is largest on the coarsest grid. The tip vortex cavitates stronger, due to higher flow velocities

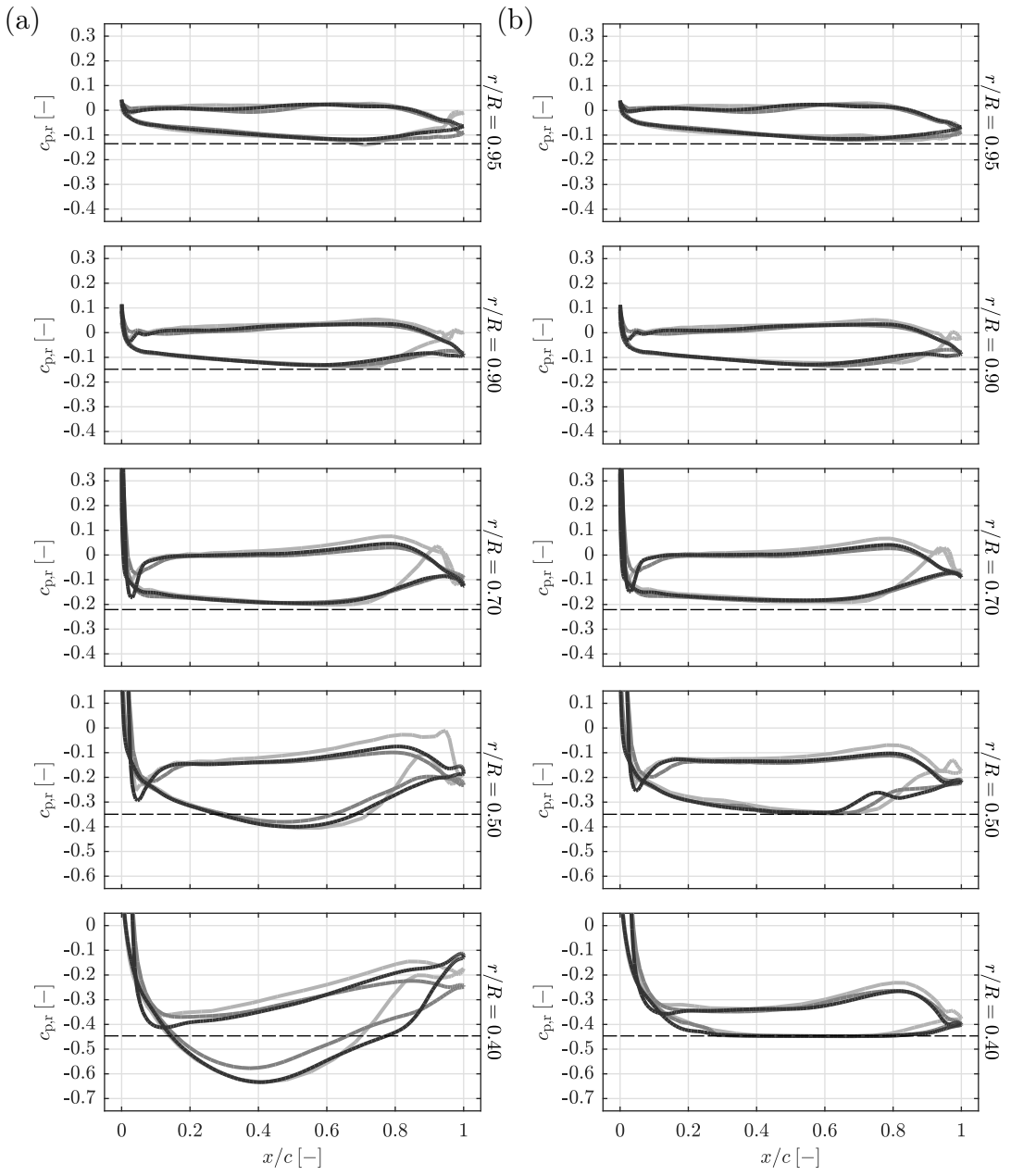

Figure 5.21: Surface pressure coefficient $c_{p,r}$ on five discrete radii $r/R = (0.4, 0.5, 0.7, 0.9, 0.95)$ predicted by ILES for the design point *2.3.2* (lvl_0 —, lvl_1 —, and lvl_2 —), under (a) non-cavitating, and (b) cavitating conditions.

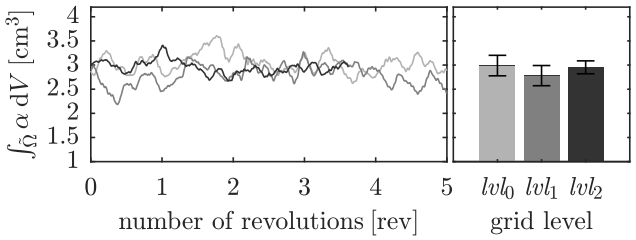

Figure 5.22: Integral vapor volume within the entire computational domain V_α for the design point *2.3.2b*, as predicted by ILES (lvl_0 —, lvl_1 —, and lvl_2 —). Juxtaposition of the time-signals, and bar plots showing time-averages and the standard deviation of the signals.

reached near the blade tip. This relates to the downstream-directed flow in the rear part of the blade tip, see again the limiting stream-lines in figure 5.16. Furthermore, the pressure side cavitation is slightly thicker, and the suction side cavitation reaches to larger radii. On the other hand, the mean extent of cavitation on lvl_1 and lvl_2 agree well. A small difference can be found for the pressure side cavitation. For lvl_2 results, the iso-surface of $\overline{\alpha} = 0.1$ extends until the trailing edge. This is caused by vapor structures intermittently detaching from the leading edge portion, and traveling towards the trailing edge, which is not resolved with mesh lvl_1.

In general, comparing the instantaneous results in figure 5.24, the finest grid allows to resolve much smaller vapor structures compared to lvl_0 and lvl_1, as expected. Without having a noticeable effect on the integral amount of vapor, these detach regularly from the main cavity regions on the suction and pressure side and advect downstream. Additionally, the finest grid lvl_2 resolves shedding cavity structures within the blade wake along most part of the trailing edge.

5.4.3*e* Summary

Owing to the large computational effort caused primarily by the required long integration times, the near-wall region is still under-resolved, even with the finest grid level. Without the application of a wall-model, no grid convergence can be expected. However, above investigations show that the influence of the spatial resolution between grids lvl_1 and lvl_2 are small. When the flow is dominated by the occurrence of cavitation, the agreement between the grids on one hand, and with the available references on the other, is slightly improved, compared to wetted flow conditions. This is caused by the fact that viscous effects play only a sub-ordinate role under cavitating conditions.

On the coarsest grid, although no turbulence is resolved, the tangentially-oriented streamlines resemble the topology of turbulent flow. Except for the propeller efficiency, this coincides with a better agreement of integral performance parameters

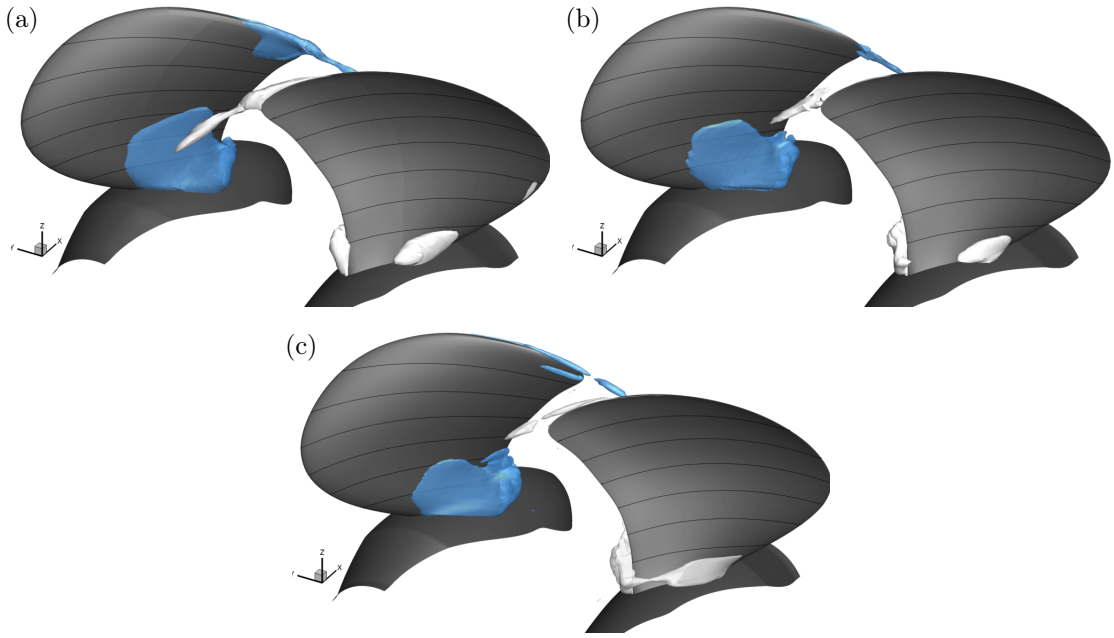

Figure 5.23: Time-averaged vapor structures shown by iso-surfaces of $\overline{\alpha} = 0.1$ for the design point *2.3.2b*, as predicted by ILES with (a) lvl_0, (b) lvl_1, and (c) lvl_2 grids.

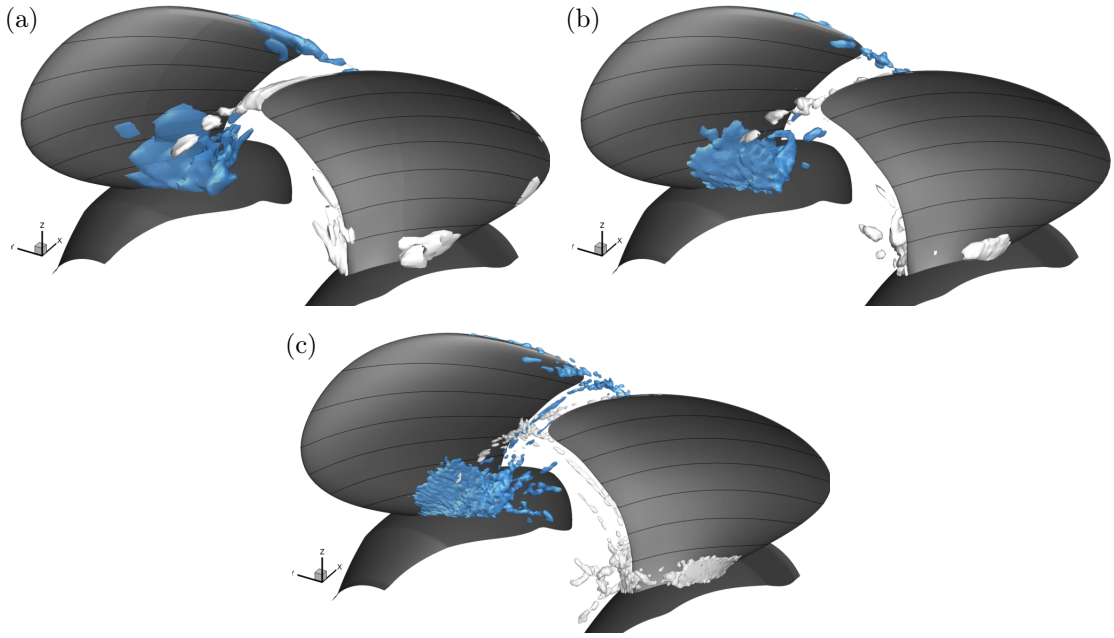

Figure 5.24: Instantaneous vapor structures shown by iso-surfaces of $\alpha = 0.1$ for the design point *2.3.2b*, as predicted by ILES with (a) lvl_0, (b) lvl_1, and (c) lvl_2 grids.

K_T and K_Q with the references, compared to the two finer grids. However, grid lvl_0 is too coarse to resolve fine-scale cavitating structures, which requires a higher spatial resolution. On both finer grid levels, a good agreement is achieved between the predicted flow topology for all investigated aspects. Yet, the flow exhibits characteristics of a laminar flow topology on the suction side, except for the region $r/R \gtrsim 0.8$.

To remedy this, several rectifications are conceivable. First, free-stream turbulence could be introduced in the upstream flow. If injected at the inflow plane, however, it will be dissipated before reaching the blade due to long upstream section, and the employed coarse grid. Preferably, turbulent forcing should thus be introduced on a plane just upstream of the propeller. Still, the characteristics and level of the free-stream turbulence in the cavitation tunnel is unknown. Moreover, if artificial turbulence is added immediately upstream of the propeller, it has to be ensured that it transitions to a physical state when reaching the blade. Alternatively, it is possible to artificially trip the boundary layer along leading edge. However, also the distribution of laminar/turbulent regions on the blade in the experiment is unknown, and the tripping has to be carefully designed. A fully turbulent suction side would be inappropriate as well, as laminar regions on the suction side certainly exist due to the moderate Reynolds numbers for this model propeller.

Due to these open issues, and because this study primarily aims at reaching comparability to the largest possible extent between the numerical setup for the baseline and ILES scheme, it is refrained from introducing one of the above measures. Furthermore, it is assumed that a much finer spatial resolution is necessary to correctly reproduce the transitional behavior of the blade boundary layer.

From this in-depth analysis of the flow, it is concluded that some uncertainties exist whether the characteristics of the boundary layer are correctly captured for the entire propeller surface. It is hypothesized that this affects only the blade suction side, since the pressure side on model propellers is generally less intricate, and more likely to exhibit a laminar boundary layer (Kuiper, 1981). Moreover, as demonstrated with cases *2.1* and *2.2*, the integral parameters are in satisfactory agreement with the available references. Likewise, predictions of lvl_1 and lvl_2 grids are in good accordance with each other. All subsequent investigations are hence carried out for grid lvl_2, only.

5.4.4 Cases *2.3.x* – Comparative Analysis of Cavitating Propeller Flow

In the following, the cavitating propeller flow for the three operating points *2.3.1b*, *2.3.2b*, and *2.3.3b* is analyzed. Case *2.3.2b* corresponds to the nominal design point of the propeller with $J = 1.269$, while cases *2.3.1b* and *2.3.3b* denote two off-design points at a lower ($J = 1.019$) and higher ($J = 1.408$) advance coefficient, respectively. Note also that the cavitation number differs for the three cases. With $\sigma_n \approx 2$ it is comparable for both off-design points, while for case *2.3.2b* a lower value $\sigma_n = 1.4$ is specified by the PPTC. For the simulations, the cavitation tunnel arrangement is utilized, in agreement to the experimental setup. Results obtained with the baseline and ILES scheme are compared to experiments by Heinke (2011a), and numerical studies by PPTC participants (Heinke, 2011b) For obtaining time-averaged results, the simulations are sampled for at least three revolutions of the propeller. The sampling periods are indicated in table 5.6.

5.4.4*a* Time-averaged flow topology

Limiting Streamlines Juxtaposing baseline and ILES predictions, the mean flow on the propeller surface for all three operating points is visualized in figure 5.25 by limiting streamlines. In addition, the extent of cavitation on the surface is shown by contours of the mean void fraction $\overline{\alpha} \geq 0.1$.

Comparing the cavity predictions of both numerical methods, the location of cavitation on the blade surface is identical. While a more detailed discussion of the cavitation patterns is provided further below, it is already observed that the amount of blade surface covered by cavitation is slightly larger for the baseline scheme. This is caused by higher fluid velocities in the near-wall region, due to the slip boundary condition and the absence of a viscous boundary layer, resulting in a lower surface pressure.

Turning to the surface flow pattern, the higher level of near-wall momentum predicted by the baseline scheme causes the flow to remain attached for the majority of the blade surface. An exception is a small region downstream of the suction side root cavity for all considered cases.

In general, the flow is directed along constant radii for the baseline scheme, and thus resembles the pattern of a fully turbulent flow. This has to be expected, as the employed inviscid flow model can be regarded as corresponding to the limit of infinite Reynolds numbers. In contrast, the flow predicted by the ILES scheme is, for the most part of the blade, directed towards the blade tip, and

Table 5.6: Time-span used for statistical sampling of baseline and ILES computations of cases *2.3.1b*, *2.3.2b*, and *2.3.3b*.

	scheme	*2.3.1b*	*2.3.2b*	*2.3.3b*
$\Delta T_{\text{sampling}}$ [rev]	baseline	4.8	6.1	6.0
	ILES	3.0	4.3	3.6

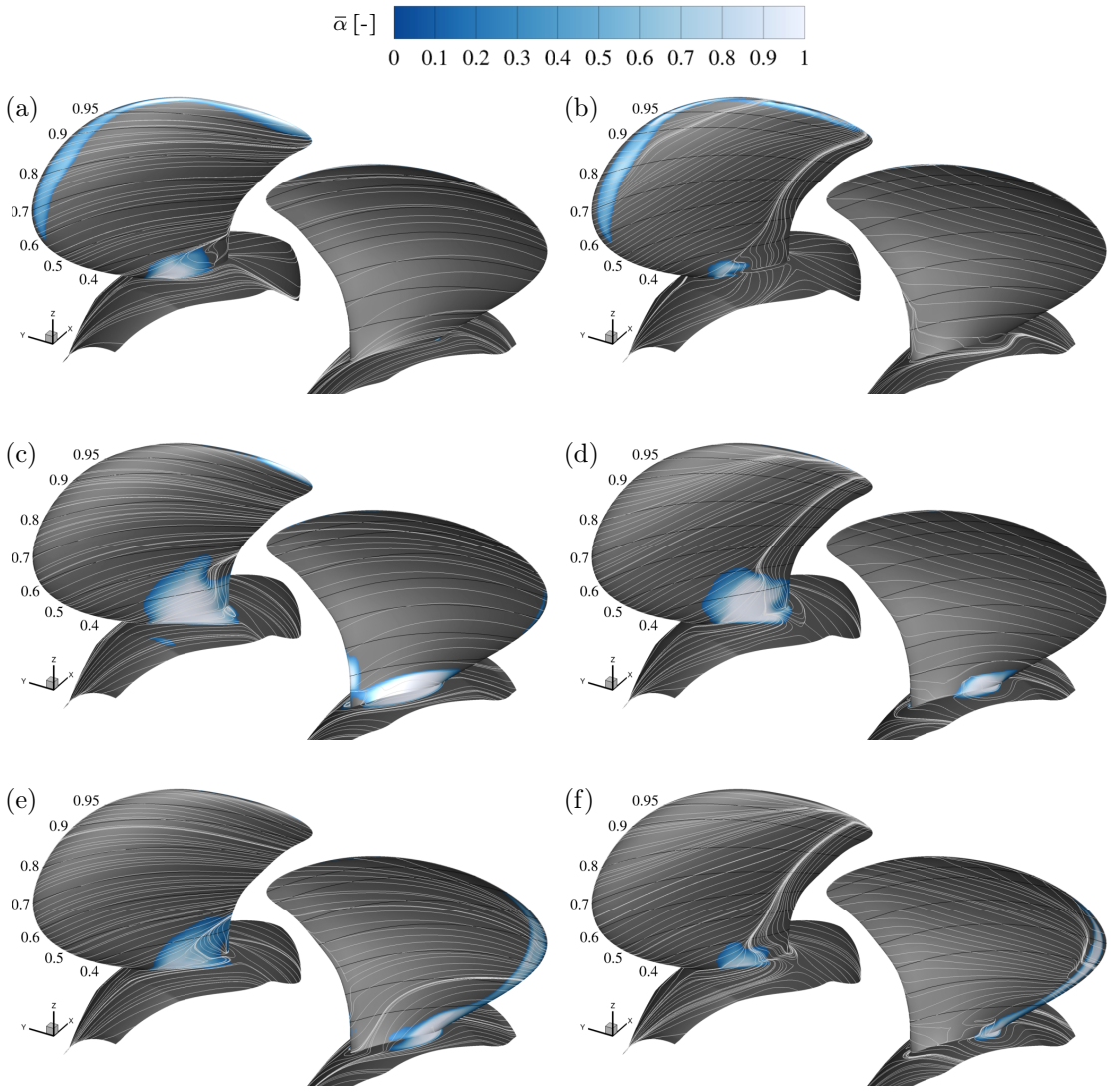

Figure 5.25: Limiting streamlines on blade and hub for cases (a,b) *2.3.1b*, (c,d) *2.3.2b*, and (e,f) *2.3.3b*. Juxtaposition of baseline (left column) and ILES (right column) results.

thus exhibits the characteristics of laminar flow. Already discussed previously for the design point, figure 5.25 shows that this is also the case for both off-design points. Correspondingly, a region of laminar separation is located along the trailing edge for the three cases, which is not found for the baseline result. For all three cases, tangentially-oriented streamlines, thereby corresponding to a turbulent flow topology, exist only near the blade tip. Originating from the leading edge at $r/R \gtrsim 0.8$, the extent of this region increases with increasing advance coefficient, i.e., Reynolds-number, thus qualitatively capturing the trend observed on model propellers.

Propeller Slip-Stream Figure 5.26 provides a visualization of the slip-stream predicted with the baseline and the ILES scheme for the three operating points. Analogously to figure 5.17, the slip-stream is shown by contours of the non-dimensional axial excess velocity $\overline{u}_{\mathrm{ax}}/V_{\mathrm{a}} - 1$ in the slice $y = 0$, while mean vortical and mean vapor structures are given by iso-surfaces of $\overline{\lambda}_2 = -1 \times 10^5\ 1/\mathrm{s}^2$, colored by axial vorticity $\overline{\omega}_x$, and $\overline{\alpha} = 0.1$, respectively.

Comparing baseline and ILES scheme, the slip-stream for three operating points is in good correspondence. For all operating points, a trailing tip vortex structure is obtained, which is strongest for case *2.3.1b*, and becomes weaker when going to larger advance coefficients with cases *2.3.2b* and *2.3.3b*. Still, differences between the two different discretization schemes can be seen at this qualitative level. The mean flow acceleration is consistently higher for the baseline method across all three operating points. Correspondingly, the contraction of the stream tube passing through the propeller disc is slightly stronger. This is associated with a larger thrust predicted with the method, as expected from neglecting physical viscosity. Compared to the ILES result, the trailing vortex de-correlates faster within the wake, caused by the larger numerical dissipation of the baseline scheme. This is in line with observations from case *2.2*, where the predicted strength of the tip vortex is larger with the ILES. Concentrating a higher level of vorticity in the vortex core, it also extends further into the propeller wake field, as shown by figure 5.26. Consequently, the cavitating portion of the tip vortices observed for cases *2.3.1b* and *2.3.2b* reaches further behind the blade for the ILES scheme. For case *2.3.3b*, in agreement, the two methods yield a non-cavitating trailing tip vortex core in the temporal mean.

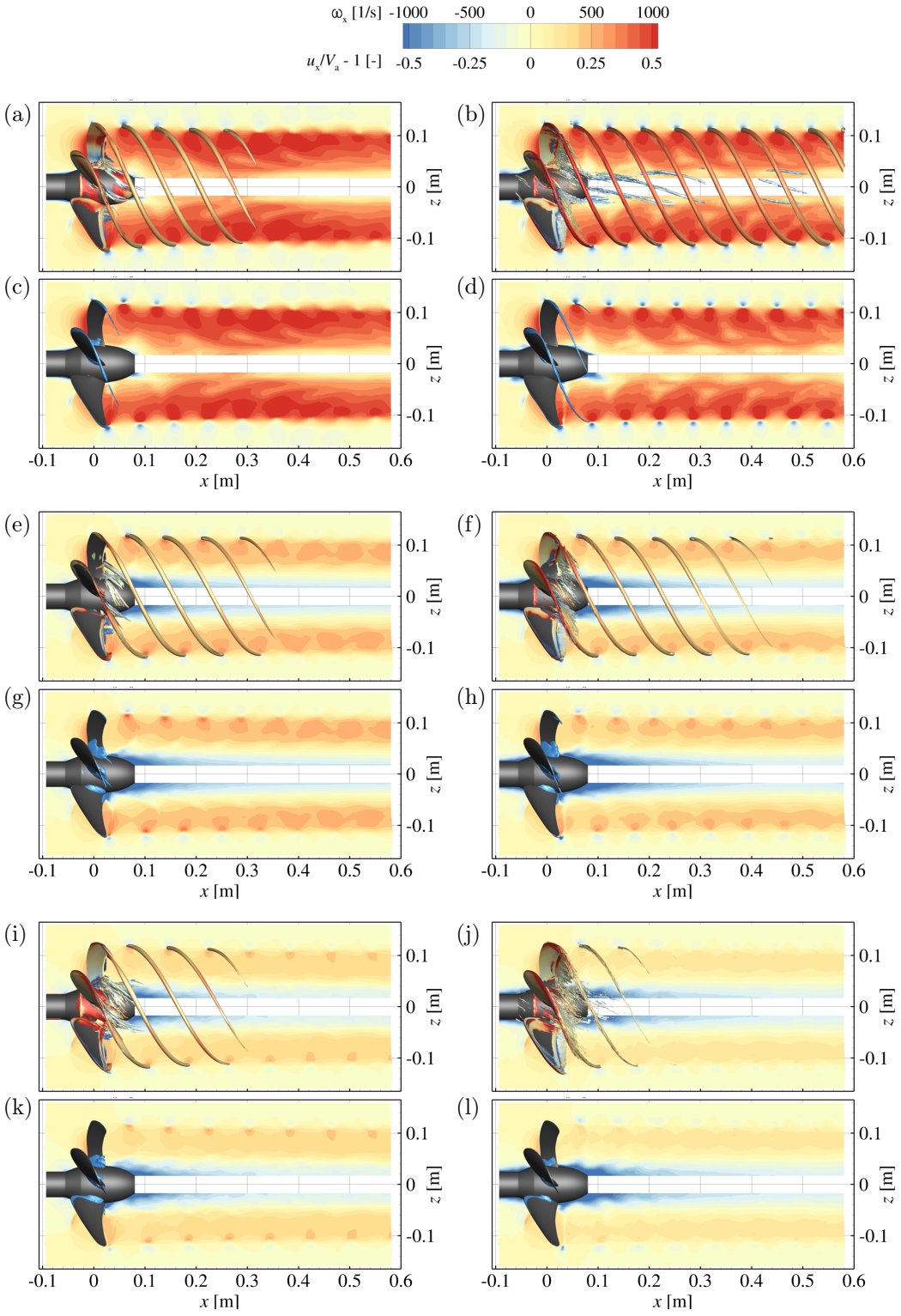

Figure 5.26: Time-averaged propeller slip-stream, showing contours of non-dimensional axial velocity $\overline{u}_{\mathrm{ax}}/V_{\mathrm{a}} - 1$ on the slice $y = 0$, and vortical structures by iso-surfaces of $\overline{\lambda}_2 = -1 \times 10^5\ 1/\mathrm{s}^2$, colored by axial vorticity $\overline{\omega}_x$, or vapor structures by iso-surfaces of $\overline{\alpha} = 0.1$ for cases (a-d) *2.3.1b*, (e-h) *2.3.2b*, and (i-l) *2.3.3b*. Juxtaposition of results obtained with the baseline (left column) and ILES scheme (right row), respectively.

5.4.4*b* Propeller Performance

Cavitation leads to a reduction of the thrust delivered by the propeller. Figure 5.27 compares the predictions of the thrust coefficient K_T from the present study with PPTC references for the three considered operating points. Time-averaged results are indicated by circles for the baseline scheme, while diamonds denote the ILES. Experimental measurements by Heinke (2011a) are indicated by solid lines, while numerical studies contributed to the PPTC (Heinke, 2011b) are given as crosses. Depending on the operating point, this includes a varying number of simulations from different institutions, as documented by table 5.7.

As anticipated in the slip-stream visualizations above, the thrust predictions of the baseline method are higher compared to the experimental references. With deviations from the experiments of +4% for the case *2.3.1b*, in contrast to +30% for case *2.3.3b*, the agreement is deteriorated at higher advance coefficients J, as similarly observed with the study of the open-water performance under non-cavitating conditions in §5.4.1. The ILES improves the prediction quality. With deviations between -2.3% for *2.3.1b*, and -13% for *2.3.3b*, the computed thrust coefficients are consistently lower than the references. The above grid study shows an increase in the thrust with finer grid levels. It can therefore be assumed that this is due to the under-resolved near-wall region while not applying a wall-model, and the associated region of flow separation along the trailing edge resulting from the laminar flow characteristics, as discussed.

For cases *2.3.1b* and *2.3.2b*, the results for the current study fall within the range of accuracy of the numerical PPTC references. For operating point *2.3.3b*, however, the agreement is less good. It is conjectured that, at this operating point with the highest investigated Reynolds-number, the flow is turbulent for the majority of the blade, and that no flow separation is present along the trailing edge. As noted above, this is not properly captured by the ILES, and could thus lead to the increased deviations from the references.

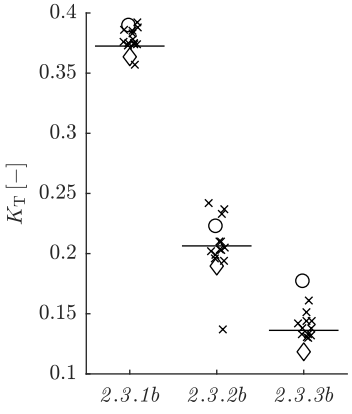

Figure 5.27: Thrust coefficient $K_{\mathrm{T,cav.}}$ for cases *2.3.1b*, *2.3.2b*, and *2.3.3b*. Juxtaposition of baseline (∘) and ILES (⋄) computations with PPTC references. Numerical references from table 5.7 (×), and experimental references (—, from Heinke, 2011a).

Table 5.7: Numerical references from PPTC workshop for performance validation, see Heinke (2011b).

	2.3.1	*2.3.2*	*2.3.3*
potential methods	INSEAN-PFC, UniGenua-Panel	INSEAN-PFC, UniGenua-Panel	INSEAN-PFC, UniGenua-Panel
viscous methods	Berg-Procal, Cradle-SC/Tetra, CSSRC-Fluent, SSPA-Fluent, TUHH-Fresco+, UniGenua-StarCCM(kw), UniTriest-CFX-FCM, UniTriest-CFX-Kunz, UniTriest-CFX-Zwart, VOITH-Comet, VTT-FinFlo	Cradle-SC/Tetra, CSSRC-Fluent, SSPA-Fluent, TUHH-Fresco+ (large coeff.), TUHH-Fresco+ (small coeff.), UniGenua-StarCCM(kw), UniTriest-CFX-FCM, UniTriest-CFX-Kunz, UniTriest-CFX-Zwart, VOITH-Comet, VTT-FinFlo	Cradle-SC/Tetra, CSSRC-Fluent, SSPA-Fluent, TUHH-Fresco+, UniGenua-StarCCM(kw), UniTriest-CFX-FCM, UniTriest-CFX-Kunz, UniTriest-CFX-Zwart, VOITH-Comet, VTT-FinFlo

5.4.4*c* Blade Pressure Coefficient

Contours of the non-dimensional pressure coefficient c_p on the blade and hub surfaces are given by figure 5.28, juxtaposing baseline and ILES results for the three operation points. Again, the contour is clipped at the vapor pressure, $c_\mathrm{p} = -\sigma_\mathrm{n}$. Already at this qualitative level, it can be observed that the baseline scheme yields a lower pressure on the suction side. This is associated with a larger extent of the region $c_\mathrm{p} \leq -\sigma_\mathrm{n}$. Caused by the higher near-wall velocities compared to the ILES result, this is due to the employed slip boundary condition and absence of a boundary layer. Furthermore, the baseline scheme yields a strong pressure recovery along the trailing edge, which is not found in with the ILES. This again is due to the fact that the flow remains attached in the baseline computations, while it separates in the ILES, as seen above.

For a validation of the surface pressure distribution, no experimental data is available. However, submissions to the PPTC workshop, see Heinke (2011b), enable a comparison with other numerical investigations of *VP1304*. Table 5.8 provides a summary of all numerical references considered in the following.

Note that in the context of the PPTC, as mentioned in §5.3.3, participants were required to perform all analysis at *thrust identity* under wetted conditions. This is achieved by altering the advance coefficient J via the inflow velocity, and thereby changing the local angle of attack. The effective deviations from the nominal

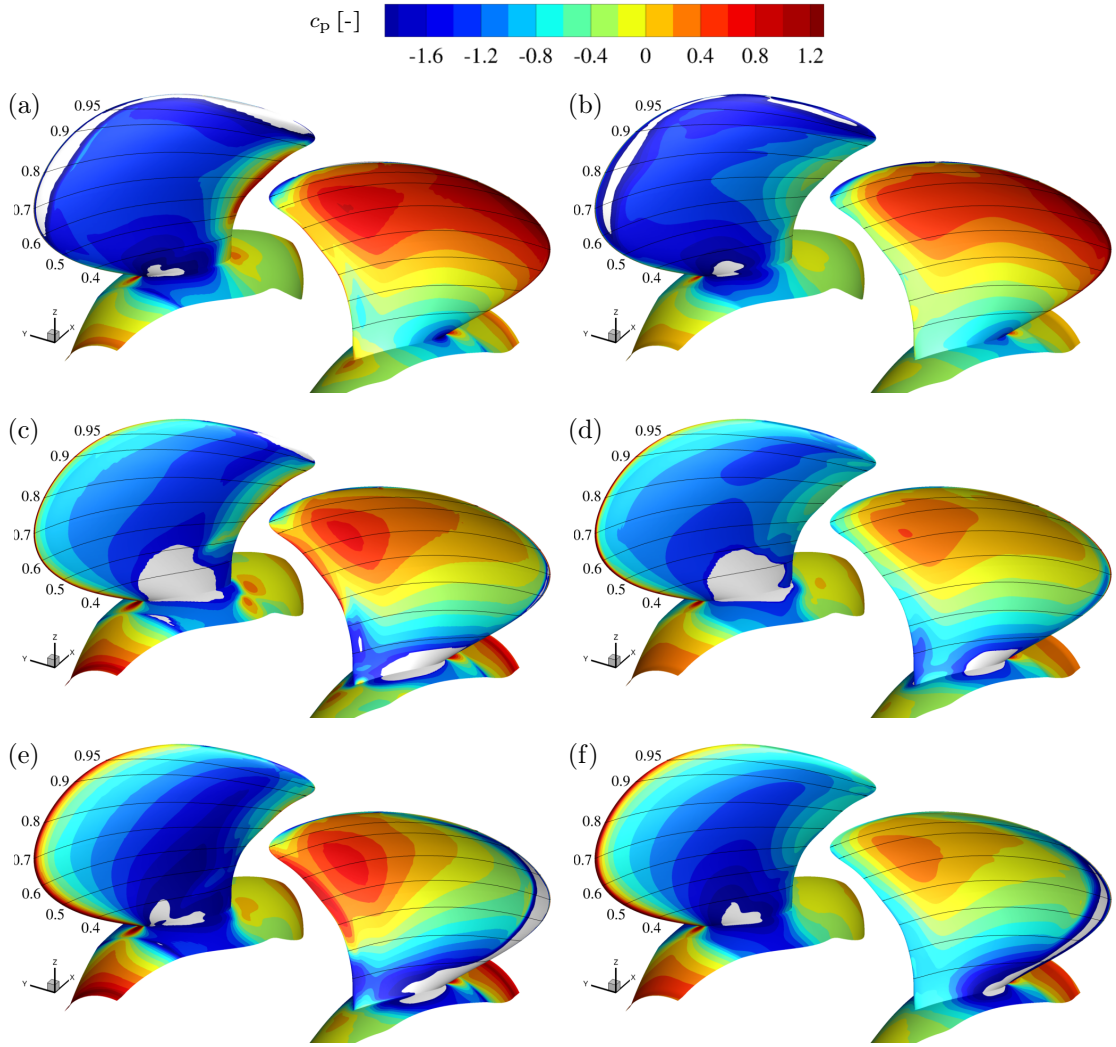

Figure 5.28: Mean surface pressure coefficient $c_p \geq -\sigma_n$ on blade and hub for cases (a,b) *2.3.1b*, (c,d) *2.3.2b*, and (e,f) *2.3.3b*. Juxtaposition of baseline (left column) and ILES (right column) results.

operating points is not documented for the submitted computations, such that the individual influence of this adjustment cannot properly be assessed. As discussed initially, simulations for the present study are conducted at *J-identity*, in contrast to the PPTC specifications, in order to avoid different inflow boundary conditions, and to reach better comparability between baseline and ILES results.

PPTC participants were required to submit the non-dimensional surface pressure coefficient $c_{p,r}$ on three radii $r/R = (0.7, 0.9, 0.95)$. This analysis, summarized figure 5.29, is repeated here, including baseline, ILES, and the numerical reference data. The level of the vapor pressure is indicated by dashed lines.

Across all investigated operating points and radii, the evolution of $c_{p,r}$ for both conducted simulations is comparable along mid-chord on either side of the blade. The magnitude of the suction and pressure peak at mid-chord is stronger in the baseline computations, consistent with the stronger flow acceleration, higher near-wall velocity due to the absence of a boundary layer, and thus higher level of thrust compared to the ILES, as discussed before. The deviation between the two conducted simulations is more pronounced towards the trailing edge. Here, the baseline result shows a better agreement with the numerical references. As discussed above, this corresponds to the region where the ILES yields an area of flow separation. The majority of PPTC contributions, however, is based on RANS approaches and employs a turbulence model. It is thus conjectured that most of the reference computations yield turbulent flow over the entire blade, and do not predict flow separation along the trailing edge. This flow topology is in closer agreement to the baseline result, and thus explains the better match of the baseline pressure distribution with the numerical references, compared to the ILES.

Comparing the three operating points, the best agreement is observed at the design point. Deviations for the off-design point *2.3.1b* are primarily located near the suction side leading edge, where most numerical references predict a larger area of attached sheet cavitation. As shown in the following section this is not observed experimentally by SVA, and the present study thus matches better

Table 5.8: Numerical references from PPTC workshop for surface pressure, see Heinke (2011b).

	2.3.1	*2.3.2*	*2.3.3*
potential methods	INSEAN-PFC, UniGenua-Panel	UniGenua-Panel	UniGenua-Panel
viscous methods	Berg-OpenFOAM, Cradle-SC/Tetra, SSPA-Fluent, TUHH-Fresco+, UniGenua-StarCCM(kw), UniTriest-CFX-FCM, UniTriest-CFX-Kunz, UniTriest-CFX-Zwart, VOITH-Comet, VTT-FinFlo	Berg-OpenFOAM, Cradle-SC/Tetra, SSPA-Fluent, TUHH-Fresco+ (large coeff.), TUHH-Fresco+ (small coeff.), UniGenua-StarCCM(kw), UniTriest-CFX-FCM, UniTriest-CFX-Kunz, UniTriest-CFX-Zwart, VOITH-Comet, VTT-FinFlo	Berg-OpenFOAM, Cradle-SC/Tetra, CSSRC-Fluent, SSPA-Fluent, TUHH-Fresco+, UniGenua-StarCCM(kw), UniTriest-CFX-FCM, UniTriest-CFX-Kunz, UniTriest-CFX-Zwart, VOITH-Comet, VTT-FinFlo

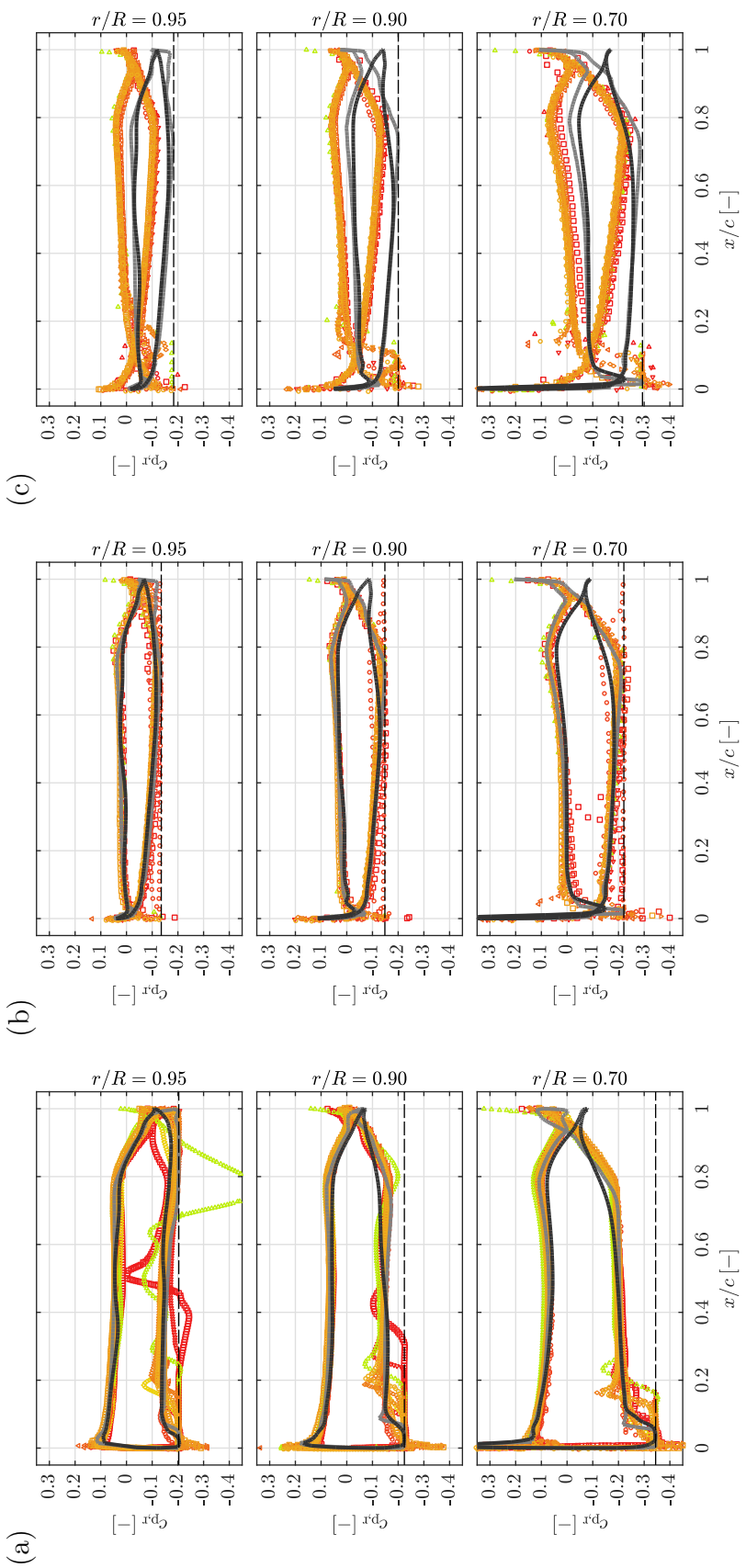

Figure 5.29: Surface pressure coefficient $c_{p,r}$ on three discrete radii $r/R = (0.7, 0.9, 0.95)$ predicted by baseline scheme (—) and ILES (—) for cases (a) *2.3.1b*, (b) *2.3.2b*, and (c) *2.3.3b*. Level of vapor pressure indicated by dashed line (– –). Comparison with numerical reference data of PPTC participants, see Heinke (2011b).

with the experimental references. The agreement with the numerical references for case *2.3.3b* is clearly deteriorated, relating to the discrepancies previously observed for the predicted thrust. It is believed that two factors play a role for this disagreement. First, *2.3.3b* corresponds to the situation with the highest Reynolds-number, and is thus the most challenging case. It is conjectured that the surface flow topology predicted with the ILES shows an increased discrepancy with the experimental references. However, also the baseline scheme exhibits a difference to the numerical references included in figure 5.29. The second hypothesis is that the deviations results from different boundary conditions between the current computations and the numerical references. As discussed above, J-identity with the experiments is utilized here, while PPTC contributors performed computations at K_T-identity under wetted flow conditions. Unfortunately, no documentation of the corrections in the numerical references is available, such that this influence can not be quantified properly.

5.4.4*d* Cavitation Patterns

Figure 5.30 shows a sketch of the experimentally detected cavitation pattern on the propeller suction side, taken from Heinke (2011b). For operation point *2.3.1b* with $\sigma_\mathrm{n} = 2$, suction side cavitation is observed along the blade tip at $r/R > 0.9$. A strong tip vortex develops, which exhibits pronounced vortex cavitation, reaching far behind the blade. Additionally, root cavitation occurs near the hub on the suction side, while no cavitation is remarked for the pressure side. At the design point *2.3.2b*, with a lower cavitation number of $\sigma_\mathrm{n} = 1.4$, pronounced root cavitation and shedding of a frothy wake is noted for $r/R < 0.45$ on the suction side. The propeller furthermore shows cavitation near the blade tip, and the trailing tip vortex exhibits a cavitating core, albeit to a weaker extent compared to *2.3.1b*. Finally, intermittent foam cavitation occurs after the mid-chord along almost the complete height of the blade on the suction side. From still images, refer to Heinke (2011b), and videos provided by SVA, root cavitation is also present on the blade pressure side. At the highest investigated advance coefficient, case *2.3.3b* with $\sigma_\mathrm{n} = 2$, sheet cavitation is seen on the pressure side along the leading edge for $0.4 \leq r/R \leq 0.95$. At the blade tip, the sheet cavity transitions to bubble cavitation at $r/R > 0.95$. These bubbles are subsequently trapped within the core of the weak trailing tip vortex. As seen from still images (Heinke, 2011b), the obtained vortex cavitation is very weak. Moreover, root cavitation is observed on either side of the blade. It remains below $r/R < 0.3$ on the pressure side. On the suction side, it ranges from the hub to a radius of $r/R < 0.4$, which can again be seen from still images (Heinke, 2011b) and SVA videos.

A visual comparison of the predicted cavitation patterns for the investigated operating points is presented in figure 5.31. Providing a view on the blade suction and pressure side, iso-surfaces of the void fraction $\alpha = 0.1$ visualize instantaneous cavity structures. Results for the baseline and ILES computations are juxtaposed in figures 5.31*a,c,e* and 5.31*b,d,f* for cases *2.3.1b*, *2.3.2b*, and *2.3.3b*, respectively. When employing a homogeneous mixture model, it is an open question which value of the vapor volume fraction corresponds best to a visual observation of cavity structures in experiments. Here, the level of 10% for the visualization is representatively chosen. For evaluating the influence of the void fraction level on the predicted cavity extent, the visualizations are repeated in the appendix for void fractions $\alpha = (0.2, 0.5, 0.8)$, in line with PPTC requirements. Refer to the appendix figures A.3, A.4, and A.5 for the three operating points, respectively.

The predicted locations of vapor structures are in good agreement for both numerical approaches, and also compare well to the experimental observation. While the best agreement with the experiment is achieved at *2.3.2b*, some deviations are noticed for both off-design points. For case *2.3.1b*, by means of iso-surfaces $\alpha \lesssim 0.2$, cavitation is predicted also on the suction side along the leading edge, which is not obtained in the experiments. As mentioned already, this is, however, also predicted by the majority of the PPTC participants (10 out of 14). It is an open question, whether this might indicate a systematic error in the employed models, including the current approach. As shown with the surface pressure in figure 5.29, other numerical methods often predict an even larger extent for the suction side sheet cavity. For case *2.3.3b*, despite showing some cavitation near the blade tip, a cavitating trailing tip vortex is not captured by the baseline scheme. Also the ILES shows only small vapor structures at the blade tip, and, in vicinity of the blade, within the trailing vortex core. This is again to some extent in alignment with the numerical references, where none of the participants predict tip vortex cavitation. Yet, it is in contrast with the experimental sketch in figure 5.30*c*. Still images from Heinke (2011b) also show only faint traces of tip vortex cavitation. It is thus conjectured that the pressure drop within the vortex core is just sufficient to merely support the existence of trapped vapor bubbles. This is a very demanding situation regarding the required spatial resolution, although the ILES at least qualitatively captures this trend.

As already discussed above and in the context of case *2.2*, the ILES yields a better reproduction of the trailing tip vortex structure, due to the higher order of spatial discretization and less numerical dissipation, compared to the baseline scheme. Correspondingly, the associated pressure drop within the vortex core is stronger, resulting in a more pronounced cavitating core. Predicting tip vortex cavitation is a challenging problem when employing an Eulerian description of the fluid. For the case *2.3.1b* with the strongest cavitating tip vortex, only 3 out of 14 PPTC

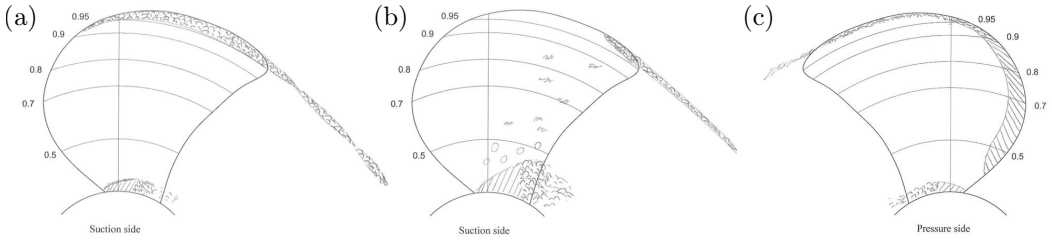

Figure 5.30: Experimental observation of cavitation for cases (a) *2.3.1b*, (b) *2.3.2b* and (c) *2.3.3b*, from Heinke (2011b).

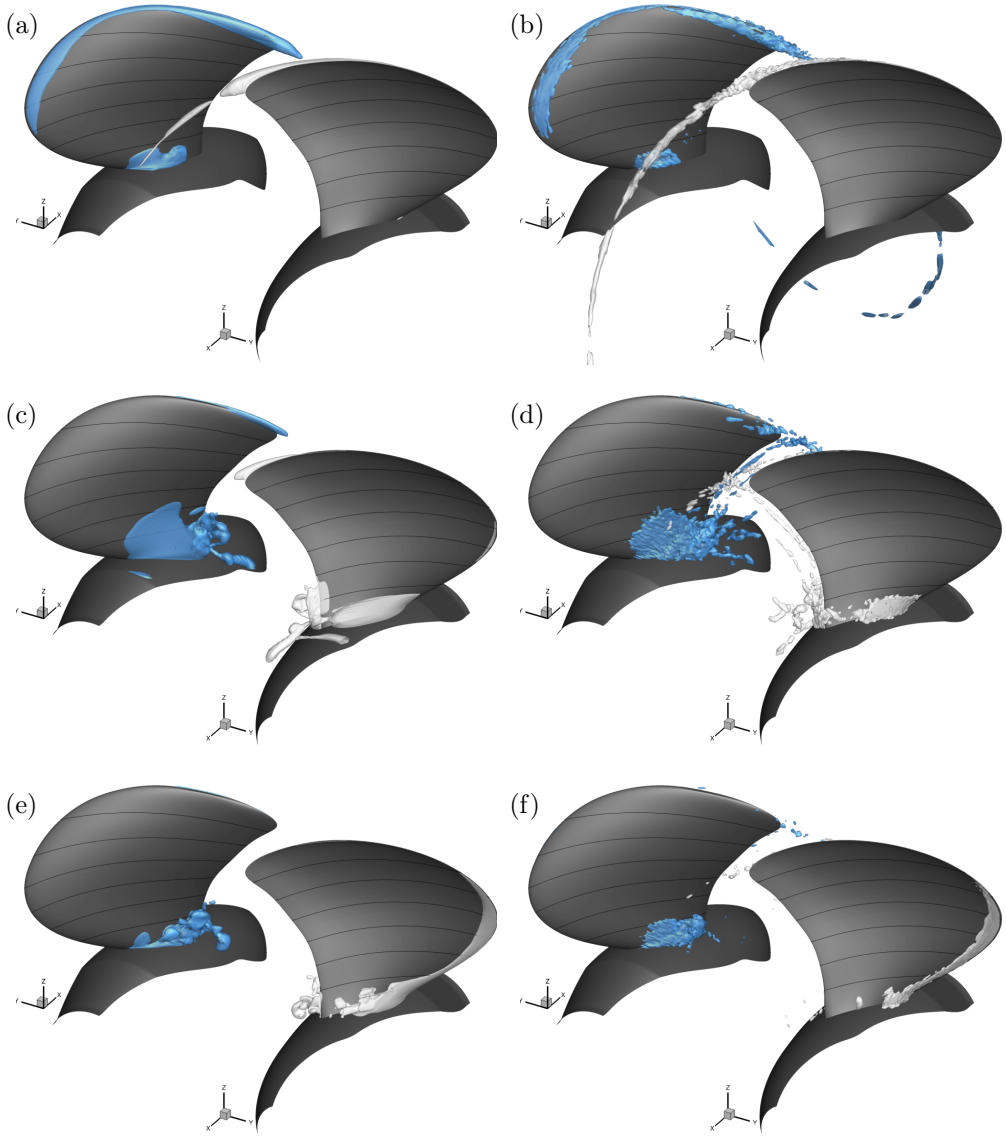

Figure 5.31: Instantaneous cavity structures by iso-surfaces of $\alpha = 0.1$ for cases (a,b) *2.3.1b*, (c,d) *2.3.2b*, and (e,f) *2.3.3b*. Juxtaposition of baseline (left column) and ILES (right column) results.

contributions yield a sustained cavitating core within the trailing portion of the tip vortex, while the majority (9 out 14) show a cavitating blade tip, comparable to the baseline result of the present study.

In general, the ILES exhibits a much higher level of vapor fragmentation. This is associated with smaller, transient cavity structures, which frequently detach from the main cavity and get advected with the flow. Especially the trailing portion of the root cavity is characterized by small-scale cavitating turbulent eddies detaching from the blade, resembling the frothy nature of the flow remarked in the experiment. In contrast, the baseline scheme predicts rather large, contiguous vapor structures. At the blade root, these also detach from the main cavity, albeit at a lower frequency. Moreover, the cavitating tip vortex for cases *2.3.1b* and *2.3.2b* is relatively stable. It only fluctuates in its volume, without disintegrating into smaller vapor pockets as in the ILES computation. Compared to the baseline results, the overall flow unsteadiness is thus higher for the ILES. This is a result of the higher order of the discretization, and the reduced numerical dissipation of the scheme.

Considering the cavity extent, the 10% iso-surface of vapor volume seem to overestimate the amount of cavitation. Analyzing figures A.3, A.4, and A.5, both simulations agree best for a value between 50% (cases *2.3.1b* and *2.3.2b*) and 20% (case *2.3.3b*). This is in alignment with PPTC findings, where similar conclusions are drawn (50% for *2.3.1b*, 20% for *2.3.3b* and *2.3.3b*).

5.4.4*e* Flow Aggressiveness

In the following, utilizing the methods introduced in §3.3, the flow aggressiveness is analyzed both qualitatively, and quantitatively. A comparative investigation is carried out, covering the three operating points, and juxtaposing baseline and ILES results.

Maximum Surface Pressures Figure 5.32 shows contours of the maximum surface pressure $p_{\max}$, recorded during the analysis intervals indicated in table 5.6, on the blade suction and pressure side for the cases *2.3.1b*, *2.3.2b*, and *2.3.3b*. Levels of $p_{\max} < 1\,\mathrm{MPa}$ are excluded from the visualizations. For both numerical schemes and the three operating points, the global maximum of the surface pressure reached in the computations, $\max(p_{\max})$, are displayed in figure 5.33*a*. Moreover, the bar plots in figure 5.33*b* show the percentages of hub and blade surface $a_{p^{\mathrm{th}}_{\max}}$ covered by a threshold pressure $p^{\mathrm{th}}_{\max}$, with $3\,\mathrm{MPa} \leq p^{\mathrm{th}}_{\max} \leq 8\,\mathrm{MPa}$.

The traces of maximum pressure shown in figure 5.32 relate closely to the cavity unsteadiness observed in figure 5.31. These are associated primarily with the

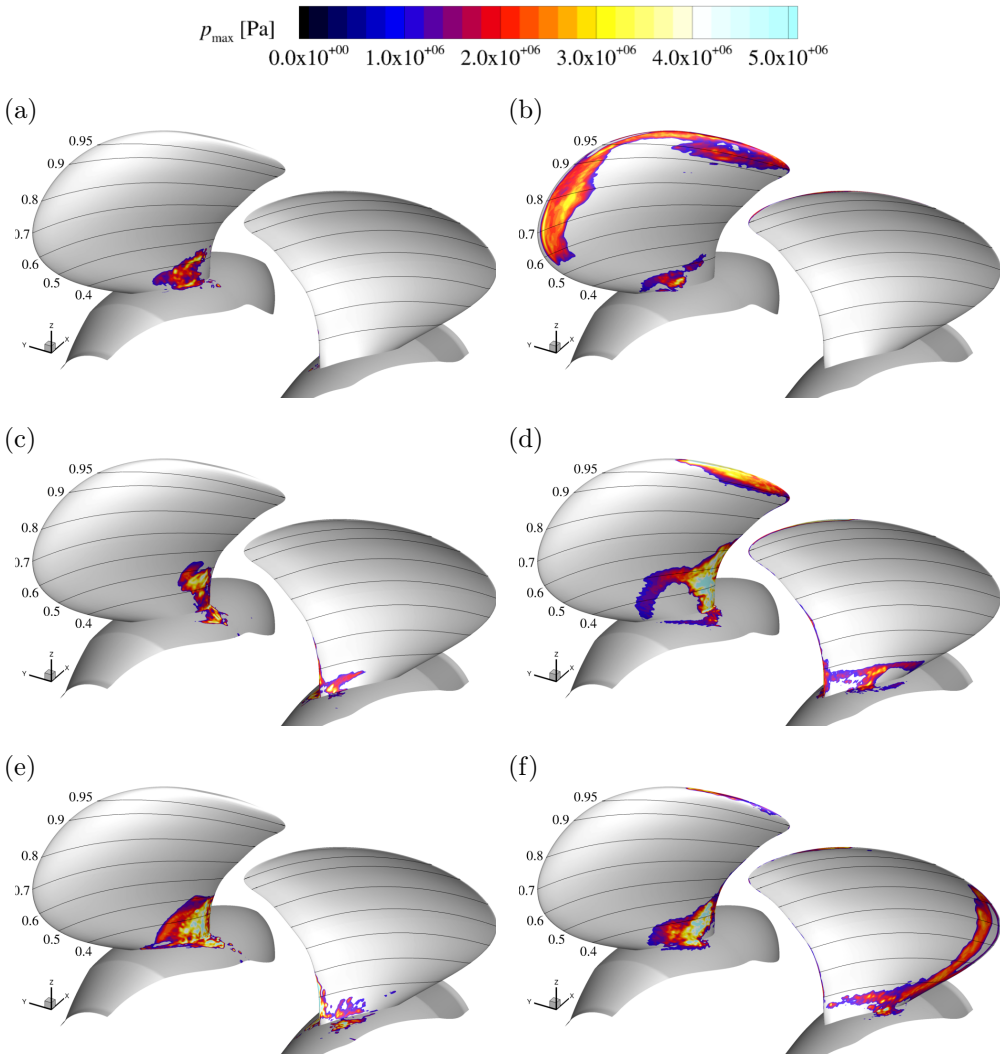

Figure 5.32: Recorded maximum pressures on blade and hub surfaces for cases (a,b) *2.3.1b*, (c,d) *2.3.2b*, and (e,f) *2.3.3b*. Juxtaposition of baseline (left column) and ILES (right column) results, obtained for the entire analysis intervals.

suction and pressure side root cavities, which frequently lead to a shedding of detached vapor structures. For all operating points, the collapse of these cavities occur in the region of pressure recovery downstream the thickness maximum of the blade, and also on the hub surface. Furthermore, the ILES yields elevated pressure levels along the blade tip for cases *2.3.1b*, *2.3.2b*, and to a smaller extent also for case *2.3.3b*. These are due to collapsing fragments of the cavitating tip vortex. As shown above, a cavitating tip vortex is also captured by the baseline method. However, the tip vortex cavity is stable in the baseline computations, without causing a detachment of vapor structures. Similarly, the leading edge cavities on the suction and pressure side for *2.3.1b* and *2.3.3b* are unsteady with the ILES, while the baseline yields a stable sheet cavity. Thus, traces of elevated

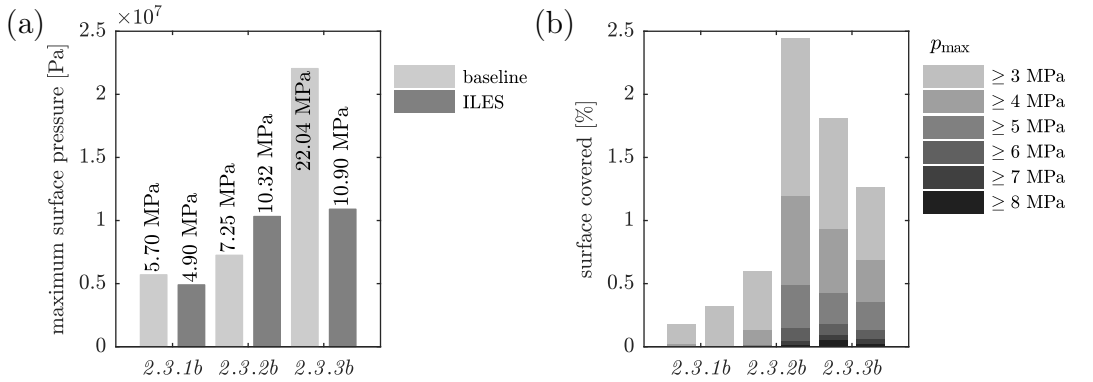

Figure 5.33: Evaluation of maximum surface pressure criterion for cases *2.3.1b*, *2.3.2b*, and *2.3.3b*. (a) global maximum $p_{\max}$, (b) surface coverage $a_{p_{\max}^{\text{th}}}$. Juxtaposition of baseline and ILES results, obtained for the entire analysis intervals.

pressure near the blade tip can only be observed with the ILES. With maximum pressures in these areas of $p_{\max} \approx 3$ MPa these collapses are weaker compared to the region of the root cavity, where the values of $5\,\text{MPa} \lesssim p_{\max} \lesssim 20\,\text{MPa}$ are reached. Qualitatively comparing the three operating points, both schemes indicate that the flow aggressiveness is highest for case *2.3.3b*, followed by *2.3.2b*, and weakest at *2.3.1b*.

This can also be concluded from figure 5.33*a*. Both methods yield the same trend for the global maximum pressure, $\max(p_{\max})(2.3.1b) < \max(p_{\max})(2.3.2b) < \max(p_{\max})(2.3.3b)$. For the baseline method, an identical conclusion can also be drawn from the surface coverage shown in figure 5.33*b*, with $a^{\text{th}}_{p_{\max}}(2.3.1b) < a^{\text{th}}_{p_{\max}}(2.3.2b) < a^{\text{th}}_{p_{\max}}(2.3.3b)$. For the ILES, only pressures $p^{\text{th}}_{\max} \geq 6$ MPa cover a larger amount of the surface. Pressures below this threshold cover more surface area at the design point. This relates to the fact that the root cavity volume at *2.3.2b* is larger, compared to the off-design points, due to a smaller cavity number.

Except for *2.3.2b*, the baseline scheme yields higher maximum pressures compared to the ILES. As noted above, the baseline in general yields larger coherent vapor structures detaching from the main cavities. This leads to stronger collapse events, and thus a higher maximum pressure on the surface.

A weakness of the maximum pressure criterion is, by definition, the emphasis of the strongest event(s), which neither accounts for the stochastic nature of cavitating flow, nor for the fact that the material is actually exposed to a load spectrum, as discussed in §3.3. The significance of the results is thus limited, and it can only provide a first indication of the flow aggressiveness.

Collapse Detection & Classification The collapse detector developed by Mihatsch *et al.* (2015) remedies above drawbacks, provides a more holistic view on the mechanisms leading to above maximum pressures, and enables a statistical evaluation of the flow aggressiveness. As an example, all collapse events detected with baseline and ILES for *2.3.2b* are given in 5.34. Similar visualizations for all operating points are provided in the appendix in figure A.6. Collapses are shown by circles, whose size and color corresponds to the associated collapse pressure p_{collapse}. Events with $p_{\text{collapse}} < 5 \times 10^5$ Pa are blanked from the visualization.

In the baseline computations, collapses are essentially only caused by vapor structures shedding from the root cavity. For the ILES, collapses are also detected (a) downstream of the trailing edge, (b) along the blade tip, and (c) downstream of the blade in the region of the trailing tip vortex. Due to the slip condition, no blade boundary layer is predicted with the baseline scheme. In contrast, the ILES yields a turbulent wake which is shed from the blade, and predicts vortex cavitation in the cores of these eddies. These collapses are very weak, and occur detached from blade surface. Thus, as observed above, no elevated maximum

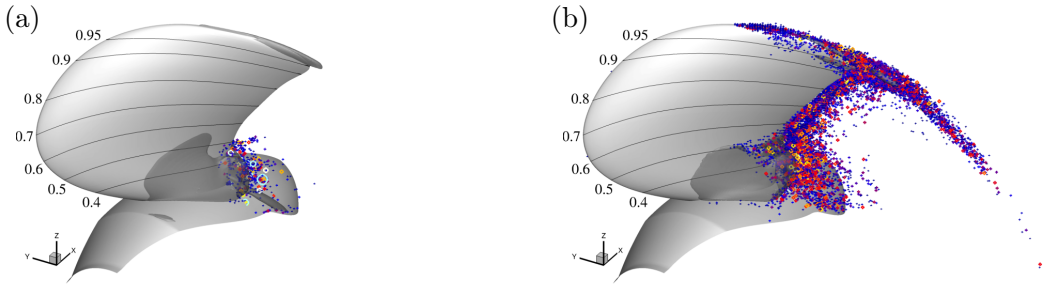

Figure 5.34: All detected collapses with $p_{\text{collapse}} \geq 5 \times 10^5$ for case *2.3.2b*. Juxtaposition of (a) baseline, and (b) ILES results, obtained for equal analysis intervals of ≈ 4 rev (see figure 5.37 for legend).

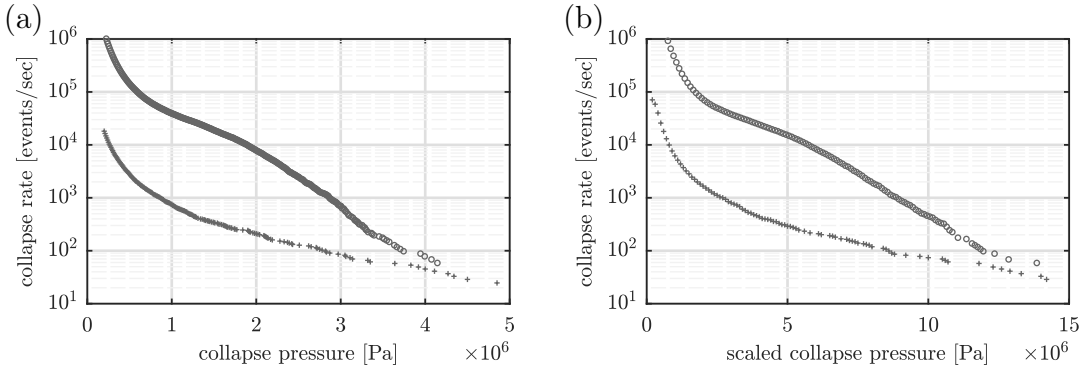

Figure 5.35: Cumulative collapse spectra for case *2.3.2b*, using (a) unscaled pressure p_{collapse}, and (b) scaled pressure $p^{\text{scaled}}_{\text{collapse}}$. Juxtaposition of baseline (+), and ILES (∘) results, obtained for the entire analysis intervals.

pressures are located along the trailing edge. Similarly, the unsteadiness of the tip vortex is not captured by the baseline scheme, thus no collapses occur in this region. Note that the collapses downstream of the blade in the ILES are caused by the fact that the coarser mesh in this region leads to a re-condensation of the cavitating tip vortex core. It is thus a purely numerical phenomenon, as the cavitating tip vortex in the experiments extends far into the propeller wake.

Overall, the ILES hence yields a larger number of collapses, which is related to the higher level of fragmentation into smaller vapor structures. In contrast, as noted above, the baseline method gives larger coherent vapor structures, which cause stronger collapse events, as observable at the root of the trailing edge.

The cumulative load spectra corresponding to the collapses shown in figure 5.34 are provided in figure 5.35. Pressure levels that have been reached less than 10 times are excluded, which applies to the highest collapse pressures. Figure 5.35*a* shows the cumulative rate of collapse events N plotted versus the collapse pressure p_{collapse}. Due to the inhomogeneous spatial resolution, as discussed in §3.3, a more appropriate measure is the scaled collapse pressure $p_{\text{collapse}}^{\text{scaled}}$. The corresponding spectra are given in figure 5.35*b*. In order to obtain a calibration of the scaling parameters d_{ref}, κ, it is necessary to quantify the impact load spectrum experimentally (Mihatsch *et al.*, 2015). To the author's knowledge, this has not been conducted for a cavitating (model) propeller, yet. Since these scalings are mandatory when comparing results from different grid levels, or, as for the current case, for grids with a strong variation of the spatial resolution, the values calibrated by Mihatsch *et al.* (2015) ($d_{\text{ref}} = 181\,\mu$m and $\kappa = 3/2$) are adopted here as well. Consequently, $p_{\text{collapse}}^{\text{scaled}}$ in this context does not provide absolute values for the collapse pressures, that can be compared, e.g., to the material yield strength.

As already observed, the ILES yields much higher collapse rates, especially for intermediate pressures, $p_{\text{collapse}}^{\text{scaled}} \lesssim 10\,\text{MPa}$. The spectra thus confirm the above observation of a larger number of collapse events in the ILES, which is connected to the higher level of fragmentation. For shedding cavities and excluding the lowest pressure at the left side of the spectrum, Mihatsch *et al.* (2015) observe an exponential relation $N \sim a\exp(-bp)$ for the scaled pressure $p_{\text{collapse}}^{\text{scaled}}$, with constant parameters a, b. Despite a small deviation for the ILES at $p_{\text{collapse}}^{\text{scaled}} \approx 5\,\text{MPa}$, a constant slope parameter b is also observed for the current computations. The slopes obtained for baseline and ILES differ, being steeper for the latter. Mihatsch *et al.* (2015) note that b is related to the amount of cavity fragmentation for a given grid level. The pressure scaling, involving a calibrated d_{ref} is utilized by Mihatsch *et al.* (2015) in order to remove this grid dependence. As shown, the fragmentation observed on identical grids is higher for the ILES, due to the higher order of the spatial discretization. This leads to the conclusion that d_{ref} is dependent on the employed numerical scheme as well.

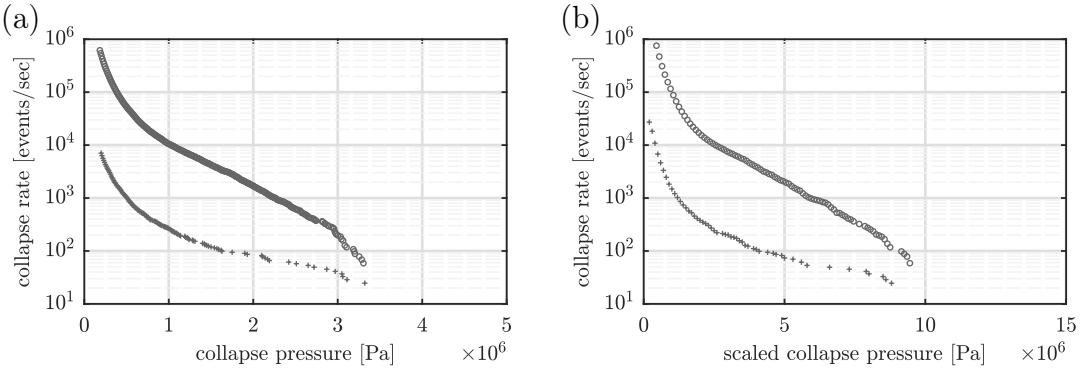

Figure 5.36: Cumulative near-wall collapse spectra for case *2.3.2b*, using (a) unscaled pressure p_{collapse}, and (b) scaled pressure $p^{\text{scaled}}_{\text{collapse}}$. Juxtaposition of baseline (+), and ILES (∘) results, obtained for the entire analysis intervals. Only collapses occurring within a distance ≤ 3 mm from a material surface included.

The above *global* collapse spectra include all collapse events recorded within the entire domain. More suitable for a comparative assessment of the aggressiveness that the propeller is exposed to, are *local* collapse spectra, which take into account only near-wall collapses events. For the subsequent evaluation, only collapses occurring within a distance of 3 mm are thus considered.

Figures 5.36*a,b* show the cumulative unscaled and scaled near-wall collapse spectra for *2.3.2b*. Although the cumulative rate of events is slightly lower due to the restriction to the near-wall region, similar conclusions as above can be drawn. In this representation, the spectra for the ILES also exhibits a constant slope, without a point of inflexion, as seen above. The main difference to the previous spectra is the exclusion of the tip vortex, which deviates in its collapse behavior from a classical shedding mechanism.

A juxtaposition of the detected near-wall collapses for all three operating points and both numerical schemes is shown in figure 5.37. The associated cumulative unscaled and scaled near-wall collapse spectra are shown in figures 5.38*a,b*. For all operating points, the strongest events are found with both methods downstream of the root cavities. Again, due to the higher level of flow unsteadiness and vapor fragmentation, the ILES yields a higher number of events overall. Furthermore, the ILES shows collapses for regions where no events are detected with the baseline method. Examples are the suction and pressure side leading edge cavity of *2.3.1b* and *2.3.3b*, which are stable with the baseline method, and exert a shedding for the ILES. These are weak events, compared to the collapses of the root cavity. The strongest collapses of all conducted simulations are found in the baseline computation of case *2.3.3b*, located at the root of the trailing edge.

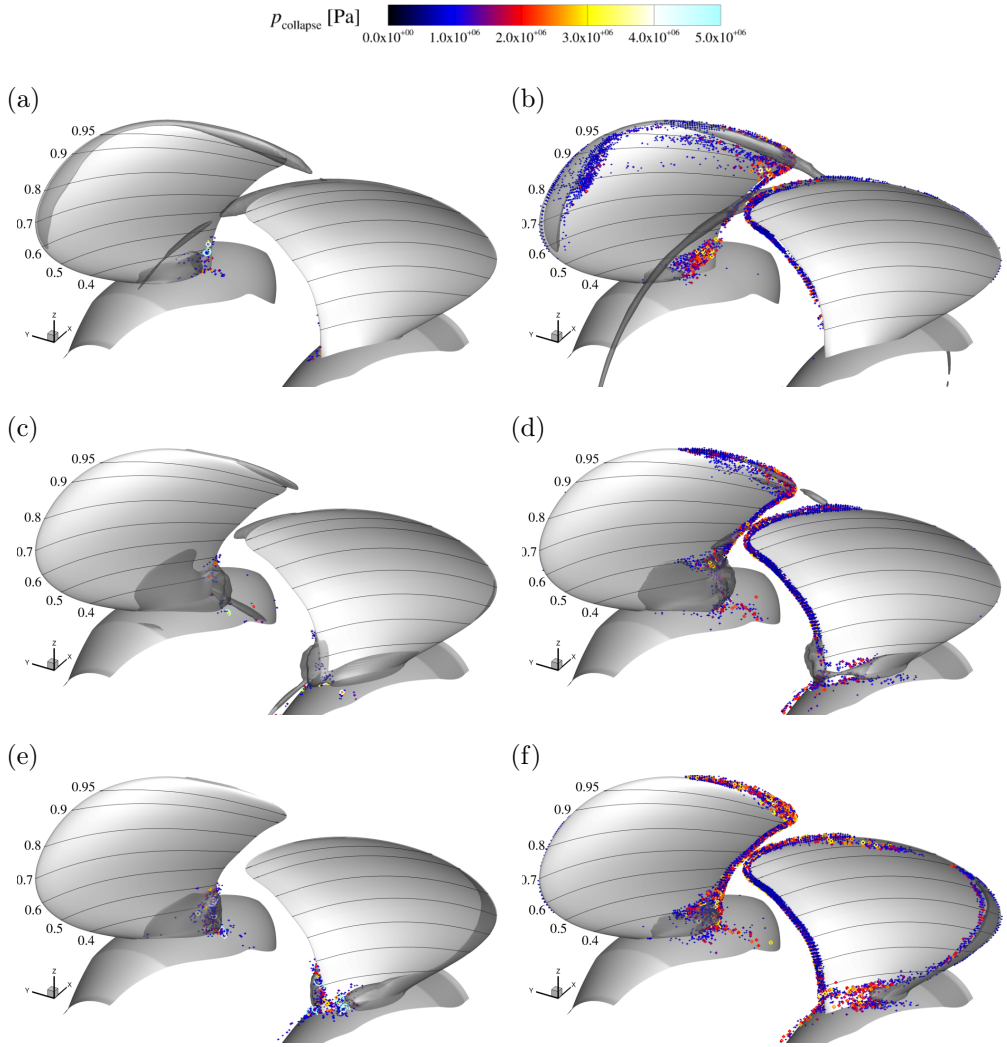

Figure 5.37: Detected near-wall collapses with $p_{\text{collapse}} \geq 3 \times 10^5$ for cases (a,b) *2.3.1b*, (c,d) *2.3.2b*, (e,f) *2.3.3b*. Juxtaposition of baseline (left column) and ILES (right column) results, obtained for equal analysis intervals of ≈ 3 rev. Only collapses occurring within a distance ≤ 3 mm from a material surface shown.

Comparing the near-wall spectra for baseline and ILES in figures 5.38*a,b*, the slopes systematically deviate from each other. This substantiates above assumption that the calibration parameter d_{ref}, which might be utilized to achieve accordance with an experimentally determined load spectra, is different for both schemes. However, the fact that also the unscaled pressure levels of the baseline scheme are higher is connected to a different disintegration behavior of the root cavity. For the baseline scheme, large, coherent vapor structures are shed, resulting in strong collapse events. Additionally, the viscosity might contribute a damping effect on the collapse pressure in the ILES.

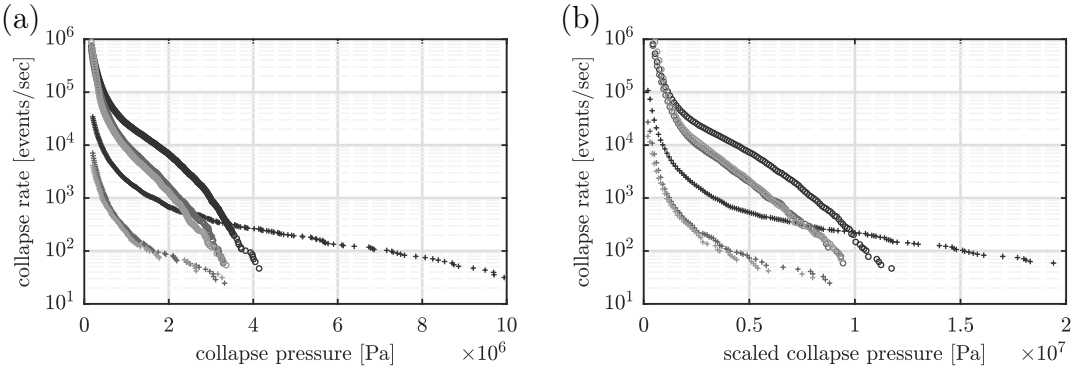

Figure 5.38: Cumulative near-wall collapse spectra (*2.3.1b* —, *2.3.2b* —, and *2.3.3b* —) using (a) unscaled pressure p_{collapse}, and (b) scaled pressure $p^{\text{scaled}}_{\text{collapse}}$. Juxtaposition of baseline (+), and ILES (∘) results, obtained for the entire analysis intervals.

Concluding, both numerical schemes equally identify case *2.3.3b* as the most aggressive operating point. In addition, result from both methods agree that the flow aggressiveness of cases *2.3.1b* and *2.3.2b* is comparable. The differences in the spectra among the numerical schemes can be traced back to differences in the underlying predicted cavity dynamics. These result from the higher order of the reconstruction, and less numerical dissipation of the ILES scheme, and are thus expected. Despite discrepancies when comparing the spectra of both schemes, the evaluation of the flow aggressiveness for the three operating points relative with each other leads to identical conclusions. Some care needs to be taken for the interpretation of the results, as the ILES also yields collapses in regions where the baseline does not show any events, due to an increased flow unsteadiness, and vapor fragmentation. However, the associated collapse events are most likely not erosive, since they are too weak. A conclusive judgment requires the calibration of the scaling parameters d_{ref} and κ. In addition to being case-dependent, as already conjectured by Mihatsch *et al.* (2015), the results of this study indicate that these parameters are dependent on the employed numerical scheme. Addressing this question necessitates the experimental determination of the load spectrum for a cavitating (model) ship propeller.

5.5 Conclusions

In this chapter, the model propeller *VP1304* is investigated by fully accounting for the two-phase compressibility of the flow. To the author's knowledge, the present study constitutes the first compressible simulation of a cavitating ship propeller.

For this purpose, a density-based approach in conjunction with a cavitation model, relying on the assumptions of mechanical, thermodynamic, and phase equilibrium is utilized, allowing to treat the flow as a homogeneous mixture of water and water-vapor. The thermodynamics are modeled with a barotropic equation of state, based on a modified Tait-equation in the liquid, and the assumption of isentropic phase change in the two-phase region. The numerical method captures all relevant time-scales of cavitating flow. It resolves cavitation-induced shock-wave dynamics, and the interaction between acoustics and phase transition.

Emphasis is put on the comparison of two different discretization schemes, using an otherwise identical numerical setup, including the numerical grids and boundary conditions. The first approach employs an upwind-biased reconstruction of flow quantities. Solving the Euler equations, viscosity is neglected in the model. It concentrates on inertial flow physics, which often dominate the dynamics of cavitating flow, see the discussions in chapter 4. The second approach, recently proposed by Egerer *et al.* (2016), utilizes a 4^{th}-order central discretization scheme in smooth regions of the flow for the convective terms. A sensor functional confines the numerical dissipation of the aforementioned upwind-biased scheme to compressible shock and phase discontinuities. For the viscous fluxes, a linear 2^{nd}-order central scheme is employed. An implicit subgrid-scale model is used, by applying a physically consistent turbulence regularization. The developed strategy enables the efficient, implicit large-eddy simulation (ILES) of compressible multi-phase flow. Utilizing identical meshes for both schemes, the viscous boundary layer is under-resolved in the ILES.

The propeller is analyzed for both wetted and cavitating conditions, reproducing a total of 10 different operating points, as specified by the Potsdam Propeller Test Case (PPTC). Referring to the established database, which consists of both experimental and numerical references, a validation study is carried out. First, the integral open-water performance of the propeller, and the velocity field in the propeller wake are investigated for wetted flow conditions. A detailed analysis of the flow topology, the blade pressure distribution, and cavitating flow characteristics are studied for the nominal design point, including an evaluation of the influence of the spatial discretization for the ILES scheme. Finally, cavitating flow conditions are studied for the design point, and two off-design points. The results obtained

with the two discretization schemes at these operating points are compared, which also includes a qualitative and quantitative assessment of the flow aggressiveness.

With the inviscid baseline method, best agreement in the integral open-water performance is found at lower advance ratios of $J \leq 1$. Specifically, at the design point with $J = 1.269$, larger discrepancies are noticeable. These are, however, consistent with results from other potential flow investigations of the propeller, indicating that these are due to the inviscid assumption. In contrast, a good match for the integral performance over the complete range of investigated advance coefficients is achieved with the incorporation of viscous effects by the ILES. The predicted propeller thrust, open-water efficiency and blade loading coefficient is in good accordance with the experimental references, and in alignment with other numerical studies of the propeller. For the torque, on the other hand, the deviations from the references are larger. It has been demonstrated that these relate to the under-estimation of the local wall-shear stress, due to the spatial under-resolution of the viscous walls. A correction method relying on the *a posteriori* application of a wall-function can be used for improving the prediction. Furthermore, the ILES approach better resolves the structure of the propeller wake, including an improved representation of the trailing tip vortex. This is related to a lower numerical dissipation, and a higher order of the spatial reconstruction scheme.

For cavitating conditions, agreement with the references regarding the integral parameters is slightly improved for both methods. This can be attributed to the fact that, as soon as cavitation occurs, it dominates over viscous effects, which are either neglected in the baseline method, or affected by an under-resolution in the ILES. Again comparing baseline and ILES scheme, the propeller thrust under cavitating conditions is better matched by the latter. For case *2.3.3b*, however, the agreement with the references is deteriorated. Corresponding to the largest investigated Reynolds-number, it is conjectured that this is caused by an increased discrepancy in the surface flow topology, as further discussed below.

Regarding the predicted locations of cavitation, good agreement is achieved both between the two numerical schemes, and the experimental references. All topologies of cavitating flow encountered in the experiment for the different operating points are reproduced. This includes root cavitation on the suction and pressure side, leading edge sheet cavitation along the pressure side, or tip vortex cavitation. Qualitatively, the baseline scheme yields larger, contiguous vapor structures, and less dynamics. Due to the higher order of the spatial reconstruction and less numerical dissipation, the ILES resolves finer cavity structures, in conjunction with a more transient behavior. This difference, however, does not noticeably affect the integral cavity volume, except for the tip vortex. While both methods slightly over-estimated the extent of cavitation compared to the experiments, they are in good alignment to the available numerical references. The cavitating

core of the trailing tip vortex is better captured by the ILES, compared to the baseline method. The trend of weaker tip vortex cavitation with increasing advance coefficient is correctly reproduced with both methods. Even with the ILES, however, a sustained vortex cavitation throughout the wake cannot be observed, owing to the coarser resolution downstream of the propeller. Capturing tip vortex cavitation is a challenge when employing an Eulerian description of the fluid, being strongly subjected by the spatial resolution. Still, compared to most of the numerical references, the conducted simulations better reproduce the cavitating trailing tip vortex. The tip vortex alignment procedure of the grid proves to be beneficial in this regard.

The employed ILES method improves the quality of prediction compared to investigations relying on the inviscid baseline method, with respect the integral performance parameters, the wake field predictions, and the dynamics of cavitation. Some differences to the experimental references remain, e.g., a larger contraction of the propeller slip-stream, or a slight over-estimation regarding the extent of vapor structures. Furthermore, the transitional behavior of the boundary layer typically found on model propeller represents a challenge for the computations. The investigation of the near-wall flow predicted by ILES reveals that it is oriented towards the tip for large parts of the blade, and that tangentially oriented streamlines are found only for a region close to the tip. Thus, for a majority of the blade suction side, the flow topology corresponds to that of laminar flow. Correspondingly, a region of laminar flow separation is located along the trailing edge in the ILES. Due to the moderate Reynolds-numbers, it can be conjectured that the suction side boundary layer is partially turbulent, although the exact character in the experiments is unknown. A laminar separation may exist in the experiments, as it is commonly found at lower radii on model propellers (Kuiper, 1981). Although the character of the boundary layer on the suction side is unknown for the experiments, it is conjectured that the extent of turbulent flow is larger as predicted by the ILES. These results are in contrast to the baseline method, where the flow is oriented along constant radii, and remains attached. Although no turbulence is resolved, this resembles the pattern of a fully turbulent flow. In consequence, the blade surface pressure is in good agreement with the available numerical references, as the majority is based on RANS equations and employ a turbulence model. The utilized inviscid flow model can be regarded as corresponding to the limit of infinite Reynolds numbers, and the flow topology predicted by the baseline method is typically found on full-scale propellers.

Conceivable rectifications for the over-estimation of laminar regions on the blade with the ILES are, e.g., the introduction of free-stream turbulence, artificial tripping of the boundary layer at the leading edge, or the application of a wall-model. These measures could be used to either trigger, or model, turbulent

flow. Wall-models certainly represent a promising approach in this regard. For being applicable in the frame of a fully compressible simulation of multi-phase flow, however, further work is needed. Open questions, e.g., in relation to their interference with near-wall cavitating structures, or regarding their interaction with collapse-induced pressure gradients, have to be addressed before wall-models can be readily employed within the current framework. Moreover, the above methods are likely to yield a turbulent boundary layer for the entire propeller. This does not necessarily satisfy the physical situation of a model propeller either. Because of the moderate Reynolds-numbers, the boundary layer is of transitional character, being comprised of both laminar as well as turbulent regions. It is thus subject of further analyses whether these measures can be used to improve the results. On the other hand, they might be advantageous for the investigation of full-scale propellers, where the flow is almost entirely turbulent.

The employed implicit subgrid-scale model is capable of predicting laminar-turbulent transition, see, e.g., Egerer *et al.* (2014a). Yet, this constitutes a challenging problem, being dependent on a multitude of factors, such as the grid resolution, pressure gradients, or local as well as free-stream disturbances, for example. Without one of the above ad-hoc modifications, it is conjectured that a finer spatial resolution is necessary in order to properly capture the laminar-turbulent transition on the blade suction side. A grid refinement, however, leads to a proportional decrease of the time step, due to the *CFL*-criterion of explicit time integration methods. Compared to the baseline method, the required time-to-solution, as, e.g., measured by the wall-clock time necessary per propeller revolution, is already increased by a factor of 1.5 when utilizing identical grids with the ILES. It is hence expected that the computational effort for a full resolution of the near-wall region with $y^+ \approx 1$ is too demanding, given the currently available computing resources. Thus, the under-resolution of the boundary layer will remain to be necessary for the compressible simulation of cavitating flow around ship propellers in the near future.

Despite the above differences in the details of the predicted cavitating flow, identical conclusions can be drawn with both numerical methods regarding the flow aggressiveness. For a comparison of the predicted pressure levels with material properties, and thus a judgement of the erosivity of the flow, a calibration of the scaling parameters d_{ref} and κ is required. As these are unavailable at the moment, only a relative assessment is possible at this stage. Still, the devised method represents a valuable tool for an objective rating of different configurations relative against each other. This can encompass various operating points, as demonstrated, or propeller designs.

CHAPTER 6

Concluding Remarks

In the scope of this thesis, two complementary studies are carried out. The first investigation considers the canonical flow configuration of a partial cavitation developing at the apex of a wedge-shaped test body within a confined duct. The second application targets the numerical simulation of wetted and cavitating flow around a model ship propeller. The numerical method employed for both subjects relies on the assumption of a homogeneous mixture, equilibrium thermodynamics, and an analytical barotropic equation of state. Utilizing a density-based approach, full two-phase compressibility is retained in the model. All relevant time-scales of cavitating flow are resolved by employing explicit integration in time. The devised method captures cavitation-induced shock-wave dynamics, its interaction with phase transition, and the feed-back with convective flow dynamics.

In the course of this thesis, two numerical flux functions, i.e., the inviscid baseline scheme of Schnerr *et al.* (2008) and Schmidt (2015), and the implicit large eddy simulation (ILES) method developed by Egerer *et al.* (2016), are utilized. The former solves the inviscid compressible Euler equations, thereby focusing on inertia-dominated flow physics, and employs an upwind-biased reconstruction of flow quantities. Relying on a physically consistent, implicit subgrid-scale model, the latter also incorporates effects of viscosity and flow turbulence. A sensor functional confines the numerical dissipation of the upwind-biased scheme to shock and phase discontinuities. In smooth regions of the flow, a higher-order spatial reconstruction based on a 4^{th}-order central discretization scheme for the convective terms is used, while viscous fluxes are discretized with a linear 2^{nd}-order central scheme. Both methods are extended in the course of this thesis to treat rotating systems, on the basis of an Arbitrary Lagrangian-Eulerian (ALE) approach.

With the first subject of investigation, partial cavities exhibiting sheet-to-cloud transition are analyzed. Good agreement is obtained with experimental references by Ganesh *et al.* (2016a) regarding the observed flow structures, growth and collapse speeds, global shedding dynamics, and the shedding Strouhal-number. The investigations confirm the experimental observation that the shedding dynamics for this configuration are dominated by a condensation shock phenomenon, instead of a re-entrant jet mechanism. While re-entrant jets are classically associated with shedding partial cavities, condensation shocks have not gained much attention in the literature, until recent experimental evidence by virtue of time-resolved x-ray densitometry is provided by Ganesh *et al.* (2016a). Alongside the re-entrant jet mechanism, condensation shocks represent an additional mechanism of instability for sheet cavitation, and the investigations give deeper insight into the flow physics of this phenomenon. The presented work complements the experimental investigation, by providing a detailed flow field analysis, including a spectral analysis within the test-section for the spatially-resolved identification of dominant frequencies, as well as velocity and pressure measurements within the entire field. The obtained data shows that condensation shocks fulfill Rankine-Hugoniot conditions of compressible flow. It is deduced that capturing this phenomenon by numerical methods requires the compressible treatment of the two-phase flow. Furthermore, analytical estimations show that the pressure loss in the channel is dominated by the presence of cavitation, which surpasses any other loss mechanisms, including the losses due to viscosity. This leads to the conclusion that the flow is dominated by inertial effects, phase transfer, and wave dynamics. The study thus substantiates the assumption that an inviscid model is sufficient for capturing the flow dynamics for this type of flow.

In the second study, the non-cavitating, and cavitating flow around the model propeller *VP1304* is numerically assessed. To the author's knowledge, the conducted studies represent the first fully-compressible investigations of cavitating propeller flow. It enables the application of previously developed methods for the assessment of flow aggressiveness to ship propellers.

With regard to the moderate Reynolds-numbers for this configurations and in addition to the baseline scheme, ILES computations are carried out, in order to explore the model uncertainties stemming from the inviscid assumption. The study reproduces the Potsdam Propeller Test Case (PPTC) for a total of 10 different operating points, considering the integral open-water performance, the propeller wake field, blade pressure distributions, and cavitating flow characteristics, including a qualitative and quantitative evaluation of flow aggressiveness. Furthermore, a grid sensitivity study is carried out for the propeller design point. For wetted flow, Euler computations give reasonable accurate results only for lower advance ratios. The ILES, on the other hand, substantially improves prediction quality

across the entire range of investigated advance coefficients. It is discussed that viscous forces are under-estimated due to an under-resolution of the boundary layer, which can be addressed using an *a posteriori* application of the generalized wall function of Shih *et al.* (1999). For cavitating conditions good agreement is achieved, both between the two numerical schemes, and with the experimental references, with respect to the predicted locations of cavitation, and cavitation topologies. This can be attributed to the fact that the presence of cavitating flow again dominate over viscous effects, although not to the same extent as for the canonical case of the partial cavity discussed above. Due to the high-order spatial reconstruction and less numerical dissipation of the ILES, finer cavity structures, in conjunction with a more transient behavior are resolved. Despite these differences, identical conclusions are drawn with both numerical methods with respect to the flow aggressiveness of the three considered operating points.

When focusing solely on propeller performance predictions, alternative numerical methods may be more suitable. For this purpose, e.g., incompressible (unsteady) Reynolds-Averaged-Navier-Stokes ((U)RANS) approaches with a properly calibrated turbulence model are able to provide results substantially faster, and with comparable or better accuracy than the presented method. The reasons is that viscosity and viscous boundary layers are important for an accurate prediction of the propeller performance. These are either neglected from the model entirely (Euler computations), or affected by the under-resolution of the near-wall region (ILES). In contrast, the presented compressible approach fully accounts for, and thus more accurately captures, the inherently transient nature of cavitating flow. Due to the Reynolds-averaging procedure, this remains limited with (U)RANS approaches. For capturing more of the flow dynamics, incompressible, two-phase large-eddy simulation approaches, as carried out by Bensow and Bark (2010), represent a promising advancement in the field. Still, since phase transfer is not modeled thermodynamically but rather based on the incompressible, i.e., kinematic, pressure, the evaluation of flow aggressiveness needs to rely on surrogate methods. When utilizing the presented compressible approach, collapse-induced pressure peaks are subject only to the spatial resolution, and can thus be leveraged for a quantification of the flow aggressiveness, which is a principal motivation for the application of the compressible approach. Furthermore, all time-scales of cavitating flow are captured in the model, thereby incorporating all relevant physical mechanisms, such as the interplay between phase change and acoustics, as well as, e.g., the above-discussed condensation shock phenomena.

The evaluation of flow aggressiveness is not free of calibration parameters, yet. Already at this stage, however, the devised method represents a valuable tool, which can be utilized for a comparative rating of different operating points, or propeller designs. The quantification of flow aggressiveness can thus be utilized

complementary to established, but for the majority qualitative, evaluation methods which rely, e.g., on experimental work.

For the current studies, the potential effect of non-condensable gas is neglected. It is suggested that the presence of non-condensable gas, by promoting liquid compressibility, can have a damping effect on the observed scatter in the shedding of the partial cavity. Furthermore, it is expected to improve the predictions of the cavity extent, which is observed for both studies to be slightly larger than the references. Incorporating effect of non-condensable gas content into the model is possible, see Mihatsch (2017).

In order to cover convective time-scales for typical technical applications, the employed compressible approach necessitates high computational cost. Therefore, the usage of acceleration techniques can be advantageous. In the scope of this thesis, time-operator preconditioning is implemented, which is employed for accelerating the convergence towards a steady-state solution during the wetted-flow initial transient phase. It is beneficial to examine the capabilities of more elaborate acceleration techniques that are applicable also for unsteady two-phase flow. A promising family of methods are Jacobian-free, and thus memory efficient, inexact Newton-Krylov methods, as reviewed by Knoll and Keyes (2004). It is conjectured that compressible phenomena acting on a larger time-scale, such as, e.g., the aforementioned condensation shocks, can still be captured. However, the inherent feed-back mechanism between wave dynamics and phase transition will potentially be lost. It has to be part of future studies to investigate whether this has an effect on overall flow dynamics. Furthermore, when the focus lies on the quantification of flow aggressiveness, the resolution of compressible shock wave mechanisms remains necessary, which limits the applicability of accelerators.

A further aspect to be addressed is the incorporation of the effects of viscosity and flow turbulence. Fully resolving viscous boundary layers is tangible for canonical flow configurations, as demonstrated by Egerer (2016) for a cavitating shear layer, a collapsing cloud of bubbles, and a generic micro channel. It is anticipated that this is also achievable for the partial cavity investigated in the first part of this thesis. However, for large-scale, technical applications such as a cavitating ship propeller, it is expected to remain infeasible in the near future. Wall-models hence represent a promising approach for alleviating the resolution requirements. Their application within a fully compressible multi-phase model, however, requires further work. Open questions, e.g., in relation to their interference with near-wall cavitating structures, or regarding their interaction with collapse-induced pressure gradients, have to be addressed before wall-models can be readily employed.

APPENDIX A

Supplementary Figures

The following chapter provides additional plots and visualizations for the investigations of the the cavitating model propeller *VP1304* presented in chapter 5. For a discussion of the individual figures, please refer to the explanations given in chapter 5.

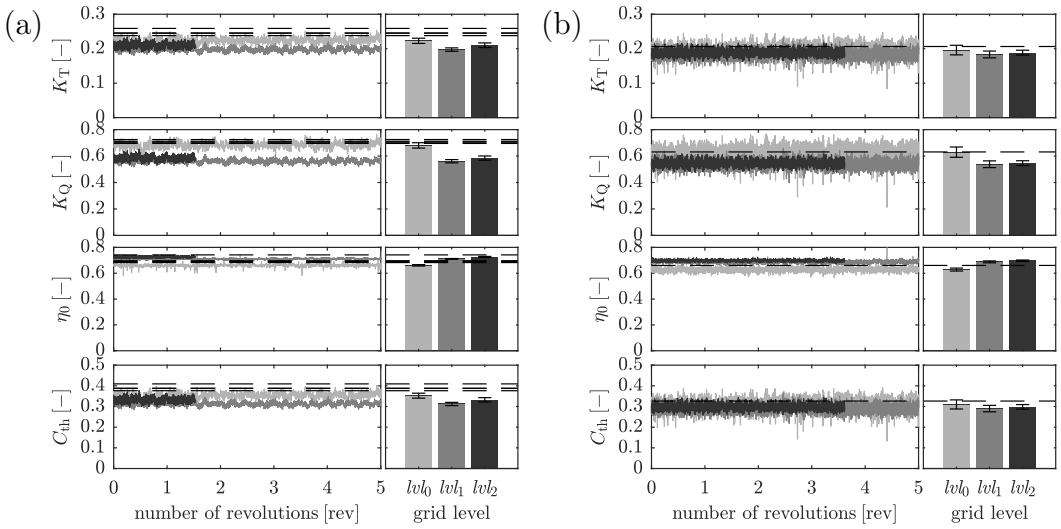

Figure A.1: Propeller performance at the design point case *2.3.2*, as predicted by ILES (lvl_0 —, lvl_1 —, and lvl_2 —), under (a) non-cavitating, and (b) cavitating conditions. Juxtaposition of time-signals, and bar plots showing time-averages and standard deviation of the signals. Including experimental references (– –, see Heinke, 2011a)

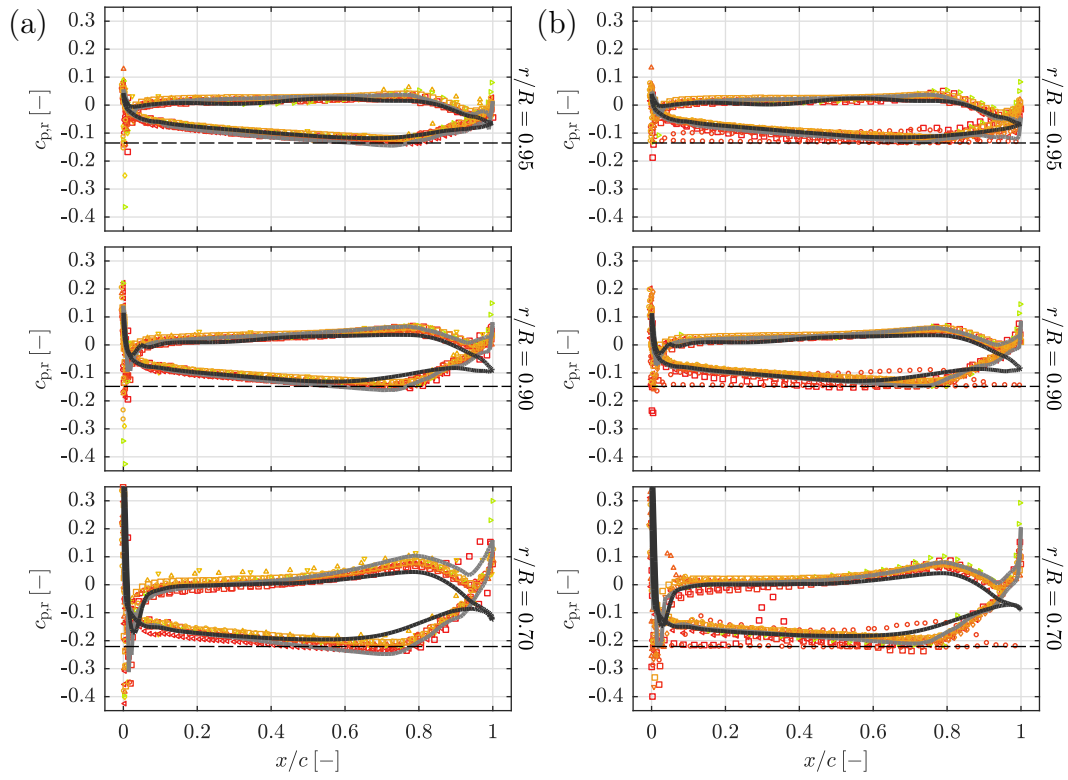

Figure A.2: Surface pressure coefficient $c_{p,r}$ on three discrete radii $r/R = (0.7, 0.9, 0.95)$ predicted by baseline scheme (—) and ILES (—) for the design point under (a) wetted conditions (*2.3.2a*), and (b) cavitating conditions (*2.3.2b*). Level of vapor pressure indicated by dashed line (– –). Comparison with numerical reference data of PPTC participants, see Heinke (2011b).

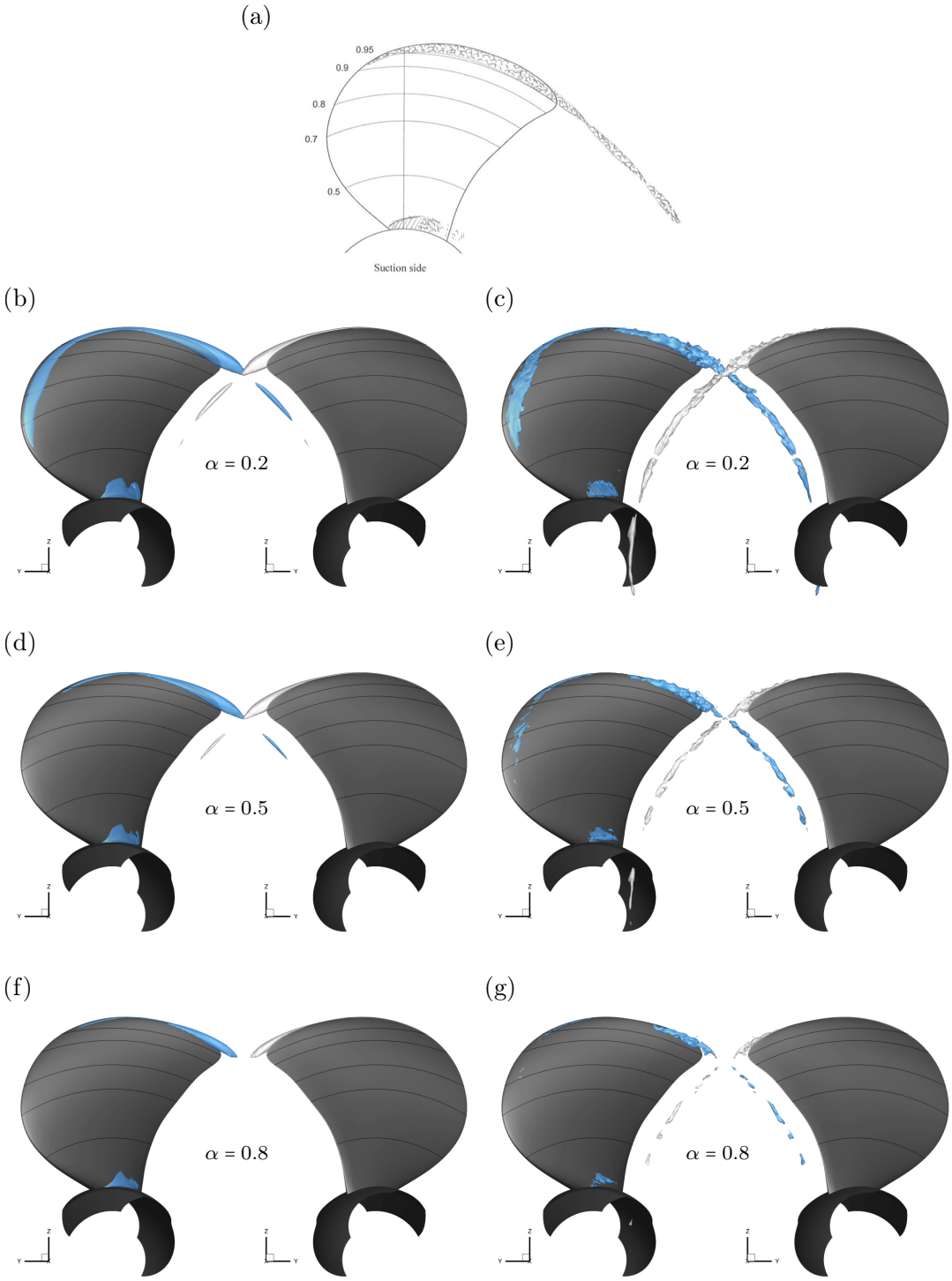

Figure A.3: Instantaneous cavity structures (axial view) for case *2.3.1b*. (a) Sketch of experimentally observed cavity pattern (Heinke, 2011a), and numerical result by iso-surfaces of (b,c) $\alpha = 0.2$, (d,e) $\alpha = 0.5$, and (f,g) $\alpha = 0.8$. Juxtaposition of baseline (left column) and ILES (right column) results.

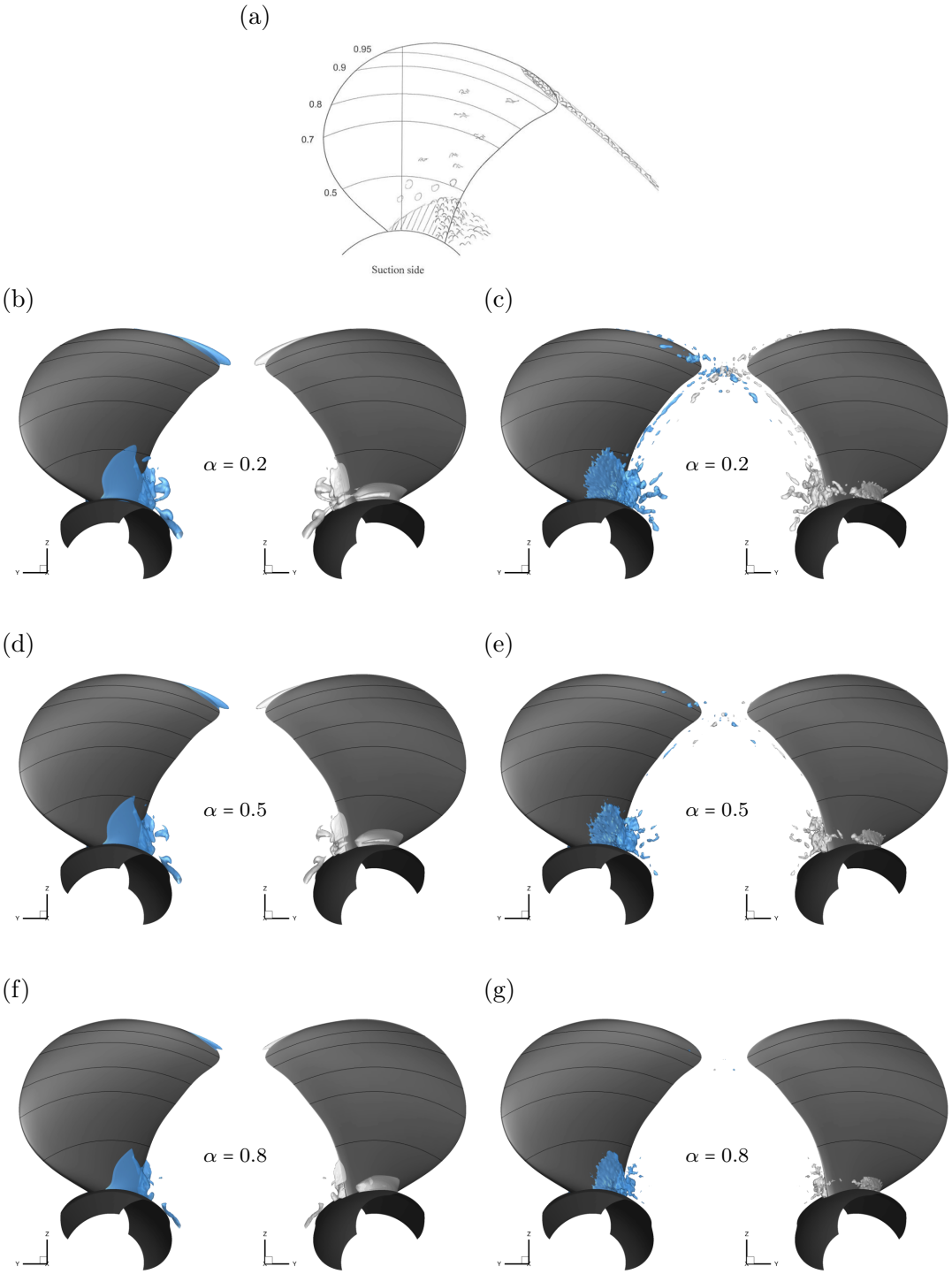

Figure A.4: Instantaneous cavity structures (axial view) for case *2.3.2b*. (a) Sketch of experimentally observed cavity pattern (Heinke, 2011a), and numerical result by iso-surfaces of (b,c) $\alpha = 0.2$, (d,e) $\alpha = 0.5$, and (f,g) $\alpha = 0.8$. Juxtaposition of baseline (left column) and ILES (right column) results.

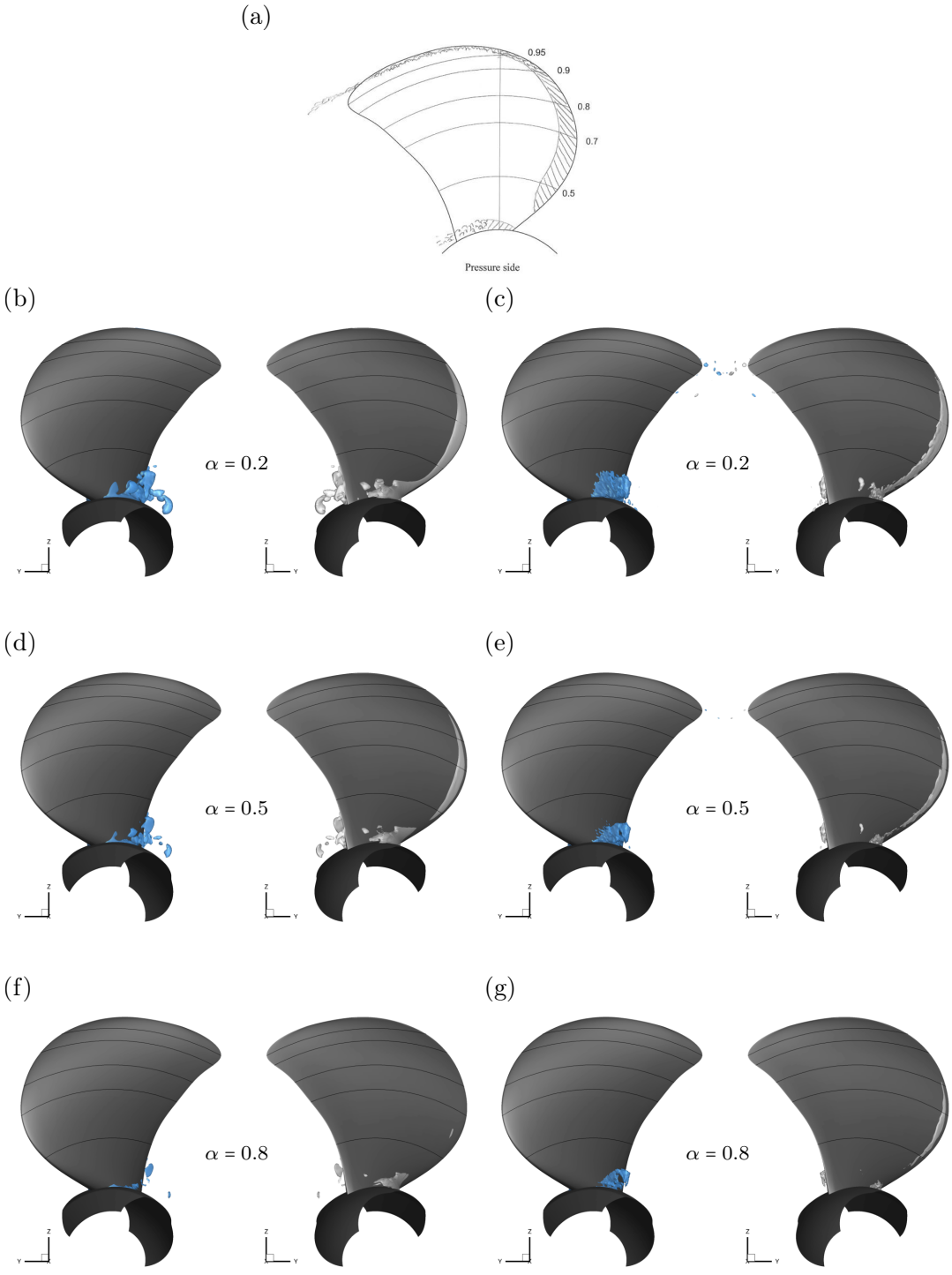

Figure A.5: Instantaneous cavity structures (axial view) for case *2.3.3b*. (a) Sketch of experimentally observed cavity pattern (Heinke, 2011a), and numerical result by iso-surfaces of (b,c) $\alpha = 0.2$, (d,e) $\alpha = 0.5$, and (f,g) $\alpha = 0.8$. Juxtaposition of baseline (left column) and ILES (right column) results.

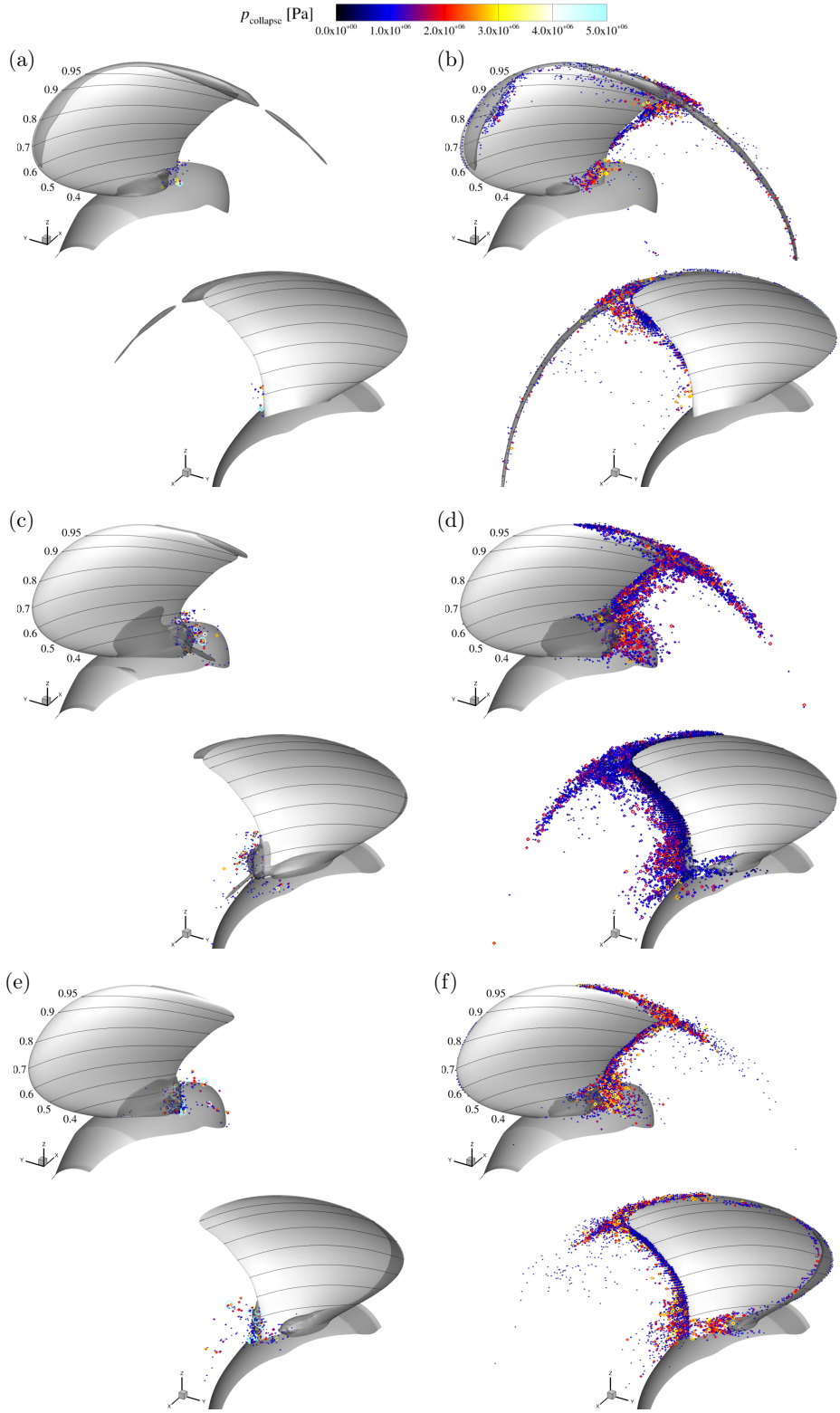

Figure A.6: Detected collapses with $p_{\text{collapse}} \geq 3 \times 10^5$ Pa for cases (a,b) *2.3.1b*, (c,d) *2.3.2b*, (e,f) *2.3.3b*. Juxtaposition of baseline (left column) and ILES (right column) results, obtained for equal analysis intervals of ≈ 3 rev.

Bibliography

Ahn, S. J. and Kwon, O. J. (2013). „Numerical investigation of cavitating flows for marine propulsors using an unstructured mesh technique“. In: *International Journal of Heat and Fluid Flow* 43, pp. 259–267. DOI: 10.1016/j.ijheatfluidflow.2013.05.007.

American Society for Testing and Materials (2017). *ASTM International - Standards Worldwide*. URL: https://www.astm.org (visited on 05/17/2017).

American Institute of Aeronautics and Astronautics (2017). *The American Institute of Aeronautics and Astronautics*. URL: http://www.aiaa.org (visited on 06/15/2017).

Arndt, R. E. A., Song, C. C. S., Kjeldsen, M., and Keller, A. (2000). „Instability of Partial Cavitation: A Numerical/Experimental Approach“. In: *Proceedings of the 23rd Symposium on Naval Hydrodynamics*. Val de Reuil, France, pp. 599–615.

Arndt, R. E. A. (1981). „Cavitation in fluid machinery and hydraulic structures“. In: *Annual Review of Fluid Mechanics* 13, pp. 273–326. DOI: 10.1146/annurev.fl.13.010181.001421.

Bark, G., Berchiche, N., and Grekula, M. (2004). *Application of principles for observation and analysis of eroding cavitation*. Edition 3.1. The EROCAV observation handbook. Göteburg: Chalmers University of Technology.

Barkmann, U. (2011a). *Potsdam Propeller Test Case (PPTC) - Open Water Tests with the Model Propeller VP1304 (Report 3752)*. Tech. rep. Potsdam, Germany.

Barkmann, U. (2011b). „Workshop: Propeller Performance, Potsdam Propeller Test Case (PPTC), Open Water Test with the Model Propeller VP1304, Case 2.1“. In: *Proceedings of the Workshop on Cavitation and Propeller Performance, 2nd International Symposium on Marine Propulsors*. Ed. by M. Abdel-Maksoud. Hamburg, Germany.

Beattie, D. and Whalley, P. B. (1982). „A simple two-phase frictional pressure drop calculation method“. In: *International Journal of Multiphase Flow* 8 (1), pp. 83–87. DOI: 10.1016/0301-9322(82)90009-X.

Bensow, R. E. and Bark, G. (2010). „Implicit LES Predictions of the Cavitating Flow on a Propeller“. In: *Journal of Fluids Engineering* 132 (4), p. 041302. DOI: 10.1115/1.4001342.

Bensow, R. E., Bark, G., and Eskilsson, C. (2013). „Towards Simulation Based Cavitation Erosion Risk Assessment“. In: *Development and Application of Advanced Experimental and Computational methods for Investigation of Cavitating Flows*. Hamburg, Germany.

Boorsma, A. and Fitzsimmons, P. A. (2009). „Quantification of cavitation impacts with acoustic emissions techniques“. In: *Proceedings of the 7th International Symposium on Cavitation*. Ann Arbor, Michigan.

Brennen, C. E. (1995). *Cavitation and Bubble Dynamics*. New York, New York: Oxford University Press. ISBN: 0-19-509409-3. URL: http://resolver.caltech.edu/CaltechBOOK:1995.001.

Budich, B., Pasquariello, V., Grilli, M., and Hickel, S. (2013). „Passive Flow Control of Shock-Wave/Turbulent-Boundary-Layer-Interactions Using Micro Vortex Generators“. In: *Proceedings of the 8th International Conference on Turbulence and Shear Flow*. Poitiers, France.

Budich, B., Schmidt, S. J., and Adams, N. A. (2014). „Numerical Investigation of a Cavitating Ship Propeller Including Collapse-Induced Wave Dynamics“. In: *Kolloquium Kavitation und Kavitationserosion*. Bochum, Germany.

Budich, B., Schmidt, S. J., and Adams, N. A. (2015a). „Numerical Investigation of a Cavitating Model Propeller Including Compressible Shock Wave Dynamics“. In: *Proceedings of the 4th International Symposium on Marine Propulsors*. Austin, TX, USA.

Budich, B., Schmidt, S. J., and Adams, N. A. (2015b). „Numerical Simulation of Cavitating Ship Propeller Flow and Assessment of Erosion Aggressiveness“. In: *Proceedings of the 6th International Conference on Computational Methods in Marine Engineering*. Rome, Italy.

Budich, B., Borrmann, F., Schmidt, S. J., and Adams, N. A. (2015c). „Assessment of Erosion Aggressiveness for the Cavitating Model Propeller VP1304 by Fully Compressible Numerical Simulation“. In: *Proceedings of the 18th Numerical Towing Tank Symposium*. Cortona, Italy.

Budich, B., Neuner, S., Schmidt, S. J., and Adams, N. A. (2015d). „Numerical investigation of shedding partial cavities over a sharp wedge“. In: *Proceedings of the 9th International Symposium on Cavitation*. Lausanne, Switzerland.

Budich, B., Schmidt, S. J., and Adams, N. A. (2016a). „Numerical Investigation of Condensation Shocks in Cavitating Flow“. In: *Proceedings of the 31st Symposium on Naval Hydrodynamics*. Monterey, CA, USA.

Budich, B., Schmidt, S. J., and Adams, N. A. (2016b). „Implicit Large Eddy Simulation of the Cavitating Model Propeller VP1304 using a Compressible Homogeneous Mixture Model“. In: *Proceedings of the 31st Symposium on Naval Hydrodynamics*. Monterey, CA, USA.

Budich, B., Schmidt, S. J., and Adams, N. A. (2017). „Compressible Implicit Large-Eddy Simulation of the Cavitating Model Propeller VP1304“. In: *7th International Conference on Computational Methods on Marine Engineering*. Nantes, France.

Budich, B., Schmidt, S. J., and Adams, N. A. (2018). „Numerical Simulation and Analysis of Condensation Shocks in Cavitating Flow“. In: *Journal of Fluid Mechanics* 838, pp. 759–813. DOI: 10.1017/jfm.2017.882.

Callenaere, M., Franc, J.-P., Michel, J.-M., and Riondet, M. (2001). „The cavitation instability induced by the development of a re-entrant jet“. In: *Journal of Fluid Mechanics* 444, pp. 223–256. DOI: 10.1017/s0022112001005420.

Caldas, A., Meis, M., and Saraquete, A. (2011). „Open Water Test for Testing Methodology“. In: *Proceedings of the 2nd International Symposium on Marine Propulsors*. Hamburg, Germany.

Campbell, I. J. and Pitcher, A. S. (1958). „Shock Waves in a Liquid Containing Gas Bubbles“. In: *Proceedings of the Royal Society A: Mathematical, Physical and Engineering Sciences* 243 (1235), pp. 534–545. DOI: 10.1098/rspa.1958.0018.

Carlton, J. S. (2012). *Marine propellers and propulsion*. Butterworth-Heinemann. Oxford. DOI: 10.1016/B978-0-08-097123-0.16001-0.

CFD General Notation System Steering Committee (2017). *CFD General Notation System*. URL: https://cgns.github.io/ (visited on 06/07/2017).

Chahine, G. L., Franc, J.-P., and Karimi, A. (2014). „Laboratory Testing Methods of Cavitation Erosion“. In: *Advanced Experimental and Numerical Techniques for Cavitation Erosion Prediction*. Dordrecht: Springer Netherlands, pp. 21–35. ISBN: 978-94-017-8538-9. DOI: 10.1007/978-94-017-8539-6_2.

Coutier-Delgosha, O., Fortes-Patella, R., and Reboud, J.-L. (2003). „Evaluation of the Turbulence Model Influence on the Numerical Simulations of Unsteady

Cavitation“. In: *Journal of Fluids Engineering* 125 (1), pp. 38–45. DOI: 10.1115/1.1524584.

Crespo, A. (1969). „Sound and Shock Waves in Liquids Containing Bubbles“. In: *Physics of Fluids* 12 (11), pp. 2274–2282. DOI: 10.1063/1.1692343.

Donea, J., Huerta, A., Ponthot, J., and Rodríguez-Ferran, A. (2004). „Arbitrary Lagrangian-Eulerian methods“. In: *Encyclopedia of Computational Mechanics*. Ed. by E. Stein, R. de Borst, and T. J. R. Hughes. Chichester, UK: John Wiley & Sons, pp. 413–437. ISBN: 0-470-84699-2. DOI: 10.1002/0470091355.ecm009.

Ducros, F., Ferrand, V., Nicoud, F., and Weber, C. (1999). „Large-eddy simulation of the shock/turbulence interaction“. In: *Journal of Computational Physics* 152 (2), pp. 517–549. DOI: 10.1006/jcph.1999.6238.

Dular, M. and Bachert, R. (2009). „The Issue of Strouhal Number Definition in Cavitating Flow“. In: *Journal of Mechanical Engineering* 11 (55), pp. 666–674.

Dular, M. and Petkovšek, M. (2015). „On the Mechanisms of Cavitation Erosion - Coupling High Speed Videos to Damage Patterns“. In: *Experimental Thermal and Fluid Science* 68, pp. 359–370. DOI: 10.1016/j.expthermflusci.2015.06.001.

Egerer, C. P., Hickel, S., Schmidt, S. J., and Adams, N. A. (2014a). „Large-eddy simulation of turbulent cavitating flow in a micro channel“. In: *Physics of Fluids* 26 (8), pp. 085102–085130. DOI: 10.1063/1.4891325.

Egerer, C. P., Hickel, S., Schmidt, S. J., and Adams, N. A. (2014b). „Large-eddy simulation of turbulent cavitating flow in a micro channel“. In: *Physics of Fluids* 26 (8), pp. 1–9. DOI: 10.1063/1.4891325.

Egerer, C. P., Schmidt, S. J., Hickel, S., and Adams, N. A. (2016). „Efficient implicit LES method for the simulation of turbulent cavitating flows“. In: *Journal of Computational Physics* 316, pp. 453–469. DOI: 10.1016/j.jcp.2016.04.021.

Egerer, C. P. (2016). „Large-Eddy Simulation of Turbulent Cavitating Flows“. PhD thesis. Technische Universität München, Germany.

Eskilsson, C. and Bensow, R. E. (2012). „A Compressible Model for Cavitating Flow: Comparison between Euler, RANS and LES Simulations“. In: *Proceedings of the 29th Symposium on Naval Hydrodynamics*. Gothenburg, Sweden.

Ferziger, J. H. and Peric, M. (2002). *Computational Methods for Fluid Dynamics*. Berlin, Germany: Springer Verlag. ISBN: 978-3-642-56026-2. DOI: 10.1007/978-3-642-56026-2.

Foeth, E.-J., Terwisga, T. J. C. van, and Doorne, C. van (2008). „On the Collapse Structure of an Attached Cavity on a Three-Dimensional Hydrofoil“. In: *Journal of Fluids Engineering* 130 (7), pp. 071303–9. DOI: 10.1115/1.2928345.

Franc, J.-P. and Michel, J.-M. (2005). *Fundamentals of Cavitation*. Ed. by R. Moreau. Fluid Mechanics and Its Applications. Dordrecht: Springer Science & Business Media. ISBN: 1-4020-2232-8. DOI: 10.1007/1-4020-2233-6.

Franc, J.-P., Riondet, M., Karimi, A., and Chahine, G. L. (2011). „Impact Load Measurements in an Erosive Cavitating Flow“. In: *Journal of Fluids Engineering* 133 (12), pp. 121301–8. DOI: 10.1115/1.4005342.

Franc, J.-P. (2009). „Incubation Time and Cavitation Erosion Rate of Work-Hardening Materials“. In: *Journal of Fluids Engineering* 131 (2), pp. 021303–14. DOI: 10.1115/1.3063646.

Fujiyama, K., Kim, C.-H., and Hitomi, D. (2011). „Performance and Cavitation Evaluation of Marine Propeller using Numerical Simulations “. In: *Proceedings of the 2nd International Symposium on Marine Propulsors*. Hamburg, Germany.

Funeno, I. (2002). „On Viscous Flow around Marine Propellers - Hub Vortex and Scale Effect“. In: *Journal of the Kansai Society of Naval Architects* 2002 (238), pp. 17–27. DOI: 10.14856/jksna.2002.238_17.

Furness, R. A. and Hutton, S. P. (1975). „Experimental and Theoretical Studies of Two-Dimensional Fixed-Type Cavities“. In: *Journal of Fluids Engineering* 97 (4), pp. 515–521. DOI: 10.1115/1.3448098.

Gaggero, S., Villa, D., and Brizzolara, S. (2011). „SMP Workshop on Cavitation and Propeller Performances: The Experience of the University of Genova on the Potsdam Propeller Test Case “. In: *Proceedings of the 2nd International Symposium on Marine Propulsors*. Hamburg, Germany.

Gaggero, S., Villa, D., and Viviani, M. (2017). „An extensive analysis of numerical ship self-propulsion prediction via a coupled BEM/RANS approach“. In: *Physics Procedia* 66, pp. 55–78. DOI: 10.1016/j.apor.2017.05.005.

Ganesh, H., Mäkiharju, S. A., and Ceccio, S. L. (2015). „Interaction of a Compressible Bubbly Flow With an Obstacle Placed Within a Shedding Partial Cavity“. In: *Journal of Physics: Conference Series* 656, pp. 012151–4. DOI: 10.1088/1742-6596/656/1/012151.

Ganesh, H., Mäkiharju, S. A., and Ceccio, S. L. (2016a). „Bubbly shock propagation as a mechanism for sheet-to-cloud transition of partial cavities“. In: *Journal of Fluid Mechanics* 802, pp. 37–78. DOI: 10.1017/jfm.2016.425.

Ganesh, H., Wu, J., and Ceccio, S. L. (2016b). „Investigation of Cavity Shedding Dynamics on a NACA0015 Hydrofoil Using Time Resolved X-ray Densitometry“. In: *Proceedings of the 31st Symposium on Naval Hydrodynamics*. Monterey, CA, USA.

Gatchell, S., Hafermann, D., and Streckwall, H. (2011). „Open Water Test Propeller Performance and Cavitation Behaviour using PPB and FreSCo+ “. In: *Proceedings of the 2nd International Symposium on Marine Propulsors*. Hamburg, Germany.

Glauert, H. (1933). *Wind Tunnel Interference on Wings, Bodies and Airscrews. R. & M. No. 1566*. Aeronautical Research Committee, Reports & Memoranda No. 1566. London: British ARC. ISBN: 9780511574481. DOI: 10.1017/CBO9780511574481.

Gnanaskandan, A. and Mahesh, K. (2016a). „Large Eddy Simulation of the transition from sheet to cloud cavitation over a wedge“. In: *International Journal of Multiphase Flow* 83, pp. 86–102. DOI: 10.1016/j.ijmultiphaseflow.2016.03.015.

Gnanaskandan, A. and Mahesh, K. (2016b). „Comparative study of RANS and LES in simulating cavitating flows“. In: *Proceedings of the 31st Symposium on Naval Hydrodynamics*. Monterey, CA, USA.

Goncalves, E., Decaix, J., and Fortes-Patella, R. (2010). „Unsteady simulation of cavitating flows in Venturi“. In: *Journal of Hydrodynamics, Ser. B* 22 (5), pp. 753–758. DOI: 10.1016/S1001-6058(10)60026-1.

Gopalan, S. and Katz, J. (2000). „Flow structure and modeling issues in the closure region of attached cavitation“. In: *Physics of Fluids* 12 (4), pp. 895–911. DOI: 10.1063/1.870344.

Heinke, H.-J. (2011a). *Potsdam Propeller Test Case (PPTC) - Cavitation Tests with the Model Propeller VP1304 (Report 3753)*. Tech. rep. Potsdam, Germany.

Heinke, H.-J. (2011b). „Workshop: Propeller Performance, Potsdam Propeller Test Case (PPTC), Cavitation Tests with the Model Propeller VP1304, Case 2.3“. In: *Proceedings of the Workshop on Cavitation and Propeller Performance, 2nd International Symposium on Marine Propulsors*. Ed. by M. Abdel-Maksoud. Hamburg, Germany.

Hickel, S., Adams, N. A., and Domaradzki, J. A. (2006). „An adaptive local deconvolution method for implicit LES“. In: *Journal of Computational Physics* 213 (1), pp. 413–436. DOI: 10.1016/j.jcp.2005.08.017.

Hickel, S. and Adams, N. A. (2007). „On implicit subgrid-scale modeling in wall-bounded flows“. In: *Physics of Fluids* 19 (10), pp. 105106–14. DOI: 10.1063/1.2773765.

Hickel, S., Egerer, C. P., and Larsson, J. (2014). „Subgrid-scale modeling for implicit large eddy simulation of compressible flows and shock-turbulence interaction“. In: *Physics of Fluids* 26 (10), pp. 106101–44. DOI: 10.1063/1.4898641.

„Proceedings of the Workshop on Cavitation and Propeller Performance“ (2011). In: *Proceedings of the 2nd International Symposium on Marine Propulsors*. Ed. by M. Hoekstra, T. J. C. van Terwisga, H.-J. Heinke, L. Lübke, M. Abdel-Maksoud, and M. Druckenbrod. Hamburg, Germany.

Innings, F., Hultman, E., Forsberg, F., and Prakash, B. (2011). „Understanding and analysis of wear in homogenizers for processing liquid food“. In: *Wear* 271 (9-10), pp. 2588–2598. DOI: 10.1016/j.wear.2011.01.084.

International Towing Tank Conference (2008). *ITTC – Recommended Procedures and Guidelines - Cavitation, Prediction of Cavitation Erosion, Damage for Unconventional Rudders or Rudders behind Highly-Loaded Propellers*. Tech. rep.

International Towing Tank Conference (2011). *ITTC – Recommended Procedures and Guidelines - Practical Guidelines for Ship CFD Applications*. Tech. rep.

International Towing Tank Conference (2017). *ITTC*. URL: http://ittc.info (visited on 05/28/2017).

Jakobsen, J. K. (1964). „On the Mechanism of Head Breakdown in Cavitating Inducers“. In: *Journal of Basic Engineering* 86 (2), pp. 291–305. DOI: 10.1115/1.3653066.

Ji, B., Luo, X., Wang, X., Peng, X., Wu, Y., and Xu, H. (2011). „Unsteady Numerical Simulation of Cavitating Turbulent Flow Around a Highly Skewed Model Marine Propeller“. In: *Journal of Fluids Engineering* 133 (1), p. 011102. DOI: 10.1115/1.4003355.

Johnsen, E. and Colonius, T. (2008). „Shock-induced collapse of a gas bubble in shockwave lithotripsy“. In: *The Journal of the Acoustical Society of America* 124 (4), pp. 2011–2020. DOI: 10.1121/1.2973229.

Karypis, G. and Kumar, V. (1998). „A Fast and High Quality Multilevel Scheme for Partitioning Irregular Graphs“. In: *SIAM Journal on Scientific Computing* 20 (1), pp. 359–392. DOI: 10.1137/S1064827595287997.

Kato, H., Yamaguchi, H., Maeda, M., Kawanami, Y., and Nakasumi, S. (1999). „Laser holographic observation of cavitation cloud on a foil section“. In: *Journal of Visualization* 2 (1), pp. 37–50. DOI: 10.1007/BF03182550.

Kawanami, Y., Kato, H., Yamaguchi, H., Maeda, M., and Nakasumi, S. (2002). „Inner Structure of Cloud Cavity on a Foil Section“. In: *JSME International Journal Series B Fluids and Thermal Engineering* 45 (3), pp. 655–661. DOI: 10.1299/jsmeb.45.655.

Kawanami, Y., Kato, H., Yamaguchi, H., Tanimura, M., and Tagaya, Y. (1997). „Mechanism and Control of Cloud Cavitation“. In: *Journal of Fluids Engineering* 119 (4), pp. 788–794. DOI: 10.1115/1.2819499.

Kim, K.-H., Chahine, G. L., Franc, J.-P., and Karimi, A., eds. (2014). *Advanced Experimental and Numerical Techniques for Cavitation Erosion Prediction*. Vol. 106. Fluid Mechanics and Its Applications. Dordrecht: Springer Netherlands. ISBN: 978-94-017-8538-9. DOI: 10.1007/978-94-017-8539-6.

Kinnas, S. A. and Fine, N. E. (2006). „A numerical nonlinear analysis of the flow around two- and three-dimensional partially cavitating hydrofoils“. In: *Journal of Fluid Mechanics* 254, pp. 151–181. DOI: 10.1017/S0022112093002071.

„Proceedings of the 2nd Workshop on Cavitation and Propeller Performance“ (2015). In: *Proceedings of the 4th International Symposium on Marine Propulsors*. Ed. by S. A. Kinnas, M. Abdel-Maksoud, U. Barkmann, L. Lübke, and Y. Tian. Hamburg, Germany.

Klasson, O. K. and Huuva, T. (2011). „Potsdam Propeller Test Case (PPTC)“. In: *Proceedings of the 2nd International Symposium on Marine Propulsors*. Hamburg, Germany.

Knapp, R. T. (1955). „Recent investigations of the mechanics of cavitation and cavitation damage“. In: *Transactions of the ASME* 77 (5), pp. 1045–1054. DOI: 10.1016/0043-1648(58)90220-5.

Knoll, D. A. and Keyes, D. E. (2004). „Jacobian-free Newton-Krylov methods: a survey of approaches and applications“. In: *Journal of Computational Physics* 193 (2), pp. 357–397. DOI: 10.1016/j.jcp.2003.08.010.

Koren, B. (1993). „A robust upwind discretisation method for advection, diffusion and source terms“. In: *Numerical Methods for Advection-Diffusion Problems*. Braunschweig: Vieweg, pp. 117–138.

Kuiper, G. (1981). „Cavitation inception on ship propeller models“. PhD thesis. Technische Universiteit Delft, The Netherlands.

Kuiper, G. (1997). „Cavitation Research and Ship Propeller Design“. In: *Applied Scientific Research* 58 (1-4), pp. 33–50. DOI: 10.1023/A:1000754928962.

Laberteaux, K. R. and Ceccio, S. L. (2001). „Partial cavity flows. Part 1. Cavities forming on models without spanwise variation“. In: *Journal of Fluid Mechanics* 431, pp. 1–41. DOI: 10.1017/S0022112000002925.

Larsson, J., Kawai, S., Bodart, J., and Bermejo-Moreno, I. (2016). „Large eddy simulation with modeled wall-stress: recent progress and future directions“. In: *Mechanical Engineering Reviews* 3 (1), pp. 15–00418. DOI: 10.1299/mer.15-00418.

Le, Q., Franc, J.-P., and Michel, J. M. (1993). „Partial Cavities: Pressure Pulse Distribution Around Cavity Closure“. In: *Journal of Fluids Engineering* 115 (2), pp. 249–254. DOI: 10.1115/1.2910132.

Lemmon, E. W., McLinden, M. O., and Friend, D. G. (n.d.). *Thermophysical Properties of Fluid Systems*. Ed. by P. J. Linstrom and W. G. Mallard. NIST Chemistry WebBook, NIST Standard Reference Database Number 69. Gaithersburg MD, 20899. DOI: 10.18434/T4D303.

Lentacker, I., De Cock, I., Deckers, R., De Smedt, S. C., and Moonen, C. T. W. (2014). „Understanding ultrasound induced sonoporation: Definitions and underlying mechanisms“. In: *Advanced Drug Delivery Reviews* 72, pp. 49–64. DOI: 10.1016/j.addr.2013.11.008.

Leroux, J.-B., Astolfi, J. A., and Billard, J. Y. (2004). „An Experimental Study of Unsteady Partial Cavitation“. In: *Journal of Fluids Engineering* 126 (1), pp. 94–101. DOI: 10.1115/1.1627835.

Li, Z. R., Pourquie, M., and Terwisga, T. J. C. van (2014). „Assessment of Cavitation Erosion With a URANS Method“. In: *Journal of Fluids Engineering* 136 (4), pp. 041101–041111. DOI: 10.1115/1.4026195.

Li, D.-Q. (2011). „Prediction of Non-Cavitating and Cavitating Performance of a SVA Potsdam Propeller “. In: *Proceedings of the 2nd International Symposium on Marine Propulsors*. Hamburg, Germany.

Li, Z. R. (2012). „Assessment of cavitation erosion with a multiphase Reynolds-Averaged Navier-Stokes method“. PhD thesis. Technische Universiteit Delft, The Netherlands.

Lindau, O. and Lauterborn, W. (2003). „Cinematographic observation of the collapse and rebound of a laser-produced cavitation bubble near a wall“. In: *Journal of Fluid Mechanics* 479, pp. 327–348. DOI: 10.1017/S0022112002003695.

Lin, S. P. and Reitz, R. D. (1998). „Drop and spray formation from a liquid jet“. In: *Annual Review of Fluid Mechanics* 30 (1), pp. 85–105. DOI: 10.1146/annurev.fluid.30.1.85.

Liu, D. and Hong, F. (2011). „The Numerical Predicted of SMP11 Propeller Performance with and without Cavitation“. In: *Proceedings of the 2nd International Symposium on Marine Propulsors*. Hamburg, Germany.

Lübke, L. (2011). „Workshop: Propeller Performance, Potsdam Propeller Test Case (PPTC), LDV Measurements with the Model Propeller VP1304, Case 2.2“. In: *Proceedings of the Workshop on Cavitation and Propeller Performance, 2nd International Symposium on Marine Propulsors*. Ed. by M. Abdel-Maksoud. Hamburg, Germany.

Lush, P. A. and Skipp, S. R. (1986). „High speed cine observations of cavitating flow in a duct“. In: *International Journal of Heat and Fluid Flow* 7 (4), pp. 283–290. DOI: 10.1016/0142-727X(86)90006-8.

Ma, J., Hsiao, C.-T., and Chahine, G. L. (2016). „A physics based multiscale modeling of cavitating flows“. In: *Computers & Fluids* 145, pp. 68–84. DOI: 10.1016/j.compfluid.2016.12.010.

Mach, K. P. (2011). *Potsdam Propeller Test Case (PPTC) - LDV Velocity Measurements with the Model Propeller VP1304 (Report 3754)*. Tech. rep. Potsdam, Germany.

Mallock, A. (1910). „The Damping of Sound by Frothy Liquids“. In: *Proceedings of the Royal Society A: Mathematical, Physical and Engineering Sciences* 84 (572), pp. 391–395. DOI: 10.1098/rspa.1910.0085.

Mihatsch, M. S., Schmidt, S. J., and Adams, N. A. (2015). „Cavitation erosion prediction based on analysis of flow dynamics and impact load spectra“. In: *Physics of Fluids* 27 (10), pp. 103302–103321. DOI: 10.1063/1.4932175.

Mihatsch, M. S. (2017). „Numerical Prediction of Erosion and Degassing Effects in Cavitating Flows “. PhD thesis. Technische Universität München, Germany.

Morgut, M. and Nobile, E. (2011). „Numerical Predictions of the Cavitating and Non-Cavitating Flow around the Model Scale Propeller PPTC “. In: *Proceedings of the 2nd International Symposium on Marine Propulsors*. Hamburg, Germany.

Morgut, M. and Nobile, E. (2012). „Numerical Predictions of Cavitating Flow around Model Scale Propellers by CFD and Advanced Model Calibration“. In: *International Journal of Rotating Machinery* 2012 (8), pp. 1–11. DOI: 10.1155/2012/618180.

MPI Forum (2017). *MPI Forum*. URL: http://mpi-forum.org (visited on 06/14/2017).

Mueller, A. C. and Kinnas, S. A. (1999). „Propeller Sheet Cavitation Predictions Using a Panel Method“. In: *Journal of Fluids Engineering* 121 (2), pp. 282–288. DOI: 10.1115/1.2822204.

Nohmi, M., Ikohagi, T., and Iga, Y. (2008). „Numerical Prediction Method of Cavitation Erosion“. In: *ASME 2008 Fluids Engineering Division Summer Meeting collocated with the Heat Transfer, Energy Sustainability, and 3rd Energy Nanotechnology Conferences*, pp. 1139–1145. ISBN: 978-0-7918-4840-1. DOI: 10.1115/FEDSM2008-55126.

Noordzij, L. and Wijngaarden, L. van (1974). „Relaxation effects, caused by relative motion, on shock waves in gas-bubble/liquid mixtures“. In: *Journal of Fluid Mechanics* 66 (01), pp. 115–143. DOI: 10.1017/S0022112074000103.

Ohl, C.-D., Arora, M., Dijkink, R., Janve, V., and Lohse, D. (2006a). „Surface cleaning from laser-induced cavitation bubbles“. In: *Applied Physics Letters* 89 (7), pp. 074102–074103. DOI: 10.1063/1.2337506.

Ohl, C.-D., Arora, M., Ikink, R., Jong, N. de, Versluis, M., Delius, M., and Lohse, D. (2006b). „Sonoporation from Jetting Cavitation Bubbles“. In: *Biophysical Journal* 91 (11), pp. 4285–4295. DOI: 10.1529/biophysj.105.075366.

Örley, F., Trummler, T., Hickel, S., Mihatsch, M. S., Schmidt, S. J., and Adams, N. A. (2015). „Large-eddy simulation of cavitating nozzle flow and primary jet break-up“. In: *Physics of Fluids* 27 (8), pp. 086101–28. DOI: 10.1063/1.4928701.

Örley, F. (2016). „Numerical Simulation of Cavitating Flows in Diesel Injection Systems“. PhD thesis. Technische Universität München, Germany.

Pereira, F. and Salvatore, F. (2004). „Measurement and Modeling of Propeller Cavitation in Uniform Inflow“. In: *Journal of Fluids Engineering* 126 (4), pp. 671–679. DOI: 10.1115/1.1778716.

Pereira, F., Salvatore, F., and Di Felice, F. (2004). „Experimental investigation of a cavitating propeller in non-uniform inflow“. In: *Proceedings of the 25th Symposium on Naval Hydrodynamics*. St. John's Newfoundland, Canada.

Pham, T. M., Larrarte, F., and Fruman, D. H. (1999). „Investigation of Unsteady Sheet Cavitation and Cloud Cavitation Mechanisms“. In: *Journal of Fluids Engineering* 121 (2), pp. 289–296. DOI: 10.1115/1.2822206.

Philipp, A. and Lauterborn, W. (1998). „Cavitation erosion by single laser-produced bubbles“. In: *Journal of Fluid Mechanics* 361, pp. 75–116. DOI: 10.1017/S0022112098008738.

Reboud, J.-L., Stutz, B., and Coutier-Delgosha, O. (1998). „Two-Phase Flow Structure of Cavitation: Experiment and Modeling of Unsteady Effects“. In: *Proceedings of the 3rd International Symposium on Cavitation*. Grenoble, France.

Reisman, G. E., Wang, Y. C., and Brennen, C. E. (1998). „Observations of shock waves in cloud cavitation“. In: *Journal of Fluid Mechanics* 355, pp. 255–283. DOI: 10.1017/S0022112097007830.

Rhee, S. H. and Joshi, S. (2005). „Computational validation for flow around a marine propeller using unstructured mesh based Navier-Stokes solver“. In: *JSME International Journal Series B Fluids and Thermal Engineering* 48 (3), pp. 562–570. DOI: 10.1299/jsmeb.48.562.

Roe, P. L. (1986). „Characteristic-based schemes for the Euler equations“. In: *Annual Review of Fluid Mechanics* 18 (1), pp. 337–365. DOI: 10.1146/annurev.fl.18.010186.002005.

Salvatore, F. and Streckwall, H. (2009). „Propeller Cavitation Modelling by CFD-Results from the VIRTUE 2008 Rome Workshop“. In: *Proceedings of the 1st International Symposium on Marine Propulsors*. Trondheim, Norway.

Salvatore, F. and Greco, L. (2011). „Computational analysis of marine propeller performance and cavitation by using an inviscid-flow BEM model “. In: *Proceedings of the 2nd International Symposium on Marine Propulsors*. Hamburg, Germany.

Saurel, R., Cocchi, P., and Butler, P. B. (1999). „Numerical Study of Cavitation in the Wake of a Hypervelocity Underwater Projectile“. In: *Journal of Propulsion and Power* 15 (4), pp. 513–522. DOI: 10.2514/2.5473.

Schmidt, S. J., Sezal, I. H., Schnerr, G. H., and Thalhamer, M. (2007). „Shock waves as driving mechanism for cavitation erosion“. In: *Proceedings of the 8th International Symposium on Experimental and Computational Aerothermodynamics of Internal Flows*. Lyon, France.

Schnerr, G. H., Sezal, I. H., and Schmidt, S. J. (2008). „Numerical investigation of three-dimensional cloud cavitation with special emphasis on collapse induced shock dynamics“. In: *Physics of Fluids* 20 (4), p. 040703. DOI: 10.1063/1.2911039.

Schmidt, S. J., Thalhamer, M., and Schnerr, G. H. (2009). „Inertia controlled instability and small scale structures of sheet and cloud cavitation“. In: *Proceedings of the 7th International Symposium on Cavitation*. Ann Arbor, MI, USA.

Schmidt, S. J., Mihatsch, M. S., Thalhamer, M., and Adams, N. A. (2014). „Assessment of Erosion Sensitive Areas via Compressible Simulation of Unsteady Cavitating Flows“. In: *Advanced Experimental and Numerical Techniques for Cavitation Erosion Prediction*. Ed. by K.-H. Kim, G. L. Chahine, J.-P. Franc, and A. Karimi. Dordrecht: Springer Netherlands, pp. 329–344. ISBN: 978-94-017-8538-9. DOI: 10.1007/978-94-017-8539-6_14.

Schmidt, E. and Grigull, U. (1989). *Properties of water and steam in SI-units: 0-800°C, 0-1000 bar = Zustandsgrößen von Wasser und Wasserdampf in SI-Einheiten*. 4th, enlarged edition. Berlin: Springer Verlag. ISBN: 3-540-09601-9.

Schmidt, S. J. (2015). „A low Mach number consistent compressible approach for simulation of cavitating flows “. PhD thesis. Technische Universität München, Germany.

Schiffbau-Versuchsanstalt Potsdam (2017). *Potsdam Propeller Test Case PPTC*. URL: http://www.sva-potsdam.de/pptc-propeller-test-case-verwandte-projekte (visited on 05/20/2017).

Sezal, I. H., Schmidt, S. J., Schnerr, G. H., Thalhamer, M., and Förster, M. (2009). „Shock and wave dynamics in cavitating compressible liquid flows in injection nozzles“. In: *Shock Waves* 19 (1), pp. 49–58. DOI: 10.1007/s00193-008-0185-3.

Sezal, I. H. (2009). „Compressible Dynamics of Cavitating 3-D Multi-Phase Flows“. PhD thesis. Technische Unviersität München, Germany.

Shih, T.-H., Povinelli, L. A., Liu, N.-S., Potapczuk, M. G., and Lumley, J. L. (1999). *A Generalized Wall Function*. Tech. rep. National Aeronautics and Space Administration, Glenn Research Center.

Sipilä, T., Siikonen, T., and Saisto, I. (2011). „FINFLO RANS-Predictions for Propeller Performance“. In: *Proceedings of the 2nd International Symposium on Marine Propulsors*. Hamburg, Germany.

Terwisga, T. J. C. van, Wijngaarden, E. van, Bosschers, J., and Kuiper, G. (2007). „Achievements and challenges in cavitation research on ship propellers“. In: *International Shipbuilding Progress* 54 (165-187).

Terwisga, T. J. C. van, Fitzsimmons, P. A., Li, Z. R., and Foeth, E. J. (2009). „Cavitation erosion - a review of physical mechanisms and erosion risk models“. In: *Proceedings of the 7th International Symposium on Cavitation*. Ann Arbor, MI, USA.

The International Association for the Properties of Water and Steam (2011). *Release on the IAPWS Formulation 2011 for the Thermal Conductivity of Ordinary Water Substance*. Tech. rep. Plzeň, Czech Republic.

Tian, Y. and Kinnas, S. A. (2015). „Prediction of Performance of a Cavitating Propeller in Oblique Inflow“. In: *Journal of Physics: Conference Series* 656, p. 012073. DOI: 10.1088/1742-6596/656/1/012073.

Toro, E. F. (2009). *Riemann Solvers and Numerical Methods for Fluid Dynamics*. Berlin, Heidelberg: Springer Berlin Heidelberg. ISBN: 978-3-540-25202-3. DOI: 10.1007/b79761.

Turkel, E. (1999). „Preconditioning Techniques in Computational Fluid Dynamics“. In: *Annual Review of Fluid Mechanics* 31 (1), pp. 385–416. DOI: 10.1146/annurev.fluid.31.1.385.

Van Driest, E. R. (1956). „On Turbulent Flow Near a Wall“. In: *Journal of the Aeronautical Sciences* 23 (11), pp. 1007–1011. DOI: 10.2514/8.3713.

Wade, R. B. and Acosta, A. J. (1966). „Experimental Observations on the Flow Past a Plano-Convex Hydrofoil“. In: *Journal of Basic Engineering* 88 (1), pp. 273–282. DOI: 10.1115/1.3645828.

Wagner, W. and Pruß, A. (2002). „The IAPWS Formulation 1995 for the Thermodynamic Properties of Ordinary Water Substance for General and Scientific Use“. In: *Journal of Physical and Chemical Reference Data* 31 (2), pp. 387–535. DOI: 10.1063/1.1461829.

Yakubov, S., Cankurt, B., Maquil, T., Schiller, P., Abdel-Maksoud, M., and Rung, T. (2011). „Cavitation Simulations of the Potsdam Propeller Test Case“. In: *Proceedings of the 2nd International Symposium on Marine Propulsors*. Hamburg, Germany.


cavitation
compressibility
condensation shock
ship propeller
simulation
wedge
wave dynamics
vortex stretching
tip vortex
torque coefficient
wall-function
wetted flow
vapor cloud
void fraction
turbulence
viscosity
thermodynamics
two-phase
partial cavity
phase transfer
shock wave
sheet cavitation
numerical method
thrust coefficient
transition
Navier-Stokes equations
propeller wake
numerical simulation
Euler equations
inviscid
re-entrant jet
spectral analysis
sheet-to-cloud vapor
Rankine-Hugoniot
maximum pressure
implicit large eddy simulation
open-water
compressible dilatation
preconditioning
thesis
incompressible
RANS
pressure
shedding
fully-compressible
cavitation pattern
collapse detector
equilibrium
homogeneous mixture
explicit time integration
cavity dynamics
convective flow
collapse
density-based
cavitating flow
equation of state
experimental reference
instability
erosion
inertial effects
grid
aggressiveness
CATUM
barotropic
advance coefficient
boundary conditions
baroclinic torque
cavity
blade
ALE
test-section